The Development of a Numerical Human Body Model for the Analysis of Automotive Side Impact Lung Trauma

by

Kin F. Yuen

A thesis
presented to the University of Waterloo
in fulfillment of the
thesis requirement for the degree of
Master of Applied Science
in
Mechanical Engineering

Waterloo, Ontario, Canada, 2009

Author's Declaration

I hereby declare that I am the sole author of this thesis. This is a true copy of the thesis, including any required final revisions, as accepted by my examiners.

I understand that my thesis may be made electronically available to the public.

Kin F. Yuen

Abstract

Thoracic injury is the most dominant segment of automotive side impact traumas. A numerical model that can predict such injuries in crash simulation is essential to the process of designing a safer motor vehicle.

The focus of this study was to develop a numerical model to predict lung response and injury in side impact car crash scenarios. A biofidelic human body model was further developed. The geometry, material properties and boundary condition of the organs and soft tissues within the thorax were improved with the intent to ensure stress transmission continuity and model accuracy. The thoracic region of the human body model was revalidated against three pendulum and two sled impact scenarios at different velocities. Other body regions such as the shoulder, abdomen, and pelvis were revalidated. The latest model demonstrated improvements in every response category relative to the previous version of the human body model.

The development of the lung model involved advancements in the material properties, and boundary conditions. An analytical approach was presented to correct the lung properties to the in-situ condition. Several injury metric predictor candidates of pulmonary contusion were investigated and compared based on the validated pendulum and sled impact scenarios. The results of this study confirmed the importance of stress wave focusing, reflection, and concentration within the lungs. The bulk modulus of the lung had considerable influence on injury metric outcomes. Despite the viscous criterion yielded similar response for different loading conditions, this study demonstrated that the level of contusion volume varied with the size of the impact surface area.

In conclusion, the human body model could be used for the analysis of thoracic response in automotive impact scenarios. The overall model is capable of predicting thoracic response and lung contusion. Future development on the heart and aorta can expand the model capacity to investigate all vital organ injury mechanisms.

Acknowledgements

I would like to thank my advisor, Professor Duane Cronin, for the support, guidance and patience. I hope that his research in the biomechanics field continues to flourish. I would not have realized my full potential without his passion for teaching, research, and mentoring.

I am thankful for the financial support from my sponsors, General Motors, the Premier's Research Excellence Award, Auto 21, the University of Waterloo and the Department of Mechanical & Mechatronics Engineering. I greatly appreciate Dr. Yih-Charng Deng for providing the model and reviewing my work throughout this research.

Thank you goes to my colleagues and friends, Karla Cassidy, Steve DeMers, and Chris Thom whom I had shared all the ups and downs with as we find our own direction through our graduate career. Also, I would like to thank Steve Samborsky and Chris Salisbury who are always looking out for the younger ones.

I am especially thankful for the support of my family and friends who have shown unconditional support throughout this entire undertaking. A special thank you goes to Vera Lau and her family, who have continually encouraged me to push forward, and kept me motivated through the dark hours. I would like to thank my parents, Raymond and Alice, and my brother, John, who have supported me and allowed me to define my own path in life.

Table of Contents

List of Figures

List of Tables

List of Equations

Chapter 1
Introduction

1.1 Background

Thoracic trauma, particularly in side impact conditions, is an important issue to understand in order to improve occupant protection in vehicles. In 2007, there were approximately 6 million police reported crashes resulted in 41059 vehicle occupant fatalities and nearly 2.5 million injuries in the United States (NHTSA, 2007). Side collision as the initial point of impact accounted for approximately 25.3% of fatalities and 25.7% of injuries. In 2001, thoracic injuries accounted for 38% of fatalities and 59% of non-fatal injuries among side impact collisions (NHTSA, 2004). If a similar proportion of fatalities occurred in 2007, approximately 4000 deaths could be attributed to thoracic injuries from side impact collisions.

Major car manufacturers recognize the importance of safety to consumers. Side impact protection is considered one of the greatest challenges for designers since the distance available between the door and the occupant to absorb energy is short. The National Highway Traffic Safety Administration (NHTSA) recognizes the need to improve side impact protection and is in the process of proposing new side impact regulations. The new regulation will impose more severe impact conditions and require crash testing with anthropometric test devices that are more representative of the overall population.

Researchers have been conducting impact experiments on post mortem human subjects (PMHS) to investigate occupant injury mechanisms and tolerance since 1960. Although experimental research have been providing insight to the human response under impact and aided the development of several injury criteria, the knowledge that can be derived from the PMHS testing is somewhat limited in its precision. The experiments are often confined to a small group of PMHS that vary in body mass, stature height, and age,

making it difficult to draw a convergent conclusion that is applicable to the overall population. Each PMHS can only be used once for a single impact condition due to the destructive nature of the experiments, thus leading to a small dataset with high variability. The instrumentation of the experiment is also restricted to monitoring gross response of the human body such as body kinematics, chest deflection, and acceleration at limited number of locations; local response of individual organs and soft tissues related to the injury mechanism is often difficult to capture.

Vehicles are experimentally tested using anthropometric test devices (ATD) that are reusable and repeatable to mimic occupant response. They are used in all automotive impacts to evaluate vehicle crashworthiness and safety features of a vehicle design, however designing a vehicle using ATDs poses several implications. ATDs are designed to be biofidelic but the injury risk assessment is limited to a specific impact direction (i.e. frontal impact or side impact). The basis of the ATD's design is built upon statistical analyses of past PMHS experimental data to correlate ATD response to the injury risk of a particular body region. Insight to the actual injury mechanism at a local organ level is critical for the development of safety protection systems, but this insight is impaired by the shortcomings of the ATD design due to the challenges in capturing dynamic material properties of human tissue in an in-situ condition. Despite these drawbacks, ATDs are being designed with the best available information at hand.

Automotive manufacturers require significant resources and costs to conduct destructive crash tests to ensure new vehicles meet the governed safety standards. In addition, there is a need to develop in-depth understanding of injury biomechanics to ensure a new vehicle design attains highest possible safety rating. Numerical analysis can provide design information at a much lower cost than PMHS and ATD investigations. With technological advances in computing power, numerical modeling has become more advanced and feasible. Automotive manufacturers have been developing an advanced numerical analysis approach to complement experimental testing to better isolate various design factors that influence the crashworthiness of a vehicle.

1.2 Research Justification

Automotive manufacturers need to develop and utilize every tool available to improve the understanding on human response and injury tolerance to minimize traumatic injuries. The development of a numerical occupant model would be a valuable analytical tool to help guide research direction and eventually vehicle design. A developed finite element numerical human body model can produce representative response characteristics from a wide array of loading conditions with definite repeatability. Two primary advantages of such models are: Firstly, they can provide insight into the injury mechanism when evaluating different loading conditions. Secondly, they provide insight into the variability of the onset of injuries across the population quantitatively and quickly (for example, injury response variation based on the differences in bone properties).

The modeler needs to be aware of every detail and assumptions that goes into the numerical model. The downside to numerical modeling is the need for an exhaustive amount of evaluation and validation data. Any discrepancy between the model and the PMHS studies can highlight a particular area for improvement that is most relevant for research. The outcome of such experimental and analytical research, however, can significantly improve automotive safety.

Although computing power continues to increase, assumptions are still required to ensure the robustness of the numerical model and to keep the simulation time as short as tolerable. Assumptions are needed as part of the development process to identify relevant material properties or modeling aspects that are most influential in the human structural response under motor vehicle crash scenarios, these influential factors can then be analyzed in greater detail.

Frontal impact collision is the most dominant mode for occupant injury, while side impact and rear impact are secondary modes. Over 89% of the total fatalities from side impact associated with a serious thoracic injury which is equivalent to an AIS of 3 or greater (Thomas and Frampton, 1999). Keep in mind that injuries often occur in

combination that increases the likelihood of fatalities. Side impact collision poses a significant threat to occupants due to the severe nature of the loading condition; the crushable zone between the occupant and the vehicle exterior is the shortest in side impact compared to frontal or rear impacts. An analysis on the frontal and near-side lateral crash data from the CIREN database had revealed 34% of the occupants that sustained blunt chest trauma also had pulmonary contusion (O'Connor, 2009). A United Kingdom Cooperative Crash Injury study on lateral vehicle collisions had revealed 69% of all struck-side occupant fatalities sustained pulmonary contusion (Thomas and Frampton, 1999). The same motor vehicle collision (MVC) study also revealed that the economic cost associated with thoracic injuries was the second highest among survivors, and the highest among fatalities. The research presented in this thesis placed great emphasis on the development of a full human body model for the study of thoracic injury, particularly lung injury, in side impact conditions.

1.3 Research Objective and Scope

This research project ultimately has three goals. The first goal is develop a full human body model with representative geometry and constitutive material models. Deng et al. (1999) developed the first iteration of the detailed numerical thoracic model and incorporated representations of the spine, ribs, heart, lungs, and major blood vessels. Chang (2001) developed the second iteration by expanding the model with outer surface muscle enclosing the ribcage, upper limbs, along with several improved material models. Forbes (2005) developed the third iteration by integrating a pelvis, lower extremities, abdomen, and head. The makeup of the shoulder complex and various aspects of the thorax were developed with a focus on the accurate representation of the human anatomy. The model was evaluated against a variety of pendulum impacts and sled tests which demonstrated the capability of the model in predicting full body response particularly the thorax. The fourth and current iteration was focused on improving the overall model numerical stability and robustness. The mesh representation of various components was refined in the existing human body model to ensure convergent response. The contact

interface between components within the thorax was improved to ensure stress transmission continuity. Various material model parameters for components such as the ribs, costal cartilage, muscle tissue, and lungs were investigated to better represent tissue response under dynamic loading.

The second goal was to compare the model with the cadaver studies through a variety of impact scenarios. This comparison defined the latest state of the model after various modeling improvements, and also highlighted areas that still need to be addressed.

The third goal was to investigate injury mechanisms of the internal organs within the thorax region, and develop an approach to evaluate organ injury with emphasis placed on the lungs. The lungs, heart and aorta serve as boundary conditions to each other. During a side impact, the lungs are the first vital organ along the stress transmission followed by the heart and aorta. Given the high frequency of trauma victims sustained pulmonary contusion, this provides the motivation for the development of an lung model because it is on the critical path to reach the objective of predicting overall vital organ injury.

1.4 Organization of the Thesis by Chapter

This thesis is presented in a format that is similar to the development process of the human body model. Chapter 2 provides the latest statistics and trends related to automotive traumas that guided the research direction. The statistics on the global estimates of automotive injuries, crash direction breakdown, and occupant injury pattern were provided. This chapter also focuses on the background knowledge related to the anatomy, physiology, and injury mechanisms of the rib, lungs, heart and aorta from the automotive perspective. Emphasis was placed on the literature review for the lungs given the inherently complex nature of its makeup as an organ. The experimental studies that contributed to the understanding of the biomechanics and injury of each vital organ are highlighted. Lastly, this chapter reviews the development of various thoracic injury criteria; a summary of all the thorax tolerances in frontal and side impact to date is provided.

Chapter 3 details the development of the human body model that builds upon the background knowledge presented in Chapter 2. An analysis of lung contusion highlighted several areas for improvement in the early development of this model. These improvements were implemented in subsequent developments and provided a more accurate response of the thorax and internal organs. Chapter 2 highlighted some of the missing information that was needed to define the physical properties of the lungs. This chapter illustrates a theoretical approach to derive these properties indirectly based on various literatures. Since experimental studies on the lungs were often conducted with reference to the stress-free state, this chapter describes the development of lung material parameters selection and the theoretical approach that corrects the lung model from the stress-free state to the in-situ condition.

Chapter 4 presents the validation between the thorax that reflects the current state of the human body model against cadaver studies using three pendulum impact and three sled impact scenarios. Validation, in this context, means the evaluation of the model performance for which the components have not been calibrated or tuned for the particular impact condition that is being compared. This chapter also describes the modeling techniques to simulate the experiments. The model response is compared to the experimental data, highlighting areas that require improvement. The simulated results of the other body regions are included in Appendix A.

Chapter 5 details a lung contusion evaluation method, justifications of different candidate injury metrics, a method to determine injury thresholds, and an analysis of lung contusion using various impact scenarios. The dynamic response of the lung model is discussed, and the limitations of the model are highlighted.

Chapter 6 summarizes the overall conclusions and recommendations for the model. The current state of the model is discussed in terms of the body response and the lung response as an organ. This chapter also outlines recommendations that are critical to the future development of the model.

Chapter 2
Literature Review

2.1 Introduction

This chapter presents the relevant background to understand how, why, and when injuries occur, and how mechanical properties of various organs and tissues were incorporated into the numerical human body model. The thorax is made up of a skeletal structure protecting vital organs such as the heart and lungs. Investigating thoracic response is complex in nature since the body is made up of many tissues that each have their unique mechanical characteristics. The interaction and connectivity of the vital organs with other organs added another degree of complexity.

This chapter covers the four main branches of impact biomechanics that are related to the development of the human body model; mechanical response, injury mechanisms, tolerance, and the biofidelity of the surrogate, which is referring to the numerical model in this thesis. Automotive crash statistics are presented to identify which types of injury that this research should focus on to yield the greatest gain in automotive safety. The anatomy and physiology of the human thorax are presented to establish the fundamental basis for the modeling development. The background research into the mechanical properties of tissue is presented; it describes the features of the tissue properties which outlines the requirements of the material models. The injury mechanisms and the consequences of the injury associated with each organ within the thorax are reviewed. The historical development of injury criteria is reviewed and various injury criteria enforced by the current governing body regulations are summarized.

2.2 Automotive Crash Statistics

Global Estimates of Road Traffic Injuries

Automotive trauma continues to be a major health challenge and often overlooked by the public. A proactive collaborative effort by automotive manufacturers, researchers, and government is needed to sustainably prevent injuries resulted from vehicle-related crashes. The latest study by the World Health Organization (WHO) had estimated 1.18 million fatalities in road crashes and as many as 50 million were injured worldwide in 2002 (WHO, 2004). Road traffic injuries were the 9th contributor to the global burden of disease and injury in 1990, and were expected to become 3rd leading contributor by 2020 (Murray, 1996). The road traffic deaths predominantly associated with the age group of 15 to 29 and male as shown in Figure 2.1. Road traffic fatalities were the 2nd leading cause of deaths among the age group of 5-14, 15-29 year old, and 3rd among 30-44 year old; Males accounted for 73% of road traffic deaths worldwide (WHO, 2004).

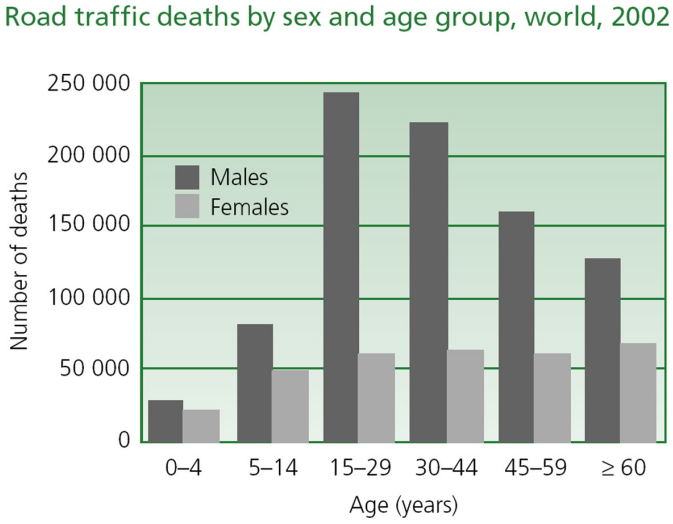

(Reproduced from WHO, 2002)

Figure 2.1: Road traffic fatalities by gender and age group, world, 2002

Road traffic death rates have been decreasing in high-income countries such as the United States, Canada, Australia, Japan, and Britain over the past 40 years; The low-income and middle-income countries have been increasing substantially and accounted

for approximately 85% of the road traffic deaths as of 2002 (WHO, 2004). Figure 2.2 gives an overview of mortality rates in the WHO regions.

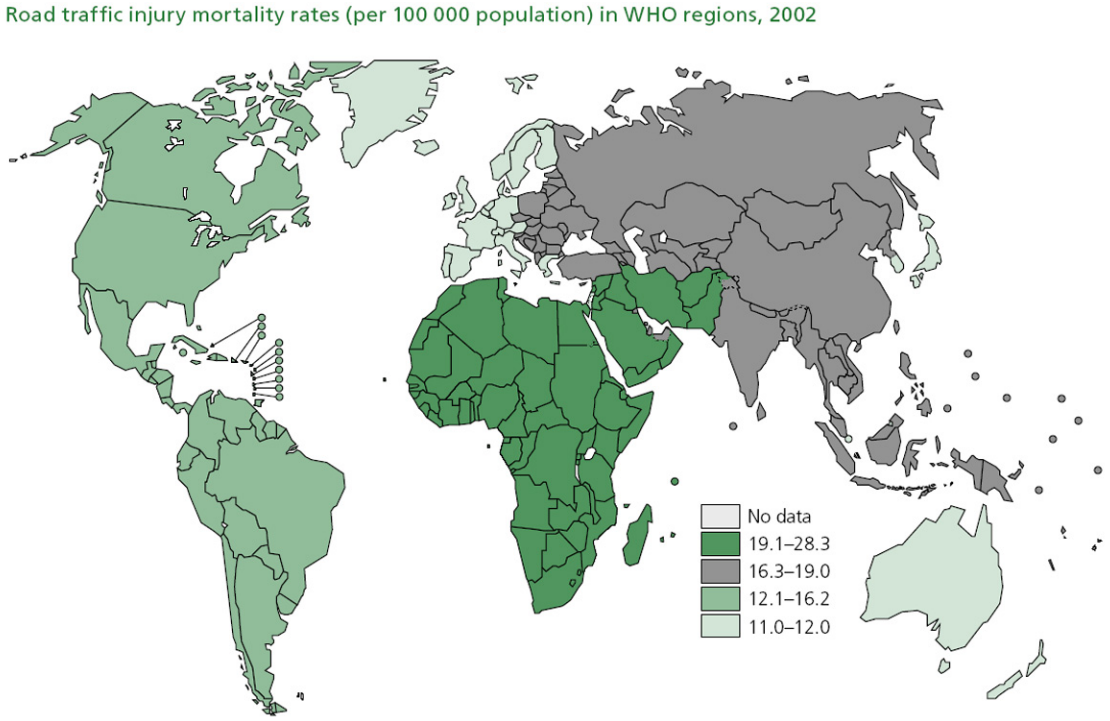

(Reproduced from WHO, 2002)

Figure 2.2: Global estimates on mortality rates

The economic cost of road crashes and injuries was estimated to be US$ 518 billions in 1997 (WHO, 2002). Despite the disproportion in road traffic deaths between the low & mid-income countries and the high-income countries, highly motorized countries like Australia, Japan, New Zealand, North America, and the western European countries accounted for US$ 453 billions of the economic cost, and the developing countries attributed to US$ 64.5 billions. A study by Blincoe et al (2002) had found the economic cost totaled US$ 230.6 billion dollars in the United States alone. The direct medical costs due to injuries were approximately US$ 32.6 billion dollars. Road traffic injuries have caused an estimated value of US$ 12.5 billion annually in developing countries like China, which is almost four times its own country's annual healthcare budget (WHO, 2002).

Trend in Automotive Trauma

Although the number of fatalities in the US remained relatively stagnant from 1975 to 2006 at approximately 40,000 fatal crashes a year, the fatalities per 100 million vehicle miles traveled had declined from 5.50 to 1.41 over the same period of time (NHTSA, 2006). Alcohol-related fatalities continued to be a dominant factor that accounted for 41% of all fatalities (NHTSA, 2006). The majority of persons killed in traffic crashes were drivers (54%) as shown in Figure 2.3.

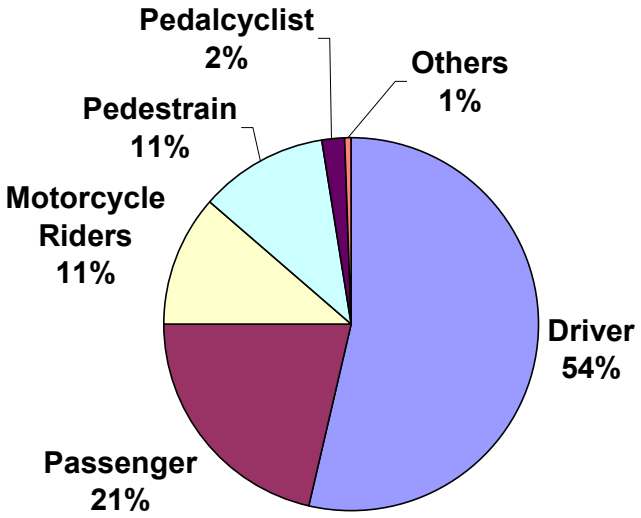

(Reproduced from NHTSA, 2006)

Figure 2.3: 2006 - persons killed in traffic crashes

Safety features such as the seatbelt do play an important role in reducing road traffic injuries, fatalities and its associated costs. The crash statistics in 2006 showed that 29.9% sustained injury and 0.4% resulted in fatalities among the occupants who used a seatbelt, compared to 52.6% sustained injury and 6.1% resulted in fatalities among those who did not use a seatbelt (NHTSA, 2006). Blincoe et al (2002) estimated that seatbelt prevented 11,900 fatalities, 325,000 serious injuries, and saved $50 billion in associated costs to the society in the year of 2000.

Impact Direction

The National Highway Traffic Safety Administration (NHTSA) summarized statistics on police-reported motor vehicle crashes broken down by initial point of impact (NHTSA,

2006). Frontal impact is predominantly associated with fatalities and injuries that involved single and multiple vehicles collisions as shown in Figure 2.4 and in Figure 2.5, respectively.

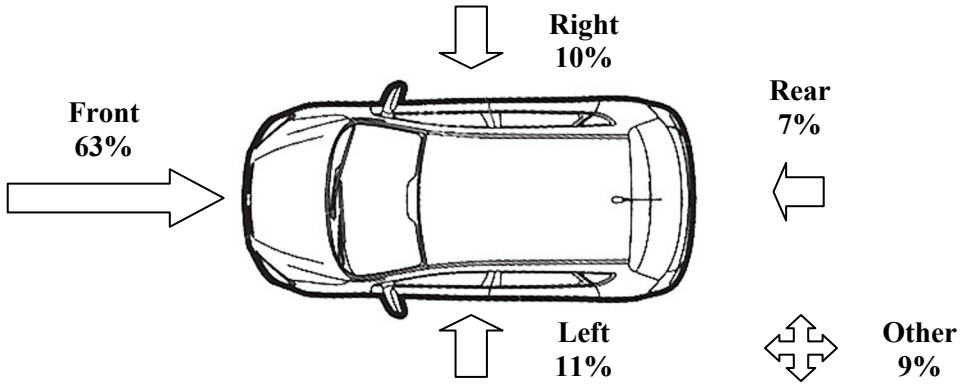

(Adapted from NHTSA, 2006)

Figure 2.4: Fatal crash distribution by initial point of impact

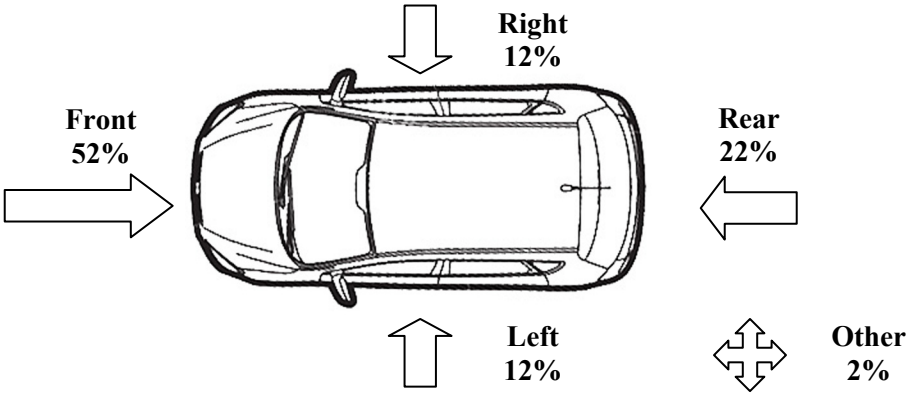

(Adapted from NHTSA, 2006)

Figure 2.5: Injury crash distribution by initial point of impact

Side impact accounted for 21% of all fatal crashes and 24% of all injury crashes. Rollover occurrences were associated with 21.6% of the involved vehicles among fatal crashes and 5.3% among injury crashes; a total of 274,000 vehicles had rollover (NHTSA, 2006). Any correlation between the initial point of impact and rollover occurrences is unclear, but utility vehicles experienced the highest rollover rates in fatal and injury crashes.

Side Impact Location & Velocity

Off-angle side impacts at the ten and two o'clock directions appeared to be the most harmful, which accounted for 48% of total side crashes and contributed to 56% of the maximum AIS = 3+ injuries (Yoganandan, 2007). In contrast, the three and nine o'clock directions contributed to 39% of the injuries. An analysis on the compiled crash databases from Australia, the United Kingdom and the United States had revealed that hospitalized and fatal occupants in side impact suffered an average change in vehicle velocity (ΔV) of 9.2, 9.7 and 10.7 m/s, respectively (Yoganandan, 2007). For collisions with narrow objects, the average ΔV was 5.3 m/s for the maximum AIS = 3+ survivors based on the UK database.

Injury pattern and severity

The serious to fatal injury distribution due to side impact collisions can be broken into four main regions: head/face, Thorax, abdomen, and others. The thorax region accounted for 53% of the serious to fatal injuries as shown in Figure 2.6 (NHTSA, 2001).

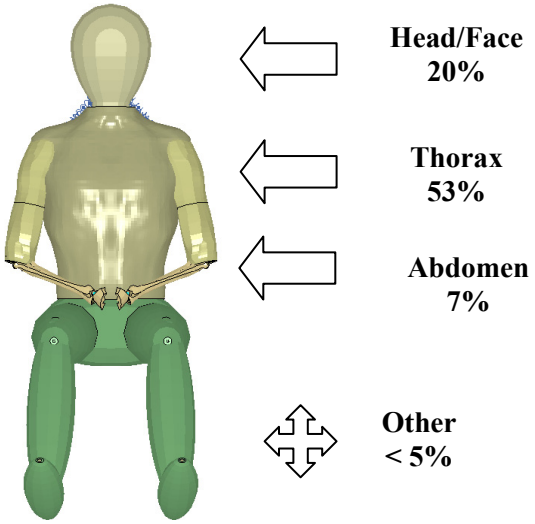

(Adapted from NHTSA, 2001)

Figure 2.6: Fatal injury distribution – side impact

Thomas and Frampton (1999) conducted an in-depth injury pattern analysis in side collisions based on the data collected from the United Kingdom Cooperative Crash Injury Study. The thorax region was the 2nd most frequent associated with the moderate or

higher injury occurrences (AIS 2+) and attributed the 2nd highest in associated economic cost among the Maximum AIS 3+ survivors as shown in Figure 2.7. The thorax region was the most frequent associated with serious injuries (AIS 3+) and attributed the most economic costs among fatalities. The associated economic costs to injuries and fatalities were gauged by using the HARM scale as developed by Malliaris et al (1985), which estimates the percentage of the total economic costs associated with each body region.

Body Regions	HARM Scale %
Head	16
Face	2
Neck	9
Thorax	23
Abdomen	4
Upper Extremities	12
Lower Extremities	34

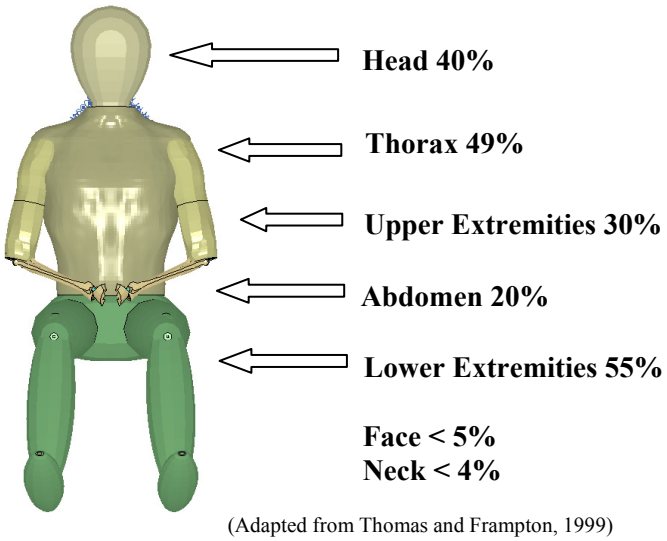

(Adapted from Thomas and Frampton, 1999)

Figure 2.7: AIS 2+ injury pattern of the MAIS 3+ survivors

Body Regions	HARM Scale %
Head	25
Face	1
Neck	17
Thorax	34
Abdomen	8
Upper Extremities	4
Lower Extremities	11

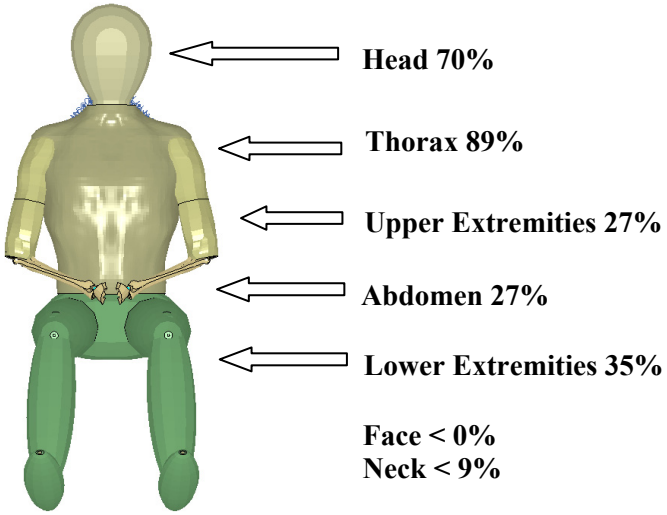

(Adapted from Thomas and Frampton, 1999)

Figure 2.8: AIS 3+ injury pattern of the fatalities

Table 2.1: Anatomical location of thoracic injuries among struck-side occupants

Anatomical Location	MAIS 3+ Survivors with AIS 2+ injuries %	Fatalities with AIS 3+ injuries %
Lungs	11%	69%
Ribcage	42%	52%
Thoracic veins/arteries	1%	31%
Heart	2%	15%
Diaphragm	2%	15%
Esophagus / Trachea / Bronchus	0%	3%
Thoracic spine	1%	2%
Other	3%	3%

(Adapted from Thomas and Frampton, 1999)

Thomson and Frampton (1999) also categorized thoracic injuries based on anatomical locations among 148 MAIS 3+ survivors (with AIS 2+ injuries) and 124 fatalities (with AIS 3+ injuries) and are shown in Table 2.1. Lung injury was correlated to 69% of all struck-side occupant fatalities. The data showed that at least 45 fatalities (36%) with an AIS 3+ thoracic injury were not associated with AIS 3+ ribcage injury. This suggested that fatal soft tissue thoracic injuries do occur at a considerable frequency which may not correlate with apparent skeletal fractures. Lung injuries among MAIS 3+ survivors were found to be low and may not be identified in these cases. Miller (2001) had cited that lung contusion may not be identified during admission but may become critical 24 hours after the trauma.

2.3 Thorax

Blunt impact deforms biological tissue in ways that alter normal bodily function and/or damage the integrity of anatomical structures (Fung, 1993). Any deformation to the human body is a form of impact energy transfer mechanism. Any means to monitor the path of energy/stress transfer and the intensity can provide insight to the injury mechanism. The following sections discuss the anatomy and physiology of the thoracic organs and highlight the different mediums that govern stress transmission and interaction within the thorax. The knowledge and the detailed thoracic numerical model presented here were built upon previous research developments made by Deng et al (1999), Chang (2001), and Forbes (2005).

Anatomical References

A specific convention as illustrated in Figure 2.9 is used to reference anatomical planes and orientation for a human body throughout this document. The anatomy field often refers to body sections by three imaginary planes: the coronal plane, the transverse plane and the sagittal plane. Three axes are used to describe the relative direction and position with respect to each imaginary plane. Each direction axis can be identified by the intersections between any two of the three planes. The third plane is defined as the midplane of each axis. Three sets of terms are used to describe relative direction of each axis: ventral-dorsal, lateral-medial-lateral, and cranial-caudal. Ventral – dorsal are opposite of each other, and are also referred as anterior – posterior, respectively. For the axis created by coronal and transverse plane, the term lateral is defined as the direction away from the sagittal plane. The medial term is referenced at the sagittal plane. Cranial – caudal are opposite of each other, and can be referred as superior and inferior, respectively.

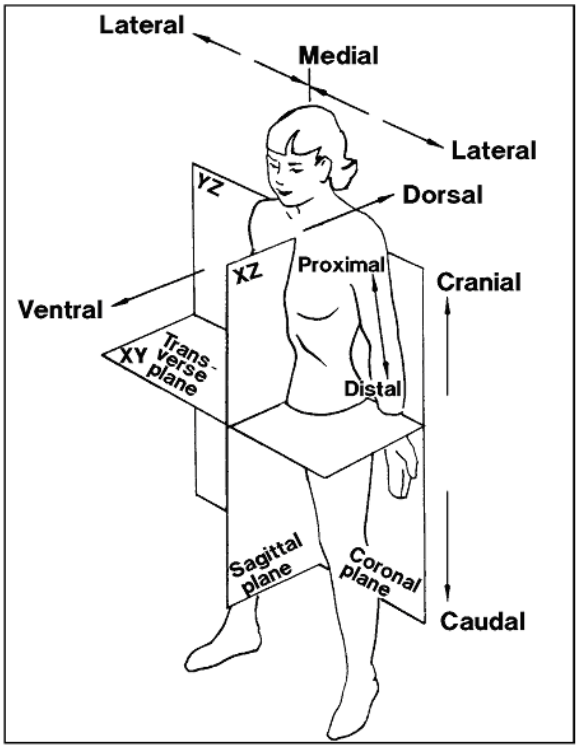

(Reproduced from NASA, 1995)

Figure 2.9: Anatomical reference planes and orientations

Three more anatomical terms, superficial, intermediate and deep are used to describe a section relative to a body surface. Superficial describes a section near the surface. Deep refers to a section away from the surface. Intermediate describes a section that is between superficial and deep.

A human body is typically subdivided into multiple segments as illustrated in Figure 2.10. Biomechanics in the automotive field emphasizes five major segment groups including the head, neck, thorax, abdomen, and extremities (upper and lower). The experimental data referenced throughout this document is typically referred and scaled to a 50^{th} percentile male subject.

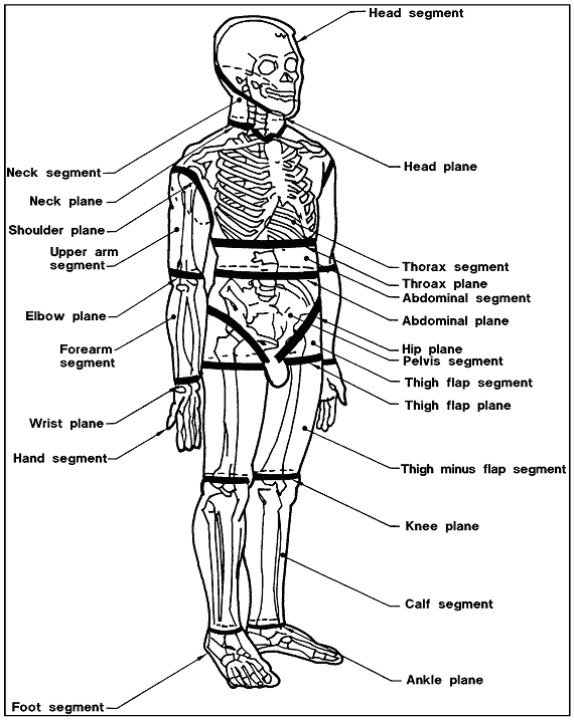

(Reproduced from NASA, 1995)

Figure 2.10: The reference segments of the body

The description of the reference segments provided here is best described by the NASA Man-Systems Integration Standard (NASA, 1995); it provides definitions with respect to clearly defined anatomical landmarks. The thorax segment is bounded by the neck plane, the shoulder plane, and the thorax plane. The neck plane is defined as a compound plane

in which a horizontal plane originates at cervical and passes in the anterior direction to intersect with the second plane. The second plane originates at the lower of the two clavicle landmarks and passes in the superior and posterior direction at a 45 degree angle to intersect the horizontal plane. The shoulder plane is originated at the acromion landmark and passes at the inferior and medial direction through the anterior and posterior scye point marks at the axillary level. The thorax plane is a transverse plane that originates at the 10th rib midspine landmark and passes horizontally through the torso. The following sections describe the anatomy and physiology of various major components including the thoracic ribcage, lungs, heart, and aorta.

2.3.1 Ribcage

Anatomy and Physiology of the ribcage

The thorax refers to the space enclosed by the ribcage containing vital organs. The skeleton of the thorax protects the principal organs of respiration and circulation. It is conical in shape, being narrow above and broad below. The thoracic cage is composed of twelve pairs of ribs, twelve thoracic vertebrae, a sternum, and costal cartilages as illustrated in Figure 2.11. The anterior face of the thorax is formed by the sternum and costal cartilages. The lateral faces are formed by the ribs separated from each other by the intercostal spaces, which are occupied by the intercostal muscles and membranes. The posterior face is formed by the twelve thoracic vertebrae that connect to each rib. The skeleton of the thorax is covered by various surface muscle groups and most skeletal part is concealed if muscles are strongly developed (Gray, 2000).

The ribs are typically made up of trabecular bone surrounded with a thin layer of cortical bone. The first seven ribs connect from the thoracic vertebral column through three facets to the sternum through costal cartilages and are referred as true or vertebro-sternal ribs. The remaining five are referred as false ribs. Three of the false ribs have their connecting costal cartilages tied to the rib above and merged with the seventh true rib's costal cartilage. The last two of the false ribs are also referred as the floating ribs, they

have their posterior ends connect to the vertebral column and their anterior ends are free floating.

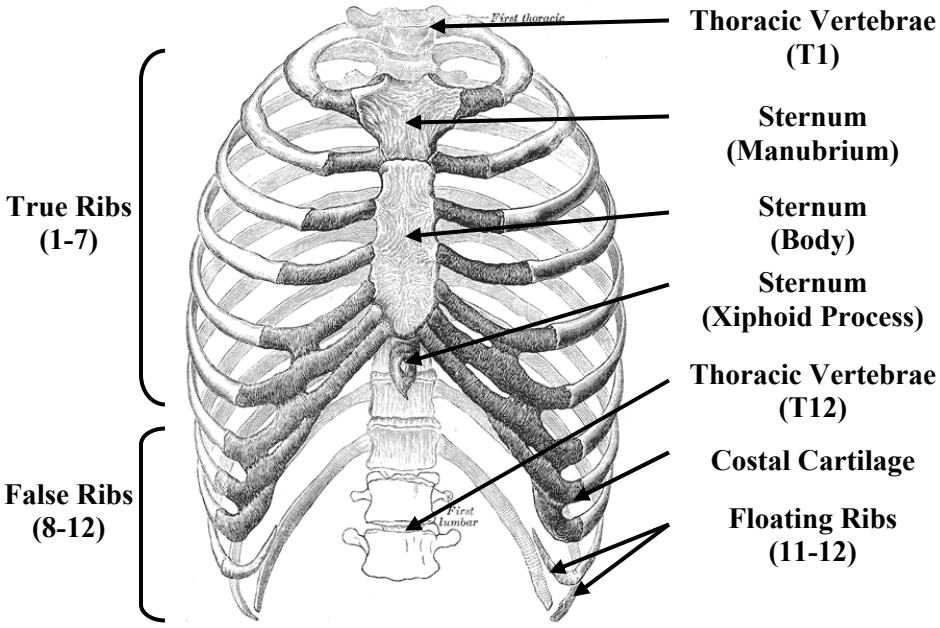

(Adapted from Gray, 2000)

Figure 2.11: Thoracic cage skeletal structure

The sternum is made up of trabecular bone surrounded with a thin layer of cortical bone. The sternum is an elongated bone which can be divided into three parts: the manubrium, the body, and the xiphoid process. The manubrium is connected to the first ribs and the clavicles. The body is connected with the second to seventh ribs. The xiphoid process is a thin and extended section that is not tied to any ribs.

The costal cartilage is made up of hyaline cartilage and provides relatively flexible movement upward and downward between the ribs and sternum. The lateral end of each cartilage is continuous with its respective rib's osseous tissue. The medial end of the first cartilage (1^{st} rib) is continuous with the sternum; the medial ends of the six succeeding cartilage (2^{nd} to 7^{th} rib) are connected through facet joints, also known as costo-sternal articulations. The medial ends of the eighth, ninth, and tenth cartilage (8^{th} to 10^{th} rib) are pointed and connect to the cartilage immediately above. The medial ends of the eleventh and twelfth cartilage (11^{th}, 12^{th} rib) are pointed and free.

The thoracic vertebral column is made up of 12 vertebrae. Each vertebra increases in size and is also labeled in sequence from superior to inferior. Each vertebra is made up of two regions: a body and an arch. The body is the massive anterior portion of the vertebra that supports the weight of the human body as shown in Figure 2.12. The arch forms a circular section posterior to the vertebra body with a large opening which the spinal cord passes through. The arch also has three processes: two transverse processes that protrude at both sides, and a spinous process that protrudes backward. The thoracic vertebra generally has one facet and two demi-facets for the head of the ribs. The connections between the ribs and vertebrae are also known as costo-vertebral articulations. All vertebrae have similar bony structure made up of trabecular and cortical bone.

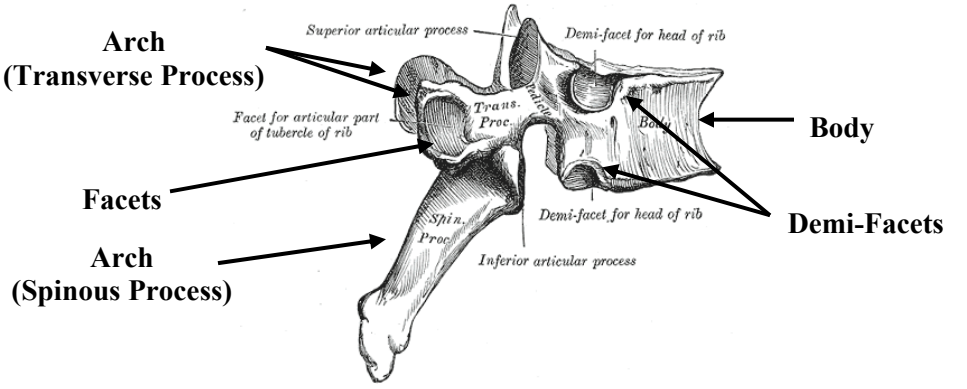

(Adapted from Gray, 2000)

Figure 2.12: Thoracic vertebra – side view

Each rib is made up of an interior cancellous core, a porous material made up of an open latticework of tubular and platen structure that is also called trabeculae, and an exterior layer of cortical shell that vary from .60 to 1.22 mm on average (Kemper et al, 2007). Cortical bone is a solid, stiffer material that is also known as the compact bone. Within an individual, there is little variation in material properties such as modulus of elasticity, ultimate stress and ultimate strain; the response variation of a rib was attributed to local changes of the rib geometry (Kemper et al, 2007).

Bones are often classified as a composite material that is orthotropic (as in the mechanical properties are different along each of the three axes, 9 independent elastic

constants) or transversely isotropic (as in the properties are the same in one plane and different in the direction normal to this plane, 5 independent elastic constants) (Cowin, 2007). Past studies have shown that both cortical and cancellous bone exhibit viscoelastic properties (McElhaney, 1966; Wright and Hayes 1976, Wood 1971, Mow and Hayes, 1997; Cowin and Doty, 2007). Previous studies have shown that the cortical bone's elastic modulus and the ultimate strength are strain-rate dependent (Mow and Hayes, 1997).

Bones can be characterized by a typical stress-strain curve behavior with a linear elastic region, a yield point, a relatively linear plastic region and a failure point. Bones do not present a significant amount of yielding prior to fracture and its failure point is correlated to the ultimate strength of the bone. The ultimate strength decreases when the loading angle varies from the bone's long axis (Cowin, 1987). Its variation in load carrying capacity is fundamentally related to the orientation of the collagen fibers that make up the bone tissue. The yield stress and ultimate stress are higher in compression than in tension (Mow and Hayes, 1997; Cowin, 1987).

Thoracic Cage Injury

The ribcage is often subjected to blunt impacts that may lead to rib fracture and flail chest. It is most probable that the rib bending fails on the tensile side of the ribs (Nahum & Melvin, 2002). When subjected to bending load, the tension side of the rib fails along the direction that is perpendicular to loading, and the compression side fails along a diagonal or oblique plane.

Rib fracture itself is not life threatening, but how and where fractures occur may indicate severity of trauma and organ injury in the vicinity. Visceral injury can occur without apparent ribcage injury at a low compression and high velocity loading that is often seen in side impact (Thomas and Frampton, 1999). There is additional risk if the fractured rib creates an open wound, or inward, possibly leads to further soft tissue injury to the lung,

heart, blood vessels, nerves, etc. Rib fractures tend to occur at impact site and at the angle of the rib, where the rib shows the greatest curvature (Pike, 1990).

Rib fractures that cause open wound increases the likelihood of pneumothorax (where a break in the visceral pleura causing air accumulation in the pleural space and interfere with breathing), lung collapse and/or infection. Flail chest is a severe case of multiple rib fractures, where at least three successive ribs fracture at two points allowing significant portion of the ribcage relatively unconstrained and impairing the respiratory function.

Costochondral separation occurs when a single rib separate from the costal cartilage. Although it is not life threatening, it can induce discomfort and impair breathing (Chapon, 1984).

Sternum fracture commonly occurs with occupant impacting the steering wheel (Chapon, 1984). However, modern safety features with seatbelts, airbag and collapsible steering column have mitigated the likelihood of such injury.

Mechanical Properties

The mechanical properties across the population have a large variation due to factors like gender, age, genetics, disease, diet, and hormone levels. The structural response variation between individuals is compounded with geometrical differences (Kemper, 2007). Extensive research has been focused on the response and failure characteristics of cancellous and cortical bone based on numerous loading patterns since the 1960s. Early work done by Yamada (1970) had demonstrated that bone's ultimate strength and ultimate deflection decrease with age. The yield strength and elastic modulus decrease with age at 2% per decade in logarithmic scale from age 20 to 90 (Mow and Hayes, 1997). This decrease is attributed to bone mineral density loss over time, thus diminish the thoracic cage ability to absorb energy during impact at old age.

Since bone is typically made up of either cancellous or cortical bone. Experimental data can be drawn from various skeletal parts of the body. It is often difficult to interpret

mechanical properties due to variation as mentioned earlier; researchers often investigate a dominant failure mode such as tension, compression or three point bending. Some experiments were designed to isolate a specific component of the bone properties, or interpret mechanical properties based on a whole bone by treating it as a continuum material for a particular loading mode.

Yamada (1970)'s work remains as a consistent source for elastic moduli and failure properties of compact, cancellous, and whole bone of both human and animals in tensile, compressive, bending and torsion modes.

Granik and Stein (1973) investigated the elastic modulus and ultimate strength of the 6^{th} and 7^{th} rib through simple bending tests on four inch segments. The results suggested that the derived elastic modulus and ultimate strength of rib bone were 15% to 50% lower than for long bone.

Schultz et al (1974) investigated whole ribs by securing the vertebral end and loading the sternal end with .25 kg incrementally to .75 kg. Each rib was loaded 6 directions, medial and lateral, superior and inferior, anterior and posterior. These results have been used for validating the rib numerical model by Deng et al (1999).

Yoganandan and Pintar (1998) conducted simply supported bending tests similar to Granik and Stein (1973); however the elastic modulus derived from the experiments were conflicting between the two sources.

Kemper (2007) believes the differences in results comparing to previous experimental work by Granik & Stein (1973) and Yoganandan and Pintar (1998) were attributed to the viscoelastic properties, loading rate and differences in the method used to calculate the elastic modulus. Granik & Stein (1973) and Yoganandan and Pintar (1998) calculated the elastic modulus based on the impactor displacement, while Kemper (2007) calculated the elastic modulus and the bending stress through strain gauge. Funk et al (2004) reported the material properties can be under predicted by approximately 40% if impactor

deflection data is used instead of strain gauge data. The calculation method for three-point bending tests often requires assumptions in the mathematical formulation and correction factors for irregular cross-sectional geometry which lead to conflicting properties among experiments (Kemper, 2007). The elastic modulus and ultimate stress do not vary significantly by thoracic region or rib level; the regional variation in strength is largely due to changes in geometry (Kemper, 2007).

Material Model

Deng (1999) derived the original rib material model based on the material properties of cortical and trabecular bone from Mow and Hayes (1991). Deng created a rib model with cortical and cancellous bone modeled separately and a rib model with a single continuum material model with the aim to decrease computational cost. The rib model was validated to Schultz's (1976) experiment. The elastic modulus of the single continuum material model was found to be higher than the cortical bone material properties, although the two rib models exhibited comparable characteristics as those reported by Schultz (1976). This difference was attributed to the single point numerical integration scheme.

Table 2.2 summarized material constants extracted from Mow and Hayers (1997) which were used as the basis for the current human body model. The rate-dependencies of the elastic modulus and the ultimate stress can be characterized by a straight line in a logarithmic scale according to the data presented by Wright and Hayes (1976) as shown in Figure 2.13. In normal activities, bone is subjected to strain rates that are generally below 0.01 sec^{-1} (Mow and Hayer, 1997). Over a wide range of strain rates (from .001 to 1000 sec), the ultimate tensile strength of cortical bone increases approximately by a factor of three and the modulus increases by a factor of two (Mow and Hayer, 1997). This strain-rate dependency effect is incorporated into the material model and is described in Chapter 3.

Table 2.2: Material constants for the bones at $\dot{\varepsilon}$=1 s^{-1}

Material Property	Cortical Bone	Trabecular Bone
Density, kg/m^3	1800	1150
Young's Modulus, GPa	24	0.24
Yield Stress, MPa	200	2.0
Modulus in the Plastic Region, GPa	2.2	0.022
Ultimate Stress, MPa	220	2.2

(Adapted from Mow and Hayers, 1997)

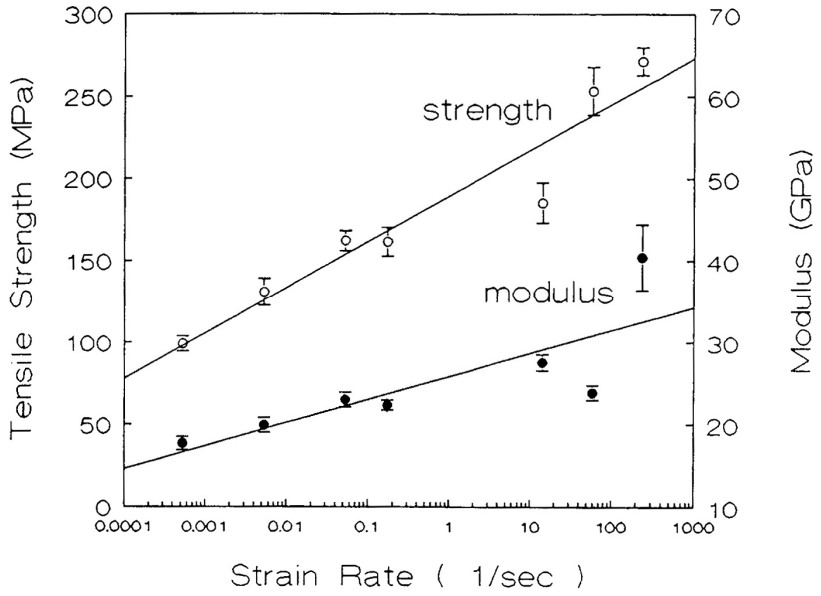

(Reproduced from Wright & Hayes, 1976)

Figure 2.13: The influence of loading rate on cortical bone's properties

Density

The cancellous bone consists of sponge like structure with the true density varies from 1050 to 1500 kg/m^3 (Mow and Hayes, 1997); the apparent density, the measurement of mass per unit volume including the voids which are inherent to the material, ranges from 100 to 1000 kg/m^3. The cortical bone consists of compact bony tissue with a true density of 1875 to 1975 kg/m^3 with apparent density of 1750 to 1950 kg/m^3. Since the finite element model uses a single continuum material model to represent the rib, the combined density was calculated based on the rib cross-section data from six cadavers as summarized in Table 2.3 (Kemper, 2007) and the apparent densities data from Mow and

Hayes (1997). The calculated density based on these two sources estimated to be 1740 kg/m^3 +/- 20.

Table 2.3: 4th to 7th ribs cross-section data summary

Region	Cortical Area (mm^2)	Trabecular Area (mm^2)
Anterior (n=24)	18.2 +/- 3.2	2.0 +/-1.2
Lateral (n=24)	23.2 +/- 4.9	2.6 +/-1.2

(Adapted from Kemper, 2007)

2.3.2 Lungs

Anatomy of the Lungs

The respiratory system consists of the larynx, trachea, bronchi, lungs, pleurae, and mediastinum as illustrated in Figure 2.14. The larynx is a cartilaginous structure at the top of the trachea, also known as a "voice box". The trachea is a membranous tube that conveys inhaled air from the larynx (located at the height of 6th cervical vertebra) into the chest cavity where it divides into two main tubular branches known as the primary bronchi. The division of the trachea occurs at the fifth thoracic vertebra (SAE, 1970).

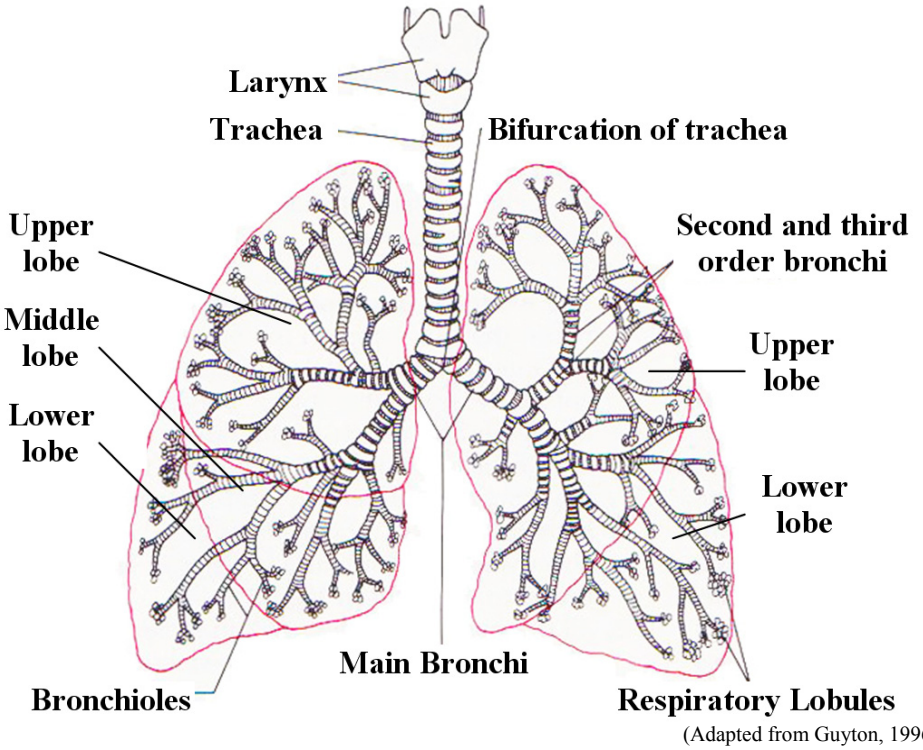

(Adapted from Guyton, 1996)

Figure 2.14: Lung lobes and bronchial tree

The primary bronchi branch air into each lung. The lungs reside on either side of the thorax, separated by the heart and other contents of the mediastinum. Each bronchus divides into smaller second order bronchi forming a pathway to each lobe of the lung. The right lung is divided into three lobes: the upper, middle and lower. The left lung is divided into two lobes: the upper and lower.

The idealized hierarchy of the human airway is best illustrated by Weibel's model as shown in Figure 2.15. In order of sequence, the air exchange occurs from the trachea, bronchi, bronchioles, terminal bronchioles, respiratory bronchioles, alveolar ducts, to the alveolar sacs. The bronchiole subdivides into two or more respiratory bronchioles throughout the entire organ. The respiratory bronchiole connects to some of the alveolar sacs directly and some indirectly through the alveoli ducts. The walls of the alveolar sacs have numerous rounded projections which are the alveoli.

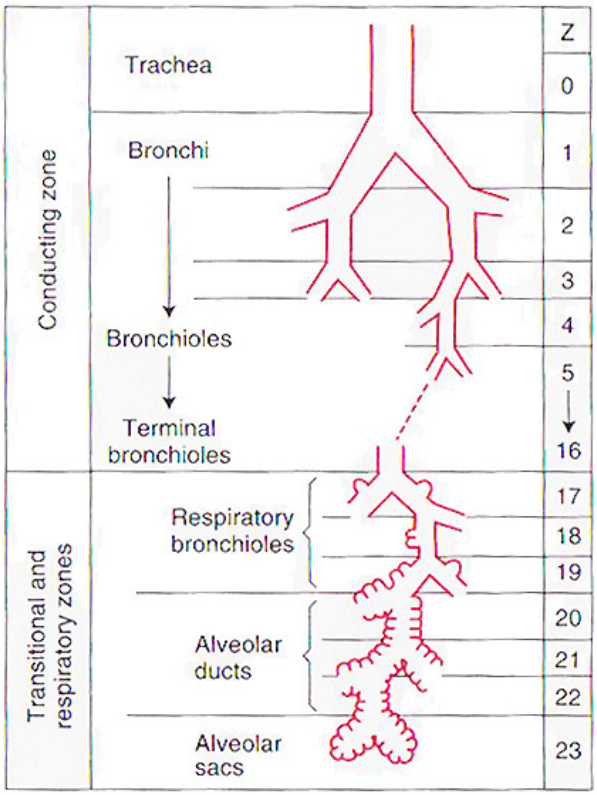

(Reproduced from West, 2005)

Figure 2.15: Weibel's idealization of the human airways

The lung contains approximately 300 million alveoli that have an estimated surface area of 600 square feet (55.74 square meters) (SAE, 1970). The right lung (625 g) is larger in size than the left (567g) (Gray, 2000). The right lung is typically shorter in the superior/inferior direction to accommodate the liver. The left lung is typically narrower in the lateral-lateral direction to accommodate the heart as it inclines to the left.

The substance of the lung is of a light, porous, spongy texture, also known as the parenchyma. The lung is composed of an external thin pleura, a subserous areolar tissue and the pulmonary substance. The subserous areolar tissue consists of mainly elastic fibers, made up of the entire surface of the lung and extends inward between the lobules. The separation between the three lobes on the right lung can be identified by a horizontal fissure and an oblique fissure as shown in Figure 2.16. The separation of the two lobes on the left lung can be identified by an oblique fissure. The interlobar surfaces are covered with the visceral pleura where the lobes contact one another. The lobes can slide against one another; the entire lung slides within the thoracic cavity (Guyton, 1996).

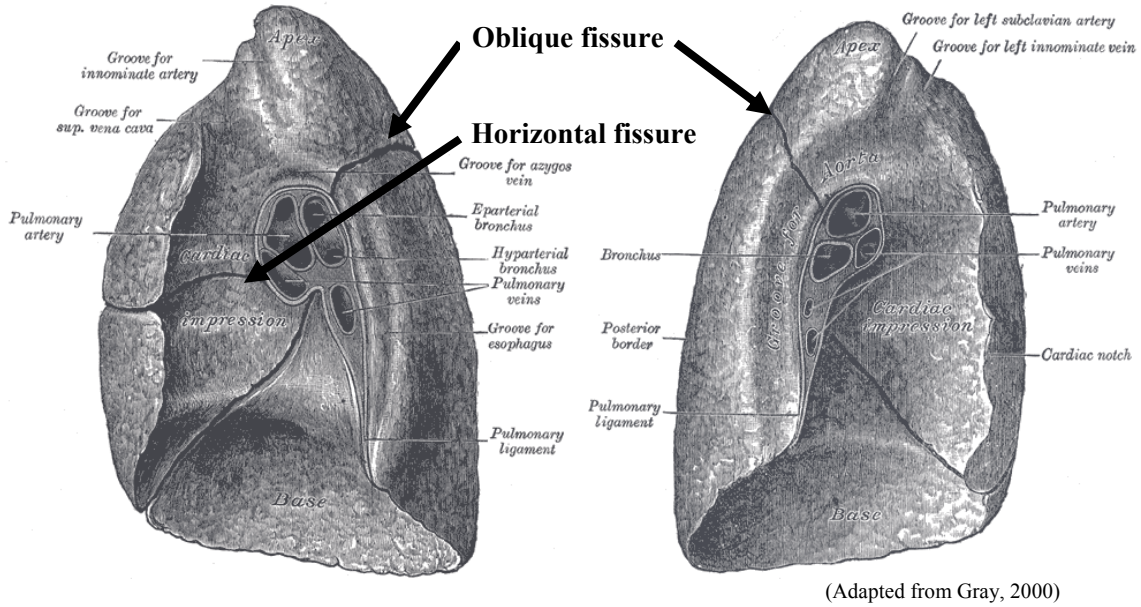

(Adapted from Gray, 2000)

Figure 2.16: Lateral view of the right and left lung

The lobes are characterized by a discrete connection with the first subdivision of the bronchial tree. The vascular, nerve and lymphatic supply from the hila to each lobe has

minimal connections with other lobes and is a relatively independent functional unit. The lobe is subdivided into multiple bronchopulmonary segments and each segment has a similar functional independence as the lobe. There are ten bronchopulmonary segments in the right lung (3 in upper lobe, 2 in middle lobe, 5 in lower lobe), and ten segments on the left (5 in upper lobe, 5 in lower lobe). Further subdivision of each segment becomes the secondary lobules.

The parenchyma is composed of secondary lobules that vary in size, connected together by the interlobular areolar tissues. Each secondary lobule is composed of several primary lobules. The primary lobule is referred as the anatomical unit of the lung, which consists of alveoli connecting with the alveolar ducts, blood vessels, lymphatics and nerves as shown in Figure 2.17.

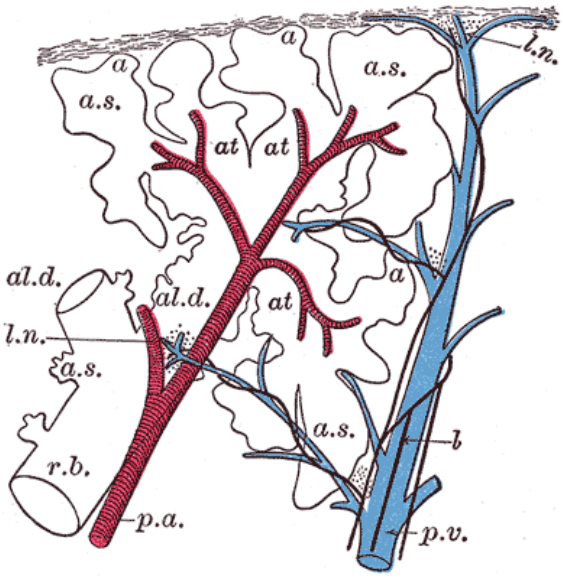

r.b.	respiratory bronchiole
al.d.	alveolar duct
at	atria
a.s.	alveolar sac
a	alveolus
p.a.	pulmonary artery
p.v.	pulmonary vein
l	lymphatic
l.n.	lymph node

(Adapted from Gray, 2000)

Figure 2.17: Schematic - longitudinal section of a primary lobule

Lung Physiology

The primary function of the lungs is to enable oxygen-carbon dioxide exchange between air and blood. The blood carries the principal metabolic waste product, carbon dioxide to the lungs. This byproduct gets removed in exchange for oxygen absorption that enables the body to maintain operation. The exchange takes place at the alveolus where

molecules diffuse through a membrane; the membrane is known as the alveolar epithelium. Each alveolus has a diameter of ranging from 0.2 to 0.3 mm at in-situ condition. The wall thickness is approximately 0.010 to 0.014 mm (Weibel, 1977). The tissue that formed between the alveoli also houses capillaries, lymphatic vessels, veins and arteries as shown in Figure 2.18.

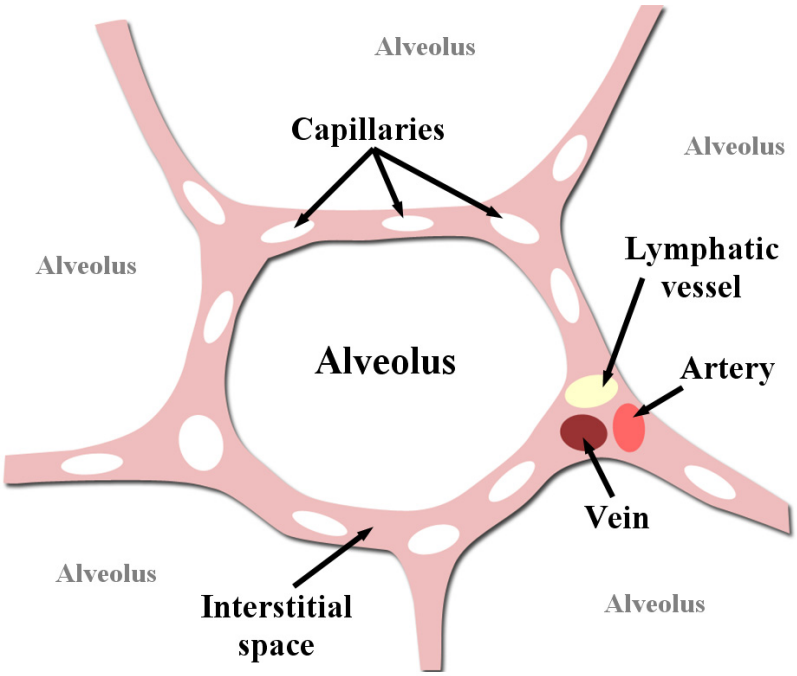

Figure 2.18: Microscopic schematic of alveolar structure

Air is made up of different gases dominantly by nitrogen and oxygen. The concentrations of these different gases in the alveoli are expressed in terms of partial pressure exerted by each. It is the pressure difference of these gases in the alveolar air and the blood in the pulmonary capillaries that drive the oxygen and carbon dioxide exchange. The schematic shown in Figure 2.19 describes different mediums that the oxygen travels through from the alveolus to the blood stream during the exchange. Any additional fluid forms between the transferring processes will impede the flow of molecule exchange, thus impede the respiratory function as a pulmonary injury.

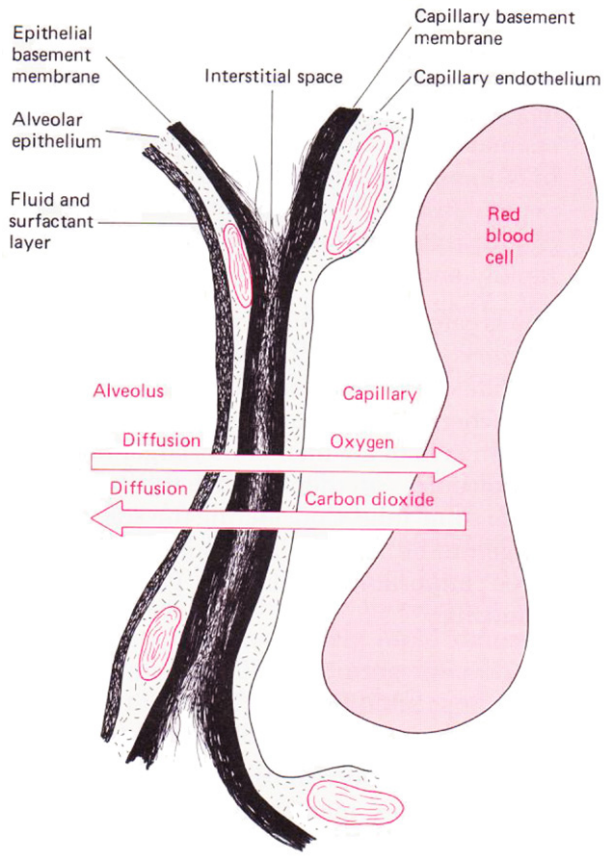

(Reproduced from Guyton, 1996)

Figure 2.19: Ultrastructure of the respiratory membrane

Lung Pressure Effects

The lung movement is driven by the pressure difference between the inside and outside of the lung since the lungs are not physically attached to the chest wall. A thin, delicate, transparent membrane, known as the visceral pleura, surrounds each lung. Another membrane, known as the parietal pleura, lines the inner surface of the chest wall covering the lower diaphragm, mediastinum and surrounding each lung. The void between the two pleura surfaces is filled with a pleural fluid and is known as a pleural sac. The pleural fluid lubricates the pleural interface and allows them to slide freely relative to each other during respiration. The fluid is produced by the intercostal arteries and continuously reabsorbed by the lymphatic system, thus maintaining suction in the pleural sac. In order for air to flow in and out of the lungs, the diaphragm is lowered and the ribcage is raised

to expand thoracic cavity volume leading to a negative pressure of approximately 3 mm Hg (~0.4 kPa, 4.1 cm H_20) (Guyton,1996). This creates a negative pressure relative to the atmospheric pressure that inhales air into the lungs. The opposite mechanic exhales air out of the lung with a positive pressure of 3 mm Hg. If a person breathes with maximal effort, the alveolar pressure can decrease to negative 80 mm Hg (~10.7 kPa, 109 cm H_20) or increase to positive 100 mm Hg (~13.3 kPa, 136 cm H_20) (Guyton, 1996).

Despite the pressure difference between the inside and outside of the lung, not all regions behave similarly during breathing. The inferior region of the lung ventilates better than the superior region in an upright position (Lee & Tai, 1979), however the transpulmonary pressure is lower at the inferior region than at the superior. The transpulmonary pressure is defined as the difference between the alveolar pressure and the pleural pressure in the lungs. Lee & Tai (1979) believed that the gravity effects on the lung, chest wall and abdomen are the most probable cause. Because the resting volume at the base of the lung is low, small changes in the transpulmonary pressure yields greater volume change as illustrated in Figure 2.20. Although a higher transpulmonary pressure is seen at the total lung capacity (TLC), it yields a diminishing volume change. TLC refers to the volume of the lungs after a maximal voluntary inspiration.

Vawter (1979) investigated the 'pressure versus volume' mechanism through a numerical model, and recognized two important findings. At low resting volume, the lung tissue elasticity has high compliance and the surface tension is minimal, thus a high volume expansion can be achieved with minimal effort. As the transpulmonary pressure gets higher, the lung tissue becomes stiff and the surface tension increases with greater surface area, thus counteracting against further inspiration. A transpulmonary pressure gradient is present along the superior-inferior axis since the lung is open to the atmospheric pressure. The lung volume is different regionally, suggesting the stress and strain in the lung tissue is not uniform. This gradient is especially substantial at the Functional Residual Capacity (FRC), as opposed at the TLC where the gradient is minimal. The FRC refers to the amount of air that stays in the lungs during normal breathing. Vawter

(1975) and Hoppin et al (1969) investigations have found that the shape of the lung have little to do with the non-uniform pleural pressure. This complicated mechanism and its implication on injury are still not fully understood. For a more comprehensive review on lung mechanics, Hoppin and Hildebrandt (1977) had summarized the developments by various researchers.

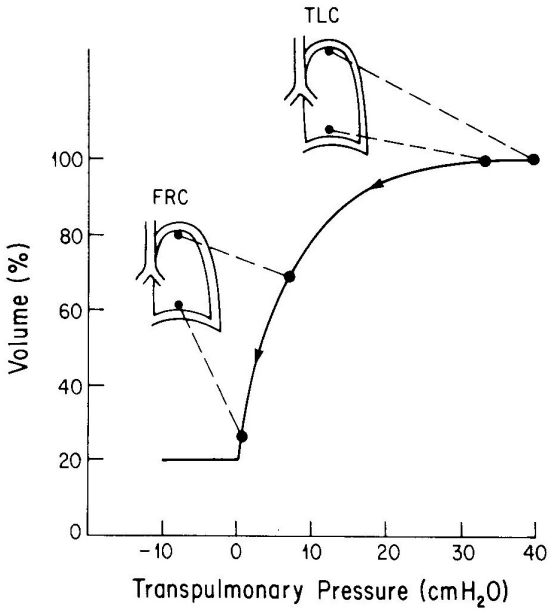

(Reproduced from Lee and Tai, 1979)

Figure 2.20: Relationship between regional volume and intrapleural pressure

Lung Volume

From a classical biomechanics point of view, a description of the mechanical behavior of the lung must be based on a known reference state (Vawter, 1977). Figure 2.21 illustrates different terminologies used to describe various lung volume states. A normal adult exchanges 500ml of air with each respiration, also known as the tidal volume (TV) (Palsson, 2003). Three terms are typically referenced in absolute volume: residual volume (RV), functional residual capacity (FRC), and total lung capacity (TLC). The vital capacity (VC) is a relative volume with respect to the RV.

Clinicians place emphasis on lung density, volume and divergence of volumes relative to a normal lung to determine whether a respiratory disease is present. The American

Thoracic Society and European Respiratory Society (Pellegrino et al, 2005) recommended a comprehensive listing of published reference equations to determine adult normal lung volumes from Quanjer (1995). The predicted lung volumes (RV, FRC, TLC) are dependent on height and age. The predictive equation was statistically confined to the Caucasian population. Since road traffic deaths significantly correlated with ages of 15 to 44, a median age of 30 was assumed as the 50th percentile male for calculation purposes as summarized in Table 2.4.

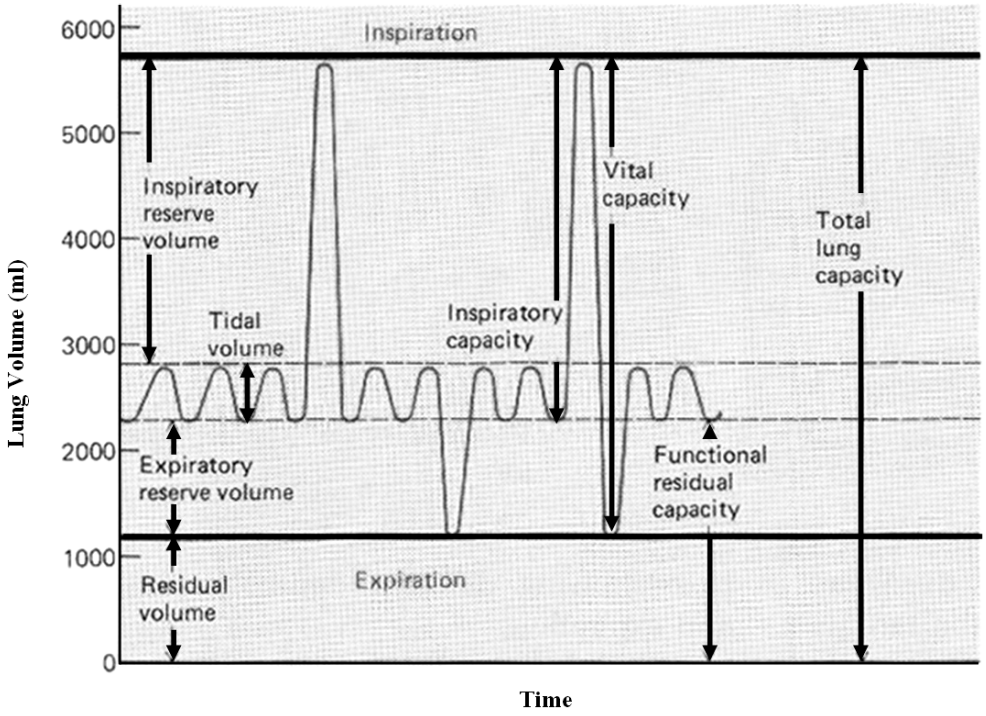

Residual Volume	Air volume of the lungs after a maximal voluntary expiration
Functional Residual Capacity	Air volume of the lungs after a resting expiration
Total Lung Capacity	Air volume of the lungs after a maximal voluntary inspiration

(Reproduced from Guyton, 1996)

Figure 2.21: Description of various lung volume terminologies

Table 2.4: Air volume of the lungs for a 50th percentile male at age of 30

Lung Air Volume	RV	FRC	TLC
Liter (10^{-3} m^3)	1.72	3.31	6.91

(Derived from Quanjer, 1995)

Lung Density

The physical density of the lungs is fundamentally determined based on the contribution of three components: lung tissue, blood, and air. The relative proportions of these components change continuously with the state of lung inflation. Changes in the transpulmonary pressure affect the amount of fluid within the capillaries and interstitial space. Pulmonary mechanics research in the past typically assumed a lung specific gravity of 0.23 (Fung 1978; Vawter 1980; Yen, 1988), this value was based on a study on dog lung tissue by Crossfill and Widdicombe (1961). Lehnert et al (1992) study had shown that lung density vary with body orientation, scan region, age, and species of the animal. The body orientation (supine, prone, upright) would cause regional differences in density within the lungs due to gravity, which increases the vascular component and decreases the alveolar space. Guenard et al (1992) have found a mean specific gravity of 0.288 ± 0.064 at FRC from their experiments; a comparable density of 0.28 was found by Brudin et al (1987). A study by Verschakelen et al (1993) measured lung density at 10%, 50% and 90% of the VC, thus enabled scaling of the lung density at different breathing states. The reference lung density and volumes for the current model are discussed in Chapter 3.

Vawter (1977) established a reference volume where the lung was in a stress-free state by eliminating body, gravitational, interfacial and externally applied forces. The experiment used intact lobes from dog lung in a saline bath. His study found that the equilibrium volume was independent of the initial volume. The average saline/tissue volume ratio at stress free state was 1.74 +/- 0.20, with a specific gravity of 0.365. Vawter's (1977) analysis suggested that the "collapsed" lung state is not exactly "stress-free" due to the likelihood of gas trapping within the lung tissue. This finding was used to verify the reference lung density and volumes in the current model, and is elaborated in Chapter 3.

Wave Speed Propagation

Stress wave propagation is an important factor that can describe lung dynamics in response to impact loading (Yen, 1986). The features of stress waves could be the

primary factor in explaining how trauma occurs, thus different factors that alter the stress wave propagation in the lung should be investigated. The lung, being a two-phase composite structure of soft tissues and gas, inherently possesses non-linear time-dependent response. Given that the speed of sound in air is 350 m/s and in soft tissue (similar to water, fat, muscles) is ~1500 m/s, the resultant wave speed of the lung where the two materials were coupled together is much lower than their individual speeds. The speed of a compression wave in an elastic continuum can be modeled by the bulk modulus, shear modulus, and density as shown in Equation 2.1. The wave speed primarily is depended on the lung volume (apparent density) and the change of lung volume due to pressure (bulk modulus).

$$c = \left(\frac{K + \frac{4}{3}G}{\rho} \right)^{\frac{1}{2}}$$

Where

c	Sound speed of the material
K	Bulk modulus
G	Shear modulus
ρ	Apparent lung density

Equation 2.1: A compressive wave speed in an elastic continuum

This formulation proved to be in good correlation with the lung wave speed experiments conducted by Rice (1983), Yen (1986), and Jahed (1989). Horse, rabbit, goat, and sheep experiments were conducted. The wave speed was found to be on the order of 3 to 70 m/sec across a range of physiological transpulmonary pressures (0 to 20 cmH_20). A low wave speed can be justified by using Equation 2.1 when the density of tissue is coupled with the bulk modulus of air (relatively high density and low bulk modulus). Much of the studies (Rice, 1983; Yen, 1986; Jahed, 1989) were focused on an undisturbed or small distortion to measure wave speed, as such the relevance of high distortion effects due to impact loading is unclear.

Bulk Modulus

Dynamically, the bulk modulus should be dependent on the gas stiffness within the lungs and change non-linearly with respect to volume change. The bulk modulus, by definition, is a ratio of the pressure change to the fractional volume change in a volume. The gas stiffness coupled with the lung density dictates the wave speed propagation (Rice, 1983; Jahed, 1989). As such, high gas stiffness indicates a high bulk modulus which would result a high wave speed. This phenomenon was demonstrated between the studies by Jahed (1989) and Yen (1986) where the airway was open and closed, respectively. The experimental bulk moduli measured by Jahed (1989) (~5kPa) were found to be 20 to 100 fold lower than by Yen (1986) (~100 kPa) although the initial transpulmonary pressure was similar.

The concept of bulk modulus with respect to various breathing states is best described through a hydrostatic pressure-volume curve of a small lung volume as shown in Figure 2.22. Point A represents the in-situ condition of the lung. When the lung is compressed from the in-situ condition, it reaches point B where the bulk modulus is smallest. Further compression leads to a collapsed lung where the gas is trapped within the alveoli, thus leads to the increase of bulk modulus.

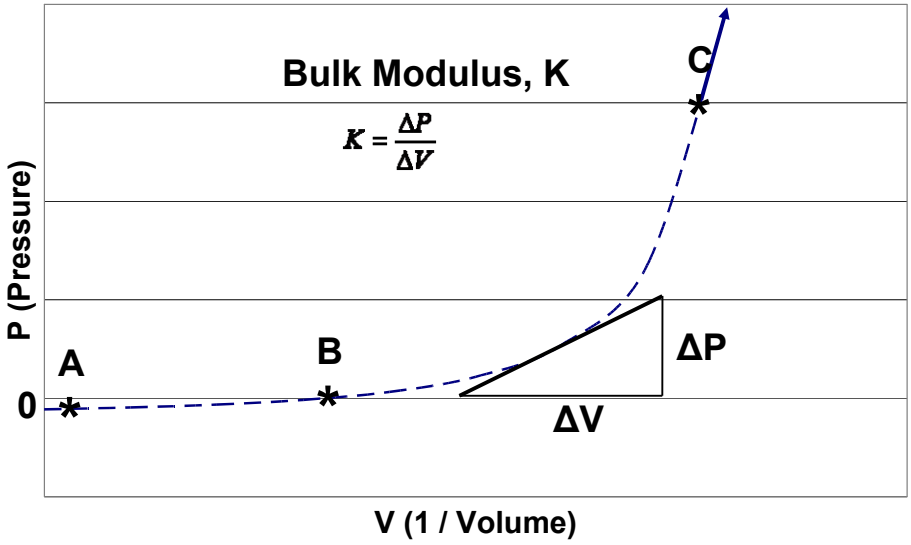

Figure 2.22: Conceptual pressure-volume curve for describing bulk modulus

From the stress wave speed perspective, the bulk effect during compressive loading is of interest and can be separated into two distinct phenomena: when the lung is within the physiological range, and when the lung is at the physiological limit.

The first phenomenon takes very little pressure to vary the lung volume. Consequently, the change of the bulk modulus is low while the change of the density is high, thus lead to a lower wave speed relative to the in-situ condition. For example, the wave speed measured in the physiological range is in the range of 3 m/s to 25 m/s (Rice, 1983; Yen, 1986; Jahed, 1989). The airflow resistance from the alveoli to the airway is low at the in-situ condition but increases with compression since the lung tissue becomes less porous; similarly the bulk modulus in the physiological range is low and increases non-linearly with compression.

The second phenomenon takes a lot of pressure to create a small lung volume change. When the lung is encountering compressive loading, the airflow resistance is increased due to the forced expiration from the alveoli to the airways in the lungs. As air begins to flow out of the alveoli due to an external pressure, the pressure drops along the airway. The pressure drop tends to close the airway especially with the lung gets less porous with compression. When air trapping occurs (lung collapse), the bulk modulus or the gas stiffness becomes high. From this point, the bulk modulus increases at a rate greater than the density, thus leads to a faster wave speed. Air could not escape through the airway even with an increase in the negative transpulmonary pressure when the lung is collapsed. This condition led to a high wave speed in the range of 465 m/s to 662 m/s based on the bulk modulus values (~130000 kPa) derived from the excised lung tissue tests (Dunn, 1961; Ward, 2005; Saraf, 2006). The approach to determine the bulk modulus used for the current study is discussed in chapter 3.

Lung Mechanics

Early research on lung mechanics was mostly focused on observing whole organ behavior as a pressure-volume relationship by placing an excised animal lung inside a

container with the lung capacity measured with a spirometer (Lee and Tai, 1979). Various negative intraplueral pressures were applied to the container as an input and lung volume changes was measured as an output. This experiment showed that the inflation and deflation response were different and this phenomenon is known as hysteresis. When a positive pressure is applied externally, the small airways in the lung would close, thus trapping gas in the alveoli similar to a collapsed lung. The lung volume would show minimal decrease even if external pressure was increased. The transpulmonary pressure, the pressure difference between the inside and outside of the lung, is known to influence the mechanical response. Three scenarios are shown in Figure 2.23 for normal breathing (solid line), the lung inflated with saline (dashed line), and the lung inflated with air (solid line). The loading and unloading curve deviates from the normal breathing curve and creates a large hysteresis when there is a large change in the air-surfactant interface area (Powell, 1979). The lung inflated with saline showed the loading and unloading response along the same curve, thus demonstrating the elimination of the air-surfactant effect.

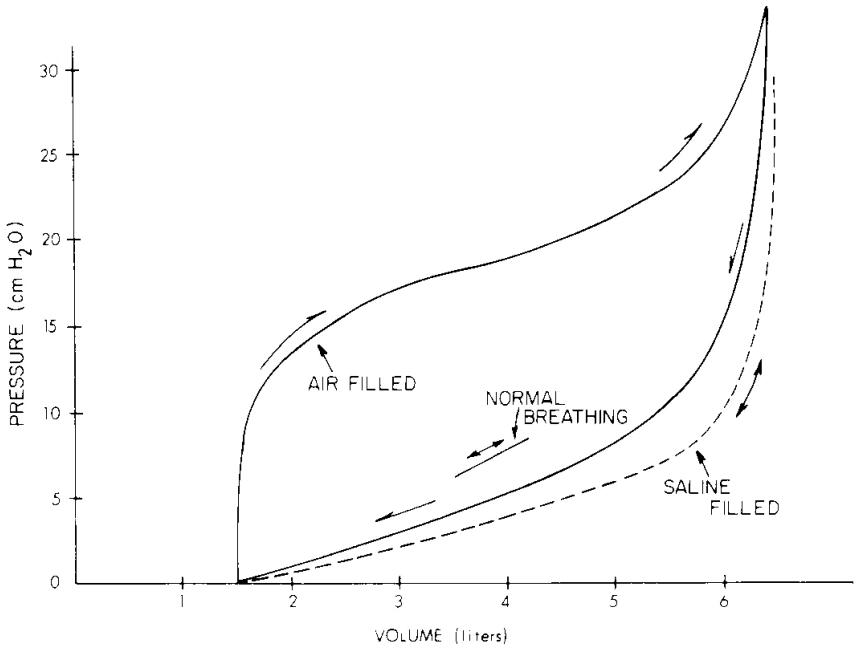

(Reproduced from Powell, 1979)

Figure 2.23: Inflating pressure vs. lung air volume curves for a human lung

Lung Tissue - Elasticity

Two authors (Fung 1975, 1978; Vawter, 1979, 1980) began researching lung mechanics as a material instead of as a whole organ. They determined that lung mechanical behavior was dominated by two major factors: the elasticity of the lung tissue, and the surface tension generated by the surfactant within the lung.

An early lung elasticity model created by Mead, Takishima and Leith (1970) considered the lung parenchyma as a mesh of membranes. This concept of the lung was modeled as a network of springs connected in a hexagonal array to describe interaction among alveoli qualitatively.

Lambert and Wilson (1973) extended the approach by visualizing lung tissue as a number of interconnected, randomly oriented, plane, elastic membranes. A linear elastic relationship (Hooke's law) was assumed to derive the stress and strain relationship based on small incremental changes. However, elastic modulus and poisson's ratio were found to vary with the inflation state depending how the perturbation was imposed.

Frankus and Lee (1974) assumed random orientations of elastic fibers and isotropic behavior within the alveolar wall. They used a constitutive equation for the strain energy density in terms of strain invariants to describe stress and strain within the lung. Constants were then derived based on the pressure-volume experiments. Although the derived constants did not represent any physical material attributes of the lung tissue, it demonstrated reasonable prediction against the experimental data.

Fung (1974) considered the histological geometry of the alveoli and derived integrals to represent the macroscopic stress. A statistical relationship between the macroscopic strain and the strain in the individual interalveolar septa was established based on a mathematical continuum approach of a statistical "average alveolus". Fung analyzed a spherical and a cubic shape alveolus mathematical model, and found that the final constitutive equation did not change much with shapes. Since the cubic model is simplest, such model was used to analyze different collapsed lung mechanisms (Fung,

1975). Also, a theoretical approach to model surface tension was incorporated as part of his analysis. Fung's approach was different from Frankus and Lee (1974) by giving physical meaning to the mathematical model that summed the contribution of elasticity and surface tension with associated constants.

Fung (1975) cited that the lung tissue as a material be referred as a viscoelastic energy function, given the hysteresis exists in the surface tension and in the elasticity of the lung tissue. Fung argued that the hysteresis response of the living tissue was insensitive in the strain rate used in his experiments. The lung tissue should be treated as a pre-conditioned specimen that has been subjected to a cyclic process such that a steady-state periodic response has been reached. He suggested at the time that the stress-strain relationship of the lung tissue can be modeled by approximating two separate hyperelastic functions for loading and unloading with strain rate dependency ignored.

Surface Tension

In addition to the elasticity of the lung tissue, surface tension is generated by the liquid surfactant that lines the alveoli which contributes to the lung response. Its contribution was found to be substantial when surface tension was removed by replacing the air in the lungs with a saline solution. The saline solution effectively eliminated the liquid-gas interface at the alveoli thus created a more compliant lung (West, 2005).

Surface tension, a well recognized phenomenon in fundamental thermodynamics, is a free surface property of a liquid where the intermolecular forces acting with adjacent molecules are stronger in liquid than in gas, surface tension is then created to minimize the surface area at this liquid-gas interface. Different liquids have different intermolecular properties which lead to various surface tension levels. Macroscopically, surface tension positively correlates with surface area. Physiologically, the surfactant within the lungs, which synthesized from fatty acid, exhibits lower surface tension properties relative to other liquids such as blood or water (Guyton, 1996). The surfactant reduces the hydrostatic pressure in the tissues surrounding the capillary. This indirectly

prevents any fluid passing through the alveolar membrane into the alveolar space. Surface tension in each alveolus is interdependent with adjacent alveoli, which opposes any tendency to decrease or increase its alveoli space relative to each other.

Material Model

Vawter (1979) used the cubic model of the alveolus by Fung (1978) to formulate a mathematical relationship to model the macroscopic stress and strain in the lung. The mathematical relationship was established to describe the behavior of an individual alveolar membrane and the membrane contributions were summed to represent the macroscopic relationship. It was hypothesized that the strain energy of the membrane could be described by Equation 2.2. The mathematical model was then restricted to isotropic behavior which led to material constants, a1 = a2. The description of the macroscopic strain energy equation would simplify to Equation 2.3. This final equation represented the elasticity contribution to the lung macroscopic behavior.

$$M_o W^1 = \frac{C'}{2} \cdot \exp(a_1 E_x^2 + a_2 E_y^2 + 2a_4 E_x E_y)$$

Where

M_o	the interalveolar septa's mass per unit of the membrane (unstressed state)
W^1	Strain energy per unit mass of the alveolar septa
E_x, E_y	Green's strain in the x and y direction, respectively
C, a_1,a_2,a_4	Material constants

Equation 2.2: Strain energy function of the alveolar membrane

$$W' = \frac{C}{2\Delta} \cdot \exp(\alpha I_1^2 + \beta I_2)$$

$$I_1 = e_{xx} + e_{yy} + e_{zz}$$

$$I_2 = e_{xx}e_{yy} + e_{yy}e_{zz} + e_{zz}e_{xx} - e_{xy}^2 - e_{yz}^2 - e_{zx}^2$$

Where

W'	Strain energy per unit volume
Δ	Typical unstressed alveolar diameter
I_1, I_2	Strain invariants
e_{ij}	Green strains
C, α, β	Material constants

Equation 2.3: Macroscopic strain energy function of the lung elasticity

Fung (1975) proposed a relationship for the surface energy density in which the surface area was based on strain invariants, and was determined with respect to a reference state.

Surface tension provides a significant contribution as long as the alveoli are not collapsed. Vawter (1978) doubled the surface energy term that Fung (1975) initially proposed because surface tension acts on the inside and outside surface of the alveoli (air-surfactant and surfactant-alveolar membrane). Vawter (1978) assumed the surface tension as a power function that was dependent on the surface area as shown in Equation 2.4(a). The final surface energy density equation represents the surface tension contribution to the lung macroscopic behavior and is dependent on four parameters: two surface tension coefficients (C_1, C2), the surface area, and the alveolar diameter as shown in Equation 2.4(b). The surface area was approximated by using the strain invariants as shown in Equation 2.4(c). Given that surface tension relationship was not well understood at the time, Vawter suggested this power function relationship could be replaced once the understanding on this phenomenon was improved.

$$\gamma = C_1 A^{C_2} \qquad \text{(a)}$$

$$E = \frac{12C_1}{\Delta(1+C_2)}(A^{1+C_2} - 1) \qquad \text{(b)}$$

$$A^2 = \frac{4}{3}(I_1 + I_2) - 1 \qquad \text{(c)}$$

Where

γ	Surface tension
A	Surface area
C_1, C_2	Surface tension constants
E	Surface energy density
Δ	Typical unstressed alveolar diameter
I_1, I_2	Strain invariants

Equation 2.4: Strain energy equation of the surface tension

Studies by Smith and Stamenovic (1986, 1986a, 1986b) had developed greater understanding of the alveolar surface tension effect on lung volume, microstructural mechanics and lung stability, and mechanical properties of lung parenchyma. A subsequent study by Prokop et al (1999) built on their development, and investigated a relationship between surface tension and recoil pressure from a thermodynamic point of view. The study demonstrated good agreement with experimental data with an expression for modeling surface tension by taking surface area, pressure, and lung volume into account. The implementation of the surface tension development has not

been implemented in existing numerical codes. However, these developments can be a great contribution to the understanding of lung mechanics.

Lung Properties

It is technically difficult to determine material properties for the human lung tissue in experiments for several reasons. Firstly, most lung tissue testing has been conducted on animals such as goat, sheep, rabbit and dog to study various response mechanisms. Lung tissue testing on human cadavers is sparse. Secondly, the elasticity has to be determined by isolating the effect of surface tension; this is usually accomplished by testing in a saline solution. Thirdly, testing tends to apply a slow loading rate (<.1/s) due to difficulty in clamping or hooking lung tissue. Fourth, lung tissue material behavioral characteristics in uni-axial testing are different from those in biaxial or triaxial loading. The specimen deformed more under biaxial loading than under uni-axial loading at the same stress levels (Vawter, 1978; Vawter 1979). It is still unclear what caused this response characteristic; Vawter (1978, 1979) cited the possibility of alveolar geometry distortion under large deformation. The author hypothesized this phenomenon had to do with the saline solution being trapped within the alveoli which hydrostatically resist to the uniaxial loading, where as the saline solution maybe able to exchange between the alveoli and the airway under biaxial loading.

Lung Elasticity Material Constants

Zeng et al (1988) conducted one of the first experiments to measure the mechanical properties of the human lung tissue based on a biaxial loading. This experiment demonstrated that the mechanical properties from different regions of the lung were not significantly different from each other. Multiple sets of biaxial test were conducted by applying a range of constant load in one axis, and a varying load is applied to the perpendicular axis.

Yen et al (1999) conducted biaxial tensile tests on human lung tissues from seven cadavers to obtain material properties with a larger sampling pool. Two types of biaxial

tests were conducted: first was conducted by applying a fixed strain in one axis and the strain in the perpendicular axis was varied. The specimen was tested at several increments of fixed strain. Second type was conducted by applying varying strain to both axes simultaneously. Subsequently, the material constants were used in the first detailed thoracic numerical model (Deng, 1999) as shown in Table 2.5. Gao et al (2006) reanalyzed Yen's (1999) data and determined a new set of elastic constants as shown in Table 2.6(Gao et al, 2006).

Table 2.5: Original material constants for the lung tissue

C/Δ (KPa)	α	β	C1/Δ (kPa)	C2
0.592	5.85	-3.21	0.0193	2.71

(Adapted from Deng, 1999)

Table 2.6: Revised material constants for the lung tissue

	C/Δ (KPa)	α	β
Avg.	0.306	4.47	-4.20
SD	±.084	±1.94	±2.55

(Adapted from Gao, 2006)

Both studies (Zeng, 1988; Yen, 1999) produced multiple sets of material constants with each set of material constants representing a biaxial test. In the study by Zeng (1988), an additional set of material constants were fitted based on the stress-strain data that had the same loading conditions. In the study by Yen et al (1999), the final set of material constants were derived by averaging all the material constants. An approach to determine a set of material constants for the current study is described in Chapter 3.

Surface tension properties

Since surface tension was not fully understood when the constitutive model was developed, a simple power function was assumed; surface tension properties were proposed as preliminary (Vawter, 1976; 1980). The surface tension properties from Vawter (1980) were originally adopted in the first detailed thoracic model (Deng et al, 1999). However, the origin of the surface tension parameters from Vawter (1980) was unclear. In a study by Vawter (1976), a set of surface tension material constants was fitted to experimental surface tension measurements by Flicker et al (1974) and validated against another set of experiments by Bachofen et al (1970). The surface tension

formulation in the study by Vawter (1976) was fundamentally the same as the one used in the current constitutive model in LS-Dyna which was shown in Equation 2.4(a), however the formulation for approximating surface area as shown in Equation 2.4(c) was different. As such, the current constitutive model was refitted with a new set of surface tension parameters according to the study by Vawter (1976). An approach to derive the surface tension material constants is presented in Chapter 3.

Material Properties derived from animal experimental studies

Stitzel (2005) and Gayzik (2007; 2008) conducted experimental impact studies on rats and utilized an optimization approach to determine six material variables that correlates with the loading conditions using a finite element model. The rats were CT-scanned after the impact to reconstruct the lung three dimensionally; contusion volume was measured. Although the lung properties are not directly applicable to the current study, a summary of the material properties is shown in Table 2.7. These are the only known sources that capture the compressive loading of the lung in an in-vivo condition.

Table 2.7: Optimized material properties of the rat lung material model

	K(N/mm^2)	C (N/mm)	Δ (mm)	α	β	C1 (N/mm)	C2
Gayzik (2007)	1.384e-1	1.187e-3	.0702	.445	-3.95	1.949e-5	1.918
Gayzik (2008)	1.18e-1	2.3e-4	.0702	.629	-1.14	2.2e-5	1.42

Lung Injury

Blunt trauma to the lungs can be categorized into two types: laceration and contusion. The injury typically disrupts the lung function by causing a lack of ventilation (inability to breathe) or by creating a barrier to oxygen exchange at the alveolar level. Both cases lead to a lack of oxygen supply to the body.

Pulmonary Laceration

Pulmonary laceration is commonly caused by penetrating trauma, but may also be caused by blunt chest trauma indirectly through rib fracture or flail chest. Wagner et al (1988) identified four types of pulmonary lacerations commonly seen with non-penetrating chest trauma that coexist with pulmonary contusion as shown in Table 2.8.

Table 2.8: Four types of pulmonary lacerations

Type 1	Compression of the chest wall against the lung parenchyma, where lung is ruptured
Type 2	A shearing of lung tissue across the vertebral bodies
Type 3	Fractured ribs penetrating and puncturing the lung
Type 4	The result of a previously formed pluero-pulmonary adhesion causing the lung parenchyma to tear when the chest wall is compressed or fractured

(Adapted from Wagner, 1988)

Wagner et al (1988) proposed that pulmonary laceration is a basic component in the injury mechanism of pulmonary contusion. There are three other common pulmonary injuries that may occur due to laceration such as open and closed pneumthorax, and hemothorax.

Closed pneumothorax results from a laceration to the lung or bronchtracheal tree causing air to escape into the pleural space. The lung may collapse as it recoils without a negative pressure within the pleural space (Moore and Dalley, 1999). Open pneumothorax results from a laceration of the chest wall which admits atmospheric air. During normal inspiration, air is drawn in through the lacerated wound into the pleural space instead of through the mouth.

Hemothorax results from bleeding associated with lung laceration. The bleeding perfuses as the heart circulates blood through the lung at a low pressure.

Pulmonary Contusion

Pulmonary Contusion is a common result of blunt trauma, where parenchymal damage occurs at a microscopic level resulting in interstitial edema and capillary hemorrhage, leading to alveolar collapse and lung consolidation (Bernard et al, 1993; Allen and Coates, 1996). Pulmonary hemorrhage is the result of bleeding from the damaged capillaries in the lung tissue. The additional fluid at the alveoli acts as a barrier to oxygen exchange and alters surface tension, thus leading to the alveolar collapse. Figure 2.24(a) shows pulmonary contusion on the surface of a rat lung 24 hours after the impact where the arrows point to the contused area. Pulmonary edema is the result of fluid accumulation in

the lungs. Figure 2.24 (b) shows pulmonary contusion on the CT scan of a trauma patient as identified by circles and the black area shows signs of pneumothorax (not lung tissue but trapped air). There are four possible injury mechanisms that can lead to pulmonary contusion as outlined in Table 2.9 (Clemedson, 1956; Allen and Coates, 1996; Cooper et al, 1997).

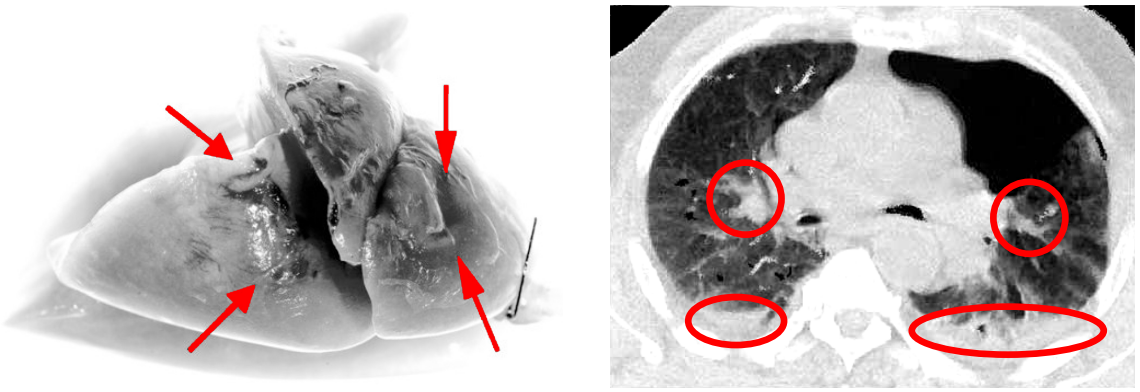

(a) Reproduced from Stitzel, 2005 (b) Reproduced from Daly, 2008

Figure 2.24: Examples of pulmonary contusion

(a) 24-hour post impact to a rat lung (b) trauma patient

Table 2.9: Injury mechanisms leading to pulmonary contusion

Implosion effect	Intrapulmonary air expansion leading to excessive alveolar stretching and tearing
Inertial effect	A concussive wave causing alveoli to strip away from bronchial structures during the differential acceleration of these tissues
Spalling effect	A concussive wave encounters a liquid-gas interface, where a compressive wave reflects with a tensile wave of the same magnitude
Pressure Differential	A large pressure differential at the barrier between alveolar space and the capillary, forcing fluid through the barrier

Implosion

The implosion effect refers to the micromechanical response of the alveoli. Fung (1988) hypothesized that when the lung is subjected to a compression at a sufficient magnitude and rate, airways may collapse while nearby alveoli remain open. Gas is trapped within these alveoli. Once the compressive wave has passed, the pressure acting on the outside of the trapped units would be reduced, leading to a gas expansion beyond its original volume and putting the alveolar walls in tension as shown in Figure 2.25 (a). As such,

the alveolar walls can be under tensile stress even when the strain wave was compressive. Fung (1988) hypothesized that the alveolar walls are damaged by tensile principal strain, thus alters the permeability with respect to the solutes and leads to edema. The pores of the endothelium and epithelium may be stretched to the point that it would leak larger solutes or even blood.

Inertial

The inertial effect comes into play when there is a vast difference in the mass densities of neighboring structures as shown in Figure 2.25 (b). When the neighboring structures encounter a stress wave, each structure may subjected to different accelerations and displacements. For example, the lighter alveolar tissue may shear from the heavier hilar structure (Constantino, 2006). Lau and Viano (1981) impact experiments on rabbits had shown that at low velocity (~5m/s) and higher impact displacement (>20mm), pulmonary injuries were predominately resulted at the bronchial region.

Spalling

The spalling effect refers to a compressive wave in an elastic medium reaches a free surface boundary and reflects back into the medium as a tensile wave of the same magnitude as shown in Figure 2.25 (c). The resulting tensile wave could damage the epithelial surface due to excessive tension, since the lung has a porous structure with multiple interfaces between the alveolar wall and the alveolar space (Clemedson, 1956).

Pressure Differentials

Pressure differentials have been proposed as a general explanation for parenchyma injury in blast loading conditions as shown in Figure 2.25 (d). A large pressure difference between the capillaries within lung parenchyma and the alveolar space may result in failure of the barrier, forcing fluids from one region into another (Cooper, 1996; Cooper, 1996b; Grimal, 2005).

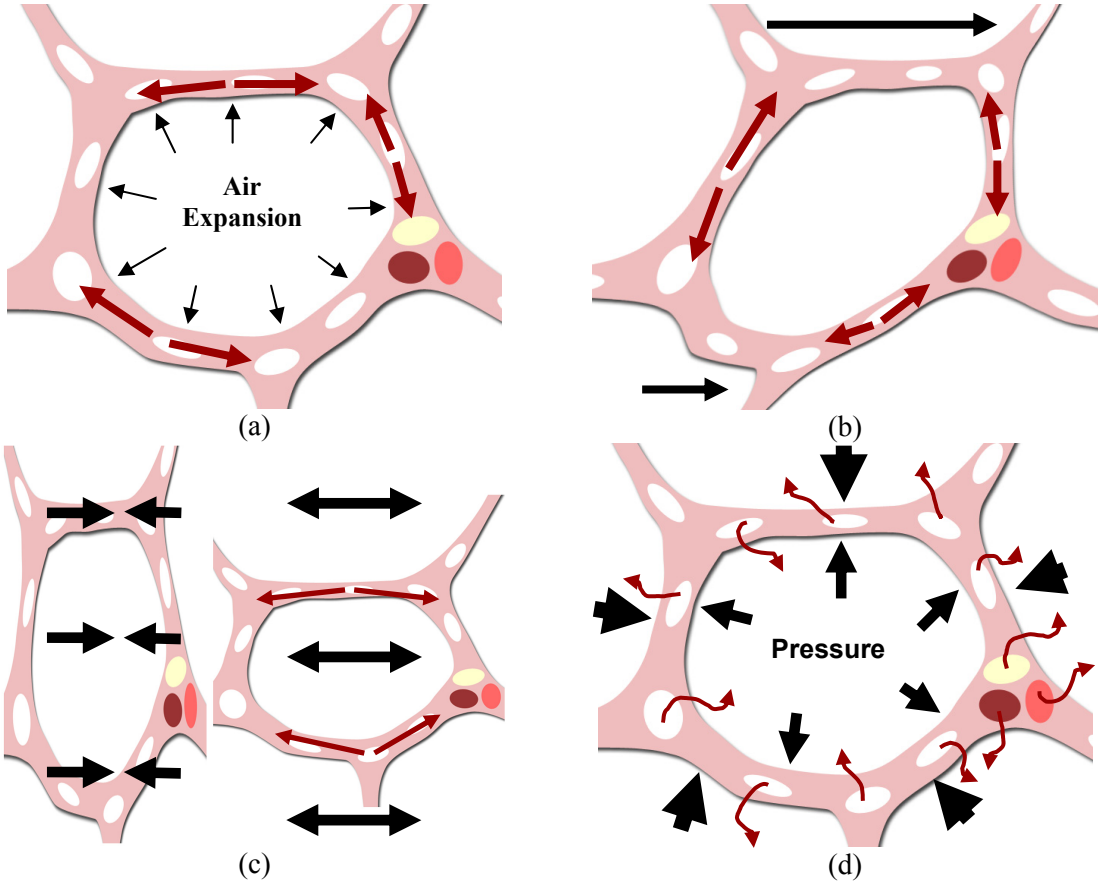

Figure 2.25: Conceptual schematic of lung injury mechanisms
(a) implosion (b) inertial (c) spalling (d) pressure differential

Various factors affecting injury mechanisms

Wave Reflection

Yen et al (1986) had shown that hemorrhagic injury in the lung is localized and is usually most severe next to the spine, heart, ribs or the edges of some lobes, rather than at the point of impact. Yen (1988) conducted air blast experiments on rabbit lungs supported by a free surface (nylon net) and a rigid surface (metal plate). Yen demonstrated that stress wave reflection has a significant effect. Lung injury was gauged based on the weight gain of the lung due to fluid accumulation within the lung. The experiments showed that the lung supported by a fixed boundary had a weight gain twice as much as the lung supported by a free boundary.

Severity correlates with stretch

Fung et al (1988) investigated the implosion mechanism by conducting series of experiments to isolate various loading effects. Their first experiment demonstrated that fluid accumulated when the alveolar wall was simply stretched by pressurizing the lung. They also showed that the amount of tissue stretch was positively correlated with the rate of fluid accumulation.

Different critical thresholds for the lung collapse and reopening

A second experiment (Fung, 1988) was performed to determine the critical reopening pressure when the lung was subjected to cyclic compression and expansion. Their experiment showed the lung volume would remain relatively unchanged when the transpulmonary pressure dropped below a critical threshold; the lung would collapse and trap about one quarter to one half of the initial gas volume in the alveoli even when the trachea remained open. There was another critical threshold that the transpulmonary pressure must reach before the collapsed lung would reopen and expand again.

Transpulmonary pressure dictates lung stability

The third experiment (Fung, 1988) demonstrated that the gas trapping mechanism depended on the material properties of the lung tissue which characterize the stability of the airway and the alveoli. It was demonstrated that the transpulmonary pressure (the pressure difference between airway and pleural) is relevant to the lung collapse, not the pleural or airway pressure alone.

Pulmonary contusion can occur without apparent rib fractures

A diffused pulmonary contusion pattern is common among the pediatric population where there is a greater musculoskeletal elasticity and no obvious chest wall injury (Allen and Coates, 1996). Patients diagnosed with rib fractures or flail chest had a more localized lung injury. Patchy, isolated pulmonary contusion was more apparent in lower velocity impact (Lau and Viano, 1981). At higher velocity impact, the contusion was small and widely distributed. Yen (1987) and Fung (1988) recognized the importance of

the wave features; reflection, refraction, and focusing of stress wave may cause large stresses and strains in small regions of the lung and induce severe injuries.

Injury Evaluation and Thresholds

Research on lung trauma is advancing on three fronts: 1) thoracic injury correlation to whole-body response, 2) dynamic behavior of the lung as an organ, 3) modeling interactions at the alveolar structure and capillary levels. However, the understanding of pulmonary contusion is still hindered in terms of differentiating and quantifying pulmonary injury from normal parenchyma. Pulmonary contusion mortality has not improved appreciably despite the advancement in pathophysiology, diagnostics, and care management (Allen and Coates, 1996). This finding stems from two factors: Firstly, a low index of suspicion in lieu of more urgent and obvious injuries (Allen and Coates, 1996). Secondly, pulmonary contusion may not be evident at admission, but may become critical in 24 to 48 hours (Miller, 2001).

Previous studies by Miller et al (2001, 2002) had identified pulmonary contusion as an independent predictor for the development of acute respiratory distress syndrome, pneumonia and associated with a mortality of 10% to 25%. The acute respiratory distress syndrome (ARDS) is a process of non-hydrostatic pulmonary edema and hypoxemia associated with a variety of etiologies that carries a high morbidity, mortality (10-90%) and financial cost (Bernard et al, 1994). It is a prevalent disease in trauma patients and may lead to long term pulmonary dysfunction (Miller et al, 2002). A less severe form is called the acute lung injury (ALI).

Miller et al (2001) piloted a method to accurately measure contusion volume from three dimensional reconstructions of CT scans to evaluate pulmonary function and to predict outcome. Patients were classified as having severe pulmonary contusion when the contusion volume exceeded 20% relative total lung volume and moderate pulmonary contusion when contusion volume remained below 20%. His analysis showed that the severe group correlated to higher occurrences of ARDS and pneumonia when compared

with the moderate group (82% vs 22% for ARDS and 50% vs 28% for pneumonia, respectively). Their data demonstrated no noticeable difference in the average patient ratings of chest AIS, ISS or rib fracture occurrences between the two groups of pulmonary contusion patients; similar finding applied to the two groups of ARDS.

An automated approach to identify, process, and evaluate lung damage through computed tomography scans was well documented in the work of Daly et al (2008). This approach was previously utilized and developed by Miller et al (2001), Stitzel et al (2005) and Gayzik et al (2007, 2008).

Stitzel et al (2005) and Gayzik et al (2007) had developed a rat model to investigate pulmonary contusion. The initial approach by Stitzel et al (2005) utilized CT scans on rats to determine initial average lung volume and used PET scan to quantify pulmonary contusion. The rats were subjected to energy-controlled (weight drop) in-situ direct lung impact. An identical impact was performed on a finite element model of the rat lung. First principal strain was used as a candidate injury metric.

The later approach by Gayzik et al (2007, 2008) utilized CT scan on rat to quantify pulmonary contusion after subjected to a constant velocity, limited-stroke direct lung impact. An identical impact was performed on a finite element model in parallel. A multi-island genetic algorithm was used to optimize the lung material parameters to best fit the simulated loading response of the impactor to the experiment. Various response metrics were evaluated as summarized in Table 2.10, the spatial distribution of the finite element model response was compared to the spatial distribution of the lung in the CT through a three dimensional registration technique to evaluate which injury predictor is best correlated with the injury outcome. Gayzik et al (2007) found the product of max principal strain and strain rate correlated well to contusion found in experiments.

Table 2.10: Response metrics ranked in order of best fit

Rank	Metric	24 hour Post-Impact Threshold
1	Max Principal Strain * Strain Rate	28.5
2	Max Principal Strain	0.154
3	Max Principal Strain Rate	304
4	Max shear strain rate	367
5	Max Shear Stress	7.10
6	Triaxial mean strain rate	58.3
7	Max shear strain	0.210
8	Max shear strain * strain rate	48.9
9	Octahedral shear stress	6.00
10	Triaxial mean strain	0.0242
11	Triaxial mean strain*strain rate	0.700

(Reproduced from Gayzik, 2007)

Future Development

The constitutive model developed by Vawter (1980) and Fung (1978) still remains as the most complete model to date, however a few challenges remain. First, the lung wave speed was measured ranging from 3 m/s to 662 m/s depending on lung volume and transpulmonary pressure. Experimentally, there has not been a viable way to measure wave propagation properties in the lung accurately at different inflation states. It has not been proven how wave propagation properties will change under deformation. Despite such shortcomings, one can only assume a constant bulk modulus as restricted by the material model implementation in numerical codes.

Second, the lung constitutive model response should be described with respect to a reference state, a state where the material should be stress free. Although it is recognized that the negative transpulmonary pressure would expand the lung to fill the thoracic cavity, the actual stress-free state of the lung relative to the in-situ condition remains difficult to determine. How the lung response changes based on the initial stress state is considered in chapter 3. The current study attempted to establish the model with respect to an in-situ condition. Future research should consider modifying the current constitutive material model such that it can easily correct the initial condition with respect to the stress free reference state.

Third, previous studies have shown that the lung has a gradient of volumetric strain vertically; with the inferior portion tend to be more compressed relative to the superior portion. However, the effect on the lung mechanical response is still unknown. It should be expected that the basal portion is more injury prone because the wave speed is low and less deformation is required to collapse this portion of the lung. For the time being, uniform initial volumetric strain is assumed until experimental evidence shows this initial condition has a substantial effect on the outcome.

Fourth, most lung material experiments have been conducted in quasi-static loading conditions, and characterized under a tensile loading. However, much is unknown when it is under a compressive loading condition. Although Vawter's (1979) observation suggested that the lung tissue can withstand some compressive load prior to buckling the alveolar membrane and resulting in a collapsed lung, more experiments are needed to quantify the compressive behavior.

Fifth, given the difficulty of prescribing a dynamic load to the lung material in experiments, the strain-rate dependence of the lung material still needs to be evaluated. For the time being, the approximate function approach is considered sufficient as a preliminary assessment of lung mechanics.

Sixth, an improved formulation of the surface tension is needed to better characterize the lung response. Although many studies have investigated the non-linearity of the lung response, the knowledge still needs to translate into an application that can investigate its relevance to the overall lung response accurately.

Summary

One must tie the relevance of various factors such as the anatomy, physiology, and material properties to the injury mechanisms for the impact condition that is being considered. When the lung is at the in-situ condition, it is recognized that that there is considerable local variation in terms of the stress and strain in the lung tissue due to gravity effects. Knowing that the total lung volume can vary from 2.6 liters to 8.5 liters

suggests that the lung tissue is a very compliant material. However, contusion often occurs under dynamic loading. The chest deflection experienced during blast loading is less than that of the automotive crash loading, yet contusion still occurs. This, in essence, highlights the importance of the bulk response of the lung tissue, which is tied to the stress wave propagation characteristics (low wave speed) and features (focusing, reflecting, refracting of stress wave). Although the current state of research cannot predict the microscopic stress in the lung tissue, the macroscopic response does provide an indication on the severity of the localized deformation that the lung tissue may experience during impact.

2.3.3 Heart

Anatomy of the Heart

The mediastinum refers to the space between the lungs; a volume that extends from the sternum to the thoracic vertebrae, and from the thoracic opening at the top extends down to the lower diaphragm. The superior mediastinum contains the trachea, esophagus, major blood vessels, nerves, and lymphatic vessels. The inferior mediastinum can be subdivided into three sections, anterior, middle and posterior section. The anterior section is referred to the section between the lungs and just behind the sternum. Its contents are mostly fat and remnants of the thymus gland. The middle section contains the heart, bronchi and blood vessels. The posterior section contains most of the structures that run from the trunk to the neck such as the aorta, the esophagus, and veins. The heart is situated approximately two-thirds of its area to the left of the sagittal plane (SAE, 1970). The organ is about the size of an adult human fist; weighs approximately 10 oz (283.5 grams) for male, and slightly less for female (SAE, 1970). The upper portion of the heart lies at the level of the second rib while the lower portion points downward and to the left resting on the diaphragm at the level of the fifth rib (SAE, 1970). The heart has two upper chambers (left and right atria) and two lower chambers (left and right ventricle) with a partition in each pair as shown in Figure 2.26. It has four valves and allows blood to flow in one direction only.

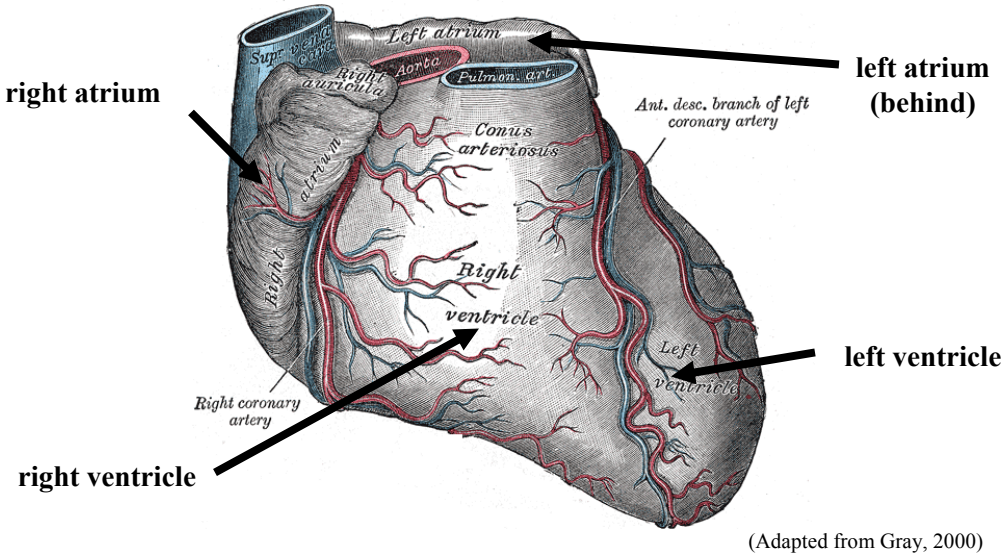

(Adapted from Gray, 2000)

Figure 2.26: Sternocostal surface of a heart

The ventricles have valves to prevent blood from flowing backward into the atria, where as the atria does not prevent backflow into veins. Although both sets of the heart chambers operate with similar functions and structures, the left ventricle pumps against approximately five times more pressure into the systemic arteries than the right ventricle pumps against the pulmonary arteries. The left ventricular muscle is two and half times thicker than the right ventricular muscle (Guyton, 1996). The external wall of the right ventricle tends to bulge outward and drape around the left ventricle. The thickness of the ventricular wall is generally five or more times thicker than the atrial wall (Guyton, 1996). The right atrium can prime the right ventricle easier than the left; the left atrial wall is thicker to compensate for the additional effort to prime.

The heart, roots of the arteries and veins are enclosed by a white fibrous sac that is known as the pericardium. This sac is attached to the heart's vessels and the diaphragm. The heart's wall is made up of three layers of tissue: endocardium, myocardium, and epicardium. The endocardium is a thin inner layer that lines the inner surface of heart cavities and valves. The myocardium is a thick middle layer of the muscular tissue that creates contraction for blood pumping action. The outer layer of the heart, known as the epicardium or visceral pericardium, forms the inner layer to the pericardium sac. The

inner layer of the pericardium sac is continuous with the outer layer of the pericardium at the roots of the vessels. The outer layer is covered by a dense fibrous covering.

Heart Physiology

The heart is a muscular pump with two functions. The right set of atrium and ventricle is responsible for drawing venous blood from the systemic circuit and pumping them to the lungs. The left set of atrium and ventricle is responsible for drawing oxygenated blood from the lungs and pumping them into the systematic circuit. As such, the blood circulates in a double circuit.

The anatomical differences between the heart chambers revealed the physiology of the heart. In general, the ventricles are larger than the atria in size, and capacity in order to pump against the blood pressure in the arteries. The heart adapts by developing heart muscles to adapt to different load and blood flow, such as the rest state versus the exercise state. The left ventricle is the strongest chamber since it drives the systemic blood circuitry; where as the right ventricle drives the pulmonary circuitry. The atria' function is to prime its respective ventricle with blood, therefore it requires less effort comparing to the ventricles.

The heart has an impulse-conducting system to rhythmically control the heart pumping action. The system consists of three conducting fibers, the sinoatrial node (SA node), the atrioventricular node (AV node), and the punkinje fibers. The sinoatrial node is located in the wall of the right atrium, and controls the rate of heart beat. This impulse spreads through the heart, causes the atrium to contract, then into the AV node, next through the Purkinje system into the ventricles, and finally through the ventricular muscle itself. The entire cycle, known as the cardiac cycle, can be observed by measuring electrical impulses on the body surface. The full cardiac cycle can be correlated to the electrocardiogram as shown in Figure 2.27. The cycle can be broken into three parts.

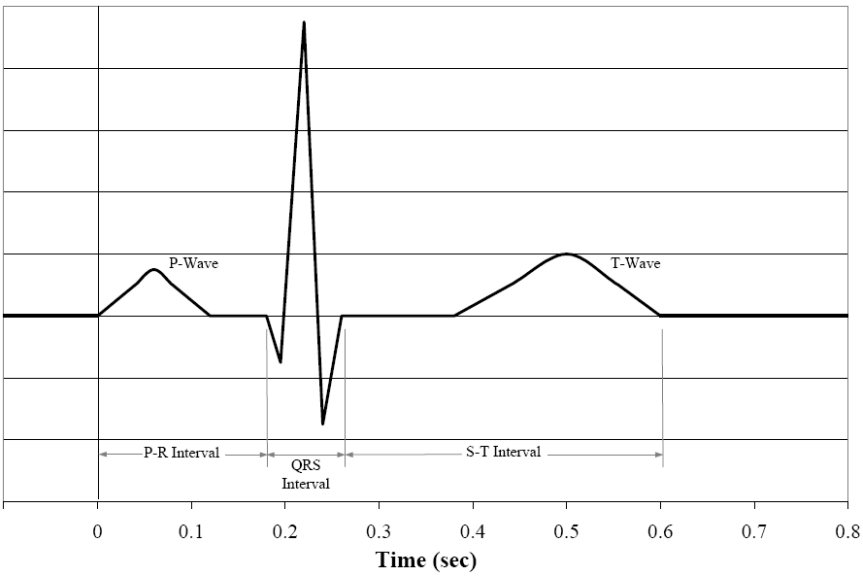

(Reproduced from Forbes, 2005)

Figure 2.27: The cardiac cycle

The first part is called the P-R interval, which includes the P-wave. The P-wave is referred to the impulse stimulating the atria to contract. The second part is the QRS complex where the impulse stimulates the ventricular muscle to contract. The third part is called the S-T interval, which includes the T-wave. The T-wave is caused by returning the membrane potential to its normal resting level at the end of ventricular contraction.

Heart Material Properties

The stress-strain response of the heart muscle tissue demonstrated hyperelasticity (Yamada, 1970). However, the heart muscle in a passive state is a viscoelastic material (Pinto & Fung, 1973). Tensile failure properties of the heart tissues from the myocardium layer of the left ventricle peak between age of 20 to 29 and in decline thereafter as shown in Figure 2.28. The ultimate strength of the muscle tissue in the transverse fiber direction was found to be approximately 1/3 of the strength in the parallel direction. The ultimate elongation in the transverse direction was 1.3 times the elongation in the parallel direction.

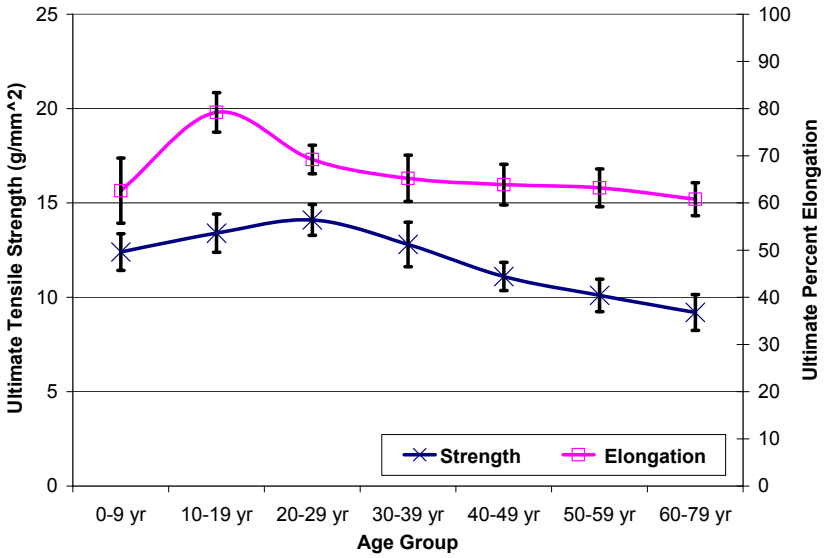

(Reproduced from Yamada, 1970)

Figure 2.28: Tensile properties of cardiac myocardium muscle

Material Model

Deng et al (1999) modeled the passive heart tissue behavior by adopting the modeling approach developed by McCulloch and Omens (1991). The strain energy function is shown in Equation 2.5.

$$W = \frac{C}{2}(e^{Q} - 1) - \frac{p}{2}(I_3 - 1)$$

$$Q = b_1 E_{11}^2 + b_2(E_{22}^2 + E_{33}^2 + E_{23}^2 + E_{32}^2) + b_3(E_{12}^2 + E_{21}^2 + E_{13}^2 + E_{31}^2)$$

Where	E_{ij}	Lagrangian strain components
	p	hydrostatic pressure variable
	I_3	third principal strain invariant
	C, b_1, b_2, b_3	Material constants

Equation 2.5: Strain energy function of the heart muscle

Yen et al (1999) performed bi-axial tensile tests on the endocardium, the myocardium and the epicardium from the left ventricle wall, each separately. All specimens exhibited a higher stiffness in the fiber direction than in the cross-fiber direction. The endocardium and the epicardium were stiffer than the myocardium. Hysteresis exists in both the fiber and cross-fiber direction. A single material model with C, b1 and b2 material parameters derived from the myocardium layer was implemented to represent all three layers since it

is the thickest band in the heart tissue (Guyton, 1996). The material parameters b_3 was adopted from Guccione and McCulloch (1991). A simplified approximate hyperelastic approach of the heart model is considered sufficient as the focus is placed on the development of the boundary condition (i.e. the lungs). The material constants of the heart muscle were summarized in Table 2.11.

Table 2.11: Material constants of the heart muscle

C (KPa)	b1	b2	b3
1.085	24.26	40.52	1.63

(Reproduced from Deng, 1999)

The heart model was constructed based on the geometric data from Viewpoint Data Labs. The four chambers in the heart were modeled and an elastic blood fluid was represented within. The valve mechanism was not modeled.

The heart position was referenced from the Visible Human Project. It is critical to verify the heart position given that the cadavers may not be reflective of the anatomy of a living human. In the study of the aortic injury by Hardy (2008), cadavers had to be repositioned to shift the heart to a more representative anatomical position. A representative position is necessary to accurately model aortic injury in the future as discussed in a later section.

A more sophisticated approach to model all three tissue layers can be incorporated to investigate heart contusion at organ level. However, this is outside the scope of the current study since it is a lower research priority given its low injury occurrences. Emphasis was placed on the development of loading interaction with the heart and its surrounding components.

Heart Injury

High velocity thoracic impact often resulted in two forms of injuries: heart contusion and laceration. High velocity impact directing at the heart can result in cardiac arrest.

Myocardial contusion refers to a bruising of the middle layer of the heart muscle. The damaged muscular fibers can lead to heart failure through a rupture, a defective rhythm,

or a ventricular aneurysm if the loading is severe. The myocardial layer of the heart tissue is the most susceptible to contusion since it is the largest muscle in the heart (Nahum and Melvin, 2002). The contusion is commonly related to the compression and the compression rate of the heart tissue. Heart rupture can occur when severely compressed between the sternum and thoracic vertebrae. The left and right ventricles are involved with equal frequency, followed by the right atrium and the left atrium (Parmley et al, 1953; Leavitt et al, 1987; Aris et al, 2000). However, the right ventricle operates at a lower pressure relative to other heart chambers; it has a reduced ability to sustain overpressure due to a thinner heart muscle (Chapon, 1984). Although a heart valve injury can occur, its occurrence after a blunt trauma is rare (Halstead et al, 2000).

Cardiac laceration can occur due to a fractured rib causing a tear in the heart or due to a severe thoracic compression over the sternum. Pericardial tamponade can result if the pericardial sac is lacerated. Fluid can accumulate within the sac and add pressure to the heart surrounding, thus preventing the heart from expanding. Perforation can occur due to a laceration from rib ends or fragments, causing a profuse bleeding internally and leads to a heart failure.

Cardiac Arrest can occur at a high loading rate and without significant physical damage. Impact velocities between 15 m/s and 20 m/s appeared to interrupt the electromechanical transduction of the heart wall resulting in a commotion cordis. Animal research had shown that the commotion cordis is associated with impact occurring during the T-wave of the electrocardiogram (Cooper et al, 1982; Kroell et al., 1986; Janda et al, 1998).

2.3.4 Aorta

Anatomy of the aorta

The major trunk of vessels that convey the oxygenated blood from the left ventricle is known as the aorta. It is about 30 mm in diameter. It ascends for a short distance beginning at the right ventricle opening of the heart, then arches backward and to the left side (Gray, 2000); it then descends along the left side of the vertebral column. The aorta

can be subdivided into three regions, the ascending aorta, the arch of the aorta, and the descending aorta as illustrated in Figure 2.29.

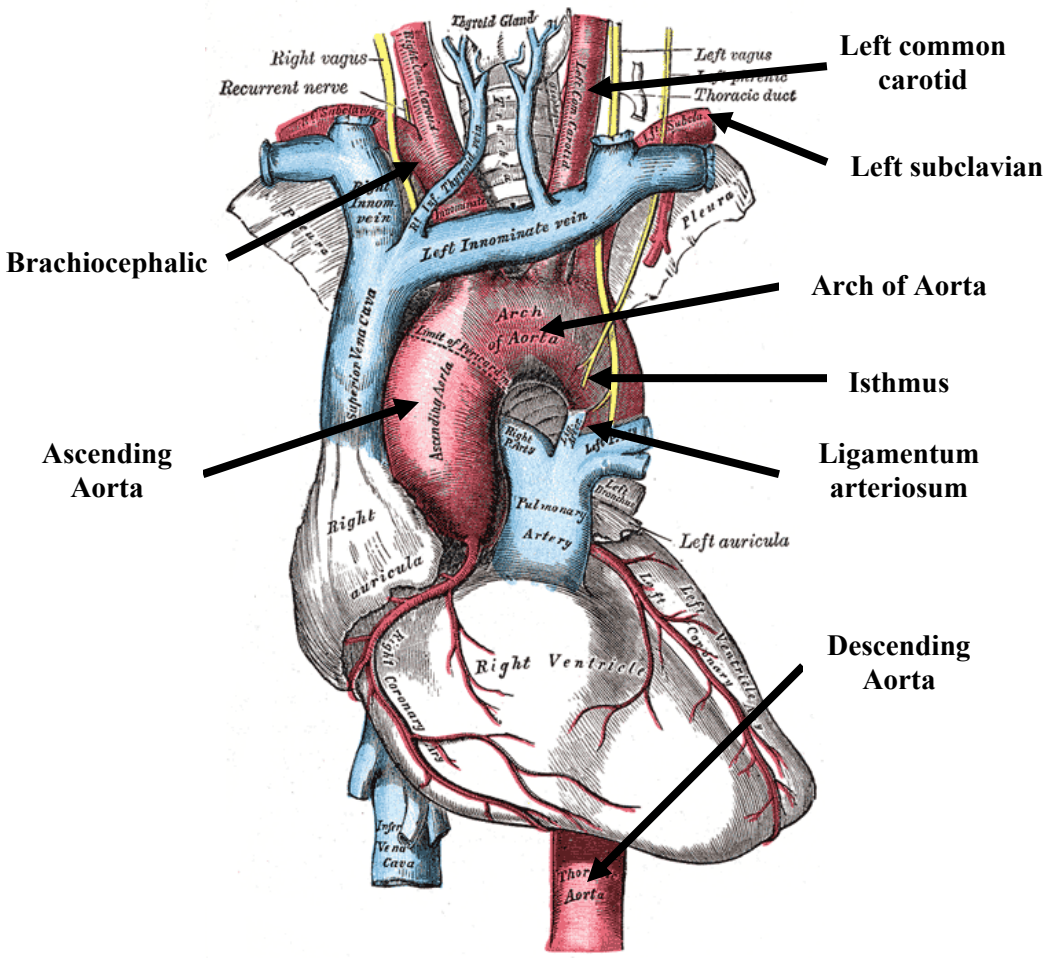

(Reproduced from Gray, 2000)

Figure 2.29: The arch of the aorta and its branches

There are two coronary arteries that branch off the ascending aorta and supply blood to the heart. The arch of the aorta has three branching arteries called the brachiocephalic (supply to the right arm and head), the left common carotid (supply to the head), and the left subclavian (supply to the left arm). The ascending aorta and the arch of the aorta are relatively unconstrained. A small ligament that ties the arch of the aorta to the left pulmonary artery is known as the ligamentum arteriosum. The section of the aortic arch between the left subclavian and the ligamentum arteriosum is known as the peri-isthmus or isthmus. The descending aorta begins at the lower border level of the fourth thoracic

vertebra and ends at lower border level of the twelfth thoracic vertebra. It is firmly tethered to the thoracic spine through branching arteries.

The aorta is a tubular structure and is made of three layers of tissue: tunica intima (inner), tunica media (middle), and tunica adventitia (outer). The intima consists of a lining of the endothelium cells exposed to the blood. A thin coat of fibrous tissue behind the lining consists of collagenous fibers and elastic fibers. The media is the thickest layer and consists of connective tissue, mostly smooth muscle fibers and small amounts of collagenous fibers. The adventitia is a thin layer consisting mainly collagenous fibers with some elastic fibers. The aorta can be referenced in two anatomical axes, a longitudinal (axial) direction that is parallel to the central axis of the tubular structure, and a circumferential (transverse) direction that is radial to the central axis.

Aorta Physiology

The aorta experiences a pulsating pressure since it is the largest blood vessel and experiences the highest blood flow. The pressure at its highest point during the pressure cycle is called the systolic pressure, and the pressure at its lowest is the diastolic pressure. The systolic and diastolic pressures usually reach 120 mm Hg (16 kPa) and 80mm Hg (11 kPa) in young adults, respectively. In old age, the average pressures are about 150 mm Hg (20kPa) and 90 mm Hg (12 kPa) (Guyton, 1996). The cardiac output refers to the amount of blood pumped by the heart, and is approximately 5 Liter/min at rest, 25 to 35 Liter/min during the most extreme exercise (Guyton, 1996).

Aorta Material Properties

Aorta, like many soft tissues, exhibits a rate-sensitive non-linear stress-strain response. From past experiments, the aortic tissue can be considered anisotropic with different material properties along the longitudinal and circumferential directions. The tensile properties of the aorta (ascending, descending, common carotid) demonstrated the mechanical behavior differences in the longitudinal and circumferential directions across various age groups as shown in Figure 2.30 (Yamada, 1970). The data showed

considerable decrease in ultimate elongation with an increase in age. The ultimate stress and strain were typically higher in the circumferential direction. The experiments demonstrated strain-rate effects and were evident that the ultimate stress increased significantly when loaded at a strain rate of 100/s compared to .01/s (Mohan and Melvin, 1982, 1983). The ratio of the ultimate true stresses between the strain rates of 100/s and .01/s was shown to be 1.23 higher in the circumferential direction and 2.04 higher in the longitudinal direction, respectively. Despite the failure stress varied with loading rates, Mohan and Melvin (1982, 1983) concluded that the maximum tensile strain theory was most applicable to predict failure. The aorta failure properties of the descending aorta are summarized in Table 2.12.

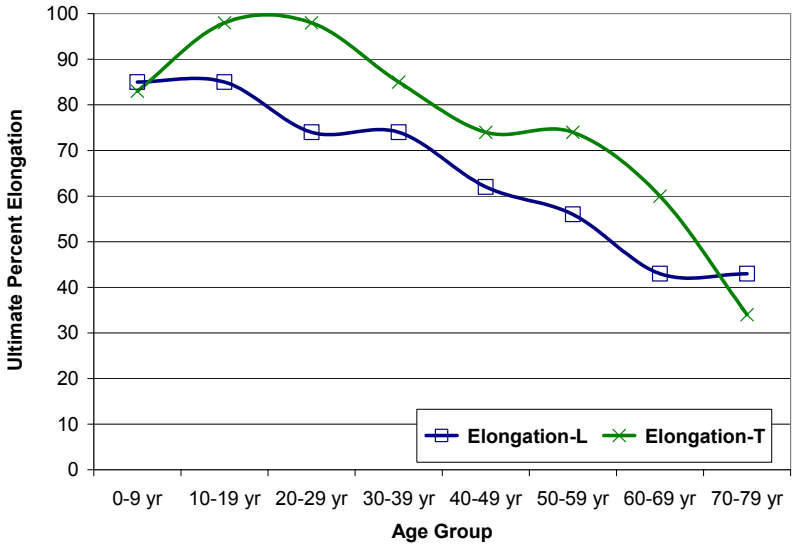

(Reproduced from Yamada, 1970)

Figure 2.30: Descending aorta, ultimate tensile percentage elongation across age groups

Bass et al (2001) carried out biaxial experiments on a porcine aorta and examined over-pressurization of the in-vitro and in-situ human aorta specimens. The authors cited no significant difference in response between the in-vitro and the in-situ conditions. A 50% risk of failure at a pressure of 101 kPa was proposed. However, most specimens' failure mode was a longitudinal laceration which is inconsistent with typical failure mode seen in automotive trauma.

Table 2.12: Aortic tissue failure properties, descending aorta

Test Conditions			Ultimate Stress (MPa)	Extension Ratio (unitless)
Uniaxial	Quasi-Static (~.01/s)	Longitudinal	1.47 ± 0.91	1.47 ± 0.23
		Circumferential	1.72 ± 0.89	1.53 ± 0.28
	Dynamic (~100/s)	Longitudinal	3.59 ± 2.04	1.64 ± 0.28
		Circumferential	5.07 ± 3.29	1.60 ± 0.28
Biaxial	Quasi-static (~.01/s)		1.14 ± 0.32	1.44 ± 0.10
	Dynamic (~20/s)		1.96 ± 0.60	1.28 ± 0.11

(Tabulated from Mohan and Melvin, 1982, 1983)

Shah et al (2005) conducted biaxial experiments on aortic tissue at the descending aorta region. The samples were cut in a cruciate shape to minimize local stress concentration effects. The samples were subjected to equi-biaxial stretch and tested at a strain rate of 44/s. The biaxial loading directions were oriented 22.5 degree from the longitudinal axis of the aorta. This was done to better characterize the material properties according to Lanir et al (1996). Estimates of the moduli were obtained by finding the slope of the true stress versus Lagrangian strain at the nearly linear middle region of the material response. The failure properties of the descending aorta are summarized in Table 2.13.

Table 2.13: Transformed moduli and failure thresholds, descending aorta

	Avg Max Principal Strain Rate (1/s)	Modulus (MPa)		Failure True Stress (MPa)		Failure Strain		
						Max Principal	Lagrangian	
		Circ.	Long.	Circ.	Long.		Circ.	Long.
Avg	37.34	9.26	7.54	1.92	1.64	.305	0.247	0.242
SD	10.31	8.32	2.22	.35	.35	.050	0.072	0.043

(Tabulated from Shah et al, 2005)

Shah et al (2006) conducted a similar study at the ascending, isthmus and descending regions of the aorta. The results demonstrated several trends. Firstly, the specimens tend to tear in the transverse (circumferential) direction. Secondly, the isthmus region failed at the highest level of stress but at the lowest strain level compared to the other two regions. Thirdly, despite testing at two different loading speeds, the deviation associated with the moduli represented a substantial overlap. The specimens were loaded at 1m/s and 5m/s biaxially to achieve an average peak principal strain rate of 90/s and 136/s. Despite the large difference in the loading speeds, Shah cited that none of the material parameters showed statistical significance between regions or between strain rates.

The structural response of the whole aorta to a longitudinal tension was also examined in the study by Shah et al (2006). The intact thoracic aorta was subjected to a longitudinal stretch, and was torn in the transverse direction within the isthmus region. The intima layer failed before the media or the adventita layer. The aorta transected completely from a 92 N of axial load and a 0.221 axial strain (Shah et al, 2006).

Material Model

Deng (1999) modeled the aorta and the superior vena cava tissues with an elastic material enclosing an elastic fluid. The material properties were derived from the data compiled in Abe et al (1996). This approach was considered an appropriate intermediate step until a proper geometry is implemented and representative loading conditions are taken into consideration. An appropriate aorta material model should account for the anisotropic behavior, possess a non-linear stress-strain response, and incorporate strain-rate dependency. Aortic tissue was demonstrated to be incompressible (Carew et al, 1968; Patel et al, 1969). The following table summarized material models used by various researchers as shown in Table 2.14. The orthotropic linear elastic material model by Shah et al (2007) was built upon all the available material data at the time and its model had been under development in parallel with material testing. As such, it was implemented in the current model to provide representative boundary conditions to neighboring components.

Table 2.14: A summary of material models used to represent aortic tissue

Material Model	Exp. Data used for characterization	Author's Reference
Blatz-Ko rubber (LS-Dyna) Isotropic linear elastic Orthotropic linear elastic Ogden rubber	The material parameters justification and validation were not provided	Richens et al (2004)
Isotropic linear elastic	Yamada (1970), Wang (1995)	Ruan et al (2003)
Isotropic linear elastic-plastic	Uniaxial, Mohan and Melvin (1982)	Shah et al (2001)
2nd order Mooney Rivlin, isotropic	Provided biaxial test data and compared to uniaxial data by Mohan and Melvin [1982]	Darvish et al (2004)
Hyperelastic, isotropic, incompressible	Provided pressure-radius experiments	Delfino et al (1997)
Hyperelastic, isotropic, incompressible	Uniaxial tests data from tissue in diseased state	Raghavan and Vorp (2000) Wang et al (2001)
Anisotropic	Biaxial tests from tissue in diseased state	Vande Geest (2005)
Ogden rubber model	Uniaxial data, Mohan and Melvin [1982]	Maddali et al (2005)
Orthotropic linear elastic	biaxial, Shah et al [2005]	Shah et al (2007)

Aortic Injury

Aortic injury can occur with a severe direct non-penetrating chest impact or compression. The terminology used to describe aortic injury is inconsistent, several terms are often loosely interchanged: tear, laceration, transection, and rupture. However, aortic injury is often a result of laceration, tearing or a torn, ragged or mangled wound (Creasy, 1997). Traumatic rupture of the aorta (TRA), is often referenced in biomechanics literatures. A rupture is defined as a forcible tearing or disruption of tissue. It is used to convey the severity of an aortic laceration. A transection provides descriptive meaning to the laceration, where the entire or nearly entire circumference of the vessel is lacerated.

The primary site of aortic laceration is at the isthmus, typically a transverse tear of the descending aorta, distal to the left subclavian artery, and above the ligamentum arteriosum on the anterior wall (Viano, 1983). 90% of aortic injuries occur in the region of the isthmus (Groskin, 1992). The tear typically involves the intima and the media, and may or may not involve the adventitia. 79.1% of TRA victims had associated rib

fractures, and 68% suffered multiple bilateral rib fractures regardless of the impact direction (Bertrnand et al, 2008). A longitudinal laceration along the aorta is probable if pressurization of the aorta is sufficient (Bass, 2001). Numerous studies have shown that it is unlikely that pressurization is the primary cause of TRA. The failure is inconsistent with transverse lacerations that were typically seen in automotive trauma, but it may be a contributing factor (Roberts et al, 1966; Mohan and Melvin, 1982; Hardy et al, 2008).

Hardy et al (2006) concluded that TRA could be generated using a simple axial tension. Any external input that causes straightening of the lesser curvature of the aorta might lead to tearing. Distraction of the aortic arch anteriorly, superiorly, or laterally to the right was shown to initiate TRA.

Factors influencing Injury Mechanism

Individual differences in age and pathological conditions affect the material response of aortic tissue, as supported by the material data in Yamada (1970) and Abe (1996). The failure strain of the aortic tissue decreases considerably with age by more than 50% over its lifetime (Yamada, 1970). Atherosclerosis is expected to increase the likelihood of TRA (Viano, 1978). Hardy et al (2008) observed numerous damage sites corresponding to the regions with atherosclerotic plaque. Also, the strain recorded at these sites was found to be lower than those with normal tissue.

The study by Hardy et al (2008) reinforced the concept that TRA is related to tension. This was the first study that was able to replicate TRA that is relevant to the automotive trauma. The heart of a cadaver in the seated position tends to be more inferior, posterior and pitch rearward than in a living human. This configuration would unlikely to generate sufficient level of longitudinal tension for TRA to occur. In Hardy et al (2008) study, cadavers were inverted and angled in such a way that the diaphragm, heart and aorta were in more anatomically correct positions. Four loading conditions were investigated to induce tensile loading on the aorta.

Firstly, the shoveling and submarining mechanisms were investigated to replicate frontal impact loading condition. The shoveling mechanism refers to the thorax impacting the steering wheel, in which the inferior section of the sternum is "shoved" superiorly and displaces the heart in the superior and inferior direction, creating a tensile loading to the aorta. An impactor was used in place of a steering wheel to induce similar loading mechanism.

Secondly, the submarining mechanism was investigated by loading the abdominal contents through a shoulder belt at an angle of 40 degree from the horizontal plane with a high-speed tensioner. The intent was to mimic an out-of-position occupant.

Thirdly, an impactor was directed at the side of the ribcage with and without engaging the shoulder and the arm to replicate side impact loading. During side impact, the ribcage and the shoulder can force the sternum away from the spine. The heart and the arch of the aorta are tethered to the sternum and can move anteriorly with the sternum. The aorta can move more anteriorly when both arms were engaged than direct impact to the ribcage (Melvin et al 1998; Cavanaugh et al, 2005; Hardy et al, 2008).

Lastly, an impactor was loaded over the sternum at an oblique angle which added medial motion to the shoveling mechanism.

Seven out of the eight tests generated TRA in the cadavers. The authors cited the one test that did not generate TRA might have to do with the specimen being relatively large and the input energy level was expected to be insufficient.

2.4 Thoracic Injury Scales and Criteria

Many injury scales have been developed over the years differentiate injuries and associated severity in trauma patients for documentation and communication purposes. Figure 2.31 summarizes common soft tissue thoracic injuries. There are currently several anatomic and physiologic scoring systems available: Abbreviated Injury scale (AIS), Organ Injury Scale (OIS), Injury Severity Score (ISS), Revised Trauma Score (RTS), and

Trauma Injury Severity Score (TRISS), etc. The most refined and commonly used scoring system to assess specific traumatic injuries is the AIS. Sometimes, the ISS system is also referenced to assess trauma patients with multiple injuries.

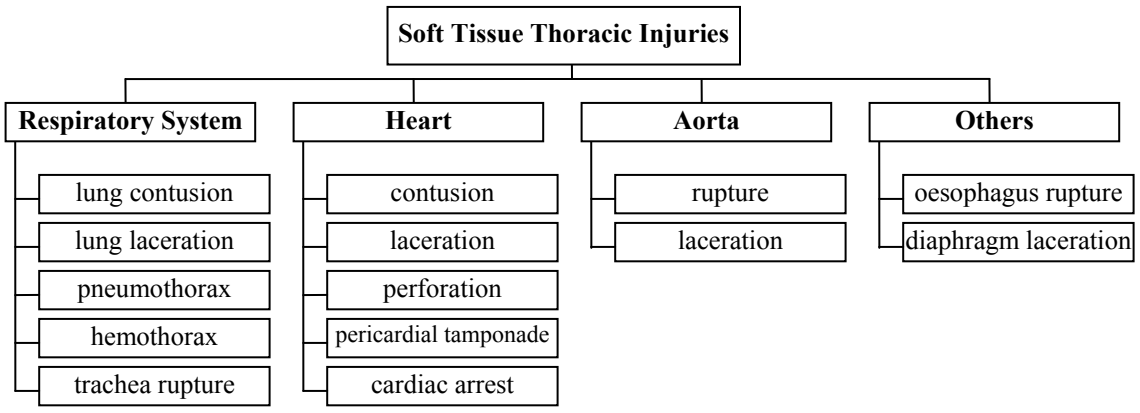

(Reproduced from Schmitt, 2007)

Figure 2.31: Possible soft tissue thoracic injuries

AIS

The abbreviated injury scale (AIS) was developed to be a widely accepted injury scale that could be used by automotive accident investigation teams to classify injury level sustained by a body region or organ [States, 1969]. The AIS uses a numerical rating system to assess impact injury severity and has been used to establish tolerance levels for various automotive injury criteria. The AIS scale starts at 1 being minor, and ends at 6 where a maximum level of injury is sustained as shown in Table 2.15.

Table 2.15: AIS (2005)

AIS	Injury Severity
1	Minor
2	Moderate
3	Serious
4	Severe
5	Critical
6	Unsurvivable

The AIS represents the threat to life associated with an injury. The scale is not intended to quantify the probability of long-term disability, medical cost, or societal costs of injury. The 2005 revision is the latest published AIS. Typical injuries to the thorax and the

respective AIS assignment are shown in Table 2.16. The AIS has multiple revisions (1980, 1985, 1990, 1998, and 2005), therefore the injury description and its injury scale assignment may change and be referenced differently. For example, a unilateral flail chest is considered an AIS 4 in revision 1990, but is an AIS 3 in revision 2005. The Maximum AIS, known as the MAIS, is sometimes used to define a single most severe AIS sustained from various points of injury.

Table 2.16: Typical skeletal and soft tissue injures to the thorax

AIS Level	Skeletal Injury	Soft Tissue Injury
1	1 rib fracture	Heart Contusion
2	2 rib fractures sternum fracture	Pericardium Laceration Pleura Laceration Unilateral Lung Contusion, minor*
3	3 or more rib fractures Unilateral flail chest	Unilateral Lung Contusion, major* Bilateral Lung Contusion, minor* Unilateral Lung Laceration, minor* Hemothorax
4		Bilateral Lung Contusion, major* Bilateral Lung Laceration, minor* Aortic Laceration, minor Heart Contusion, major
5	Bilateral flail chest	Bilateral Lung Laceration, major* Tension Pneumothorax Aortic Laceration, major
6		Aortic Laceration with hemorrhage, not confined to mediastinum
*minor means < 1 lobe, major means 1 or more lobes, at least on one side		

(Reproduced from AIS, 2005)

Injury Severity Score

The Injury Severity Score (ISS) was introduced to account for several injuries of differing degrees (Baker et al, 1974). It is an anatomical scoring system that provides an overall score for patients with multiple injuries. The ISS is based on the highest AIS score to each of the six body regions (Head & Neck, Face, Chest, Abdomen, Extremities including pelvis, External). The ISS score is calculated by the sum of squaring the top three most severely injured body regions ($ISS = AIS_1^2 + AIS_2^2 + AIS_3^2$). The ISS takes values from 0 to 75. If any resulting injury has an AIS of 6, then the ISS is automatically assigned to 75.

2.4.1 Global Injury Criteria

Acceleration Criteria

The acceleration criterion was first developed to establish whole-body rapid deceleration tolerance limits in airplanes. In an effort to protect military personnel, Stapp (1951, 1970) conducted a series of rocket-sled experiments demonstrating the whole body tolerance with seatbelt constraints. Eiband (1959) combined his experimental data with the experiments by Stapp (1951), and concluded that the whole-body deceleration tolerance increased as the duration of the exposure decreased as outlined in Figure 2.32. The deceleration tolerance also changes depending on the impact direction. The deceleration tolerance has been well established for all six impact directions as a general design guideline in regard of human performance and safety in aerospace vehicles (NASA, 1995). The rotational acceleration limits have also been considered.

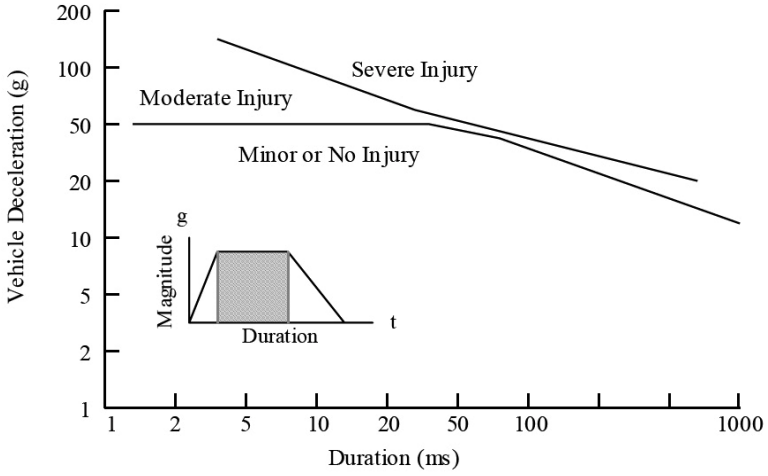

(Reproduced from Eiband, 1959)

Figure 2.32: Vehicle deceleration magnitude and duration for human volunteers

This deceleration tolerance is currently used in the European and North American safety standards for frontal impacts. The deceleration tolerance criterion calls for the resultant acceleration shall not exceed 60 g's, except for intervals whose cumulative duration is not more than 3 milliseconds (FMVSS 208, 2008).

Force Criteria

The development of a force tolerance was first initiated in the early 1960s due to the increasing pattern of occupants who sustained thoracic injuries from impacting the steering wheel. The objective was to design an energy-absorbing steering column that limit the yielding force. Frontal impact experiments by Patrick et al (1965), Gadd and Patrick (1968) and Patrick et al (1969) revealed that the sternum can tolerate a maximum force of 3.3kN and the shoulders and chest can tolerate a distributed load of 8.8kN with only a minor trauma.

Compression Criteria

Although the understanding of injury tolerance was improved from the cadaver impact experiments, it became clear that the whole-body deceleration and force did not adequately describe the thorax response or the risk of internal organ injury. Kroell's (1974) analysis on a series of blunt thoracic impact experiments confirmed that the maximum acceleration of the thoracic spine was a poor indicator of chest injury potential, and the maximum chest compression was a better predictor.

Kroell's (1971) experiments demonstrated that a chest compression up to 20% during a frontal impact (over a moderate duration) was fully reversible with no detectable injury. When the chest compression was greater than 20%, the compression level positively correlated with the risk of skeletal fractures in the ribcage. Multiple skeletal injuries resulted at 40% chest compression indicative of flail chest. Viano (1978) reasoned that when the protective function of the ribcage was compromised, the unstable chest structure could load the intrathoracic vital organs and cause injuries to the heart, lung and great vessels.

The statistical analysis by Neathery et al (1974, 1975) showed that a normalized sternal deflection of 75mm correlated with a 50% probability of AIS 3 for a 45 year old, 50^{th} percentile male. The deflection limit of 76mm (3 inch) was set for the FMVSS 208 when testing with a Hybrid III dummy (Cavanaugh, 1993b).

Mertz et al (1997) reanalyzed past data from Neathery et al (1974) to develop a normalized injury risk curves for measurements made with the CRABI and Hybrid III family of dummies based on the new AIS codes. The injury tolerance data were normalized for size and strength considerations. From his analysis, rib fractures were the predominate injury in the AIS $\geq$ 3 dataset, where as heart and/or aortic ruptures were the predominate injury in the AIS $\geq$ 4 dataset. The normalized sternal deflection of 64.3mm corresponded to a 5% risk of AIS $\geq$ 4 heart injury. Although the deflection limit was recommended to adjust from 76mm to 64mm for the FMVSS 208, the threshold limits was harmonized with Transport Canada and adopted 63 mm for chest deflection (NHTSA, 2000).

Viscous Criteria

Lau and Viano (1985) formulated the Viscous Criterion (VC) to evaluate the risk of soft tissue injury as shown in Equation 2.6. This criterion accounts for soft tissue injury by the instantaneous product of velocity of deformation and chest compression.

$$VC = V(t) \times C(t) = \frac{d[y(t)]}{dt} \times \frac{y(t)}{D}$$

Where
- V(t) Velocity of deformation
- C(t) Chest Compression
- y(t) Chest Deflection
- D Initial Chest Depth

Equation 2.6: The viscous criterion

Kroell et al (1981), Lau and Viano (1981) and Viano and Lau (1983) conducted studies to determine the compression and loading rate relationship through experiments. These studies have shown that the injury resulted from high velocity-low compression impacts were greater than low velocity-high compression impacts. Lau and Viano (1981) studied lung injury using anesthetized rabbits, and recognized that the alveolar region was more sensitive to the rate of loading than the bronchial region. Kroell et al (1981, 1986) verified the validity of the VC. Kroell's (1986) analysis showed that VC_{max} and $V_{max}C_{max}$ were good predictors of the probability of heart rupture and a thoracic MAIS > 3 injury. C_{max} proved to be a poor predictor.

Using this criterion, Viano and Lau (1988) proposed $[VC]_{max}$ values for frontal injury levels based on past PMHS experiments (Kroell et al. 1974). Viano et al. (1989a, 1989b) subjected PMHS to free-flight oblique pendulum impacts to develop the lateral injury criteria. The VC response was correlated to various AIS level probabilities.

Given that the VC takes rate effects into account, the injury evaluation does not necessary applicable across all impact velocities. The typical VC response begins to increase at contact, reaches a maximum value, and then reaches zero once compression has reached the maximum. However, the compression criterion had proved that the peak compression of the human torso correlated with injuries. This suggested that there should be a transition velocity threshold; the compression criterion is more applicable and robust at an impact velocity that is below the transition threshold, while above the transition threshold, the vicious criterion becomes applicable and more robust in injury prediction. Lau and Viano (1986) had investigated the applicability of compression and viscous criteria, and concluded that the viscous criteria should be used for impact velocities between 3 m/s and 30m/s. For a sub 3m/s impact, the compression criterion should be used. For a high impact velocity, neither compression criterion nor VC is applicable. Ridella and Viano (1990) reanalyzed the transition impact velocity statistically, and revised the previously suggested 3m/s transition velocity to 4.5m/s.

Thoracic Trauma Index

The development of the thoracic trauma index (TTI) was an effort to establish lateral impact injury indices and was formally presented by Eppinger et al (1984). The use of TTI was based upon lateral impact experiments conducted on PMHS seated in actual cars and in side sled test devices. The results suggested that the spine and/or rib acceleration might correlate to thoracic injuries. The TTI was defined based on age, body mass, rib and T12 vertebra lateral acceleration (Klaus et al, 1983, 1984). Similar to other injury criterion, TTI was used to predict specific AIS levels based on the PMHS side impact experiments (Morgan et al, 1986). However, Viano (1987) performed similar analysis on different side impact PMHS experiments and found that the TTI was insensitive to the

total kinetic impact energy. Since the TTI is derived from spine and/or rib accelerations, its value is determined within the first milliseconds of impact. This criterion may be misleading and indicate a safe exposure to injury when the full event of an impact may indicate extensive injuries.

2.4.2 Injury Criteria and Tolerance Levels Summary

Cadaver studies over the past 50 years had provided significant insight to the biomechanical response of the thorax where tolerance values can be determined for various load conditions. Numerous injury criteria were developed based on differing interpretations and limitations. Table 2.17 and Table 2.18 summarized the most commonly used thoracic injury tolerances for frontal and side impact conditions. Keep in mind that the occupant protection standard is always evolving; the summary reflected the tolerances specified as of the start of year 2009.

Table 2.17: Frontal impact tolerances of the thorax

Tolerance Level	Injury level	Reference
Force		
3.3 kN	Minor Injury to sternum	Patrick et al (1969)
8.8 kN	Minor Injury to chest and shoulders	Patrick et al (1969)
Acceleration		
60 g within 3ms	Limit for Hybrid III	FMVSS 208*
Deflection		
75 mm	AIS 3 @ 50% probability	Neathery et al (1974, 1975)
50 mm	Limit for Hybrid III (50%)	ECE-R94*
52 mm	Limit for Hybrid III (5%)	FMVSS 208*
63 mm	Limit for Hybrid III (50%)	FMVSS 208*, Mertz (1997)
70 mm	Limit for Hybrid III (95%)	FMVSS 208*
Compression		
20%	Onset of rib fracture	Kroell et al (1971, 1974)
40%	Flail chest	Kroell et al (1971, 1974)
VC_{max}		
1.0 m/s	25% probability of AIS $\geq$ 4	Viano and Lau (1985, 1988)
1.3 m/s	50% probability of AIS $\geq$ 4	Viano and Lau (1985)
1.08 m/s	50% probability of AIS $\geq$ 4	Viano and Lau (1988)
1.0 m/s	Limit for Hybrid III	ECE-R94*
*Referenced as of year 2009 (updated from Cavanaugh, 1993)		

Table 2.18: Lateral impact tolerances of the thorax

Tolerance Level	Injury level	Reference
Force		
5.5 kN	AIS $\geq$ 4 @ 25% probability	Viano (1989)
Acceleration		
T8-Y 45.2 g	AIS $\geq$ 4 @ 25% probability	Viano (1989)
T12-Y 31.6g	AIS $\geq$ 4 @ 25% probability	Viano (1989)
60 g	AIS $\geq$ 4 @ 25% probability	Cavanuagh et al (1993)
82 g	Limit for ES-2 re, SID IIs	New FMVSS 214*
TTI		
TTI (d) – 85g	Max in SID for 4 door	Current FMVSS 214*
TTI (d) – 90g	Max in SID for 2 door	Current FMVSS 214*
TTI - 145g	AIS $\geq$ 4 @ 25% probability	Cavanaugh et al (1993)
TTI - 151g	AIS $\geq$ 4 @ 25% probability	Pintar et al (1997)
Deflection		
44 mm	Limit for ES-2 re	New FMVSS 214*
Compression		
33 % - half	AIS $\geq$ 4 @ 25% probability	Cavanaugh et al (1993)
38.4% - full	AIS $\geq$ 4 @ 25% probability	Viano (1989)
VC_{max}		
0.85 m/s – half	AIS $\geq$ 4 @ 25% probability	Cavanaugh et al (1993)
1.00 m/s	Limit for ES-2	ECE-R95*
1.00 m/s – full	AIS $\geq$ 3 @ 50% probability	Viano (1989)
1.65 m/s – full	AIS $\geq$ 4 @ 50% probability	Viano (1989)
*Referenced as of year 2009, new FMVSS 214 projected phase-in by September 1, 2012 (updated from Cavanaugh, 1993)		

Chapter 3
Model Development

3.1 Introduction

The detailed thoracic model in this study went through three iterations of major development and transformed into a full body model with a detailed thoracic representation. The first iteration of the thoracic model incorporated three-dimensional geometry of the spine, ribs, heart, lungs, and major blood vessels. Early development was focused on the skeletal response of the ribcage, synthesized appropriate material models for various soft organs, and conducted tissue experiments to derive relevant material properties (Deng et al, 1999). The second iteration of the thoracic model incorporated ribcage surface muscles, upper extremities, shoulders, and improved several material constitutive models (Chang, 2001). The third iteration of the thoracic model development transformed the thoracic model into a full body model by implementing the head, abdomen, pelvis and lower extremities, and improving the representation of the surface muscles, shoulders, and costal cartilage. The improvements made to the model expanded the applicability of the thoracic model to a variety of pendulum type and sled type loading scenarios (Forbes, 2005). Subsequently, the full body model was used as part of an investigation on the door-to-occupant interaction within a representative in-car environment under a lateral crash condition (Campbell, 2009).

The human thorax is a complicated human body region from the modeling perspective. Researchers have attempted to model the human thorax from using a lumped-mass model since the 1980's to a finite element thoracic model in the late 1990's. Various finite element thoracic models have mostly focused on the thoracic skeletal structure, while the representation of the internal organs is weak (Yang et al, 2006). The makeup of the human thorax is inherently complex, the overall response are made up of contributions from the ribcage, costal cartilage, ligaments, muscles and internal organs at varying

degree. An erroneous assumption on one component could be compensated by another erroneous assumption on another component despite the overall model response proved to be in good agreement (Yang et al, 2006). The available material properties either had large variations due to the test condition, age, gender, or they were simply not available.

The motive of the current study was to develop a detailed finite element thoracic model to investigate traumatic injuries to the vital organs. To mitigate the drawbacks as mentioned earlier, the conceptual approach to the development of the thoracic model was to develop components at the local tissue or organ level. If each component was modeled accurately at the component level, then the assembly of these components should provide an accurate response given that their connections are also accurately represented. When the thoracic model encompasses detailed representations of each component, the model will predict body response in a greater level of detail that can complement the design of experiments and enhance the interpretation of experimental data.

3.2 Model Construction

The thoracic model is composed of many components interconnected together with each part being developed at the component level prior to a full assembly. A schematic outlining major components of the full human body model is shown in Figure 3.1. The ribcage was made up of 12 pairs of ribs, with 10 pairs connected to the sternum through costal cartilages. Two sets of facet joints (spine to rib, costal cartilage to sternum) were modeled as spherical joints with stiffness properties derived from test data through various literatures (Panjabi et al, 1976; Schultz et al, 1974). The ribs were connected by the internal and external intercostal muscles. Two diaphragms were implemented to enclose the superior and inferior openings of the ribcage, thus created an enclosed thoracic cavity containing the heart, the lungs and the major blood vessels. The shoulder assembly was made up of deformable bodies such as the clavicle and scapula with joints connected to the humerus and sternum. There were seventeen sets of muscles connected the shoulder assembly to the thoracic cage at their representative anatomical insertion points. A layer of surface muscle covered the entire torso area to simulate soft tissue

response. The detailed thoracic model was complemented with a head, an abdomen, a pelvis, and the upper and lower extremities to create the full human body model. Each of these components was implemented as a single continuum model to provide representative response with minimal computational costs.

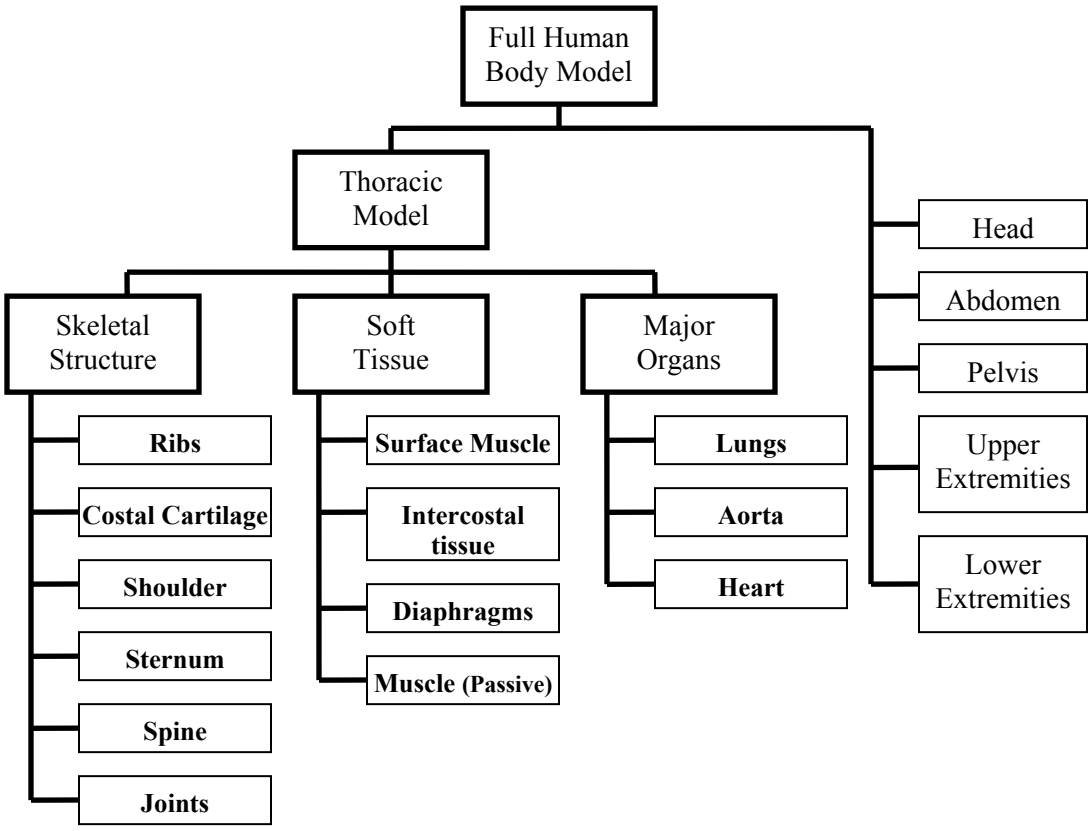

Figure 3.1: Hierarchy of development for the thoracic model

The current study was focused on two aspects:

- Refine various components within the thoracic model in terms of geometry, material properties, and boundary conditions
- Predict internal organ injury, pulmonary contusion.

During a frontal impact, the load transmits from the impactor through outer surface muscle, ribcage and intercostal muscles to the vital organs including heart, aorta and

lungs as shown in Figure 3.2. During a side impact, the load path is similar to the frontal impact except the heart and the aorta are loaded through the lungs as shown in Figure 3.3.

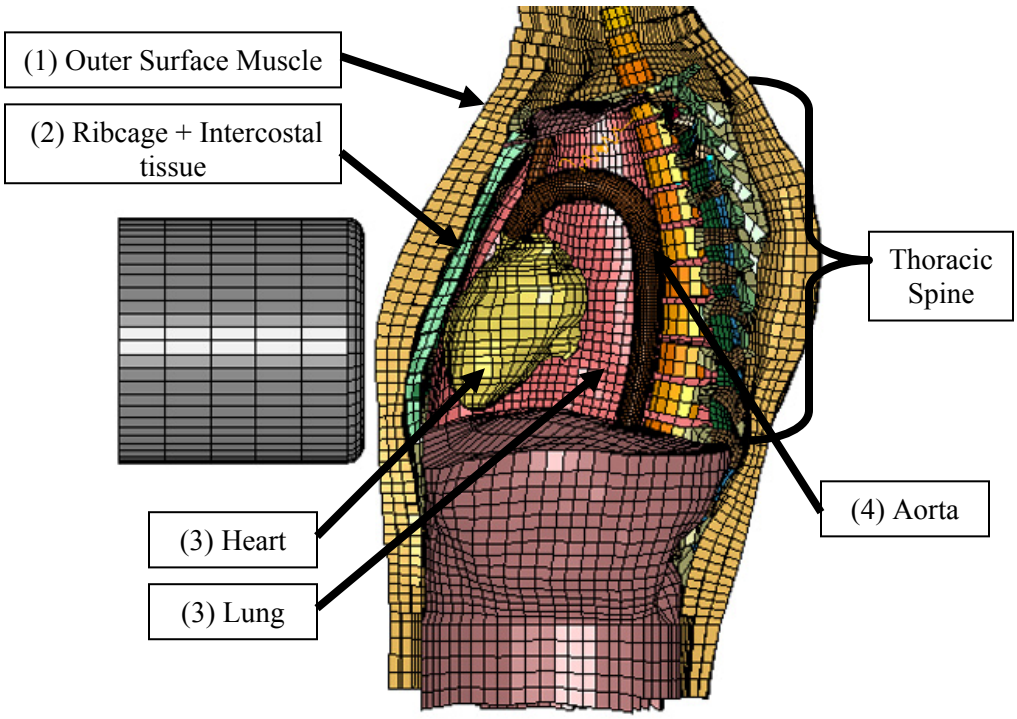

Figure 3.2: Frontal impact – load transmission path within thorax

The boundary conditions between the ribcage and the vital organs have to be accurate enable vital organ injuries investigation. Since these vital organs are inherently soft and relatively unconstrained, their contribution to the overall thoracic response is low relative to the ribcage. The vital organs were implemented in the original thoracic model; however voids exist within the thoracic cavity which led to poor representations of the boundary condition and geometry.

Given the full human body model demonstrated good agreement in providing representative thoracic response (Forbes, 2005), the next logical development was to predict internal organ injury. Emphasis was placed on the lung model for several reasons. Firstly, the lungs were found to be undersized and the boundary conditions surrounding the vital organs needed improvement. The surrounding boundary conditions around the lungs became the driving factor for the modeling development. It required special

attention since it was a prerequisite to modeling lung response accurately. Since the lung is a compliant, low impedance, low density, multi-phase material, its behavior is very sensitive to the boundary condition.

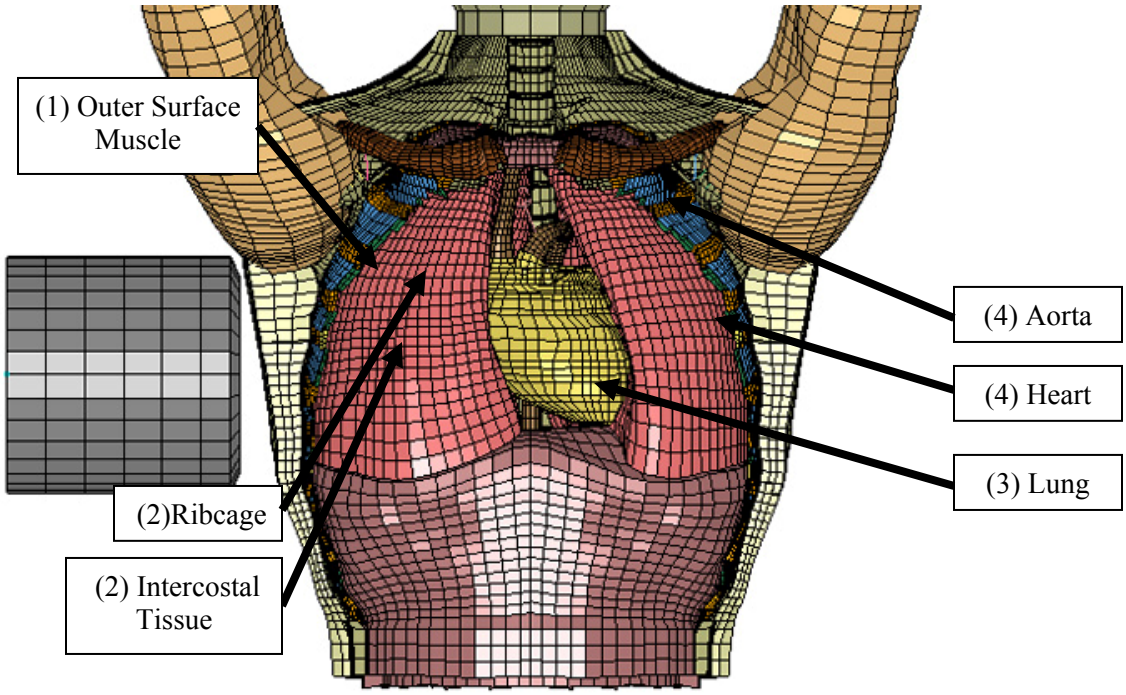

Figure 3.3: Side impact – load transmission path within thorax

The following chapter presents several improvements to the thoracic model with the intent to refine contact interaction between the vital organs, increase numerical stability, and improve material properties. Some of these changes required assumptions and compromise in modeling techniques due to the lack of available data. The implications of these changes are discussed throughout the chapter, followed by recommendations for future development.

3.3 Outer Surface Muscle

The thoracic cage is surrounded by a surface layer of soft tissue consisting of muscles and fats. Soft tissue has a non-linear stress-strain response and strain rate dependency. The fats and muscles were modeled as a single continuum layer around the thoracic cage;

the initial mesh representation was based on the 3d dataset from Viewpoint Datalabs (Orem, Utah). With the lack of soft tissue material data, Chang (2001) modeled the outer surface muscle using a heart constitutive material model. The material parameters were based on the heart constitutive material model from Deng et al (1999).

Forbes (2005) recognized the lack of strain-rate dependency of the model which led to inaccurate force response in addition to excessive strain level. Forbes (2005) combined the experimental bovine muscle compression data (McElhaney, 1966; Van Sligtenhorst, 2003) and the experimental tensile data (Yamada, 1970; Abe, 1996) to model the outer surface muscle more appropriately. Since the outer surface muscle loading is predominantly in compression, the selected compression data accounted for strain rates ranging from $0.001s^{-1}$ to 2250 s^{-1}. Forbes (2005) considered a simplified approach by modeling human tissue as a rate dependent hyperelastic material model (Du Bois, 2003) given the loading is essentially monotonic. The bulk modulus was calculated based on the human tissue density and sound speed from experiments, with the assumption that the bulk modulus greatly exceeds the shear modulus.

However, the thoracic response had a higher peak force and an elevated compression relative to the cadaver data largely due to an elevated mass density of the thorax. Chang (2001) adjusted the mass density to match the estimated thorax mass of a 50^{th} percentile male to compensate for voids and missing mass within the torso. This mass density adjustment resulted 2.4 times the mass density of human tissue (~1000 kg/m^3). The elevated mass density within the model in combination with the theoretical bulk modulus would result a higher sound speed as captured by the rapid force response.

Another major issue with the outer surface muscle was hourglassing, where the combination of the mesh and the contact interface made it susceptible to zero energy modes. Hourglass modes are non-physical zero-energy modes of deformation and are inherent with single-point integration formulation (LS-Dyna, 2006). Depending on loading condition and impact velocity, the model became numerically inaccurate due to

significant hourglassing triggered by contact interaction near the shoulder area. The outer surface muscle was connected to the ribcage through the inner surface using discrete tensile beams. The nodal loading nature of these beam elements is prone to trigger undesirable hourglass modes.

Improved Outer Surface Muscle Model

Three areas were improved to address the model deficits. First, the outer surface muscle geometry was modified to fill in the void between the tissue and the thoracic cage. A mass distribution study was conducted to mitigate the elevated mass density. Second, a mesh convergence study was conducted to determine an appropriate mesh density. Third, the method of constraining the outer surface muscle to the thoracic cage was improved.

Geometry

The inner surface of the outer surface muscle geometry (light yellow) was projected onto the outer surface of the thoracic cage to improve the contact interface. The section of the outer surface muscle at the abdomen level (blue) was mated to the abdomen continuum model (pink), made their contact interface coincident as shown in Figure 3.4.

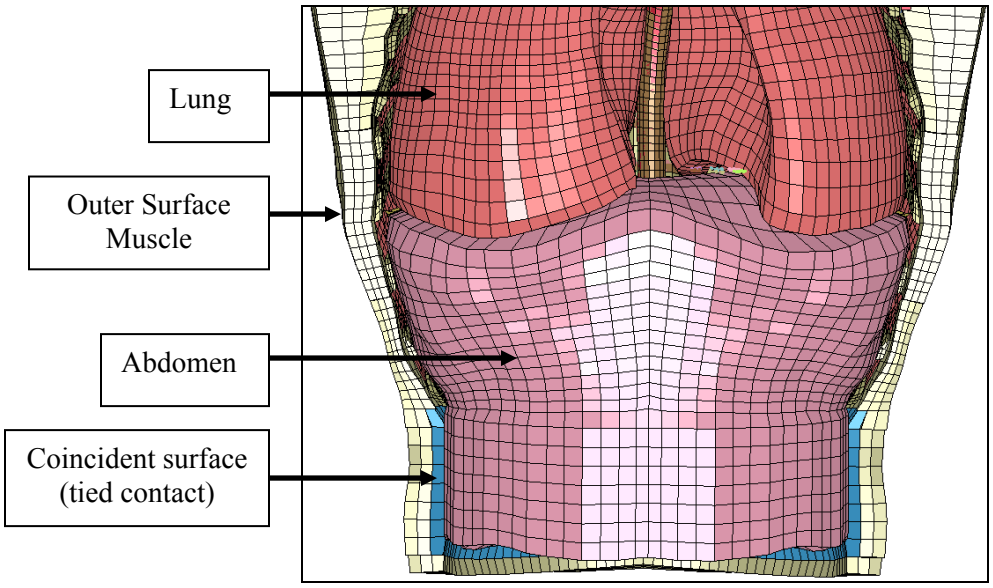

Figure 3.4: Thoracic cavity (front cut-out view)

Mesh Convergence

A mesh convergence study was conducted with a simple compression on a cylindrical block of tissue with element sizes at 20mm, 10mm, 5mm and 2.5mm. One face of the tissue was subjected to 50% strain with a relative boundary velocity of 1.5m/sec and a fixed boundary at the opposite face. The deformation rate was derived from the simulation of the limited-stroke lateral pendulum impact cadaver study by Chung et al (1999). The outer surface muscle achieved 50% strain in 6.5ms across an approximate 20mm initial tissue thickness. The contact force was monitored. The convergence study demonstrated a high inertial effect with large mesh sizes. The overall response shapes were consistent except the force magnitude varied from each other. The peak force response of the 20mm, 10mm, 5mm relative to the 2.5mm mesh were 1.65, 1.33, 1.05 times higher, respectively. The 5mm mesh was chosen as the target mesh size; it is computationally efficient without sacrificing accuracy.

New Geometry

The new outer surface tissue mesh was targeted to have an overall average of 5mm mesh density. The original mesh had two elements across its tissue thickness for the upper torso section, and one element thickness for the lower torso section. To accommodate varying thickness from 9 mm to 43 mm, the surface tissue was modeled with three elements across its tissue thickness throughout the torso. Impact-prone regions of the outer surface muscle were verified to ensure the mesh density was close to the target size. The mesh quality was driven to have an overall aspect ratio of 3 and a jacobian rating of 0.75 over 90% of the mesh. Figure 3.5 shows the old and new outer surface muscle mesh.

After the voids within thoracic cavity were filled and the mass distribution throughout the model were revisited, the mass density of the outer surface muscle was readjusted from 2400kg/m^3 to 1200 kg/m^3 to maintain the overall body mass of a 50th percentile male at 76.6kg (UMTRI, 1983). The current geometry took considerable effort to achieve appropriate fit with the thoracic cage and abdomen. From hindsight, the outer surface of the tissue model should have been scaled to achieve a more appropriate volume to avoid

mass density scaling altogether. The abdomen dimensions should be verified based on anthropometric data. Some of the missing mass was redistributed along the neck due to the lack of representation of soft tissue in the vicinity.

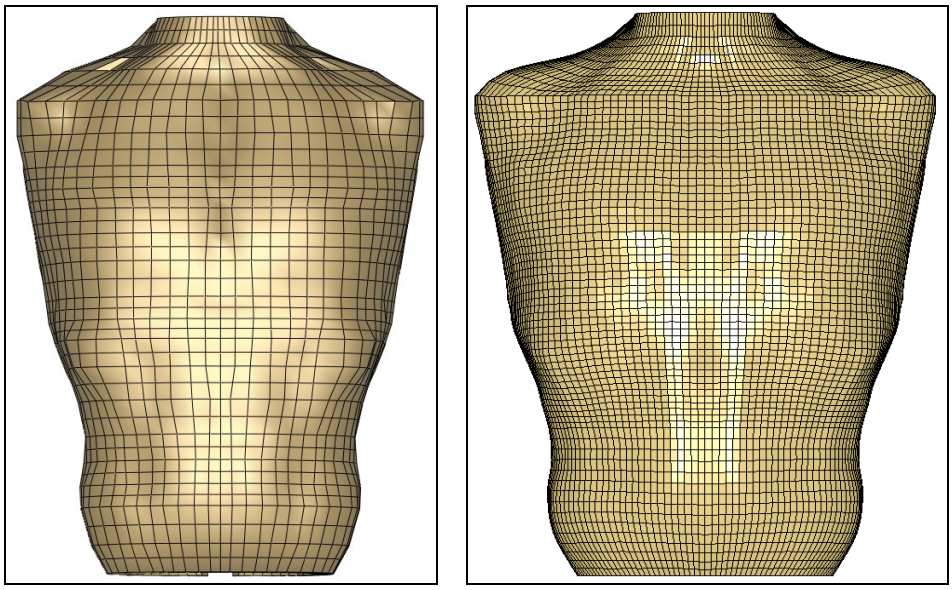

(a) (b)

Figure 3.5: Outer surface muscle mesh refinement (a) old (b) new

Outer Surface Muscle Interface

The original model utilized two approaches to constrain the outer surface muscle to the ribcage. The outer surface muscle layer was attached to the ribcage and spine through beam elements. The beam elements only transmit tensile forces to ensure the muscle layer move with the body. Contacts were defined between the surface muscle and the underneath structures such as the thoracic cage, intercostal tissue, abdomen and shoulders to transmit compression loading. In the current model, the beams were connected to the middle layer of the muscle mesh instead of the surface layer. The other end of the beams was connected to the skeletal structures and not to the soft tissues to minimize hourglassing and high nodal inertial mismatch. Aside refining the mesh and filling the voids to mitigate hourglass problems, the tied-contact interface was applied over the interface around the abdomen. A surface to surface contact interface was typically defined for all other components.

Interface consideration

The outer surface muscle should ideally enclose the thoracic cage and constrain the interface between them instead of free-sliding as in the current configuration. However, the mesh and geometry between the two components were too dissimilar making it not feasible to implement a tied contact interface. Stability issue may arise when rib element failure erosion is taken into account. When the rib elements reached the failure point, elements were deleted to simulate rib fractures. If the tied contact was used, numerical instability may occur at the fracture site due to the eroded interface. Care must be taken at the contact interface where the contact surface is relatively unconstrained such as the shoulder. For example, the outer surface muscle contact interface with the shoulder cannot adapt to the rotating shoulder motion without causing numerical instability if a tied contact was used.

Hourglass Considerations

An appropriate material model, ideal mesh, and uniform loading condition are all essential to minimize hourglassing. Viscous or stiffness based hourglass control should be the last resort to ensure appropriate response. Viscous type hourglass control is more appropriate for soft tissue as stiffness type tends to artificially stiffen the response. The recommended value for hourglass control is .15 for metals (LS-Dyna, 2006). A low value is ideal to avoid artificial stiffening and high hourglass energy consumption for soft tissues. Too little control however would lead to a high-distorted or negative volume element. From a sensitivity study conducted on a side pendulum impact simulation by varying hourglass control coefficient from .15 to .001, a value of .005 was found to be most ideal for soft tissues.

3.4 Intercostal Muscles

The spaces between the ribs are occupied by two groups of intercostal muscles. From impact point of view, the intercostal muscles are situated along the load transmission path to the vital organs. The original intercostal model utilized two layers of shell elements representing the inner and outer intercostal layers at 3 mm thick. Contacts were defined

between the outer surface muscle against the outer intercostal muscle, and between internal organs against the inner intercostal muscle; however contact was not defined between the intercostal muscle layers due to initial mesh penetrations. They were initially modeled with a fabric material model by Deng (1999), and then modeled as an elastic material model due to numerical instability by Forbes (2005). The original model of the intercostal muscles is shown in Figure 3.6.

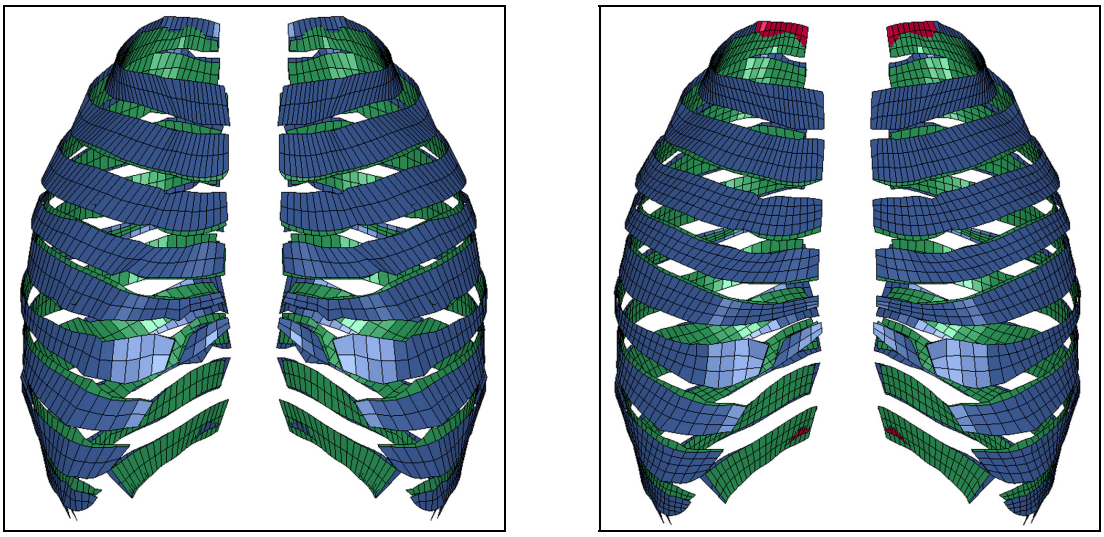

(original) (new)

Figure 3.6: Intercostal tissue model comparison

Improved intercostal muscle model

The new intercostal muscle model utilized the same material model for the outer surface muscle. The mesh was refined to have similar mesh density as the ribs and the outer surface muscle. The aspect ratio of the mesh was improved. Appropriate spacing was made between the two intercostal muscle layers to enable a surface-to-surface contact definition between them to create contact continuity.

3.5 Ribcage

The rib is composed of trabecular bone enclosed by an outer layer of cortical bone. The two material compositions are dissimilar as noted in Chapter 2. The original rib model was made up of a geometry using solid elements representing the effective properties of the two materials. Deng (1999) calibrated the material properties to mimic whole rib

response by comparing deflection response between two different rib cross-sections. One cross-section (with four elements across its thickness) was made up of solid elements representing the trabecular bone and an outer layer of solid elements with cortical bone material properties. Another cross-section (with two elements across its thickness) was made up of a rib model with a calibrated effective bone model for the solid elements only.

Based on the response comparison, the modified cross-section was deemed appropriate to mimic similar response in place of the cross-section with the trabecular bone and cortical bone modeled separately. An elastic-plastic material model was utilized by Deng (1999); strain-rate dependency was applied to the ultimate strength and elastic modulus based on literature data (Mow & Hayer, 1991) as illustrated in Figure 3.7. At the beginning of this study, it was discovered that the material model only included the strain-rate dependency applied to the yield strength and the ultimate strength.

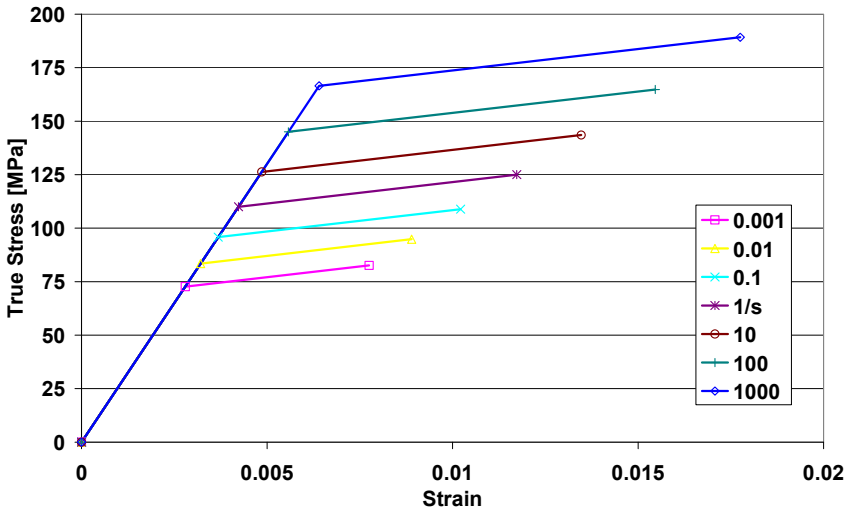

(Derived from Deng, 1999)

Figure 3.7: Original rib stress-strain relationship

The effective elastic and tangent modulus were higher than both cortical and trabecular bone to compensate for stiffness loss due to the single integration point elements. Single integration point scheme also imposed another limitation on the failure mechanisms. As the rib was loaded to its failure point, failed elements were eroded. However, a complete rib fracture could not be simulated through this modeling approach since an eroded cross-

section had only one solid element across its thickness. A single integration point element with one element across its thickness cannot provide bending stiffness, a complete through fracture due to bending would not be possible. Given these deficits, the human body model had a high compression response during lateral impact, but a low compression response during frontal impact given that both force response behaved within the response corridor in both scenarios (Forbes, 2005).

Recalibrated Rib Model

The original material model assumed strain rate dependency for the elastic modulus and ultimate stress based on the experimental data presented in Mow and Hayer (1991). However, there was no data on the yield stress and the tangent modulus scaling in terms of strain rate to create a complete strain rate dependent material model. Without these data, the current model scaled the yield stress with the same ratios applied to the ultimate stress. Similarly, the tangent modulus was scaled with the same ratios applied to the elastic modulus.

An elastic-plastic material model can be defined by using four out of six material parameters (elastic modulus, tangent modulus, yield strength, failure strength, yield strain, failure strain). Scaling factors were applied to the four material parameters to incorporate strain-rate effects and the material properties were referenced at the strain rate of 1/s.

A parametric approach was taken to recalibrate the effective material properties using the free-flight oblique pendulum 6.7m/s scenario (Viano, 1989). The new material model was evaluated against the frontal pendulum (Kroell et al, 1974), limited stroke lateral pendulum (Chung, 1999) and 4.3m/s free-flight oblique pendulum (Viano, 1989). The evaluation cases were not used as part of the recalibration process. The original material parameters developed by Deng (1999) were used as a starting point. The material model was calibrated with strain-rate effect implemented. Objective Rating Method was used to aid the peak and shape response of the compression evaluation in the parametric study. The force response was not used as part of the calibration but as a response verification.

The elastic modulus was adjusted such that the compression rate is as representative to the impact scenarios as possible in increments of 2GPa. Since tangent modulus was unknown, the original tangent modulus was kept as a starting point. A parametric study was conducted to determine an optimal set of yield strain and failure strain such that the compression fell within one standard deviation of the average response. Given the recalibration strategy, deficits inherent to the model were exposed. Rib fracture is critical in reaching an optimal peak compression, and the timing of the rib fracture is critical to reaching an ideal shape of the force and compression response. It was observed that the compression response was comparable to the experimental study but tended to lag in the loading region. This lag in response was inherent to the makeup of the ribcage model and not the material properties. Although the rib was modeled with an effective material model, the model still possessed adequate load carrying and chest deformation characteristics.

A parametric study of each material parameter was conducted to establish the trend in terms of how response shape peaks, loads and unloads. After the combination of elastic modulus and tangent modulus was established that best match the shape response, yield stress and failure stress were fine-tuned in increments of corresponding .001 strain to match peak compression.

Table 3.1 shows the material constants for the effective rib which represented the cortical bone and trabecular bones. It was calibrated specifically to the current rib geometry, therefore is not applicable to other ribcage models. The final pendulum simulation results are presented in Chapter 4.

Table 3.1: Effective material constants for rib bone at $\dot{\varepsilon}=1s^{-1}$

Elastic Modulus GPa	Yield Stress MPa	Tangent Modulus GPa	Ultimate Stress MPa
18	90	2.1	138.3

Future Development

The modeling approach should be revisited later as the development of a sophisticated rib material model was considered outside the scope of this project due to the lack of appropriate rib geometry data. The current rib geometry is one of the major deficits in the current model. Various rib sections were tested using a 3-point bending test similar to the study by Kemper (2007), the relative rib elastic stiffness between anterior and lateral sections, and between different rib levels were inconsistent with the trend shown in the experimental data (Kemper, 2007). For example, the anterior section of the 4th rib was considerably stiffer than the lateral section, where as opposite was true in experiments. The current rib geometry should be verified, and reconstruct the ribs such that the trabecular bone and the cortical bone can be modeled separately. The cortical bone should have a varying thickness along the rib with appropriate area of inertia. Considerable effort should be placed on separating the geometrical properties from the material properties such that the material model does not need to be calibrated to compensate for the geometrical deficits. The new ribcage model should demonstrate good biofidelity regardless of impact direction.

Strain Rate Dependency

It was apparent that the rib model should exhibit strain-rate dependency when the human body model simulated a cadaver oblique pendulum impact study at three different velocities (Viano, 1989). Without accounting for strain-rate dependency, any model that demonstrated good response in a particular pendulum case at a specific velocity would under predict compression at a lower impact velocity and over predict compression at higher impact velocity. This was evident during the development of the current rib model.

3.6 Costal Cartilage

The costal cartilage is the most compliant section of the ribcage structure. It was originally represented by a linear elastic isotropic material with an elastic modulus of 12GPa (Deng, 2000). The costal cartilage is a viscoelastic composite material that

contains a fluid phase and a solid phase. Its mechanical properties are highly non-uniform; the properties become more compliant with depth relative to the cartilage surface. The stress and strain response consists of a toe region, a linear region and a failure point. Despite its non-linearity, it is commonly assumed as a linear elastic material model (Mow, 1991).

Although it was recognized that the material properties varied across its cross-section, a sensitivity analysis by varying the elastic modulus by an order of magnitude affected no more than 10% of the overall torso force and deformation response in the frontal pendulum impact simulation with the current numerical model. Its influence on response was even lower when subjected to lateral impact. Viano (1986) reported an elastic modulus of 12 MPa for articular cartilage under compressive load. Mow (1991) presented a two-parameter exponential stress-strain relationship to model bovine articular cartilage tensile properties, and derived an effective elastic modulus for the elastic relationship that ranged from 42.2 MPa (at the surface) to 2.6 MPa (away from the surface) under tensile load. The two stress-strain relationships of the bovine articular cartilage based on the surface properties are illustrated in Figure 3.8.

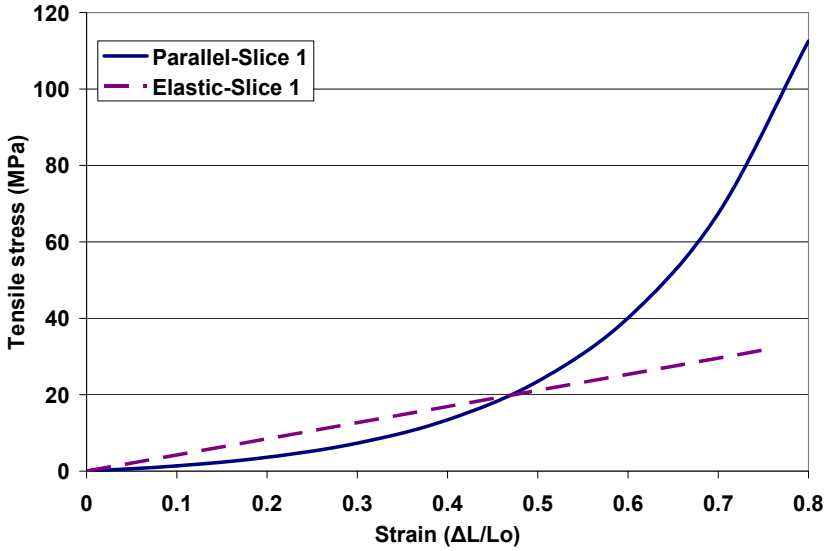

(Derived from Mow, 1991)

Figure 3.8: Stress-strain relationships of bovine articular cartilage

During the first two iterations of the model development, an elastic modulus of 12 GPa was used. The reasoning at the time was to account for the bone-cartilage-bone complex, where the material properties should possess a gradual transition as it was believed to be more representative in actual human (Deng, 2000). During the third iteration of the model development by Forbes (2005), an elastic modulus of 400 MPa was used, an approximately one order of magnitude larger than the experimental value. The reasoning for an elevated coastal cartilage was to minimize the high compression seen in side impact; however the elevated stiffness decreased compression in frontal impact. In the current development of the thoracic model, it became apparent that the elevated costal cartilage induced more rib fractures by stiffening costal cartilage to attain more appropriate chest compression response.

A viscoelastic model of the costal cartilage was presented by Ruan (2003). Subsequently, the material model was compared to the current elastic model by using a three-point costal cartilage bending simulation. The impactor was displaced to achieve similar strain and strain rate seen in the current human body model during the oblique pendulum impact simulations. The overall impactor force response was similar for both material models. The material model presented by Ruan (2003) was implemented to capture the viscoelastic effects of costal cartilage and is more suitable to predict high strain levels.

3.7 Heart and Aorta

Although the heart and aorta modeling were not the focus of the current research, their interaction with the lungs should be considered from an injury mechanism perspective. Much insight was gained on the heart and aorta modeling through the lung injury development, and several aspects should be considered for future model development.

The initial heart and aorta geometry was originally imported from Viewpoint Datalabs (Orem, Utah). The original model consisted of a heart model with four chambers. The aorta and the superior vena cava were modeled using shell elements with blood represented by an elastic fluid using solid elements. There should be three blood vessels

branching off the arch of the aorta. Only the brachiocephalic trunk, and the left subclavian artery were represented in the model, and the left common carotid artery was not modeled. The descending aorta was attached to the lower diaphragm, and largely unconstrained. The inferior surface of the heart was connected to the diaphragm.

Given the focus was on lung modeling, the heart and aorta model were modified to be more representative in terms of boundary condition. The heart was repositioned to be closer to the posterior face of the sternum. The heart model was remeshed to improve mesh quality. The new aorta geometry was implemented. The superior vena cava extended superiorly beyond the upper diaphragm to provide a full boundary along its length against the lungs. All three blood vessels that branched off the arch of the aorta were represented with beam elements. The descending aorta ran along the spine and was relatively constrained; the small arteries that branch from the aorta to the spine were represented by beam elements. Two layers of soft tissue connected the aorta to the spinal column and ran along the superior-inferior direction to create a more appropriate boundary condition against the lungs. The inferior face of the heart was connected to the diaphragm with six beam elements. The new heart and aorta models with improved boundary condition to the lungs are illustrated in Figure 3.9.

Geometry Considerations

The initial heart position may influence the likelihood of the aortic rupture (Hardy, 2008). It should be recognized that the heart position and orientation change when human body switches from an upright position to supine position. Care must be taken when deriving human body geometric data in the future, since most body scans are done at the supine position. The lower diaphragm of a cadaver tends to sag lower than living human, and thus also influence cadaver response and alter vital organs' positions.

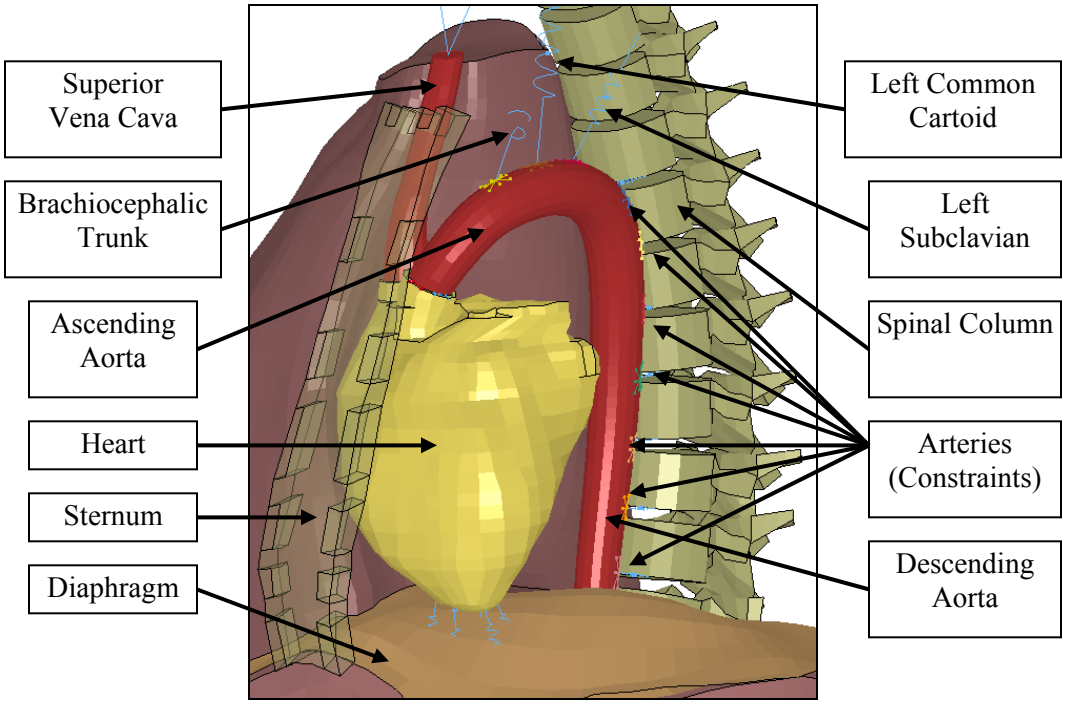

(Tissue layers that connect the descending aorta to the spinal column are not shown)

Figure 3.9: Cutout view of the new heart and aorta model configuration

3.8 Abdomen

An abdomen did not exist in the first two iterations of the model development. A lower diaphragm was modeled to form a lower boundary to the lungs and heart. Although the focus of the model development was on thoracic injuries, an abdomen was modeled as part of the full human body model. Since the abdomen is largely unprotected and consists of organs and soft tissues, it plays a critical role in the thoracic deformation as well as forming the lower boundary to the heart and lungs.

A simplified approach was taken by Forbes (2005) to model the abdomen as a soft tissue continuum. There are ten organs within the abdominal region. Each organ has its individual mechanical properties with some organ being hollow and some being solid. During the first two iterations of the model development, the abdomen was represented as point masses along the Lumbar Vertebrae (L1 to L4), with a total mass of 4.835 kg. This approach was found to be acceptable in simplified pendulum loading conditions by Deng et al (1999) and was validated by Chang (2001). A simplified abdomen model was

developed by Forbes (2005) that extended from as high as the 6th rib with the lower diaphragm being the upper boundary to the pelvis model as the lower boundary. The abdomen model was meshed in a layered fashion with the circumference of the lower abdominal section mated with the inner surface of the outer surface muscle model through coincident nodes. The edge of the inferior surface of the abdomen was tied to the pelvis through tied connections. The overall abdomen material model response was derived based on experimental testing on Rhesus monkey kidneys and livers through direct impacts. The material response was found to be similar to the bovine muscle tissue material model that was used for the outer surface muscle; thus, the same strain rate-dependent hyperelastic model was used. The density was calculated based on the abdominal mass as noted from the previous model developments (Deng, 1999; Chang, 2001).

Enhanced Abdomen Model

The original lower diaphragm model had a convex downward curvature with the inferior surface of the lungs mated to the superior surface of the diaphragm and the abdomen mated to the inferior surface as shown in Figure 3.10. This curvature was quite aggressive from modeling perspective. The lung model accommodated to the diaphragm curvature as much as the mesh quality of the lung model can tolerate (Jacobian > 0.7) to ensure model stability. The diaphragm curvature was modified to fit with the lungs model as closely as possible. The lower diaphragm was modeled with shell elements and maintained a 3mm thickness similar to the previous model.

The meshing strategy of the new abdomen model was similar to Forbes (2005). The superior surface of the abdomen was extended up to the diaphragm and eliminated any void between them. The abdomen was refitted within the ribcage to fill in any voids between them as well. The circumference of the lower half abdomen was mated to the inner surface of the outer surface muscle, but a tied surface contact was used in place of the coincident nodes. The inferior surface was projected to the spheriodal pelvis and a tied surface contact was used between them in place of nodal tied connections.

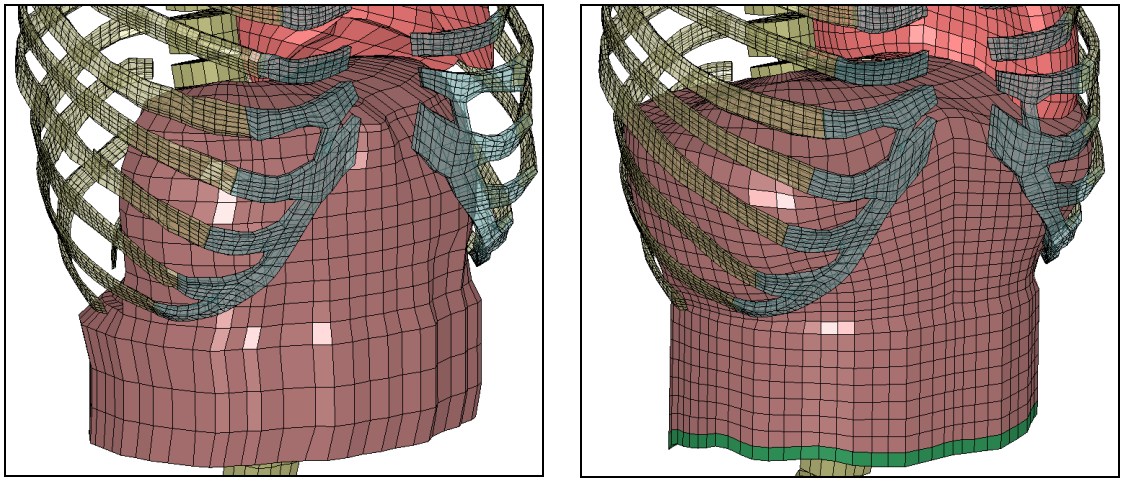

(original) (new)

Figure 3.10: Abdomen model comparison

3.9 Lungs

As part of the current model development, the major organ anatomical size and positions were evaluated. The Visible Human Project (VHP) was used as a geometrical reference. The model geometry was compared to the VHP at several cross-sections by calculating relative cross-section area of the heart and lungs to the thoracic cavity. There were a lot of voids within the thoracic cavity since only the major organs (the heart, the lungs, and the aorta) were modeled. The pulmonary artery, the esophagus and the bronchi were not modeled. The implementations of these components were considered outside the scope of the current development, such research effort should tie to aortic injury investigation to ensure accurate boundary conditions.

The original lung geometry was based on the 3d dataset from the Viewpoint Datalabs (Orem, Utah) as shown in Figure 3.11, and the lung model was implemented in the first iteration of the model development (Deng, 1999). The adopted lung material model was based on a strain energy function that takes elastic properties and surface tension into account as developed by Fung et al (1978) and Vawter (1980). A sub-project was initiated to identify elastic material properties of cadaveric lung tissues using biaxial tensile tests (Yen, 1999). However, the lung model development at the time was only preliminary.

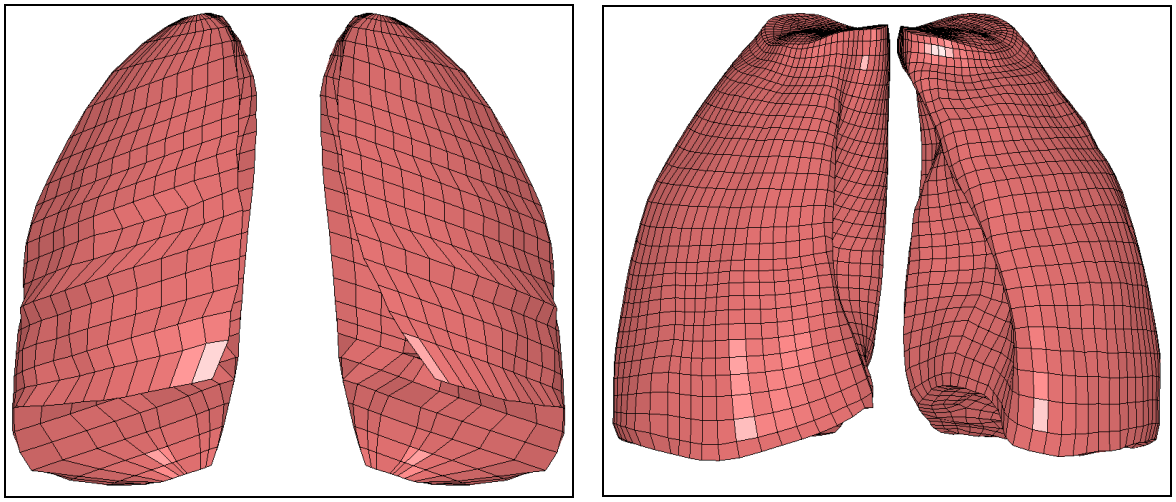

(original) (new)

Figure 3.11: Front view - lung model comparison

New Lung Geometry Model

The heart was repositioned, and the new aorta model was implemented based on the VHP (VHP, 2001) and Visible Body software (Argosy, 2009). The lung model geometry was redefined to fill the remaining voids. There were no reported cases where the interactions of the lungs with the esophagus, bronchi, and major blood vessels have any relevance to the lung injury (Miller, 2007). Therefore, it was deemed acceptable not to model them for the time being to minimize modeling complexity. The lung model was enlarged to fill the voids left by the esophagus, the bronchi, and pulmonary artery.

The original lung geometry was imported into Altair Hypermesh 8SR1 (Altair, 2009). A shell element mesh was created over the surface of the original lung geometry; the basal surface was modified to form a close-fit contact surface against the lower diaphragm. Altair Hypermorph (Troy, MI) was used to resize the lung to fit the thoracic cage as closely as possible. Penetration tool was used to check and remove any nodal penetration. The surface curvature had to be smooth such that the software can recognize the surface mesh as a primitive form of a cylinder.

Similar to a cylinder, the superior and inferior faces of the lung formed the end surfaces. Additionally, two surfaces were formed along the circumference of the cylinder. The

geometry was meshed in a layered fashion along the superior-inferior axis. A mesh convergence study was conducted to set a target mesh size which is discussed in a later section. The goal was to generate a mesh with an overall element size of 5mm with an upper limit no larger than 8 mm based on the mesh convergence study. The target aspect ratio was 2.5 and a jacobian rating no less than 0.70. Mesh quality is critical to the accuracy of the model as the mesh convergence study demonstrated sensitivity to various mathematical predictors of pulmonary contusion (Yuen et al, 2008). The current mesh was limited by the complicated curvatures which made it hard for the software to adapt to the surface boundary. The inferior surface of the lung was modified to have a more gradual curvature to maintain mesh quality.

A layer of subserous areolar tissue, also identified as the pulmonary fissure, which forms a physical boundary between lobes were modeled with a layer of shell elements surrounding the lung. The thickness of the pulmonary fissure is in the order of ~2 mm (Zhang et al, 2008). The model treated the lung as a single continuum and was not segmented into multiple lobes although it should be considered in the future. The technique for lobe segmentation is still under development (Zhang et al, 2008; Wei et al, 2008).

Contact & Hourglass Considerations

The mesh density should be compatible to its surrounding components. Since the lung has a low wave speed in the order of ~ 30 m/s while other solid soft tissues is in the range of ~ 1500 m/s, elements can be made smaller without limiting the minimum time step and inheriting computational penalty. The specific gravity of the lung tissue is typically small, in the order of .288 while most tissues are over 1. High density and stiffness mismatch between neighboring contact elements could lead to numerical instability. Fully integrated formulation is not recommended as it tends to be unstable and inaccurate at high strain.

The lung model used a viscous formulation to control hourglass, however high hourglass energy was observed with increasing hourglass control value up to the recommended limit of .15 (LS-Dyna, 2007). A high hourglass control value (~.15) artificially stiffened tissue response and increased hourglass energy. A low viscous control (~.0001) is ineffective where elements deform excessively, become highly distorted and form a negative volume. A stiffness formulation for hourglass control is not considered here since it would create undesirable oscillatory stiffening response to soft tissue materials.

A parametric study on hourglass control for every soft tissue material is recommended, where lung tissue should be the most sensitive case within the human body model. A parametric study of the hourglass control value from .0001 to .15 was conducted based on the oblique impact at 6.67m/s scenario. The optimal value was found to be in the order of .005 for the lung model. Hourglass control calibration should be the last resort to minimize hourglass energy; emphasis should be placed on selecting an appropriate material model, and developing high quality mesh and contact interface. The contact interface was the primary factor for triggering hourglass modes in the current model, especially when the interface contained sections with high stiffness mismatch such as the inner surface of the ribcage where the stiff surface (rib) is alternated with soft surface (intercostal muscle between ribs). Care must be taken to ensure smooth transition between contact surface interfaces such as the lower diaphragm to the ribcage, aorta to spine, etc.

Lung Material Model

The background on the material model development was discussed in Chapter 2. The lung as a material was by far the most unique and challenging to model due to its tissue-air interaction, multi-scale structure, natural damping behavior, low impedance, high compliance, and varying density. Figure 3.12 provides an overview of all the necessary parameters associated to the lung material model. There were four aspects of the model development pertained to the current material model. Firstly, a reference human lung density, lung air volume, total lung volume, and stress-free reference state relative to in-

situ condition were established. Secondly, an effective bulk modulus pertained to the stress wave propagation was determined. Thirdly, representative tissue properties for the lung elasticity and surface tension were determined. Fourth, the lung model was referenced with respect to the in-situ condition.

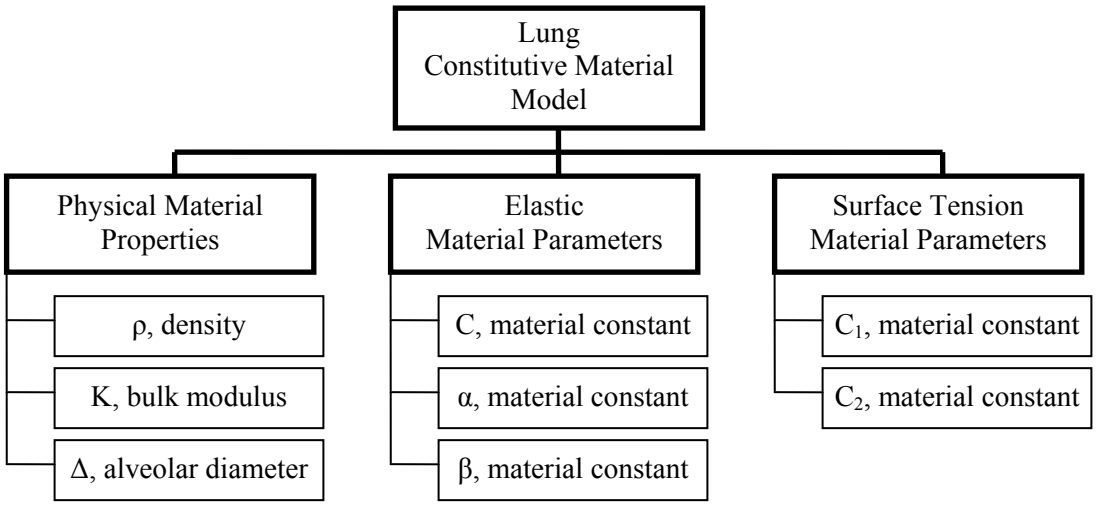

Figure 3.12: Lung constitutive model overview

Physical Material Properties of the Lungs

The lung volume changes significantly with breathing where the air volume capacity varies from 1.72 liters to 6.91 liters (Quanjer et al, 1995). The regional apparent density of the lung varies due to gravity effects. Despite these variations, a reference set of physical properties were established for a 50^{th} percentile male in the current study. The initial condition of the lungs should be established at the in-situ condition where the lung tissue is pre-stressed under tension by the transpulmonary pressure. The in-situ condition should be referenced relative to the stress-free state, since the tissue testing was typically conducted at a stress-free state and free from external loads. The material parameters were first determined at the stress-free state, and the material was subjected to volumetric strain to correct to the in-situ condition. A new set of material parameters were then refitted with respect to the in-situ condition based on a representative load case.

The following sections describe the approach to derive the lung density and volume across the physiological range, specifically at the stress free state, collapsed lung state, and in-situ condition (FRC). These properties are particularly important given they were never clearly established in past literature.

Lung Density at In-situ condition

A uniform density across the lung was assumed in the current model. Past lung research typically referenced an initial lung specific gravity in the order of 0.23, which was derived from dog lung experiments by Crossfill and Widdicombe (1961). Typical values for lung density range from 200 to 400 kg/m^3 (Crossfill and Widdicombe, 1961; Goss, 1978; Fung, 1985; Yen, 1986). The lung density depends on the applied transpulmonary pressure. In the current study, an average apparent lung density of 0.288 ± 0.064 at the Functional Residual Capacity (FRC) was established as the reference (Guenard et al, 1992). Apparent density is defined the mass per unit volume of a material including alveoli inherent in the material.

Lung Volume at In-situ condition

Since there was no anthropometric study that had measured the lung size, an analytical approach was taken to establish these properties. The apparent lung density is related to the air volume and the total lung volume based on the conservation of mass as shown in Equation 3.1. The conservation of mass of the lung is based on the mass contribution of air and tissue (including blood) to make up the lung mass with each mass being a product of the density and the volume. The lung volume is the sum of air and tissue volume. The lung tissue and blood was assumed to have an equivalent density of water. Since the mass of air relative to the mass of lung tissue and blood is smaller by 3 orders of magnitude, it was reasonable to assume that air mass had negligible effect. With the density of air set at zero, the formulation can be reduced to Equation 3.2.

By assuming a 30 year old, 50th percentile male with a height of 1.751m (UMTRI, 1983), the resultant FRC was calculated to be 3.31 liters (Quanjer et al, 1995). By assuming the

specific gravity of 0.288 (Guenard et al, 1992) at the FRC, a total lung volume (air + tissue + blood volume) was calculated to be 4.79 liters (4.79e-3 m^3) with a lung mass of 1.34 kg. A summary of the assumed properties of the lungs to derive the final lung mass and lung volume is shown in Table 3.2.

$$\rho_{tissue+blood} \cdot V_{tissue+blood} + \rho_{air} \cdot V_{air} = \rho_{lung} \cdot V_{lung}$$
$$where \rightarrow V_{lung} = \left(V_{tissue+blood} + V_{air}\right)$$
$$\rho_{air} \approx 0$$

Where	$\rho_{tissue+blood}$	tissue and blood density
	$V_{tissue+blood}$	Tissue and blood volume
	ρ_{air}	air density
	V_{air}	Air volume
	ρ_{lung}	Apparent lung density
	V_{lung}	Total lung volume

Equation 3.1: Conservation of mass equation for the lung

$$\frac{V_{air}}{V_{tissue+blood}} = \frac{\rho_{tissue+blood}}{\rho_{lung}} - 1$$

Equation 3.2: Conservation of mass equation with applied assumptions

Table 3.2: Summary of the lung theoretical properties at the FRC

Properties	Value	Reference
$\rho_{tissue+blood}$	1000 kg/m^3	Assumed as water
ρ_{air}	0	Assumed massless
V_{air}	3.31e-3 m^3	Quanjer et al, 1995
ρ_{lung}	288 kg/m^3	Guenard et al, 1992
$V_{tissue+blood}$	1.48e-3 m^3	Calculated
V_{lung}	4.79e-3 m^3	Calculated

Lung Density and Volume at RV, FRC, and TLC

Since the lung volume and mass vary depending on the transpulmonary pressure, a reference set of values was established across the physiological range. The lung density trend was established using data points at 10%, 50%, and 90% of the vital volume (Verschakelen et al, 1993). Since the vital volume varies with individuals, the lung density trend was shifted such that the density at the FRC coincided to 288 kg/m^3. Once the lung density was established with respect to the three breathing states (RV, FRC, TLC), other properties such as the gas/tissue volume ratio, lung air volume, total lung

volume (air + tissue + blood) and lung mass were derived. The properties at the RV, FRC, and TLC are summarized for a 50th percentile male in Table 3.3.

Table 3.3: Calculated lung properties at the RV, FRC, and TLC

	units	Residual Volume	Functional Residual Capacity	Total Lung Capacity
mean lung density	kg/m^3	344	288	183
gas/tissue volume ratio	unitless	1.91	2.47	4.46
lung air volume	liter	1.72	3.31	6.91
relative %TLC	%	25	48	100
total lung volume	liter	2.62	4.65	8.46
	m^3	2.62e-3	4.65e-3	8.46e-3
lung mass	kg	.900	1.34	1.55
transpulmonary pressure*	cmH_20	0	7.3	33.5
*derived from Powell (1979)				

Lung Density and Volume at Stress-Free State

The stress-free state was initially established by degassing the lungs and replacing air with a saline solution (Vawter, 1977). A saline solution was typically used to remove surface tension within the lungs such that the stress-strain response only pertained to the elasticity of the lung. The study found the saline to tissue volume ratio was 1.74 at the stress free state (Vawter, 1977). However this volume ratio is a relative quantity, it cannot determine the absolute size of the lung without one of the three corresponding properties, such as the density, tissue volume, or saline volume. A trend line was fitted to the air/tissue volume ratio with respect to the percentage of TLC based on the three states tabulated earlier in Table 3.3 and yielded the Equation 3.3.

$$\frac{V_{air}}{V_{tissue}} = 1.452 * \exp(1.118 \cdot TLC\%)$$

Equation 3.3: Air to tissue volume ratio based on the TLC percentage

The RV state is equivalent to a collapsed lung, and the air to tissue volume ratio was calculated to be 1.93 based on Equation 3.3. This equation correlated well with the study by Crossfill and Widdicombe (1961) on dog lungs where the air to tissue volume ratio at the collapsed lungs state was 1.91.

When the saline and tissue volume ratio of 1.74 from the study by Vawter (1977) was applied to the Equation 3.3, the stress-free state corresponded to 16.1% of the TLC (1.12 Liters). Based on this trendline correlation, the theoretical total lung volume for human at the stress-free state and at the in-situ condition (FRC) were 1.76e-3 mm^3 and 4.65e-3 mm^3, respectively. The ratio of the lung volume at the in-situ condition relative to the stress-free state is 2.64 times. The ratio of 2.64 is relatively close to the ratio of 2.74 reported from the experiments by Vawter (1976).

Reference Lung Density and Volume

In the current model, it was assumed that the lung expanded from stress-free state to in-situ condition hydrostatically where it uniformly expanded to 2.64 times of the stress-free volume; a stretch ratio of 1.38 is implied along each axis. Table 3.4 summarizes physical properties of the lung at the in-situ and stress free conditions. For the saline to tissue volume ratio of 1.74 (1.74 unit volume of saline for every 1 unit volume of tissue), the lung density was calculated to be 364 kg/m^3 at the stress free state using Equation 3.2.

Table 3.4: Lung physical properties at in-situ condition

Lung State	lung density (kg/m^3)	air volume (m^3)	total volume (m^3)	total mass (kg)	stretch ratio* (unitless)
In-Situ	288	3.31e-3	4.65e-3	1.34	1.38
Stress-free	364	1.12e-3	1.76e-3	.64	1
*relative to the stress-free state					

Lung Size Comparison

The current lung model (4.74e-3m^3) is oversized by 1.4% based on the calculated lung size (4.65e-3m^3). The volume difference was attributed by two factors: First, the lung filled the voids left by the components that were not represented such as the esophagus, pulmonary blood vessels, and bronchi, etc. Second, the inferior section of the lung geometry was cropped to maintain mesh quality. The two factors offset one another, leading to a small difference between the current volume and the calculated volume.

Dynamic Properties of the lungs

Lung wave speed, bulk modulus and density were discussed in great length in Chapter 2. It should be emphasized that the density and bulk modulus change non-linearly throughout the range of deformation, therefore both variables must be considered in predicting the wave speed. Given the non-linear relationship of the wave speed with respect to the lung properties, bulk properties at different reference points (with respect to the breathing state) need to be established.

Bulk Properties at In-Situ

The initial transpulmonary pressure at the FRC state was estimated to be nominally at 7.3 cm H_20 for the current study based on the P-V curve of the human lungs (Powell, 1979). The baseline bulk modulus was interpolated to be at 2713 cmH_20 (266.0 kPa) at the corresponding transpulmonary pressure of 7.3 cmH_20 from the study by Rice (1983). The human lung density at the FRC state was 0.288 kg/m^3 as defined previously. The bulk modulus was assumed to be significantly higher than the shear modulus; the shear modulus can be neglected when calculating the wave speed using Equation 2.1 (Yen, 1986). The calculated theoretical human lung wave speed based on the assumed bulk modulus and lung density was 30.4 m/s at the FRC state. Table 3.5 summarizes the baseline dynamic properties at the FRC state, which was established as the initial condition of the current model.

Table 3.5: Dynamic properties of the lung at the FRC

Density (kg/m^3)	Bulk Modulus (kPa)	Transpulmonary Pressure		Theoretical Wave Speed (m/sec)
		(cmH_20)	(Pa)	
288	266	7.3	720	30.4

Bulk Properties at zero transpulmonary pressure

The lungs would collapse and trap air in the alveoli when the transpulmonary pressure is at zero (Vawter, 1978; Yen, 1986; Fung, 1988). The transpulmonary pressure at zero should represent the lower limit of the wave speed given the bulk modulus was nearly unchanged across the physiological range as indicated in experiments (Yen et al, 1986). The density of a collapsed human lung (at the RV) was previously calculated to be 344

kg/m^3. The decrease of wave speed relative to the FRC was predominantly caused by the increase of the lung density. The Table 3.6 summarizes the lower limit of wave speed at the collapsed lung condition.

Table 3.6: Dynamic properties of the lung at zero transpulmonary pressure

Density (kg/m^3)	Bulk Modulus (kPa)	Transpulmonary Pressure		Theoretical Wave Speed (m/sec)
		(cmH_20)	(Pa)	
344	265	0	0	27.8

Bulk Properties beyond collapsed lung

Ward (2005) conducted experiments on excised human lung tissue using a modified Kolsky bar and fired from 1 to 50m/s. The experiments measured an average bulk modulus of 130 MPa with the initial lung density at 0.6 kg/m^3. Saraf (2006) conducted similar testing using a Kolsky bar setup and had found a bulk modulus of 150 MPa. Both tests had measured the shear modulus in the order of 10kPa, five orders of magnitude lower than the bulk modulus. Based on Ward's (2005) experimental data, the resultant wave speed was 465.5 m/sec using Equation 2.1. The properties at the collapsed state during dynamic compression are summarized in Table 3.7.

Table 3.7: Dynamic properties of the excised lung tissue

Density (kg/m^3)	Bulk Modulus (kPa)	Strain Rate (1/s)		Theoretical Wave Speed (m/sec)
		Lower	Upper	
600	130000	500	2100	465.5*
*Calculated Theoretical Wave Speed				

(Derived from Ward, 2005)

Effective Bulk Properties

The wave speed of the lung should be a non-linear relationship with respect to the lung deformation due to the varying density and bulk modulus at different deformation and deformation rate. In theory, the wave speed should decrease as deformation occurs due to an increase in density while the bulk modulus remains nearly unchanged. The wave speed should reach its lowest when the lung is near a collapsed state, where the bulk modulus is low and the density is high as demonstrated in the studies by Rice (1983) and Yen (1986). The role of gas stiffness becomes dominant once air trapping occurs, further compression should result in increase in bulk modulus and density leading to a high wave

speed as observed in the experiments by Ward (2005) and Saraf (2006). A summary of bulk moduli and corresponding densities from various experiments is shown in Figure 3.13.

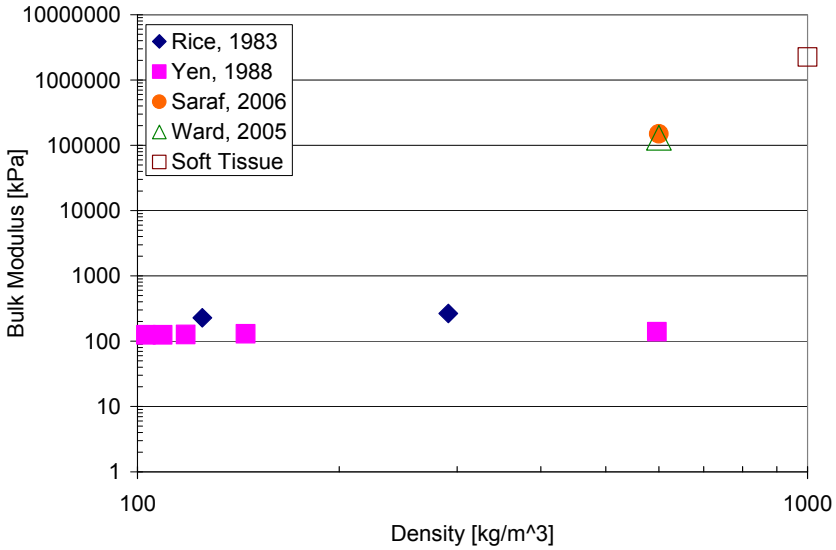

Figure 3.13 - A summary of bulk moduli versus lung densities

The bulk modulus was limited as constant input in the current constitutive material model, therefore when compression increases, the wave speed decreases in the numerical model where the experiments demonstrated the opposite. During compressive loading of the lung, the pressure response relative to the volume should follow the non-linear trend as shown in Figure 3.14. If the bulk modulus is assumed too low, then the lung would be too compliant leading to excessive deformation in addition to a low wave speed. If the bulk modulus is assumed too high, then the lung would be too stiff leading to high stress response but lower strain response in addition to a high wave speed.

To address this limitation, an effective bulk modulus was assumed to be in between the lower and upper limit of the bulk moduli. The bulk modulus derived from the study by Rice (1983) as shown in Table 3.6 was set as the lower limit. The bulk modulus derived from the study by Ward (2005) as shown in Table 3.7 was set as the upper limit. It was assumed that the model would see deformation between these limits. The bulk modulus was derived based on an approximate linear trend formed by the two reference points

(Rice, 1983; Ward, 2005) and the bulk modulus of soft tissue in the log scale. The resultant bulk modulus was found to be 5870 kPa. The effective wave speed would range from 217 m/s to 99 m/s corresponded with a lung density of 288 kg/m^3 and 600 kg/m^3, respectively.

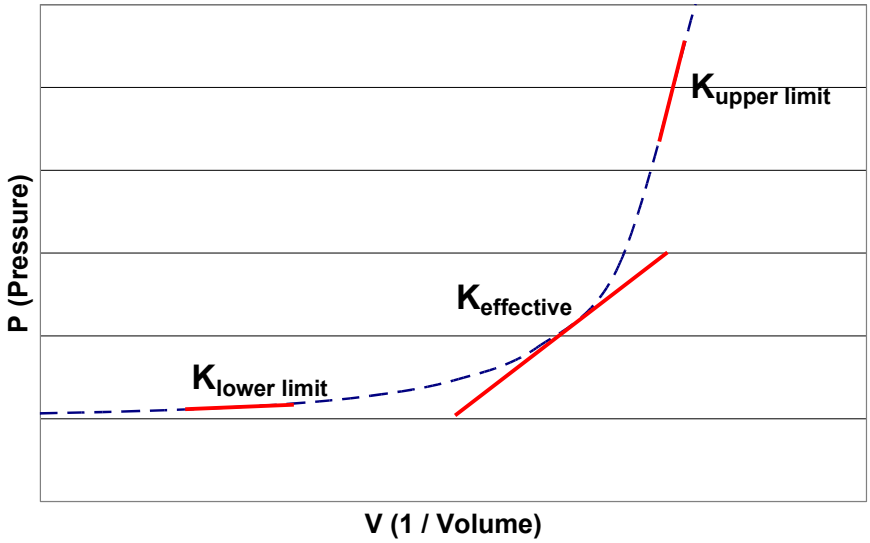

Figure 3.14: Schematic of a pressure vs volume curve

The effective bulk modulus can be readjusted in the future based on the lung response from various simulations. However, development effort should be focused on improving the constitutive model to better model the wave propagation as it would provide greater insight into the stress wave characteristics and the influence on the injury mechanism.

Material Properties of the Lungs

The current lung model adopted the approaches developed by Fung et al (1978) and Vawter (1980) in which the elastic and surface tension properties of the lung tissue were modeled by a macroscopic strain energy function as shown in Equation 3.4 and Equation 3.5. The C, C_1, C_2 α, β are material constants, Δ is the average alveolar diameter when unstressed, and I_1 and I_2 are the strain invariants. The hydrostatic work was incorporated in terms of the bulk modulus and the third strain invariant, J.

$$W = \frac{C}{2\Delta}\exp(\alpha I_1^2 + \beta I_2) + \frac{12C_1}{\Delta(1+C_2)}[A^{(1+C_2)} - 1]$$

$$A^2 = \frac{4}{3}(I_1 + I_2) + 1$$

(Reproduced from Vawter, 1980)

Equation 3.4: Macroscopic strain energy function of the lungs

$$W_H = \frac{K}{2} \cdot (J-1)^2$$

(Reproduced from Dyna, 2006)

Equation 3.5: Hydrostatic work function of the lungs

The first set of the biaxial human lung tissue tensile tests was published by Zeng et al (1987). Subsequently, the second set of biaxial tests was conducted by Yen et al (1999) as part of the thoracic model development by Deng (1999). The data by Yen (1999) was reanalyzed to establish an optimized set of material constants (Gao et al, 2006). The following sections describe the available lung material data and the approach used to derive the material constants.

Elastic Material Properties

A biaxial test setup was strictly focused on obtaining elastic properties of lung tissue. The specimen had to be submerged in a saline solution to eliminate surface tension effects. The third axis was stress free to minimize hydrostatic effects. The biaxial experiments by Zeng et al (1987) consisted of four increments of constant tensile loads from 5 to 30 g/cm^2 (490 Pa to 2942 Pa) applied to one axis while the stretch ratio varied from 0.6 to 1.8 in the perpendicular axis at each increment. The results were fitted to the constitutive model developed by Fung et al (1978). Figure 3.15 shows the stress-strain relationship of loading response with the isotropy assumption.

Yen et al (1999) conducted a similar study as Zeng et al (1987), except the biaxial experiments were strain-controlled instead of stress-controlled. The first test protocol subjected the excised lung tissue with a constant stretch ratio along the x-axis at different increments ranged from 1.000 to 1.274. At each x-axis stretch ratio increment, the stretch ratio was varied along the y-axis. The second test protocol was simultaneously cycled

through the minimum to maximum load at both axes, the applied stretch ratio on both axes were synchronized. However, the applied strain limits were not explicitly stated. Two samples were subjected to the first test protocol and nine samples were subjected to the second test protocol.

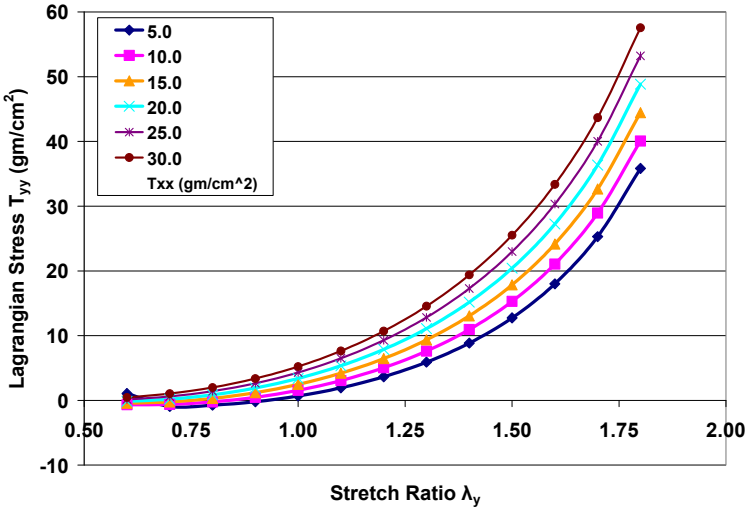

(Derived from Zeng et al, 1987)

Figure 3.15: Loading stress-strain relationship by global approach, Isotropy assumed

Upon examining the experimental data from the second test protocol (Yen, 1999), there was a discrepancy in the boundary conditions. From the stress-strain plots of 1181, both axes showed the peak Kirchhoff stress were 50 gm/cm^2. The corresponding strains should be near each other, however the strain measured along the x-axis was 0.25 and y-axis was near 0.40. For a specimen that was simultaneously loaded in both axes, it was unclear why the measured strain levels were so different. Since the experimental data were plotted each axis response independently, it was not possible to crosscheck if the boundary conditions were properly imposed. Therefore, this set of material data was discarded from the current material curve fit.

Upon reviewing the data, it should be more accurate to impose a constant load condition rather than a constant strain condition. This has to do with the difficulty with determining the zero strain state. A strain-free state is difficult to attain and to measure

given the lung is quite deformable at low stress level. This might explain the high variability in the Gao et al (2006) data.

Biaxial Data Comparison

Table 3.8: Test protocols for experimental data comparison

Test Protocol	Description	Test range	Reference
1	x-axis Lagrangian stress–constant	0, 5, 10, 15, 20 g/cm^2	Zeng et al, 1987
	y-axis stretch ratio – varied	~0.8 to ~1.8	
2	x-axis stretch ratio –constant	1, 1.068, 1.134, 1.208, 1.274	Gao et al, 2006
	y-axis stretch ratio – varied	~0.9 to ~1.2	

Table 3.8 shows the boundary conditions correspond to each biaxial test protocol as described in the studies by Zeng (1987) and Gao (2006). The material model and the optimized material parameters as recommended by each study were subjected to both biaxial tests analytically. Figure 3.16 shows a sample of Gao's (2006) material model response with Zeng's (1987) loading conditions. Figure 3.17 shows a sample of Zeng's (1987) material model response with Gao's (2006) loading conditions. Figure 3.16 and Figure 3.17 were plotted up to the upper limit of the corresponding loading conditions.

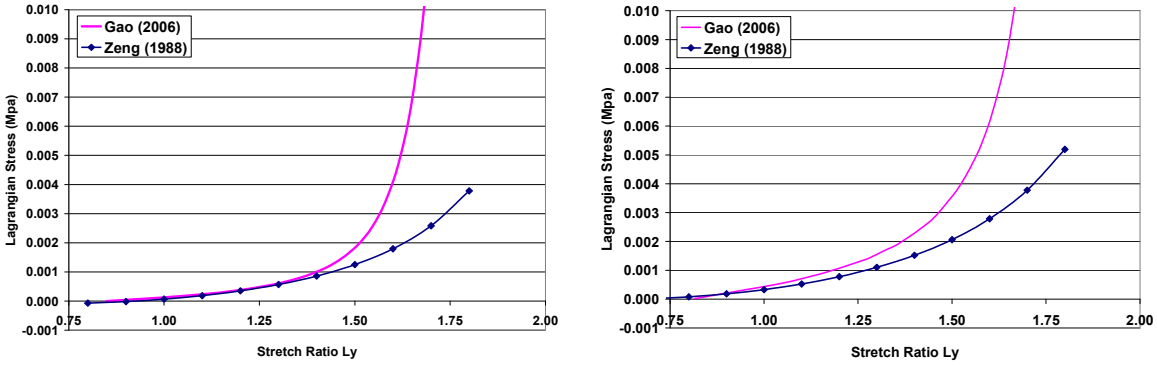

x-force = 5g/cm^3 x-force =20 g/cm^3

Figure 3.16: Stress-strain curves comparison based on Zeng (1987) biaxial test

The comparison showed that the two material models were in good agreement at low stretch ratio. The differences became more profound as the x-axis was imposed with a higher stress or stretch ratio. Overall, Gao's (2006) material model was generally stiffer, but was validated with a very limited stretch ratio range. The material response from Zeng's (1987) study should be more representative of the human lung tissue response,

given Zeng's (1987) material response was in good agreement with Gao's material model in low strain and was tested with a wider range of stretch ratio.

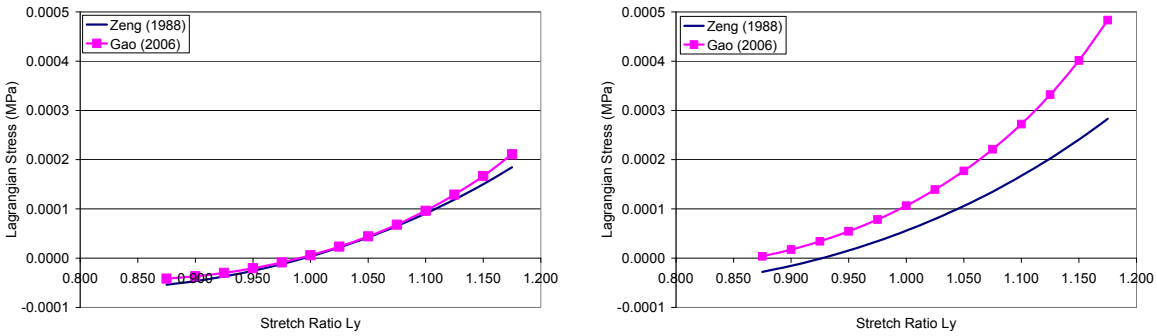

x-stretch ratio =1.068 x-stretch ratio =1.274

Figure 3.17: Stress-strain curves comparison based on Gao (2006) biaxial test

Lung Elastic Properties Curve-fit

Only Zeng's (1987) experimental data was utilized to derive the elastic properties of the human lung given the material parameters were validated against a wide range of strain. The following describes the approach to determine the appropriate material constants that fitted the Zeng's (1987) experimental data based on the constitutive material model by Vawter (1980). The curve-fitting approach was similar to the one used in the studies by Zeng (1987) and Gao (2006). The derivative of the strain energy function (Vawter, 1980) with respect to the strain component yielded the Kirchhoff stress components. The Kirchhoff stress related to the Lagrangian stress when multiplied by the corresponding stretch ratio. A macro was written to identify material constants by minimizing the sum of the errors squared. The original experimental data was not available, therefore the optimized material parameters from the study by Zeng (1987) as shown in Table 3.9 were plotted to derive a set of data points. The material model from Zeng et al (1987) was used to generate twelve data points along the y-axis at six constant Lagrangian stress levels applied to the x-axis (5,10,15,20,25,30 g/cm^2). This established the baseline experimental data for material curve fit. The sensitivity and variation of the lung tissue properties across the human population was not considered in the current study and should be investigated in the subsequent development iteration.

The curve-fitted material parameters based on Vawter's constitutive material model (1980) are tabulated in Table 3.10 and refers as the 'stress-free material model' in the current context. The derived material parameters for the Vawter's (1980) constitutive material model produced an excellent fit against Zeng's (1987) experimental data as shown in Figure 3.18. Only the two load limit out of the six loading cases (5 and 30 g/cm^2) were shown.

Table 3.9: Material parameters determined by the global approach

C* (kPa)	a1, a2	a4
.862	.63	.39

(Derived from Zeng, 1987)

Table 3.10: Stress free material model, optimized for Vawter's (1980) material model

C/Δ (kPa)	α	β
1.38	.764	-.894

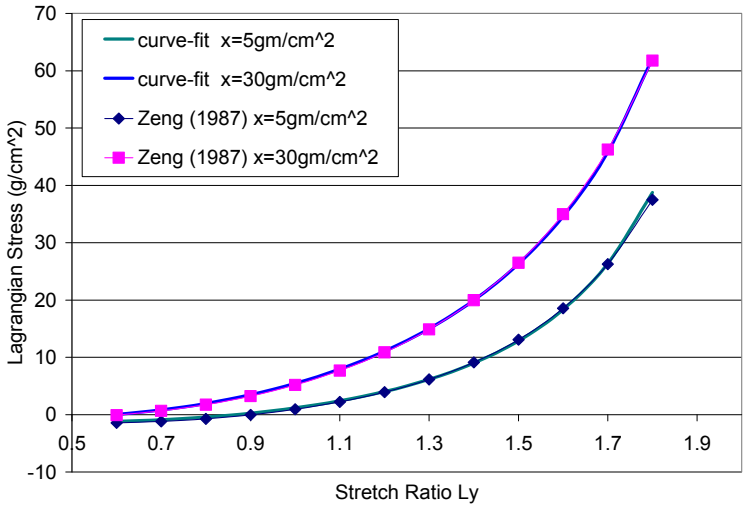

Figure 3.18: Lung elastic properties curve-fit comparison

Stress-free state to In-situ condition

The derived material parameters from the previous section were defined with respect to the stress free state of the human lung tissue. The lung model should be defined with respect to the in-situ condition in the current human body model. The stress-strain curve should be shifted with respect to in-situ condition such that any change to the strain

energy relative to the initial condition is realistic. The following section details the approach in determining the stress-strain curve with respect to the in-situ condition.

To maintain constancy of the volume as an initial condition, the multiplication of the stretch ratio with respect to x, y, and z was set to 1 as shown in Equation 3.6. This was a simplification as an initial condition for the current model; similar approach was used in a study by Vawter (1976) to investigate surface tension relative to the stress-free state.

$$\lambda_x \lambda_y \lambda_z = 1$$

Equation 3.6: Constancy of a macroscopic lung tissue at stress free state

Previous section detailed the approach that determined the lung volume at the stress-free state and the in-situ condition as summarized in Table 3.4. From the analytical calculations, the lung volume at in-situ condition was found to be 2.64 times larger than the lung volume at the stress-free state. It was assumed in the current study that the lung would hydrostatically expand to the in-situ condition governed by Equation 3.7 and yielded a stretch ratio of 1.38 to each axis. The original stress-strain curve was shifted such that the new material parameters were defined with respect to the stress-strain point at the in-situ condition.

$$\lambda_x \lambda_y \lambda_z = 2.64$$

Equation 3.7: Constancy of a macroscopic lung tissue at in-situ condition

At the in-situ condition, it was assumed that the transpulmonary pressure applied to the lung throughout the impact, thus a constant pressure was applied in the stress-free model throughout the load case. In the in-situ material model, this pressure was considered inherent in the material model and be established as the reference point at zero pressure. Figure 3.19 provided an example comparison between the stress-free model and the in-situ model in terms of pressure and volume. The pressure and volume are analogous to the stress and strain, respectively.

To transform the stress-free model into the in-situ material model, a single element was subjected a uniaxial load after the stress-free model was subjected to a hydrostatic

expansion to achieve the in-situ at a volume of 2.64 times. A constant pressure was applied to the two axes of the stress-free material model and the third axis was subjected to uniaxial stretch from 1 to 1.8. The data points created from the stress-free model needed to be adjusted such that the stress and strain were defined with respect to the in-situ condition. To normalize the stress and strain with respect to the in-situ condition, each data point was subtracted by the true stress corresponded to the applied constant pressure and the stretch ratio was divided by 1.38. This dataset which was shifted with respect to the in-situ condition refers as '*the simulated in-situ uniaxial data*' in this context.

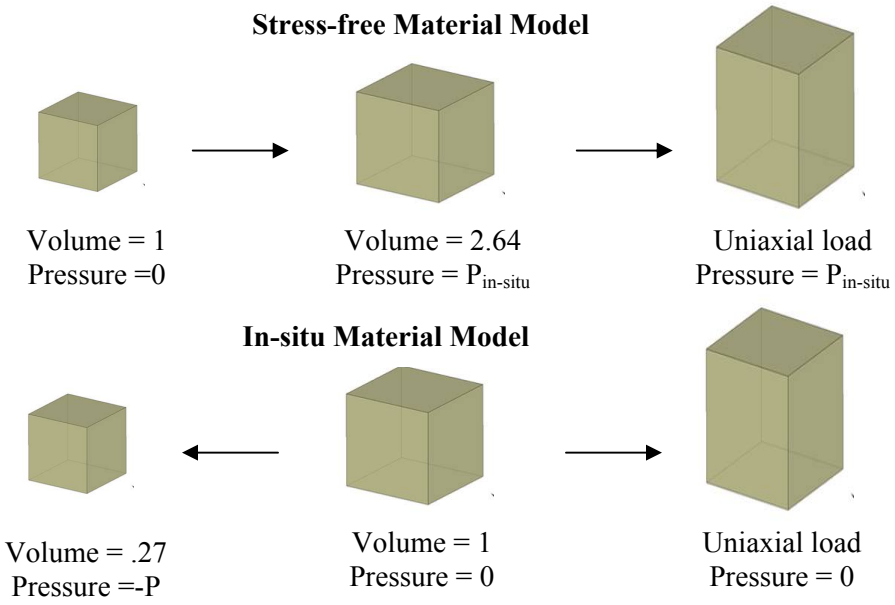

Figure 3.19: Material models reference comparison

Material Parameters Comparison

A study by Gayzik et al (2008) approached the material parameter determination through a finite element optimization to correlate the lung response to the measured impact load in the experiments. The experiments were conducted on live rats under an in-vivo condition (Gayzik, 2008), which also implied that the material parameters were determined with respect to the in-situ condition.

The current stress free material model was derived based on biaxial tensile load cases, while Gayzik's (2008) material model was derived primarily based on compressive loads. The simulated in-situ uniaxial data and Gayzik's simulated uniaxial data were compared and showed that the tensile response were similar, where as the compressive response were divergent as shown in Figure 3.20. The corresponding strain in the transverse direction, while remain stress-free, were different between the two curves.

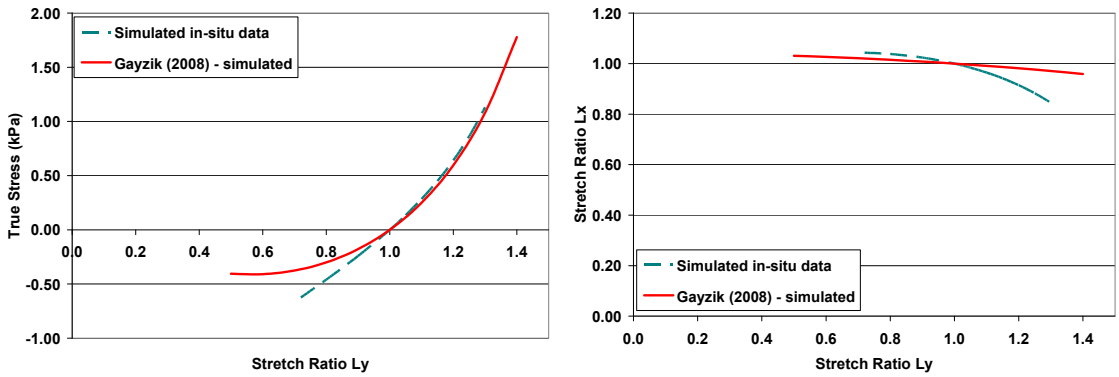

Figure 3.20: Simulated in-situ uniaxial test

Loading Consideration

The lungs are always subjected to compressive loading during impact; however the material response of the lungs under compression is relatively unknown. Fung (1978) and Vawter (1979) suggested that the alveoli could provide some buckling resistance, but exactly how the lung behaves under compressive load is still unclear. From the observation of the uniaxial simulation, it was apparent that the compression response of Gayzik's model was unconventional as shown in Figure 3.20. However, this is the only indirect observation available on the lung response during compressive loading. Experiments are needed to better understand the compressive response of the lung. In order to determine the in-situ material parameters that cover full range of loading, it was assumed that the lung response should behave similar to *the simulated in-situ uniaxial data* during tension and similar to Gayzik's simulated uniaxial data during compression. Although a uniaxial loading case was used for comparison, the loading case was triaxial in nature due to the transpulmonary pressure which already incorporated in the development of the material parameters.

Final In-situ Material Parameters

The current approach should represent the major features in the lung response, although it was recognized that it cannot account for the complex and non-linear behavior of the human lung in every detail. This approach came with the same limitations in the development of the constitutive model as discussed in the studies by Fung (1978), and Vawter (1976, 1979, 1980). Figure 3.21 shows the uniaxial true stress-stretch ratio curve of the in-situ material model after incorporating the simulated in-situ data under tension and the simulated Gayzik's data under compression. The stress response was in good agreement with both datasets, while the transverse strain response was compromised. Table 3.11 shows the final material parameters for the elasticity aspect of the constitutive model.

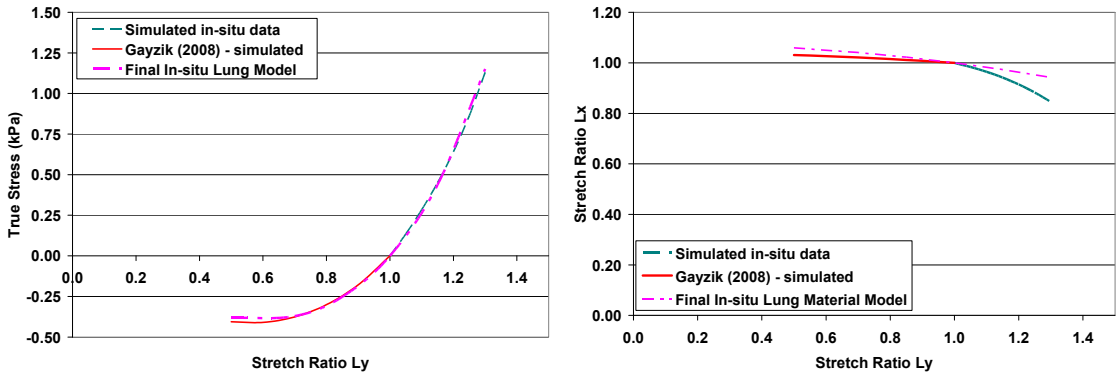

Figure 3.21: Stress-strain curve, in-situ condition, before and after correction

Table 3.11: Elastic properties of the lung, adjusted in-situ condition

Model Type	C (kPa)	α (unitless)	β (unitless)
Adjusted In-Situ	1.115	.213	-.343

Surface Tension

Surface tension plays a critical role in terms of determining the stress and strain the lung tissue. Surface tension exists regardless of the deformation as long as the air-tissue interface exists. The surface tension contribution to the stress of the tissue diminishes during compression but increases during rebound. The constitutive model developed by Vawter (1980) approximated a power function to account for the surface tension as shown in Equation 3.8.

$$\gamma = C_1 A^{C_2}$$

	Γ	Surface tension
Where	A	Surface area
	C_1, C_2	Surface tension constants

(Reproduced from Vawter, 1976; 1980)

Equation 3.8: Surface tension formulation

Although the function to approximate surface tension used in the study by Vawter (1976) was the same function implemented in the Vawter's (1980) constitutive model, the formulation that determine the normalized surface area was not the same. Vawter (1976) initially investigated the surface tension effect by validating the response to the in-situ pressure-volume measurements of the lung (Flicker and Lee, 1974). Equation 3.9 shows the normalized surface area calculation in the study by Vawter (1976). Equation 3.10 shows the surface area calculation as implemented in the Vawter's (1980) constitutive model which was initially developed by Fung (1978). Vawter et al (1976) modeled the loading and unloading response with separate formulation. Vawter's (1980) constitutive model implemented the formulation that modeled the loading characteristics (inflation). Considering the sequence of event during an impact, the surface tension effect is much higher in loading (inflation) than unloading (deflation). It should be clear that loading in this context refers to deformation towards tension, while unloading refers to deformation towards compression. As such, the current model was curve-fitted after the loading data (inflation of the lung) to mimic the surface tension effect as presented in Vawter (1976).

$$A = \frac{\left(\lambda^3 - \frac{1}{k'}\right)^{\frac{2}{3}}}{\left(1 - \frac{1}{k'}\right)^{\frac{2}{3}}}$$

	λ	Stretch ratio
Where	k'	Ratio of stress free lung volume to tissue volume
	A	Normalized surface area

(Reproduced from Vawter, 1976)

Equation 3.9: Normalized surface area

$$A^2 = \frac{4}{3}(I_1 + I_2) - 1$$

Where		
	A	Surface area
	I1, I2	Strain invariants

(Reproduced from Vawter, 1980)

Equation 3.10: Surface area calculation for the constitutive model

As part of the current study, parameter identification was carried out in a similar manner as the study by Vawter (1976). A set of surface tension parameters for the stress free condition was identified based on the measurement data (Vawter, 1976) and the normalized area formulation from Vawter (1980). Another set of parameters were then fitted to the stress-free surface tension data that were adjusted to the in-situ condition. The in-situ condition adjustment was similar to the approach that determined in-situ material parameters for the elasticity of the lung in the previous section.

Figure 3.22 shows the surface tension versus surface area curves for four sets of surface tension parameters. First, Vawter (1976) curve was originally fitted to the in-situ measurements by Flicker and Lee (1974) with respect to the stress-free state. Second, Vawter (1980) curve was based on a new set of parameters that was fitted to the Vawter (1976) data using the surface area formulation developed by Vawter (1980) as shown in Equation 3.10. Third, the *final in-situ surface tension model* used the Vawter (1980) data points and renormalized the surface area with respect to the in-situ reference stretch ratio of 1.38. The surface tension had to be more sensitive to compensate for the same change of length after the data was re-normalized to a larger reference length. Fourth, Gayzik (2007) obtained surface tension parameters through optimization and was plotted for reference. Gayzik's (2007) elevated surface tension response may be attributed to the dynamic loading effects of the surface tension. Until more research is conducted on the surface tension effect relative to dynamic loads, it was outside of the scope of this project to investigate it extensively. This believed to be as rigorous approach as it could be given the limitations imposed by the constitutive model and the limited understanding of the complex behavior of surface tension. Table 3.12 summarizes the surface tension properties for the current lung model under the stress-free and in-situ conditions.

Table 3.12: Surface tension properties of the lungs, stress-free & in-situ condition

Model Type	C_1 (N/mm)	C_2(unitless)
Stress Free	2.913e-4	3.934
In-Situ	1.002e-3	2.040

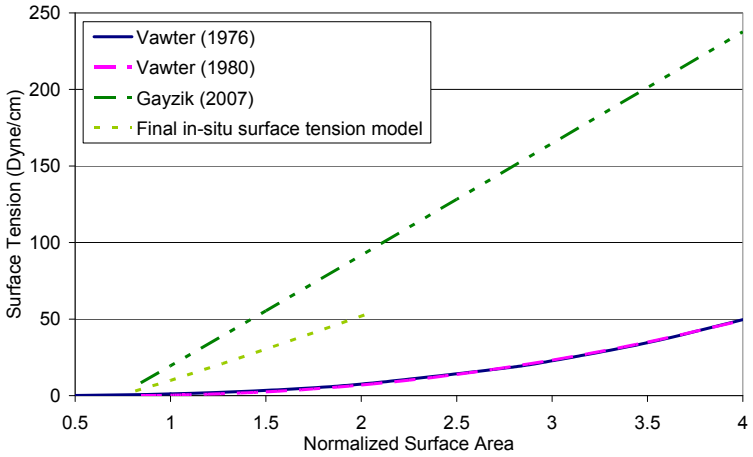

Figure 3.22: Surface tension - surface area curves

The Lung volume to tissue volume ratio

Vawter (1976) determined the k' value, defined as the ratio of the lung volume relative to the tissue volume at the stress-free state, to be 2.74 from an unpublished observation in his experiments. From the earlier analysis that established the stress-free state as summarized in Table 3.4, the derived k' value was found to be 2.75. This demonstrated that the dog lung and human lung have similar ratio of the lung volume to the tissue volume at the stress-free state.

Material Model Summary

Table 3.13 summarizes the complete material model for the current lung model with parameters adjusted for the in-situ condition.

Table 3.13: Current lung material model, in-situ condition

Model Type	ρ (kg/mm^3)	K (MPa)	Δ (mm)	C (MPa)
Adjusted In-Situ	.288	2.66	1.00e-1	1.115e-3
	α (unitless)	β (unitless)	C_1 (MPa)	C_2(unitless)
	.213	-.343	1.002e-3	2.040

Chapter 4
Lateral Impact Response

4.1 Introduction

Numerical models, like Anthropomorphic Test Devices (ATD), need to possess a high degree of biofidelity. A numerical model should provide human-like response and predict human injury consequences to be considered biofidelic. The International Organization for Standardization (ISO) had developed a set of test procedures and impact response requirements for assessing the biofidelity of anthropomorphic side impact dummies that is specific to each body region. The assessment established the 50^{th} percentile adult male as the reference. The basis of the current study works within the guidelines and procedures as outlined in the latest revision, ISO-TR9790 (1999).

This chapter is focused on evaluating the numerical human body model against post-mortem human subjects (PMHS) in various impact conditions with emphasis placed on the thorax region. The current study focused on rigid impact tests as the loading condition of the padded tests is difficult to mimic in a numerical environment without the material data of the pad. The simulated results from various pendulum and sled impacts were compared to the response corridors provided by the corresponding experiments.

The following sections provide descriptions of each PMHS experiment and the equivalent representations of the experiment within the numerical environment. Three pendulum thoracic impact tests were chosen to assess regional response and two sled tests were selected to assess various body regions simultaneously. Studies pertained to regions other than the thorax were not presented here in detail; however their results are organized in Appendix A. The assessment of the numerical results provided insight into the assumptions that were made throughout the development of the detailed thoracic

model. The discrepancies between the model and the experimental results were discussed, and the recommendations to address these discrepancies were explained.

4.2 Pendulum Impact Descriptions

Four pendulum tests with three different setups were chosen to validate regional thoracic response of the human body model. Thorax tests 1 and 2 from the ISO standard (1999), known as the oblique pendulum thoracic impacts, were chosen. The setup conditions for the thorax test 1 and 2 were the same except the pendulum was subjected to different impact velocities. A frontal pendulum thoracic impact and a lateral limited-stroke pendulum thoracic impact test were included.

Pendulum Impact Selection Justification

This set of impact tests applied to the thorax were intended to provide greater insight and better expose deficits on any specific component. These impacts were chosen because they are representative of the dynamic conditions of those in automotive crash and demonstrate the applicability of the human body model with respect to various impact directions.

The current model development emphasized lateral impact situations; however, including the frontal pendulum impact has its merit. The frontal impact was included as it directly loads the sternum which is dependent on the properties of the ribs and the costal cartilage. The sternum and its joints to the ribcage also play a crucial role in the response.

The experimental setup of the oblique pendulum impact was initially developed to minimize body rotation during impact (Viano, 1989); it was directed at the center of gravity of the body. Due to its oblique angle, its thoracic response was considerably influenced by bending of the costal cartilage as it is more compliant than the ribs.

The lateral limited-stroke pendulum impact specifically placed emphasis on the rib deformation. Since it was a direct impact in the lateral axis, the costal cartilage and the sternum material properties have minimal response contribution relative to the ribs.

Experimental Data Normalization Method

The experimental data is typically normalized with respect to the 50th percentile male since the cadavers from each study have different body mass and stature. The ISO standard (1999) utilized the normalization method as described by Mertz (1984) for each response study; the force, displacement, and time were normalized based on body mass and effective stiffness of the impacted area. Other studies that were not presented in the ISO standard were normalized as described by Eppinger et al (1984) to represent the 50th percentile male as shown in Equation 4.1 and Equation 4.2. F and D are referred to the measured force and deflection, respectively, and M is referred to the subject mass. F_{norm} and D_{norm} are referred to the normalized force and deflection respectively. The reference mass of a 50th percentile male is 75 kg (Eppinger et al, 1984).

$$F_{normalized} = F \cdot \left(\frac{75kg}{M} \right)^{2/3}$$

(Reproduced from Eppinger et al, 1984)

Equation 4.1: Normalized force

$$D_{normalized} = D \cdot \left(\frac{75kg}{M} \right)^{1/3}$$

(Reproduced from Eppinger et al, 1984)

Equation 4.2: Normalized deflection

Frontal Pendulum Thoracic Impact, 6.7 m/s

Kroell et al (1971, 1974) conducted frontal thoracic pendulum impact tests on thirty seven unembalmed PMHS with varying impactor mass (1.64kg to 23.4kg) and velocities (4.9 m/s to 14.3 m/s). A wood impactor was centered over the sternum, at the fourth costal interspace as illustrated in Figure 4.1. Each subject was in a seated upright position. The arms were restrained at the horizontal position but were released prior to impact. Since it was unclear what filter was applied to the experimental data, a SAE 1000 filter was applied to remove artificial noise from the numerical force data; compression data was unfiltered. Five PMHS were subjected to a 6.7m/s impact with a 23.4 kg impactor; this impact condition was the most aggressive in the studies that best

represent the automotive car crash scenarios. Table 4.1 lists the anthropometric data for the PMHS. A summary of the frontal pendulum impact setup is provided in Table 4.2.

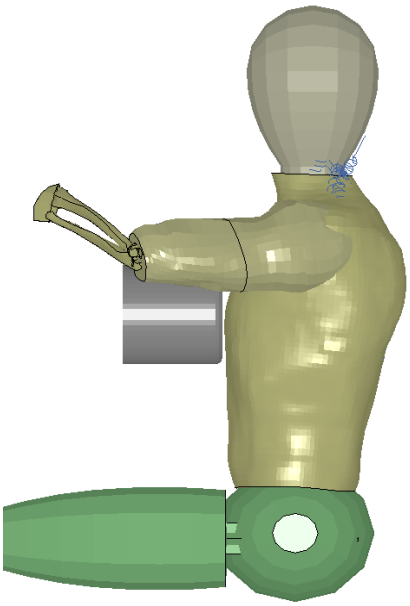

Figure 4.1: Frontal pendulum thoracic impact

Table 4.1: Frontal pendulum thoracic impact - PMHS anthropometric data

Test	Age	Mass (kg)	Chest Depth (mm)	AIS
15FM	80	53	200	4
18FM	78	66	219	4
19FM	19	66	203	2
20FM	29	57	203	0
22FM	72	75	225	4
Model	-	76	238	

(Reproduced from Kroell et al, 1971, 1974)

Table 4.2: Frontal pendulum thoracic impact - experiment summary

Impact Type	Frontal Pendulum
Loading Condition	Initial 6.7 m/s
Impactor mass	23.4 kg
Impactor Diameter	152.4 mm
Arm Position	Horizontal

Derived from Kroell et al, 1971, 1974

Measurable Responses

In the experiment, the impact force was measured using a load cell attached to the impactor. The chest deflection was measured by monitoring markers at the spine and at

the impactor using high-speed film. The simulation response was compared to the experimental normalized force and deflection data as presented by Forbes (2005). A sample size of five PMHS that were subjected to an impact velocity of 6.7m/s was used for the current analysis. Viscous Criterion (VC) response and number of rib fractures were analyzed. The extracted experimental force and compression data had been normalized as described by Eppinger et al (1984). The following responses were compared:

Force	Impact force between impactor and body
Compression	Deflection divided by the initial thorax depth from surface to surface at the 6th rib level
VC	Viscous criterion; instantaneous product of the rate of deflection and compression
Injury	Number of rib fractures

Oblique Pendulum Thoracic Impacts, 4.3 and 6.7 m/s

Viano et al (1989) conducted the oblique pendulum impact tests on the thorax. Each subject was seated in an upright position. The arms were raised so that the thorax was exposed to the impact as illustrated in Figure 4.2. The impactor face was centered vertically and fore/aft on the lateral section of the 6^{th} rib. The impacts were conducted at three velocities; however, the ISO standard (1999) only recommended the two lower impact velocities to be considered. The subject was rotated 30 degrees relative to the impactor face. The pendulum was aligned perpendicular to the lateral side of the thorax, and vertically aligned with the xiphoid process, equivalent to 75mm below mid-sternum. The axis of the impactor direction was horizontal and aligned through the approximate center of gravity of the torso, where the center was approximately 20mm anterior to the intrathoracic surface of the vertebra. A sample size of four PMHS that were subjected to 4.3m/s impact and three PMHS were subjected to 6.7m/s impact for the current analysis. Table 4.3 lists the anthropometric data for the seven PMHS. A summary of the oblique pendulum impact setup is provided in Table 4.4.

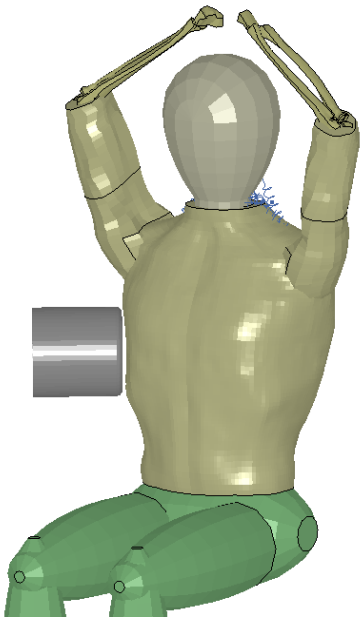

Figure 4.2: Oblique pendulum thoracic impact

Table 4.3: Oblique pendulum thoracic impact - PMHS anthropometric data

Velocity	Test	Cadaver	Age	Mass (kg)	Chest Depth (mm)	AIS
4.3m/s	17	986	29	70.3	300	0
	29	008	52	53.1	285	0
	36	UOM1	37	67.6	305	0
	40	UOM2	64	75.8	335	2
	41	UOM2	64	75.8	335	0
6.7m/s	4	935	63	69.9	280	3
	5	947	38	56.3	290	2
	7	954	66	56.3	270	3
	9	RNY2	64	61.7	280	3
	11	956	40	76.2	295	3
	Model	-	-	76	330	

(Derived from Viano, 1989)

Table 4.4: Oblique pendulum thoracic impact - experiment summary

Impact Type	Oblique Pendulum Impact
Loading Condition	Initial 4.3 and 6.7 m/s
Impactor mass	23 kg
Impactor Diameter	150 mm
Arm Position	Up (overhead)
Analog Filter	SAE 1000
Acceleration Filter	FIR 100
Force Filter	FIR 100
Derived from Viano (1989)	

Measurable Responses

In the experiment, the force response was derived from an accelerometer which was mounted to the impactor. The chest deflection was determined through film analysis. The deflection data was digitized from the NHTSA database (2009) and was normalized in accordance to Viano (1989). The deflection and VC corridors were defined by one standard deviation above and one below the experimental average since the corridors were not available from literature. The following responses were compared:

Force	Impact force between impactor and body
Compression	Deflection divided by the initial thorax depth from surface to surface along the impact axis
VC	Viscous criterion; instantaneous product of the rate of deflection and compression
Injury	Number of rib fractures

Lateral Limited Stroke Pendulum Thoracic Impact

Chung et al (1999) conducted the lateral limited-stroke pendulum impact tests on four unembalmed PMHS. An impactor was centered over the lateral side of the sixth rib. The last 51mm of the impactor stroke was occupied by the test subject. Each subject was suspended in a seated upright position with arms at the overhead position as illustrated in Figure 4.3. This impact was chosen because a deflection-controlled pendulum impact that has high energy, limited stroke, with a velocity pulse would be more representative on typical occupant during side impact (Deng, 1999). The impactor was initially accelerated to a nominal velocity of 5.6 m/s, then was decelerated by a piece of paper honeycomb and a piece of aluminum honeycomb. The honeycomb served two purposes: limit the impactor stroke and reduce peak acceleration when the impactor bottoms out. Four PMHS were subjected to this impact configuration, however only the male PMHS experimental data was selected for analysis. Table 4.5 lists the anthropometric data for the PMHS used for the pendulum impact analysis. A summary of the limited stroke pendulum impact setup is provided in Table 4.6.

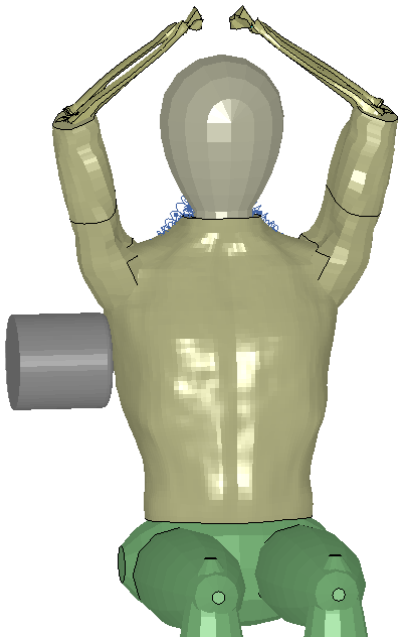

Figure 4.3: Lateral limited stroke pendulum thoracic impact

Table 4.5: Lateral limited stroke pendulum thoracic impact - PMHS anthropometric data

Test Number	Age	Mass (kg)	Chest Depth (mm)	AIS
CAD1	51	103	336	3
CAD4	71	76	335	3
CAD6	45	82	326	3
Model	-	76	338	

(Derived from Chung et al, 1999)

Table 4.6: Lateral limited stroke pendulum thoracic impact - experiment summary

Impact Type	Lateral Limited Stroke Pendulum Impact
Loading Condition	Initial 5.6 m/s, prescribed velocity profile
Impactor mass	50 kg
Impactor Diameter	152.4 mm
Arm Position	Up (overhead)
Analog Filter	SAE 1000
Acceleration Filter	SAE 180, FIR 100
Force and Disp. Filter	BW 300
Derived from Chung et al, 1999	

Measurable Responses

In the experiment, the impact force was measured using a load cell in the impactor and the chest deflection was measured using a chest band. The simulation response was compared to the experimental normalized force and deflection data as presented by

Forbes (2005). The VC response and number of rib fractures were analyzed. Similar to the frontal pendulum impact analysis, the force and deflection response were normalized according to Eppinger et al (1984). The following responses were compared:

Force	Impact force between impactor and body
Compression	Deflection divided by the initial thorax depth (surface to surface) at the 6^{th} rib level
VC	Viscous criterion; instantaneous product of rate of deflection and compression
Injury	Number of rib fractures

4.3 Sled Impact Descriptions

Sled impact tests are intended to replicate a full body automotive crash and provide insight into the interactions between body regions. The current study focused on two types of sled tests: the WSU-type and the NHTSA-type sled tests.

Sled Impact Selection Justification

Sled impact tests applied to the full body were intended to provide insight into the interaction of different body regions. There were only three types of sled impact tests to date with each setup replicating a different boundary condition that model after side impact car crashes. Only rigid wall impacts were considered, although each sled type had conducted experiments with various other boundary conditions such as pelvis offset and padded contact. The sampling pool for the rigid wall impacts was large (at least 3 cadavers) and were conducted at two different velocities, where as other boundary conditions were only conducted with 2 cadavers.

The Heidelberg-type sled test was the first sled developed for cadaver testing. The WSU-type sled test was a derived version of the Heidelberg-type sled with five impact plates. Both sled tests were recommended by the ISO standard for the full body side impact validation. The Heidelberg-type sled test was not presented in-depth since the test was largely focused on force response but not chest deformation, however the force response

are presented in Appendix A. The WSU-type sled configuration had five impact plates, which provided greater understanding on the load distribution between regions that included the shoulder, thorax, abdomen, pelvis and knee.

The NHTSA-type sled test had four impact plates and was introduced to represent the boundary condition seen during a side impact car crash. There was no shoulder contact plate, and the upper edge of the thoracic plate was at the approximate average height of a window sill. The contact plates were larger than those in WSU-type where the load was more distributed and the body was engaged over a larger surface area. The NHTSA-type sled test was selected because it provided greater level of understanding into the chest deformation.

WSU-type Side Sled Impact

The WSU side sled was a derived version of the Heidelberg sled test by Kallieris et al (1981). The focus of the study was to understand the cadaver interaction with boundary conditions that had different regional stiffness. Cavanaugh et al (1990) conducted side sled impact tests on 31 unembalmed cadavers. Each subject was seated in an upright position on a bench with arms down and with wrists tied together as illustrated in Figure 4.4. A sled was accelerated to approximately 6.67 m/s or 8.89 m/s and suddenly decelerated to a stop causing the PMHS to slide along the bench and make contact with a series of impact plates. There were five contact plates in total. The first plate was aimed at the shoulder, the second at the thorax, the third at the abdomen, the fourth at the pelvis and the upper section of the lower limb, and the fifth at the knee. The study tested four different wall surface conditions: a rigid wall, soft paper honeycomb padding, stiff paper honeycomb padding and 152.4 mm pelvic plate offset with rigid wall. Only the rigid wall configuration was used for the current analysis. Three PMHS were subjected to 6.67 m/s impact and two PMHS were subjected for 8.89 m/s. Table 4.7 lists the anthropometric data of the PMHS. A summary of the WSU-type sled impact setup is provided in Table 4.8.

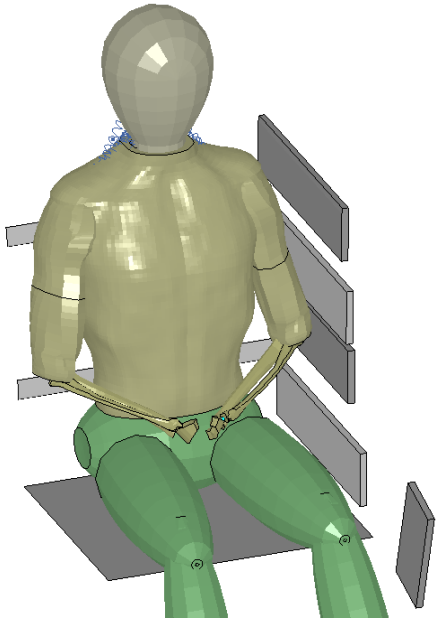

Figure 4.4: WSU-type side sled impact

Table 4.7: WSU-type side sled impact - PMHS anthropometric data

Velocity	Test Number	Cadaver Number	Age	Mass (kg)	AIS
6.67	2585	SIC05	67	44.0	4
	2587	SIC07	66	74.8	4
	4933	SC131	48	75.0	4
8.89	2584	SIC04	69	57.6	4
	2586	SIC06	60	61.2	4
	Model		-	76	

(Derived from Cavanaugh et al, 1990; 1993)

Table 4.8: WSU-type side sled impact - experiment summary

Impact Type	WSU Type Sled
Loading Condition	6.67 m/s and 8.89 m/s
Impact plates	5
Arm Position	Down
Analog Filter	SAE 180

Derived from Cavanaugh et al (1990, 1993)

Measurable Responses

The simulation response was compared to the experimental normalized force, and compression data as presented by Forbes (2005). The original force data were acquired from the NHTSA biomechanics test database, and were normalized accordance to Eppinger et al (1984). Chest deflection data were not available in the NHTSA database; chest compression average and standard deviations were digitized from Cavanaugh et al

(1990) and Yoganandan & Pintar (2001). The compression was obtained by tracking the deflection of the upper and lower sternum, and they were averaged to obtain a mid-sternum deflection. This average deflection was then averaged with the deflection obtained at the fifth thoracic vertebra. The half thorax width and half thorax deformation included the struck-side arm (Cavanaugh et al, 1993). Similar measurement protocol was used to derive chest compression in the numerical model. The following responses were compared:

Force	Impact force between rigid plate and body
Impulse	Impulse measured at each rigid plate
Compression	Half width compression measurements from the T5 at the spine to the outside surface of the left arm
VC	Viscous criterion; instantaneous product of rate of deflection and compression
Injury	Number of Rib Fractures

NHTSA-type Side Sled Impact

The NHTSA side sled was the second derived version of the Heidelberg sled test by Kallieris et al (1981). The focus of this study was to better model the door to occupant interaction by choosing an appropriate average window sill height to represent real world vehicles (Pintar et al, 1996). Pintar et al (1997, 2001) conducted side sled impact on 26 unembalmed cadavers. Each subject was seated in an upright position with arms down as illustrated in Figure 4.5. A sled was accelerated to approximately 6.67 m/s or 8.89 m/s, suddenly decelerated to a stop causing the PMHS to slide along the bench and make contact with a series of contact plates. There were four contact plates in total. The first plate was aimed at the mid thorax, the second at the abdomen, the third at pelvis and upper section of lower limb, and the fourth at remaining section of the lower limb. This configuration was intended to mimic occupant making contact with the door without the shoulder engaging as the average windowsill height is typically lower than the shoulder. Only the rigid wall configuration was considered, although the experiment conducted

with three different wall surface conditions. Only male subjects were used for the analysis, three subjects for the 6.67 m/s impact and five subjects for the 8.89 m/s impact. Table 4.9 lists the anthropometric data for the PMHS. A summary of the NHTSA-type side sled setup is provided in Table 4.10.

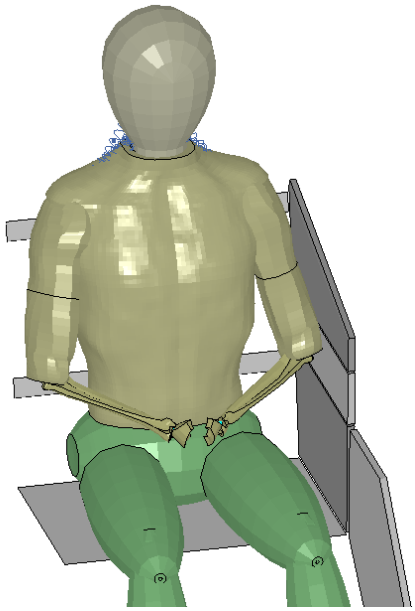

Figure 4.5: NHTSA-type side sled impact

Table 4.9: NHTSA-type side sled impact - PMHS anthropometric data

Velocity	Test Number	Cadaver Number	Age	Mass (kg)	AIS
6.67	3120	SC101	73	89	4
	3122	SC102	27	73	0
	3155	SC103	55	76	3
8.89	3322	W9305	73	72	4
	3324	W9302	77	75	4
	3422	SC108	44	83	2
	3423	SC109	49	62	4
	3579	W9310	68	98	3
	Model		-	76	

(Derived from Pintar, 1997;2001)

Table 4.10: NHTSA-type side sled impact - experiment summary

Impact Type	NHTSA-Type Side Sled
Loading Condition	6.67 m/s and 8.89 m/s
Impact plates	4
Arm Position	Down
Analog Filter	SAE 180
Derived from Pintar et al (1997, 2001)	

Measurable Responses

The simulation response was compared to the experimental normalized force, and compression data as presented by Forbes (2005). In the experiments, the contact plates were instrumented with load cells. The chest deflection was measured with three chest bands at the following locations: the transverse plane at the 4th rib, at the xiphoid process, and at the 10th rib. These are termed upper band, middle band, and lower band, respectively. The raw data was acquired from the NHTSA Database (2004), and were normalized according to Eppinger et al (1984). The following responses were compared:

Force	Impact force between rigid plate and body
Impulse	Impulse measured at each rigid plate
Compression	Full width compression measurements made at three chest bands
VC	Viscous criterion; instantaneous product of rate of deflection and compression
Injury	Number of Rib Fractures

4.4 Simulation Setup

Pendulum Simulation

Pendulum impactor was modeled as a rigid part with shell elements representing an enclosed volume. The edges of pendulum were rounded with a 10mm radius with three elements mapped around the fillet to mitigate contact issues between the sharp edges and the soft tissue. This effectively decreased hourglassing in the soft tissue, and improved the model stability. The mesh density of the impactor was chosen to reflect the mesh density of the thoracic surface to avoid numerical instability.

For contact purposes, the impactor was modeled with an elastic modulus equivalent to aluminum or wood as defined in the experiments. The high stiffness of the impactor material relative to soft tissue produced near negligible deformation to the impactor. As such, it was deemed appropriate to model impactor as a rigid part to improve computational cost.

The impactor was typically confined to a loading direction and the rotation was restricted since the mass moment of inertia was not defined. This was considered representative for most experiments since the impactor was restricted as such. Mass elements were added to the part to compensate up to the physical mass of the impactor due to the shell elements implementation.

Gravity was not applied to the simulation. Preliminary analysis showed that the influence was minimal on the impact response. Forbes (2005) conducted his sled simulation with gravity applied and the effect was only noticeable during post-impact. This assumption was deemed acceptable given the focus of the current study was on investigating peak loadings resulted from the impact and not the kinematics after the impact (> 60 ms).

Limited Stroke Lateral Pendulum Thoracic Impact

Instead of replicating the experimental setup of the limited-stroke pendulum impact in the numerical environment, the pendulum in the simulation was prescribed with a velocity profile that was extracted from the experimental study (Chung, 1999). Since details on how the initial pendulum position was defined relative to the cadaver were unclear, the pendulum setup was determined as follows in the current study. The pendulum travel was determined based on the direction axis of the pendulum; 51 mm depth was calculated with respect to the intersection of the center axis to the outer surface muscle. The pendulum travel was limited by cropping the velocity curve.

Sled Simulation

For the sled impact scenarios, the impact plates were modeled as solid elements, and the seat bottom, footrest plate, back support bars were modeled as shell elements. All parts were rigid, modeled as steel and were constrained from any translational or rotational movement. The entire body was prescribed with an initial velocity of 6.67 or 8.89 m/s towards the contact plates depending on the impact scenario.

The arms were positioned to reflect the “arms-at-rest” position similar to Forbes (2005), but the arms were then rotated 10 degrees such that they were anterior to the mid-axillary

line. This angle was approximated such that the arm position was consistent with cadaver preparation as discussed in Cavanaugh et al (1993) and was verified with the chestband results from Pintar et al (1997). This setup would be more representative of the initial body position in the experiments.

Model Assessment Criteria

The International Standards Organization (ISO) had a quantitative method to objectively evaluate the biofidelity of side impact dummies against the PMHS. The ISO approach assigned a score of 10 when the response was within corridor, 5 when the response fell outside the corridor but within one corridor width, and 0 when fell outside the corridor by more than a corridor width. Table 4.11 summarizes the ISO's response evaluation. A weight factor method was used to determine the overall model biofidelity based on responses from different body regions.

Table 4.11: Quantitative response evaluation classification

Score = 10	Falling within the corridor of the experimental data
Score = 5	Falling outside the corridor of the experimental data but within one corridor width
Score = 0	Falling outside the corridor by more than one corridor width

Forbes (2005) derived a qualitative measure based on the ISO approach to evaluate the biofidelity of the numerical model, since not all the simulations could be compared to the studies outlined in the ISO (1999). The model comparison by Forbes (2005) was more in-depth, greater insight was gained by evaluating various deflection responses that were typically not considered in the ISO standard (1999). Forbes (2005) assigned the qualitative measures as follows:

Table 4.12: Qualitative response evaluation classification

Good	Falling within the corridor of the experimental data
Reasonable	Falling outside the corridor of the experimental data but within one corridor width
Poor	Falling outside the corridor by more than one corridor width

The assessment achieved a greater detail by splitting the evaluation in terms of loading, peak, and unloading regions as illustrated in Figure 4.6. This approach was typically applied when there were three or less PMHS used for a particular impact condition.

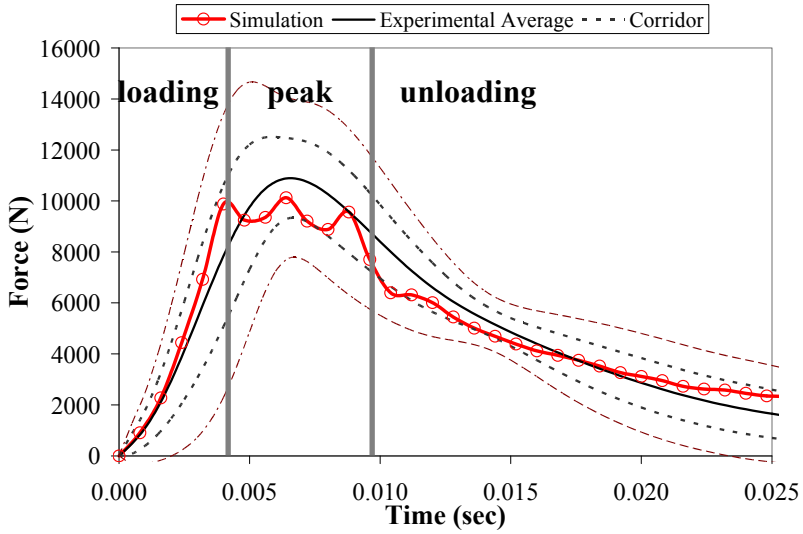

Figure 4.6: Example of a metric response over time

The simulation curve was compared to the experimental response corridors which were developed from the original experimental study or the experimental analysis as documented in ISO (1999). Corridors were constructed around the normalized response versus time history (ISO, 1999). When a response corridor was not available, the upper and lower corridor limits were set at a standard deviation of the normalized experimental data relative to the average. The individual responses were normalized according to the method by Eppinger et al (1984) based on body mass.

Data Processing

The force and acceleration data were taken at a minimum sampling rate of 10000 Hz. The deflection data was taken at a sampling rate of 1000 Hz. The filters specified in the experiments were applied to the data. If a filtering procedure was not provided, then the data was filtered in accordance with the SAE J211 procedure. The data presented in this thesis was plotted in a lower resolution to provide greater clarity and was observed by the author that the curve shape was not affected.

4.5 Pendulum Impact Simulation Results & Discussions

Frontal Pendulum Thoracic Impact

Force Response

The force response began with a brief initial peak dominated by the inertial effects of the impacted area where the area quickly accelerated to coincide with the speed of the impactor as shown in Figure 4.7 (a). After the oscillation, a plateau force was developed and eventually the torso response decreased to zero. Overall force response behavior was similar as those from the experiment; however the first peak force was dependent on the applied filter due to the high frequency content of this response.

Compression Response

The simulated peak compression was lower than the experimental peak as shown in Figure 4.7 (b), and the unloading response was more rapid than the experiment. The simulation showed the heart was physically compressed between the spine and the sternum. The simulated peak chest deflection (87mm) was higher than the experimental average (84 mm). Although the deflection responses were similar, the peak compression was low due to the model's chest depth which was 24mm longer than the longest chest depth among the cadavers tested.

There are three possibilities that may explain the unloading deficit. One reason had to do with the cadavers where their lower diaphragm tended to sag compared to a living human being, which offered less viscous resistance to the impact. As such, the abdomen contributed relatively more resistance in the simulation as the force response was more elevated and lagged behind the experimental response during the unloading phase.

Another possible explanation had to do with the assumptions made in the rib material. The lateral section of the rib was stronger than the anterior and posterior sections in a physical sense; however the whole rib geometry was meshed as a single continuum model that assumed uniform properties throughout the rib. This suggested that regional

variation of the rib material properties and geometry was critical in predicting response under varying load scenarios.

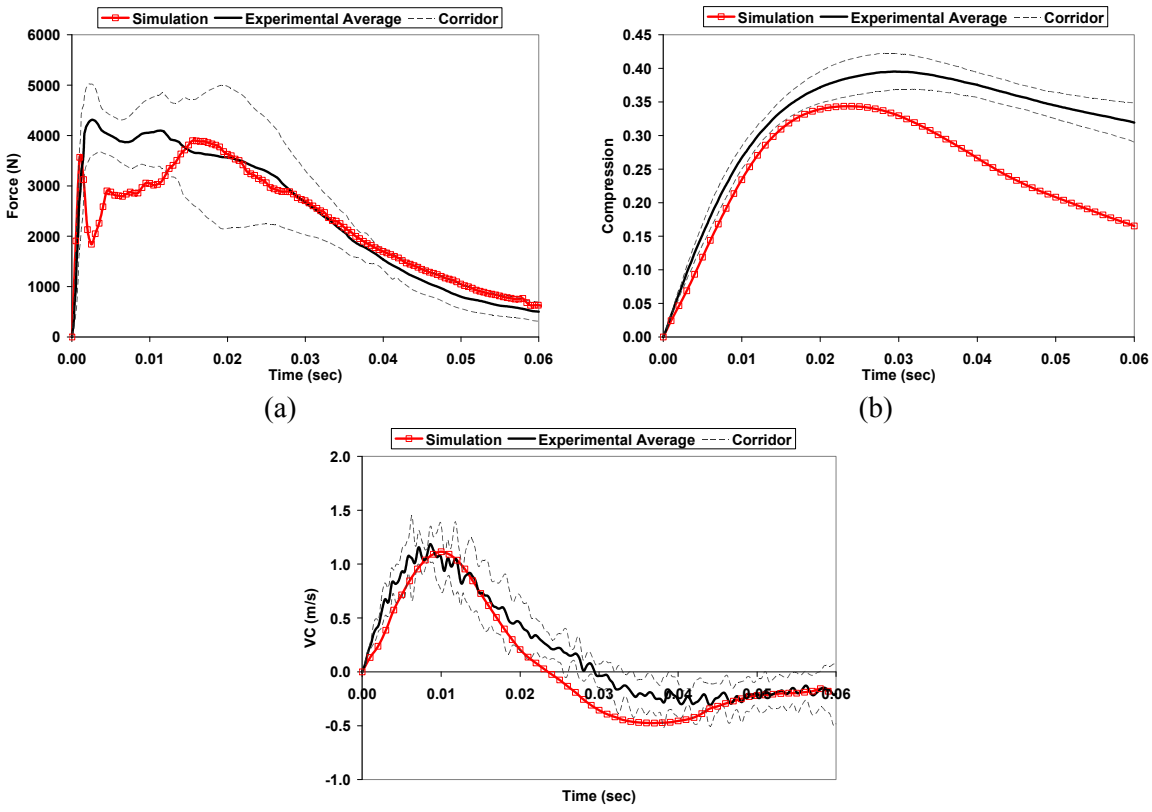

Figure 4.7: Frontal pendulum impact simulation results

(a) Force (b) Compression (c) VC

The third explanation was related to the costal cartilage material properties. Costal cartilage material properties are known to be highly non-linear and non-uniform. The dynamic properties of the costal cartilage are largely unknown. The current model utilized the same material properties from Ruan (2003). Ruan's model had similar response as the previous elastic material model (Deng, 1999) except it was based on a viscoelastic model and possessed a non-linear loading feature. For the current focus on side impact, this assumption was considered adequate given that the influence of the costal cartilage on lateral response is low. However, this deficit should be addressed with experiments focused on obtaining dynamic properties of the costal cartilage if the model

were to progress towards predicting response for a wider range of impact conditions. Even with the discrepancy, the VC response was reasonable as shown in Figure 4.7 (c).

Rib Fracture Prediction

The simulation revealed fewer rib fractures overall and more fractures in the first rib than the experiments as summarized in Table 4.13. The lack of rib fractures explained the discrepancy in the shape of the compression response. The first rib connected to the manubrium of the sternum, and its cartilage was continuous with the sternum, where as all other costal cartilages were connected to the sternum through facet joints. The lack of representation of this transition prohibited the first ribs' movement, thus increased the likelihood of multiple rib fractures at the first rib level.

Table 4.13: Frontal pendulum thoracic impact – rib fracture summary

Rib	PMHS Test Number								Simulation	
	19FM	20FM	15FM		18FM		22FM			
			Left	Right	Left	Right	Left	Right	Left	Right
1						1			2	2
2			1	1	1	1	1	1		
3			2	2	1	1	2	3		
4			2	1	1	1	3	2	1	1
5			2	1	1		2	1		
6				1	2	2	1	1		
7					2					
Subtotal	0	0	7	6	8	6	9	8	3	3
Total	0	0	13		14		17		6	

Oblique Pendulum Thoracic Impact

Force response

The loading region of the experimental force response was gradual and took over 10 ms before the first peak developed as shown in Figure 4.8 (a). This may be related to the experimental instrumentation where an accelerometer was used to derive the pendulum impact force, where as the frontal impact and limited-stroke side impact used load cells. The unfiltered experimental acceleration data contained high-frequency contents upon initial contact; a FIR100 filter was applied to the data, which may explain the gradual toe region during the initial impact. The simulated force shape may seem uncharacteristic

when compared to the experiment; however the loading region was quite similar to the experimental response of the 'cadaver 4'.

The discrepancy in the plateau region of the force response was related to the uniform rib material model. A high force developed early in the response and relied more heavily on the rib to support the impact due to the bending stiffness of the rib being higher than the costal cartilage. The compression response was not as aggressive as the experiment, thus the simulated maximum VC was low as shown in Figure 4.8 (c). The simulation showed that the fractures of the 4th to 8th ribs occurred within a 2 ms time frame at approximately the 10ms point which explained the plateau force response. The rib fractures typically occurred between the lateral and the posterior region of the ribs in the simulation. A top view cross-section of the thorax at 5th and 6th level is shown in Figure 4.9.

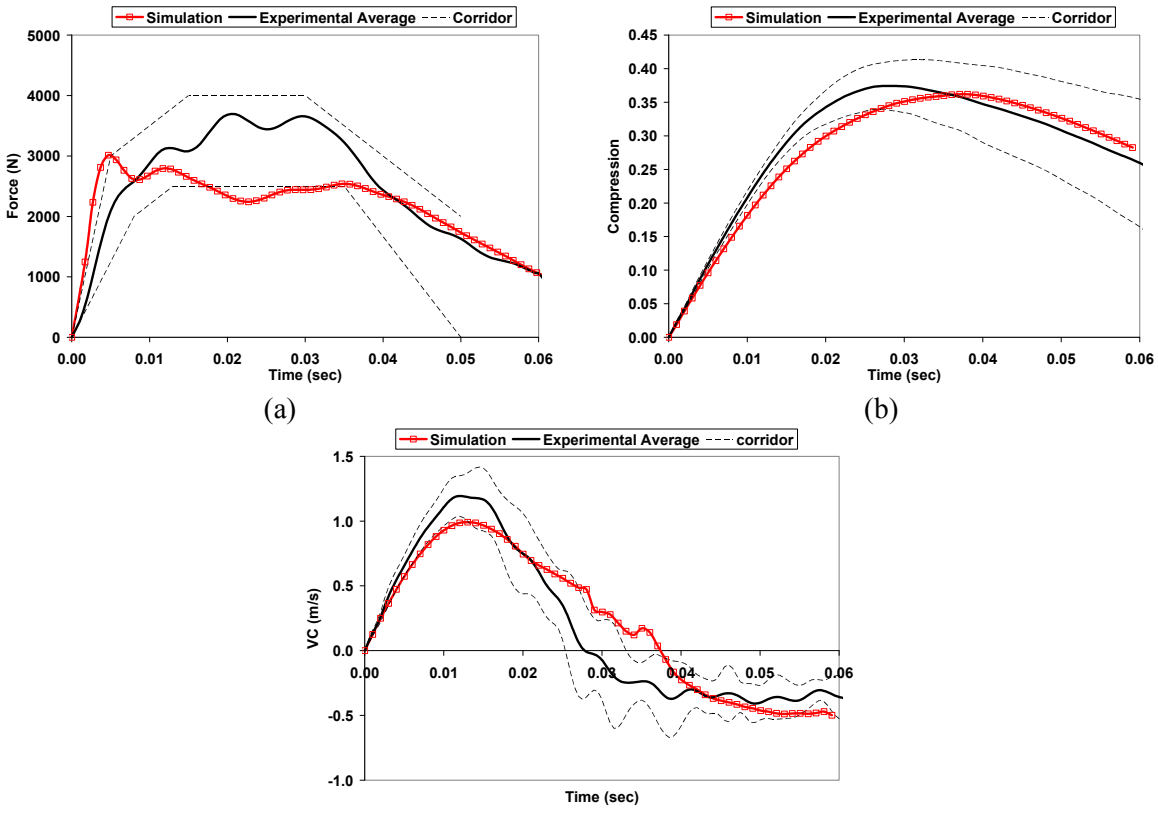

Figure 4.8: Oblique pendulum 6.67 m/sec impact simulation results

(a) Force (b) Compression (c) VC

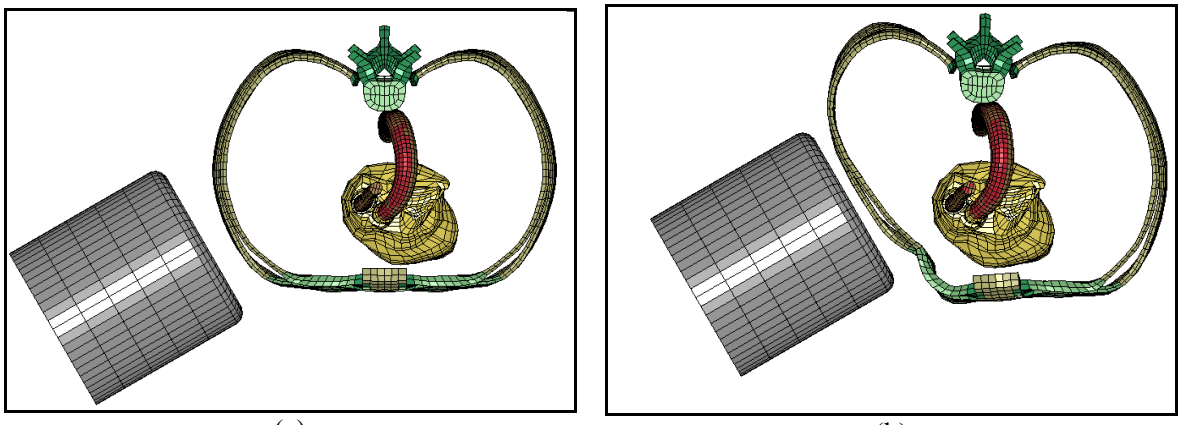

(a) (b)

Figure 4.9: Cross-section view of oblique pendulum impact (5th, 6th rib level)

(a) 0 ms (b) 10 ms

Compression Response

The simulated compression levels at low speed, medium speed, and high speed were all within the peak deflection tolerances as defined in the study by Viano (1989) largely due to the implementation of the strain-rate dependent rib material model. A strain-rate dependent material model was required to predict representative response across a wide range of impact conditions. The low speed (4.3m/s) impact results are presented in Appendix A. The high speed impact case was not presented due to numerical instability caused by excessive deformation prior to reaching a peak compression.

Rib Fracture Prediction

A more representative rib model and geometry were needed to improve the force response and rib fracture location prediction. It was observed that the ribcage directly impacted the heart which suggested a high likelihood of a heart contusion in the 6.67 m/s impact scenario. The simulation predicted more rib fractures than the experiment as shown in Table 4.14.

Table 4.14: Oblique pendulum impact 6.67 m/s– rib fracture summary

Rib	PMHS Test Number					Simulation
	4	5	6	9	11	
3						2
4			1	1	1	2
5	3	1	1	1	1	1
6	1	1	2		1	1
7	1	1	1		1	1
8	2				1	1
Non-struck side	0	0	1	3	0	0
Total	7	3	6	5	5	8

Lateral Limited-Stroke Pendulum Thoracic Impact

Force Response

The force response of the experimental study can be observed with three distinct regions as shown in Figure 4.10 (a); a rapid loading region, a peak load region, and a rapid unloading region. The simulation revealed similar characteristics except it had a longer duration in the unloading region. The duration of the velocity profile for the simulation was approximately 20ms, from the time when the contact was initiated to the time when the impactor reached zero velocity.

Compression Response & Rib Fractures Predictions

In the study by Chung et al (1999), the C_{max} and VC_{max} were calculated by dividing the chest deflection using the half-thorax length. In Forbes' (2005) analysis on Chung et al's (1999) study, the C_{max} and VC_{max} were divided by the full-thorax length as shown in Figure 4.10 (c). The compression between the studies was different by a factor of two due to the reference thorax length.

Compression unloading was much more rapid than the experiments as shown in Figure 4.10 (b). The peak chest compression was low due to a lack of rib fractures in the numerical model. The experiment observed multiple rib fractures, but the current model only predicted one rib fracture as summarized in Table 4.15. This suggested the need for a representative rib geometry model that incorporated regional variation. Although the experiment did not specify rib fracture locations, rib fracture typically occurs at the angle

curvature (Cavanaugh, 1991). Stitzel et al (2003) and Kemper (2007) under took material testing which revealed that the anterior section of the rib was inherently weaker than the lateral section, however differences in material and geometrical properties were not fully represented in the current model.

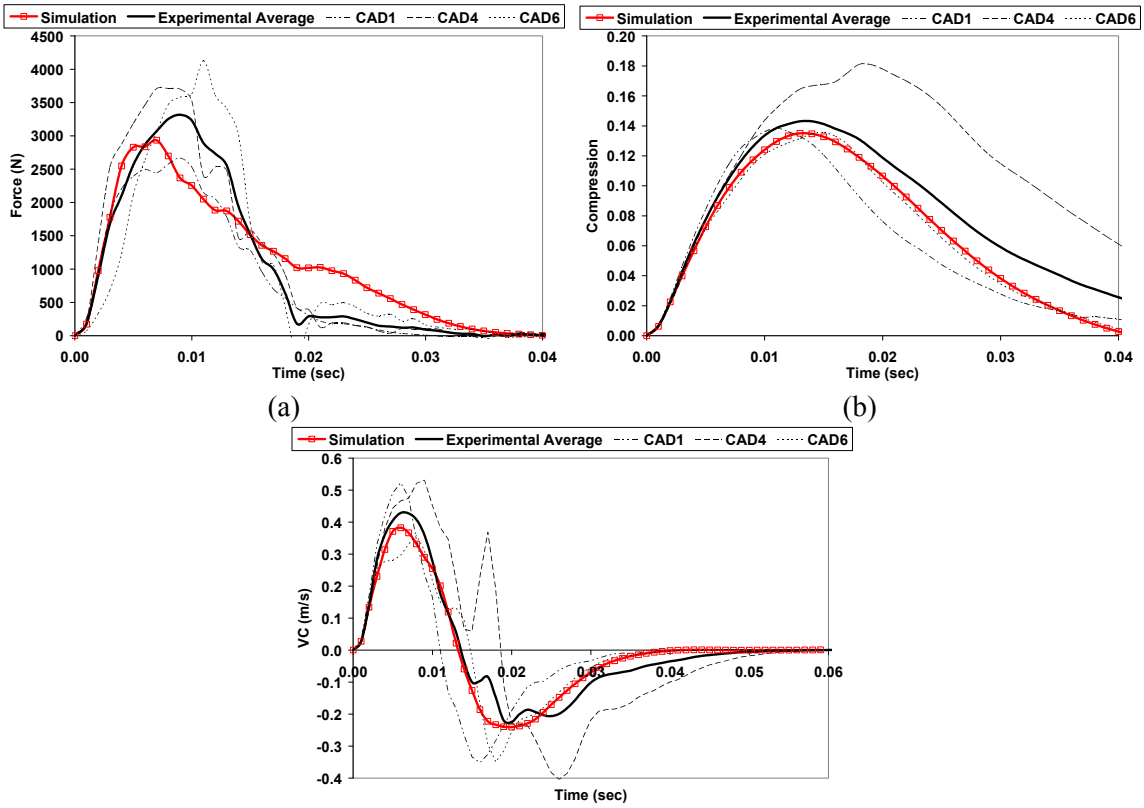

Figure 4.10: Lateral limited stroke impact simulation results

(a) Force (b) Compression (c) VC

Table 4.15: Lateral limited-stroke pendulum thoracic impact – rib fracture summary

Rib	PMHS			Simulation
	1	4	6	
8				1
Total	4	15	10	1
*Note: rib fracture by level was not reported in the experiment				

The study by Chung (1999) specified a 51mm stroke limit, but the maximum deflection measured on the four cadavers were 51.7mm, 61.0 mm, 55.5 mm and 44.7 mm; three out of four cases were greater than the stroke limit. One possibility was the variation in the

experimental setup where the contact occurred more than 51mm of stroke, however there was not enough experimental data to verify if this was the case. The inertial effect of the fractured ribs may elevate the chest deflection but it was not the factor based on the previous sensitivity analyses on the rib properties using the current numerical model. Since it was difficult to verify the proper loading condition on the cadaver in the simulation, the simulation data should be interpreted with care.

4.6 Pendulum Impact Summary

In all pendulum simulations, most responses showed good to reasonable correlation throughout the impact except the unloading of compression response in the frontal impact case. The force and compression correlation summary for the three pendulum impact scenarios are provided in Table 4.16 and Table 4.17, respectively. Overall, the improvements made to the current human body model had demonstrated greater biofidelity in all areas. Despite the ribs being modeled as a single continuum, the force and compression response showed good correlation. These responses can be improved if more development was placed on the rib model to account for the geometrical variation between the anterior, lateral and posterior section of the rib. Such development would also improve the accuracy of the torso shape and rib fracture pattern predictions.

Table 4.16: Pendulum impact - force correlation summary

Pendulum Tests	Impact velocity	Loading	Peak	Unloading
Frontal	6.7 m/s	Good	Good	Good
Oblique	4.3 m/s	Good	Good	Good
	6.67 m/s	Good	Good	Reasonable
Lateral limited-stroke	5.6 m/s profile	Good	Good	Reasonable

Table 4.17: Pendulum impact - compression correlation summary

Pendulum Tests	Impact velocity	Loading	Peak	Unloading
Frontal	6.7 m/s	Reasonable	Reasonable	Poor
Oblique	4.3 m/s	Good	Good/Reasonable	Good
	6.67 m/s	Reasonable	Good	Good
Lateral limited-stroke	5.6 m/s profile	Good	Good	Good

The oblique pendulum impact scenario had demonstrated the importance of incorporating strain-rate dependency into the rib material model to predict torso response accurately across a wider variety of impact conditions. It was critical for injury evaluation be verified across a wider range of impact velocities than only one impact velocity condition for a given test scenario.

From the three impact scenarios, the experimental results clearly demonstrated that younger subjects sustained less rib fractures. From rib modeling perspective, it would be beneficial to focus on developing a rib model that was representative of a particular age group than developing an 'average' rib model which may produce conflicting results. It would give greater meaning to the model to focus at the age group from 15 to 29 that was most vulnerable as indicated by the crash statistics in chapter 2.

4.7 Sled Impact Simulation Results & Discussions

It should be mentioned here that the sled test results should be interpreted with care. Since the sled test involved PMHS in a full-body interaction with contact plates, the response timing may change with different body stature and size. The average of the experimental data may result in multiple peaks and greater variation in the shape of the response. The individual response may only have distinct response features than those presented by the experimental average. As such, the sled test results were best evaluated qualitatively based on response trends and peak values.

WSU Sled Impact

Force Response

The simulated shoulder and thorax force responses were comparable to those from experiments as shown in Figure 4.11 (a) and (b). A high peak force was observed in the abdominal plate response where the elbow made contact and caused the initial spike as shown in Figure 4.11 (c). The peak pelvic force fell outside the response corridor, but the peak remained within two corridor width from the average as shown in Figure 4.11 (d).

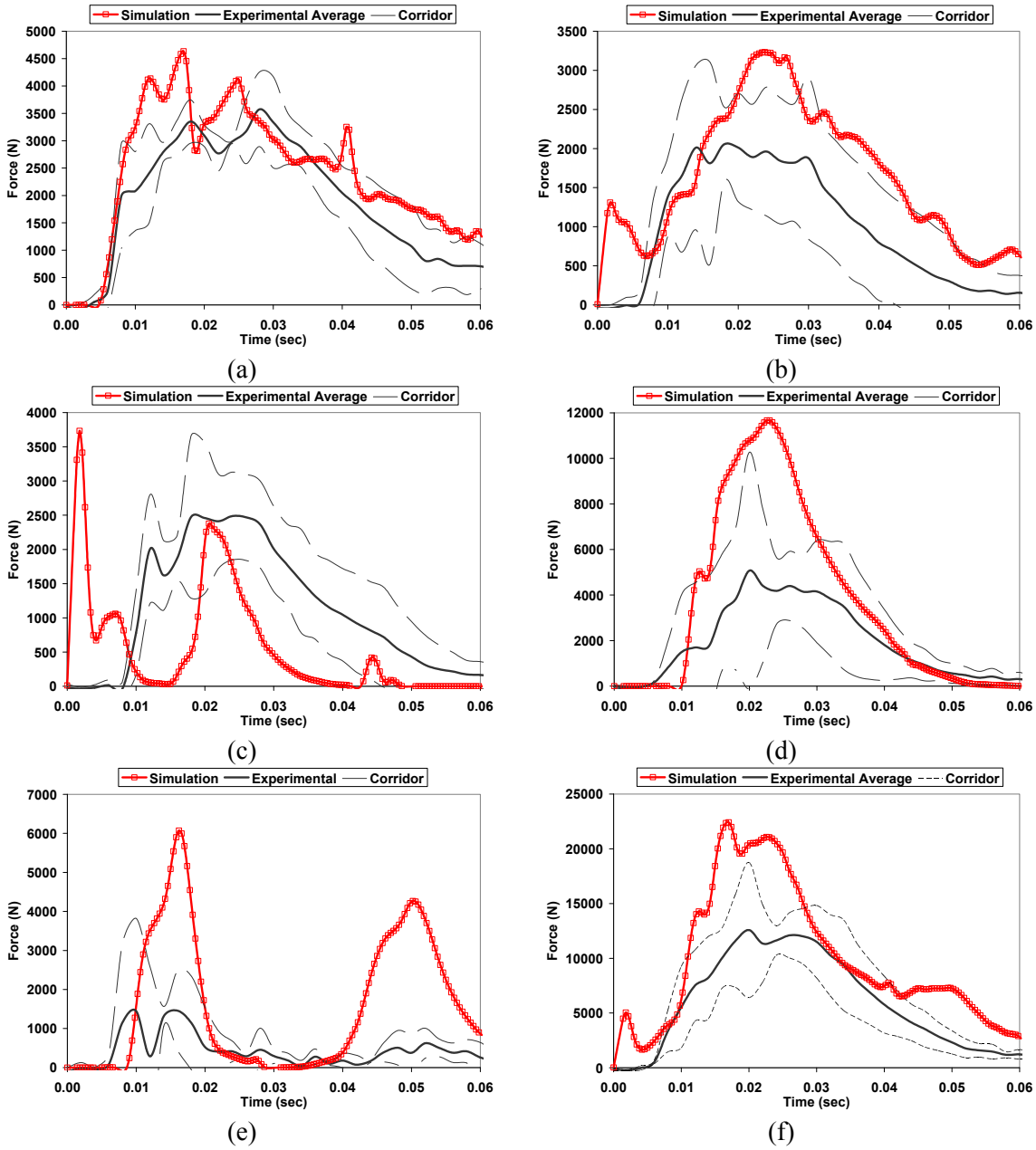

Figure 4.11: WSU sled impact at 6.67 m/s – force plate response
(a) shoulder (b) thorax (c) abdomen (d) pelvic (e) knee (f) total

It became apparent that the pelvis model required more development to account for pelvic fracture to better agree with corridors. Since the current human body model had a slim abdominal region, the abdominal region did not absorb the load as well as the experiments. The pelvic response had partially compensated this effect with an elevated

force response. Improving the geometry of the abdomen may improve the pelvic response but it was not the primary factor of the pelvis' elevated response.

The knee contact plate was small and the plate position was fixed relative to the rest of the sled; the force response measurement may not be directly comparable given that the point of impact was highly dependent on the anthropometric leg measurements. Figure 4.11 (e) shows the two apparent force peaks from the simulation, one correlated to the left knee contacting the plate, and the second peak was correlated to the right knee contacting the plate through the left knee.

Compression Response

The compression response of the model fell within the experimental corridor as shown in Figure 4.12 (a). The compression shape lagged from those in the experiments, especially apparent between 10 to 30 ms when the peak VC occurred, as shown in Figure 4.12 (b). This lag maybe related to the rib fracture or the arm position; it was inconclusive since the chest deformation was not measured in the experiment. This experiment measured the deflection of the torso between the sternum and 5th vertebra relative to the impact wall; therefore it did not fully capture the localized deformation of the ribcage.

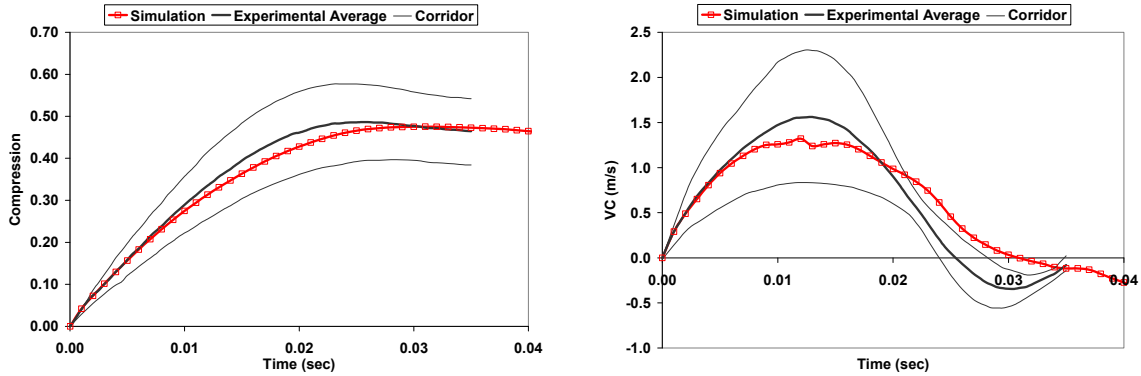

(a) (b)

Figure 4.12: WSU sled impact at 6.67 m/s – compression & VC response

(a) Compression (b) VC

Rib Fracture Prediction

The PMHS typically sustained six to seven rib fractures consecutively in terms of rib level (1st to 6th, 1st to 7th, 4th to 11th), where as the simulation predicted rib fractures from 1st to 9th as shown in Table 4.18. Only rib fractures on the struck (left) side of the thorax were tabulated. The fracture pattern was influenced by the arm position and body stature.

Table 4.18: WSU sled Impact 6.67m/s – rib fracture summary

Rib	PMHS Test Number			Simulation
	2585	2587	4933	
1	2	1		2
2	2	2		1
3	2	2		3
4	2	2	2	2
5	2	2	1	2
6	2	2	1	1
7		2	1	2
8			1	1
9			1	2
11			1	
Non-struck side	8	3		2
Total	20	16	11	18

NHTSA-Type Sled Impact

Force Response

The simulated force response at the thoracic region demonstrated good agreement with the experiment, but under predicted in the abdominal region and over predicted at the pelvic and lower limb regions as shown in Figure 4.13. The lack of force response in the abdominal region was related to the narrow waist breath, thus relied on other regions to decelerate the body as mentioned previously. The current waist breadth of the model, measured at the approximate level of the anterior superior iliac spine anatomical location was 267 mm, where the PMHS in the NHTSA study average was 301 mm, ranged from 275 to 333 mm. The simulation over predicted the body rotation due to a recoverable unloading characteristic of the pelvis model. The kinematics in the post-impact time frame (>60 ms) may not be representative.

Impulse Response

The total impulse response at 60 ms as calculated from the simulation was 563 Ns (where the calculated impulse response plateau), and the experimental average was 360 Ns. Theoretically, a 50th percentile male of 76.6 kg with an impact velocity of 6.67 m/sec carried a total impulse of 511 Ns. Given the low experimental average of momentum transfer, there was a discrepancy in the force measurement of the lower limb plate. The lower leg segment mass was calculated to be 20.6 kg, regionally would require 137 Ns transfer before coming to a complete stop, the experimental average was calculated to be 39 Ns. This discrepancy suggested the momentum transfer was not completely captured through the impact plates. Given this preliminary momentum calculation was not exact, but this should be investigated further.

Compression Response

One of the advantages of this study was the use of chest bands at three thorax levels. This provided a greater insight into the chest deformation shape and the corresponding arm position. From the experimental PMHS chest contour measurements, the arm position was typically anterior to the coronal plane. The previous model results by Forbes (2005) had the arm position aligned with the coronal plane, his reasoning was to produce a conservative estimate of injury. The current model results were reflective of an arm position closer to the experiments.

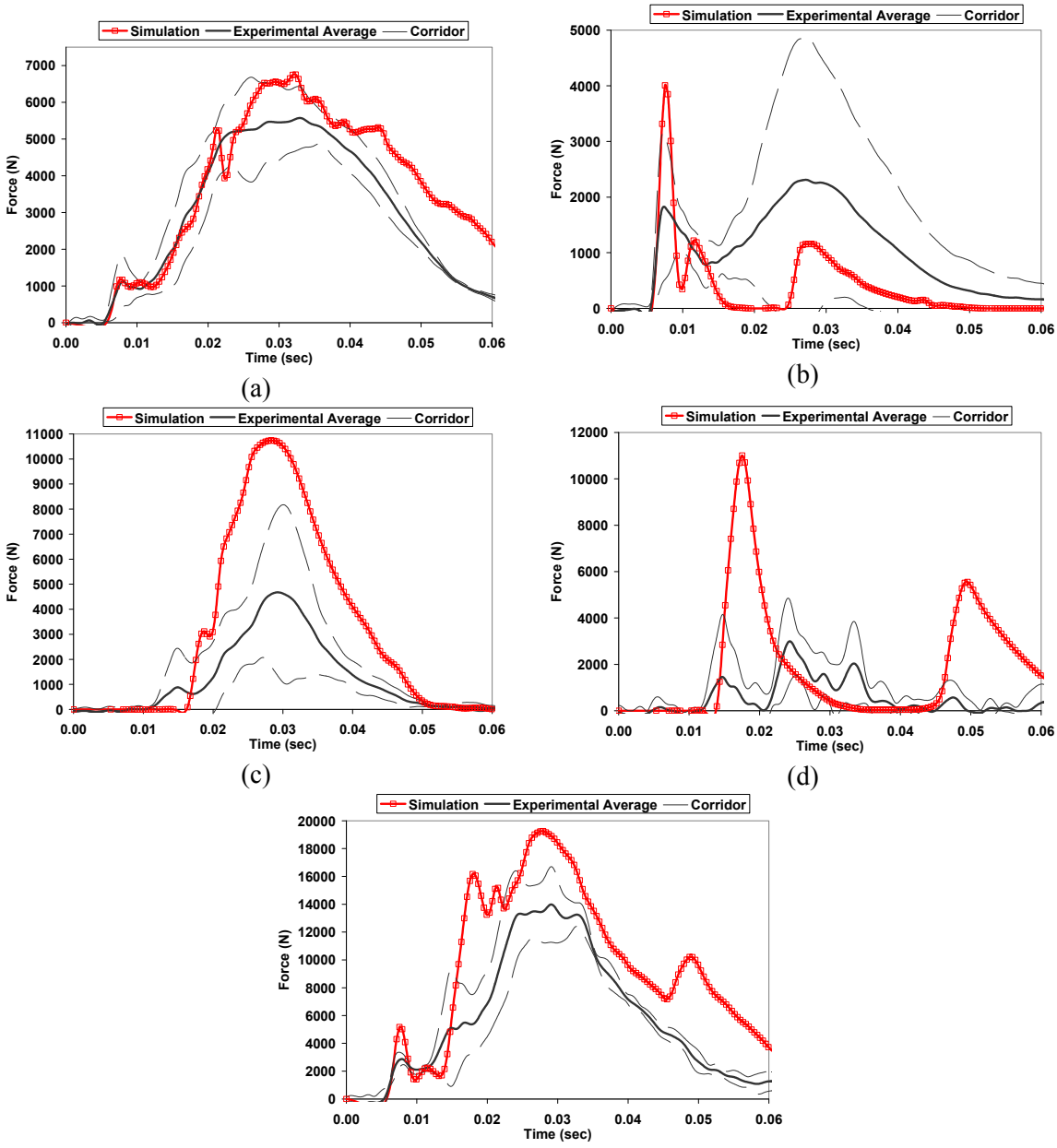

Figure 4.13: NHTSA sled impact at 6.67 m/s – force plate response

(a) thorax (b) abdomen (c) pelvic (d) lower limb (e) total

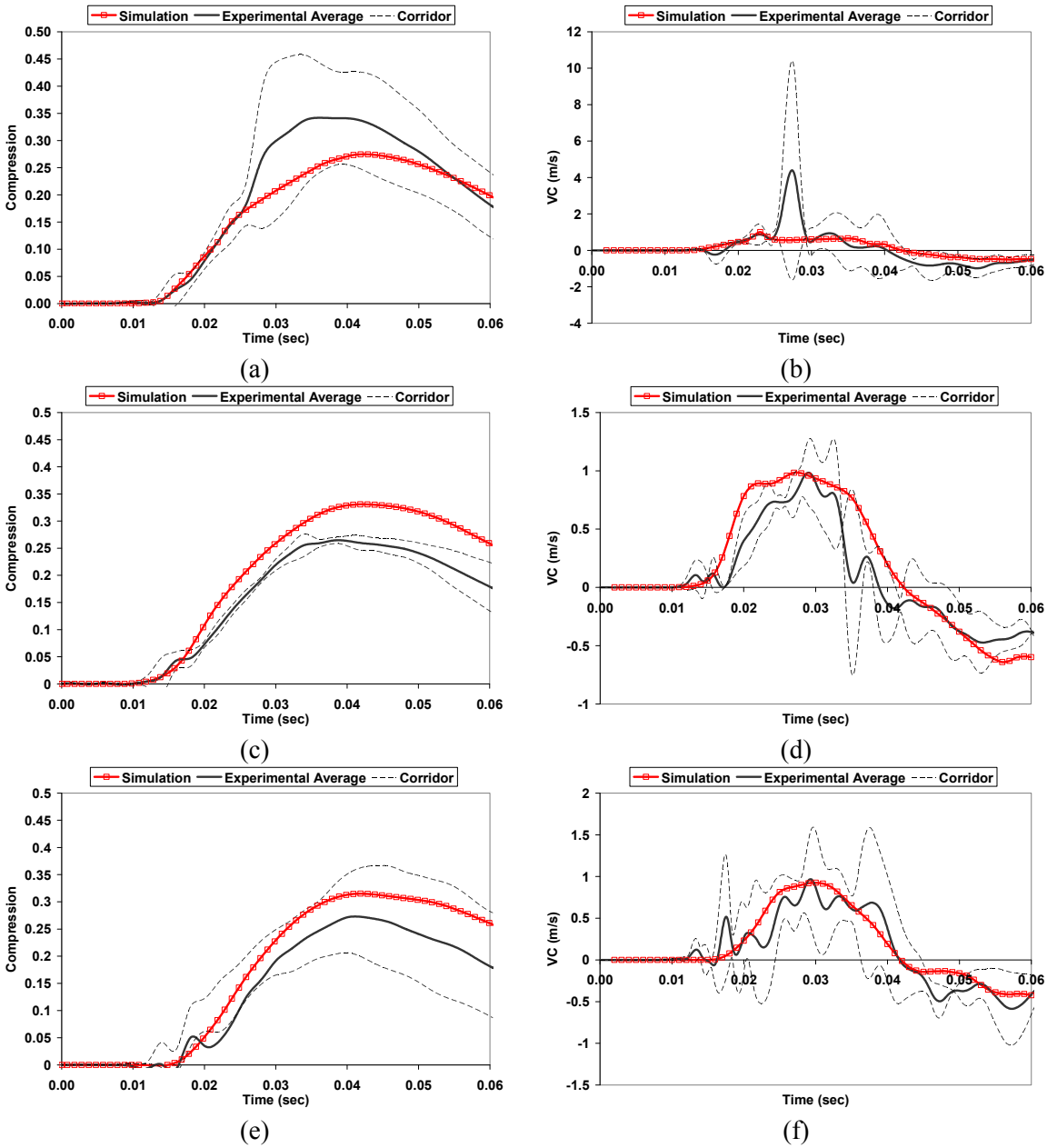

Figure 4.14: NHTSA sled impact at 6.67 m/s – compression and VC response (a,b) upper band (c,d) middle band (e,f) lower band

The model showed that the upper chest band under predicted deflection, the middle and lower chest bands showed reasonable deflection relative to the experimental data as shown in Figure 4.14 (a), (c), and (e). The peak VC for middle and lower band were in agreement to the experimental results. The upper band in the 6.67 m/s experiment

showed an atypical rise during the onset of the peak compression, resulting in a higher VC as shown in Figure 4.14 (b). The upper chest band wrapped around the chest just under the axilla (at the 4th rib level). The chest band might slide towards the axilla superiorly along the ribcage which may abruptly elevate the chest compression measurements since the surrounding area is made up of primarily fat tissue and the ribcage is conical in shape. This discrepancy was confined to the test subject 3120 for the 6.67 m/s impact where the experimental peak VC was calculated to be 11.3 which skewed the experimental average. The experimental averages for the medium velocity (6.67 m/s) and high velocity (8.89 m/s) scenarios were 4.39 and 1.54, respectively. From the simulation, the upper chest band was laterally aligned with the upper edge of the thorax plate. The momentum would carry the upper body over the upper edge of the thorax plate, and drive the shoulder upward.

Rib Fracture Prediction

The simulation predicted rib fracture from the 1st to 9th rib as summarized in Table 4.19. Only rib fractures on the impact (left) side of the thorax were tabulated. One of the three PMHS did not sustain any skeletal injury; the other two PMHS sustained flail chest. The simulation predicted flail chest from the 4th to 8th rib.

Table 4.19: NHTSA sled impact 6.67 m/s – rib fracture summary

Rib	PMHS			Simulation
	3120	3122	3155	
1				2
2	2		2	1
3	3		2	1
4	3		2	2
5	3		2	2
6	2		1	2
7	2		1	2
8			1	2
9				1
Non-impact side	1	0	0	0
Total	16	0	11	15

4.7.1 High Velocity Sled Impact

The NHTSA and WSU sled tests were simulated with a higher impact velocity of 8.89 m/s. Impacts at this velocity are aggressive in nature and typically resulted in severe injuries at AIS equal or greater than 4. The intent here was to demonstrate model applicability at high velocity. The overall force response from both tests was consistent with the experiment. Similar deficits were identified as in the previous medium speed (6.67m/s) sled test results; the force response was low in the abdominal region and high in the pelvic region. The model can become numerically unstable at this impact velocity due to excessive deformation of the ribcage especially when the ribs sustained multiple fractures. When the numerical model was tested against a wider range of impact velocities, it demonstrated the need for a rib material model that possessed strain-rate dependency. Without the implementation of a strain-rate dependent material model, ribs would fracture and lose structural integrity prematurely resulted in low force response and excessive ribcage deformation.

In both sled studies, the compression and VC response were in good agreement. The abdominal and pelvic force shapes in the WSU simulation were poor although the peak response of the abdominal region was in good agreement. The model response in the NHTSA simulation demonstrated the lack of load bearing at the abdominal region, but the thoracic force response remained unaffected and behaved within the corridor. The force and deflection responses at the thorax region produced good agreement for both sled simulations, and the results are presented in Appendix A.

4.8 Sled Impact Summary

The applicability of the human body model was evaluated across different complex sled impact scenarios and demonstrated good or reasonable correlation for all impacts. Table 4.20 and Table 4.21 summarize the simulated force and compression response correlation with the experimental data, respectively. The thoracic response, in particular, was characterized good or reasonable for all cases. Poor ratings were associated with the

lower leg and pelvic response. Despite the poor responses in these two regions, they had minimal effect on the thoracic response. Overall, the model response had greatly improved over the previous human body model particularly in the chest compression response, rib fracture predictions and numerical stability.

The assumptions needed to be address at the abdominal, pelvic, and lower limb regions to improve the overall model biofidelity. The anthropometry of the abdominal region should be investigated to improve its interaction with the other regions during full body impact. The pelvis material model can be improved to better mimic the response during pelvic fractures and unloading. It was difficult to determine whether the poor lower limb response had to do with the experiment setup or the assumptions that were related to the modeling of the lower limbs.

Table 4.20: Sled impact – force correlation summary

Sled Test	Impact velocity m/s	Contact Plate	Loading	Peak	Unloading
WSU	6.67	Shoulder	Good	Good	Good
		Thorax	Good	Good	Good
		Abdomen	Poor	Good	Reasonable
		Pelvis	Reasonable	Reasonable	Reasonable
		Knee (1st peak)	Good	Reasonable	Good
		Knee (2nd peak)	Poor	Poor	Poor
NHTSA	6.67	Thorax	Good	Good	Reasonable
		Abdomen	Good	Good	Good
		Pelvis	Reasonable	Reasonable	Poor
		Lower limb (1st peak)	Poor	Poor	Poor
		Lower limb (2nd peak)	Poor	Poor	poor

Table 4.21: Sled impact – compression correlation summary

Sled Test	Impact velocity m/s	Contact Plate	Loading	Peak	Unloading
WSU	6.67	Thorax	Good	Good	Good
NHTSA	6.67	Upper	Good	Good	Reasonable
		Middle	Reasonable	Reasonable	Reasonable
		Lower	Good	Good	Good

Given the aggressiveness of high speed sled impacts, the current model results produced conservative response estimates. Table 4.22 and Table 4.23 summarize the simulated force and compression response correlations with the experimental data, respectively. Overall, the model response had greatly improved over the previous model, particularly in the chest compression response. The human body model was more biofidelic in the NHTSA scenario than the WSU scenario, particularly in the lower body and limb regions. This may be related to the larger contact plates in the NHTSA scenario which provided a more robust and distributed boundary condition.

Table 4.22: High speed sled impact - force correlation summary

Sled Test	Impact velocity m/s	Contact Plate	Loading	Peak	Unloading
WSU	8.89	Shoulder	Good	Good	Good
		Thorax	Good	Good	Good
		Abdomen	Poor	Good	Poor
		Pelvis	Poor	Poor	Good
		Knee (1st peak)	Good	Poor	Good
		Knee (2nd peak)	Reasonable	Good	Reasonable
NHTSA	8.89	Thorax	Good	Good	Reasonable
		Abdomen	Good	Reasonable	Reasonable
		Pelvis	Good	Reasonable	Good
		Lower limb (1st peak)	Reasonable	Reasonable	Reasonable
		Lower limb (2nd peak)	Good	Good	Good

Table 4.23: High speed sled impact - compression correlation summary

Sled Test	Impact velocity m/s	Contact Plate	Loading	Peak	Unloading
WSU	8.89	Thorax	Good	Good	Good
NHTSA	8.89	Upper	Good	Good	Good
		Middle	Good	Good	Good

The improvements in the chest compression among the sled simulations had to do with the arm placement which was more representative of the experimental setup. With the voids within the thorax removed, improved the rib and coastal cartilage material models, the overall thoracic response was consistent regardless of impact direction. It was clear that rib fracture predictions and torso shape response can be further improved by accounting for geometrical variation between different rib sections.

Chapter 5
Numerical Modeling of Pulmonary Contusion

5.1 Introduction

The focal point of the current model development was to predict internal organ response and injury. Much of the injury evaluation approach in the past was often confined to a global-based injury criterion, as in a global measure of a single point (the direct or derived measure of displacement, velocity, acceleration) or two points (the measure of relative displacement, velocity, acceleration). The measure was typically dependent on the direction of the impact. The measurements were correlated to the probability of an overall injury risk. Some commonly recognized global thoracic injury criteria include acceleration criterion, compression criterion, force criterion and the viscous criterion.

A local based injury evaluation required different sense of thinking and tied the evaluation method to a specific injury. In the current study, the model was applied to predict pulmonary contusion, which is a parenchymal damage occurring at a microscopic level resulting in interstitial edema and capillary hemorrhage. The current study explored the relationship between loading conditions to the pulmonary contusion by evaluating injury severity quantitatively through various finite element-based injury metrics. In essence, a local based injury evaluation was a three step evaluation approach. The first step was to evaluate injury at small increments of volume within an organ. The second step was to evaluate the injury risk to the lung based on the cumulative volume that is predicted to be contused. The third step was to evaluate overall injury threat to life based on the cumulative volume in both lungs.

The current study explored three areas that require development. First was to determine representative material parameters and investigate the feasibility of using the constitutive material model to capture dynamic response of the lung (Chapter 3). Second was to

explore various localized injury metrics, to understand response sensitivity to the impact conditions and the evaluation method. Third was to subject the human body model to various impact conditions and evaluate the local injury correlation to the global injury predictors such as viscous criterion. The latter two aspects are discussed in this chapter.

The background related to the lung anatomy, physiology, and injury mechanisms of pulmonary contusion are described in Chapter 2. The following sections describe the development in the injury mechanism, mechanical response of the lung tissue, human tolerance, and the finite-element based injury evaluation approach that pertained to lung contusion prediction.

5.2 Finite Element Based Injury Evaluation Approach

The conceptual method to evaluate pulmonary contusion was divided into three steps as shown in Figure 5.1. The concept consisted of evaluating response at the local level, at the whole organ level and the cumulative response with respect to both lungs.

The first step was to evaluate the organ in terms of small increments of elements that represent a small volume of tissue, and predict the stress and strain in each element during an impact scenario. A local injury metric was used to gauge the injury severity of an element. The elements were evaluated and classified as injured or not based on a local injury threshold. The results were summed in terms of contused volume per lung in the second step. The volumetric based injury metric was used to estimate whether the lung can function based on the predicted sustained injury. The third step was to evaluate the injury severity based on the cumulative injury sustained by both lungs and classify the associated lung contusion AIS level.

The AIS level described lung injury in terms of lobes; however there was a lack of anthropometric data that quantify lobe size and shape. As such, the current approach of evaluating pulmonary contusion was restricted to quantifying contusion with respect to each lung. The AIS severity level was evaluated by the author based on whether majority of the contusion was restricted to one lobe or more.

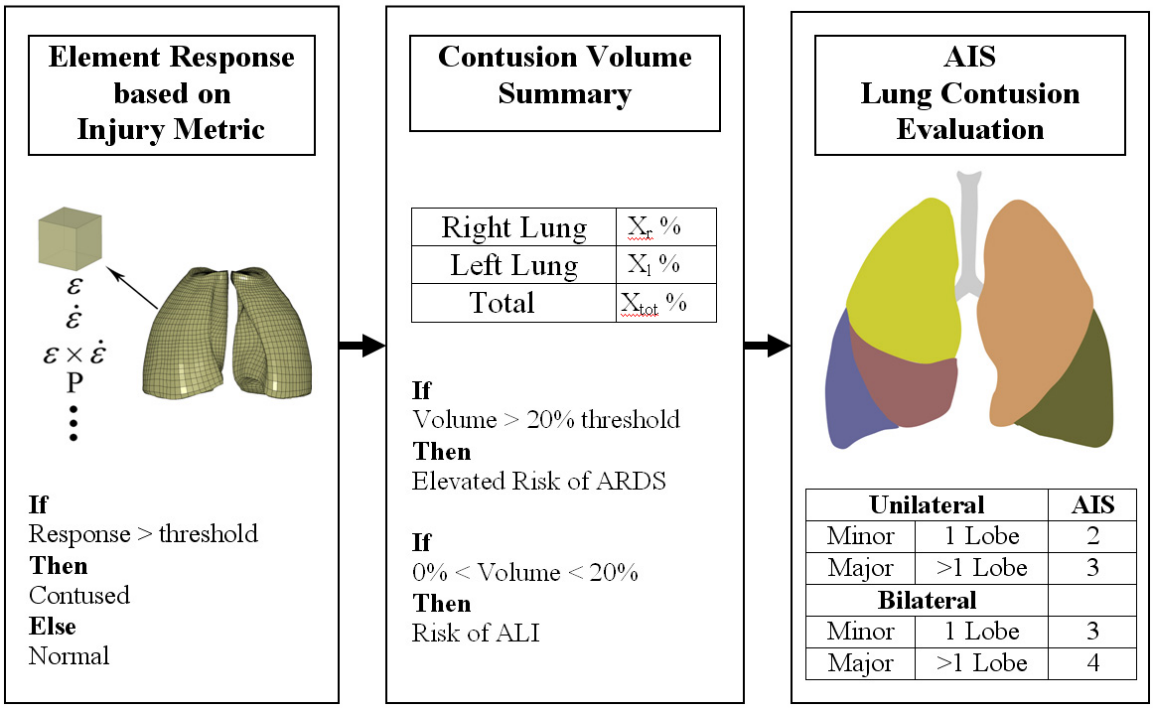

Figure 5.1: Finite-element based injury evaluation approach

Miller et al (2001) suggested that there was a high risk of developing the acute respiratory distress syndrome when the lung contusion cumulative volume was over 20%. It was assumed in this study that the 20% lung contusion was correlated to an AIS level of 3 and be used to establish injury thresholds. This is discussed in a later section.

5.3 Proposed Injury Metrics

The development of a numerical human body model served as a tool for researchers to understand injury mechanisms. However, selecting a numerical injury predictor that correlates with a localized injury requires extensive research experimentally and numerically. For the purpose of evaluating contused volume after impact, the injury metric has to quantitatively correlate the microscopic damage of the lung tissue to the macroscopic representation of the lung tissue in the numerical model. The microscopic damage is referred to the parenchymal damage at the alveolar structure such as alveolar duct, interalveolar septa, blood vessels, etc. The lung tissue modeled in a macroscopic sense is referred to the stress and strain measure over a small volume; the volume is small

when compared with the overall dimensions of the lung structure, but is large when compared with the individual alveolus (Fung, 1978).

The hypothesis proposed by Fung et al (1988) was still the most descriptive theory on the lung injury mechanism to date. Microscopically, the damage to the epithelial membrane of the alveolar wall changed its permeability and led to edema, or to the extent that the endothelium and epithelium would leak larger solute such as blood. The tentative injury metric by Fung et al (1988) was maximum principal strain. From their experiments, they demonstrated that transient stretch of the lung correlated with edema or hemorrhage. There were two hypotheses that would induce tensile strain in the alveolar walls. One was based on the macroscopic dynamic response of the lung and the other was based on the microscopic response of the alveoli. When a lung is compressed, some airways collapse while the alveoli around them remain open leading to gas trapping. When a compressive stress wave passes as the expansion wave arrives, the pressure difference can cause the alveoli to expand which puts the alveolar walls in tension. This was believed to be the mechanism where the macroscopic compressive stress could induce microscopic tensile stress in the alveolar walls.

Since the current study was a macroscopic continuum model of the lung tissue, it could not directly investigate stress and strain at the alveolar level. However, the induced stress wave from the impact loading that was often seen in an automotive crash could be observed through the numerical model. The features of the stress wave were found to be a significant aspect of the lung injury. The hemorrhagic injury in the lung were found to be localized and were usually most severe next to the spine, heart, ribs or at the edges of lobes (Yen, 1988). Yen (1988) also suggested the importance of the wave features of the phenomena: high stress concentration, focusing, reflection, and localization.

Stitizel et al (2005), and Gayzik et al (2007, 2008) investigated a rat model to correlate experimental impacts with pulmonary contusion measured through the CT scan data. A finite element model was developed to investigate lung tissue response in parallel.

Various candidate injury metrics were evaluated (Gayzik et al, 2007). The instantaneous product of maximum principal strain and its strain rate correlated well as a predictor for contused lung tissue. It should be one of the ideal injury metrics because the basis formulation is similar to the viscous criterion, where the deformation and the velocity of the deformation are taken into account. The maximum principal strain and the maximum principal strain rate were also found to provide reasonable correlation independently.

Stuhmiller et al (1988) and Josephson et al (1988) suggested the existence of a dynamic pressure threshold which lung trauma might occur. Cronin (2004) and Greer (2005) quantified different levels of injury in the lungs under blast environment by evaluating dynamic pressure in the lung tissue through their FE model. The pressure thresholds were developed through FE analysis by comparing model response to the injury outcome of the experiments by Bowen (1968) where sheep were subjected to blast loading. A relationship between dynamic pressure and injury was established (Salisbury, 2006).

In the current study, four candidate injury metrics for lung contusion were considered as shown in Table 5.1. The numerical aspects of these injury metrics were also investigated through a mesh convergence study in the following section.

Table 5.1: Candidate injury metrics for pulmonary contusion

$\varepsilon_{\max}$	First principal strain
$\dot{\varepsilon}_{\max}$	First principal strain rate
$\left(\varepsilon \times \dot{\varepsilon}\right)_{\max}$	Instantaneous product of first principal strain and first principal strain rate
$P_{\max}$	Dynamic or transient pressure

5.4 Lung Convergence Study

A lung mesh convergence study was undertaken to assess mesh dependence and response under representative loading conditions. A 160 mm diameter, 80 mm length cylinder of lung material was deformed with a prescribed velocity 6.5 m/s to provide 50% nominal deformation within 20 ms, to simulate typical impact conditions. The model response was

investigated for four different element sizes (2.5 mm, 5 mm, 10 mm, and 20 mm). Distribution of element response in terms of volume percentage was compared in terms of pressure, principal strain, and principal strain rate as shown in Figure 5.2. For each response metric, a corresponding cumulative volume fraction represented the percentage of elements that had a peak response at that level or lower.

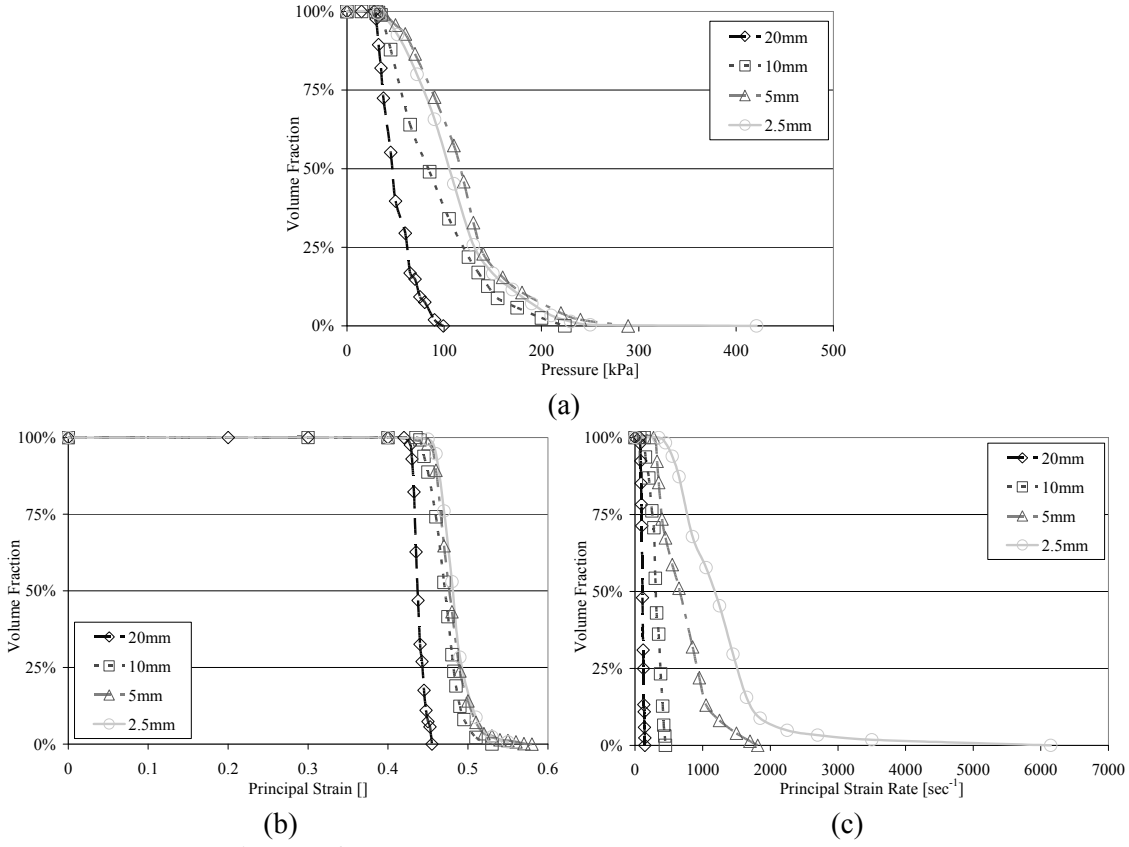

Figure 5.2: Mesh convergence study - response results

(a) dynamic pressure (b) principal strain (c) principal strain rate

The results showed that the range of peak principal strain response was relatively small, with a trend towards convergence with smaller element size. Principal strain rate became less linear with a trend toward higher peak response with smaller element size. The local deformation of a low wave speed material was expected to be mesh dependent. In contrast, the dynamic pressure demonstrated a consistent trend when elements were smaller than 10 mm.

This convergence study concluded that the response can be highly dependent on mesh density, with principal strain and pressure response being least dependent and principal strain rate being most dependent on element size. The corresponding injury predictions would also show the same dependencies, and must be considered when selecting an injury metric. Based on these results, the lungs were meshed with an average element size 8 mm with maximum element size no larger than 10 mm. This ensured consistency in response prediction based on the convergence of the peak dynamic pressure.

5.5 Injury Thresholds

Determining an injury threshold was fundamental to the development of the injury evaluation by enabling direct comparison between different injury metrics. Since the injury metrics are outputs, the variation on the injury thresholds only alter the interpretation of an injury but not the mechanical response to a given loading condition. A reference set of thresholds should be established based on a specific impact condition to enable interpretation of lung injury across different impact conditions. It should provide relative significance between different impact conditions although the absolute response may change with the improved understanding of the material properties, boundary conditions, or various factors that influence the absolute outcome. It was assumed that the pulmonary injury did not alter material response during the impact event and the time scale for injury development was longer than the transients of the impact event. Care should be taken when interpreting these thresholds since the mesh convergence study showed that the response changes with mesh density, therefore the threshold associated with a particular mesh would also change.

In Yuen et al (2008), the oblique lateral blunt pendulum impacts utilized by Viano (1989b) were chosen to establish the candidate injury metric thresholds because the input energy was clearly defined. The proposed thresholds for all candidate injury metrics were determined based on the 6.7 m/s pendulum impact scenario where the resultant AIS was 3 with a 50% probability. Miller et al (2001) suggested that there was a high risk of developing the acute respiratory distress syndrome when the lung contusion cumulative

volume exceeded approximately 20%. In the current study, the candidate metric threshold values were set to have corresponding 20% contusion volume for this impact case by hypothesizing that the resultant contusion level was equivalent to an AIS level of 3. The following table summarizes the injury thresholds that were used to evaluate contusion volume for various impact scenarios.

Table 5.2: Proposed injury thresholds

Candidate Injury Metric	Injury Threshold
Principal Strain	0.780
Principal Strain Rate [s^{-1}]	243
Strain*Strain Rate [s^{-1}]	103
Pressure [kPa]	52.4

5.6 Data Analysis

The maximum principal strain, the maximum principal strain rate and dynamic pressure for each element in the model were monitored at 40000 Hz to ensure adequate resolution for capturing peak pressure and strain rate. The simulated impact cases were ran in LS-Dyna version 971.1224 (Livermore, CA) for minimum of 60 ms, the element data were processed using LS-Prepost at each time points. The post-processed data were unfiltered. For a given metric, elements whose value was either above or below a threshold were partitioned into two respective groups: one represented contused lung parenchyma, and the other represented normal uninjured lung parenchyma.

Eight impact cases were examined as part of the lung contusion investigation, as summarized in Table 5.3. These impact cases were previously used as part of the whole model comparison as discussed in Chapter 4. The oblique pendulum impact, WSU style sled and NHTSA style sled cases were chosen since they demonstrate injury response at different impact velocities. The frontal pendulum impact and limited-stroke lateral pendulum impact were considered to explore the lung response with respect to different impact directions.

Table 5.3: Impact scenarios used for pulmonary contusion investigation

Impact Scenarios	Initial Impact Velocity	References
Frontal pendulum impact	6.7 m/s	Kroell et al (1974)
Oblique pendulum impact	4.3 m/s and 6.7 m/s	Viano et al (1989)
Limited-stroke lateral pendulum impact	Prescribed velocity profile (5.6 m/s)	Chung et al (1999)
WSU-style sled	6.7 m/s and 8.9 m/s	Cavanaugh et al (1993)
NHTSA-style sled	6.7 m/s and 8.9 m/s	Pintar et al (1997)

5.7 Simulated Results

The first principal strain, first principal strain rate, the product of principal strain & strain rate and dynamic pressure for each element were monitored for the eight simulated test cases. Table 5.4 and Table 5.5 summarize the lung contusion volume prediction for the pendulum impact scenarios and the sled impact scenarios, respectively. Table 5.6 summarizes the lung contusion with respect to both lungs for each metric. For pendulum type scenarios, the right lung was referred as the struck side. For sled type scenarios, the left lung was referred as the struck side. Figure 5.3 shows the graphical response of the human body model and the internal organ motion.

Results indicated that all the metrics predicted only modest damage levels for the non-struck side for the pendulum type scenarios (excluding frontal impact). The oblique pendulum 4.3 m/s case and the limited-stroke lateral pendulum impact case both registered little contusion. The lung contusion was fairly distributed over both lungs in the frontal pendulum impact case as predicted by all four metrics. For the WSU style sled scenarios 6.7m/s and 8.9m/s, the predicted contusion total volumes were relatively consistent among the candidate injury metrics except the principal strain predicted less than the other three metrics for both impact velocities. The predicted contusion total volumes by the various candidate injury metrics in WSU sled impact scenarios were more convergent than the NHTSA sled impact scenarios.

The analysis on the results of the oblique pendulum 6.7 m/s and the NHTSA sled 6.7 m/s impact scenarios are presented here in greater detail. Lung response results of the other simulated scenarios are presented in Appendix B.

Table 5.4: Individual lung contusion volume summary, pendulum impacts

	Frontal Pendulum		Oblique Pendulum 4.3m/s		Oblique Pendulum 6.7m/s		Limited-stroke lateral pendulum	
	Left	Right	Non-struck (Left)	Struck (Right)	Non-struck (Left)	Struck (Right)	Non-struck (Left)	Struck (Right)
ε_{max}	10%	15%	0%	3%	0%	37%	0%	0%
$\dot{\varepsilon}_{max}$	38%	33%	1%	3%	8%	30%	0%	5%
$(\varepsilon \times \dot{\varepsilon})_{max}$	21%	23%	0%	1%	3%	35%	0%	0%
P_{max}	40%	39%	0%	6%	4%	34%	0%	10%

Table 5.5: Individual lung contusion volume summary, sled impacts

	WSU sled 6.7 m/s		WSU sled 8.9 m/s		NHTSA sled 6.7 m/s		NHTSA sled 8.9 m/s	
	Struck (Left)	Non-struck (Right)	Struck (Left)	Non-struck (Right)	Struck (Left)	Non-struck (Right)	Struck (Left)	Non-struck (Right)
ε_{max}	73%	16%	94%	48%	53%	5%	90%	37%
$\dot{\varepsilon}_{max}$	70%	27%	99%	66%	64%	12%	100%	63%
$(\varepsilon \times \dot{\varepsilon})_{max}$	77%	22%	100%	61%	66%	6%	99%	57%
P_{max}	80%	19%	100%	65%	90%	15%	97%	82%

Table 5.6: Overall lung contusion volume summary, all impacts

	Frontal pendulum	Oblique pendulum 4.3m/s	Oblique pendulum 6.7m/s	Limited-stroke lateral pendulum	WSU sled 6.7m/s	WSU sled 8.9m/s	NHTSA sled 6.7m/s	NHTSA sled 8.9m/s
ε_{max}	13%	2%	20%	0%	43%	69%	27%	61%
$\dot{\varepsilon}_{max}$	35%	2%	20%	3%	47%	81%	36%	80%
$(\varepsilon \times \dot{\varepsilon})_{max}$	22%	1%	20%	0%	48%	79%	34%	76%
P_{max}	40%	3%	20%	6%	47%	81%	50%	89%
Exp. Avg. VC_{max}	1.41	0.62	1.10	0.47	1.56	1.44	1.06	3.00
Exp. AIS	4	0-2	2-3	3	4	4	0-4	2-4
Simulated VC_{max}	1.11	0.40	1.01	0.39	1.26	2.13	0.98	2.00
Predicted Lung AIS*	3-4	0	3	0	4	4	4	4

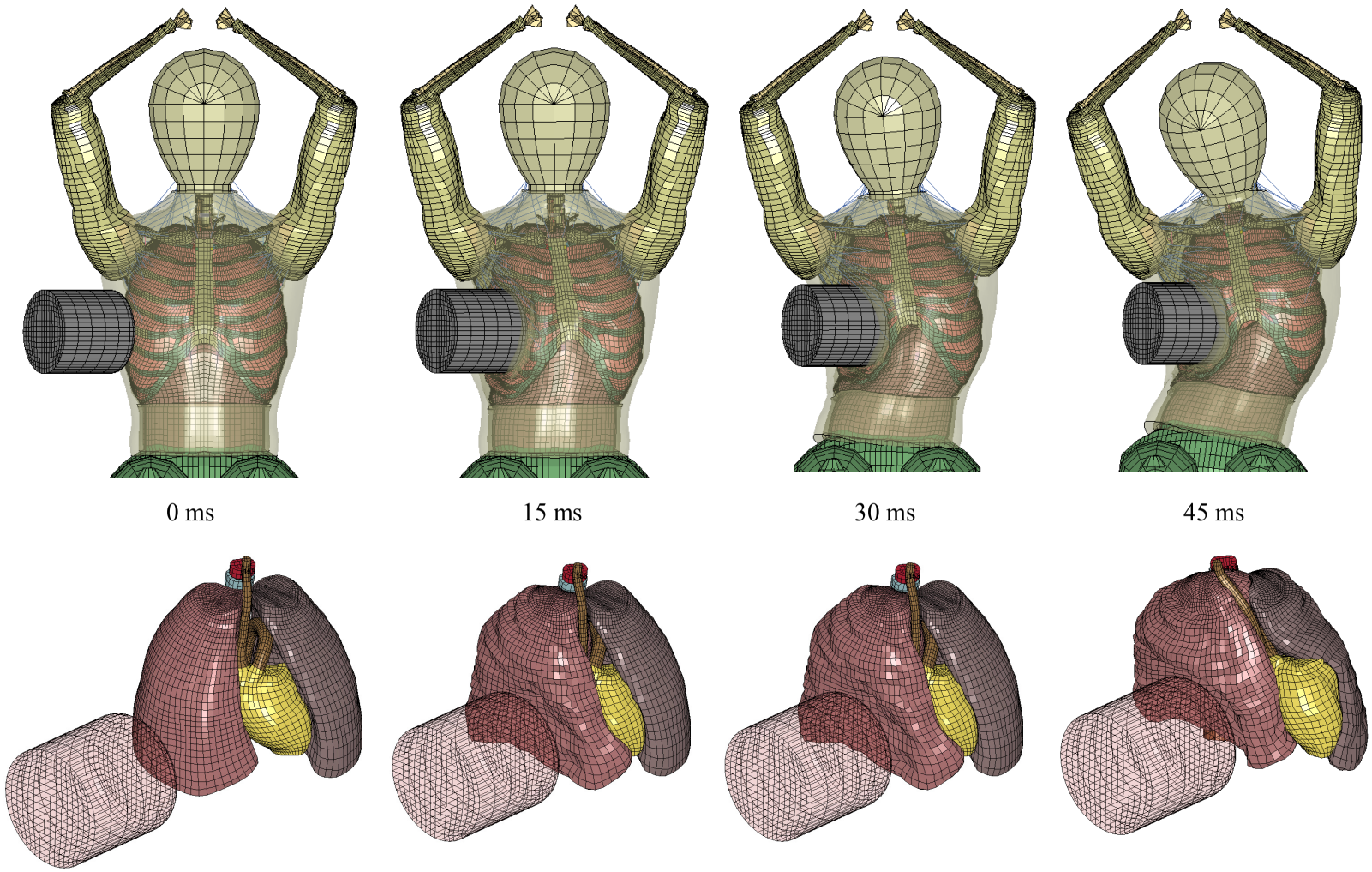

Figure 5.3: Time-lapsed model displacement during oblique pendulum impact simulation

Figure 5.4 shows the response distribution in terms of cumulative percentage volume for the four candidate injury metrics for oblique pendulum 6.7m/s. Figure 5.4 (a) shows the first principal strain response, (b) shows the first principal strain rate, (c) shows the maximum of the instantaneous product of principal strain and its strain rate, and (d) shows the dynamic pressure. Figure 5.5 shows the response distribution for the NHTSA sled 6.7m/s scenario. For each response metric, the percentage was referred to the cumulative volume of the elements that achieved a peak response or higher. The response shape can be segmented into three sections: non-linear, approximate linear, and non-linear. The non-linearity became more apparent and amplified with more severe loading.

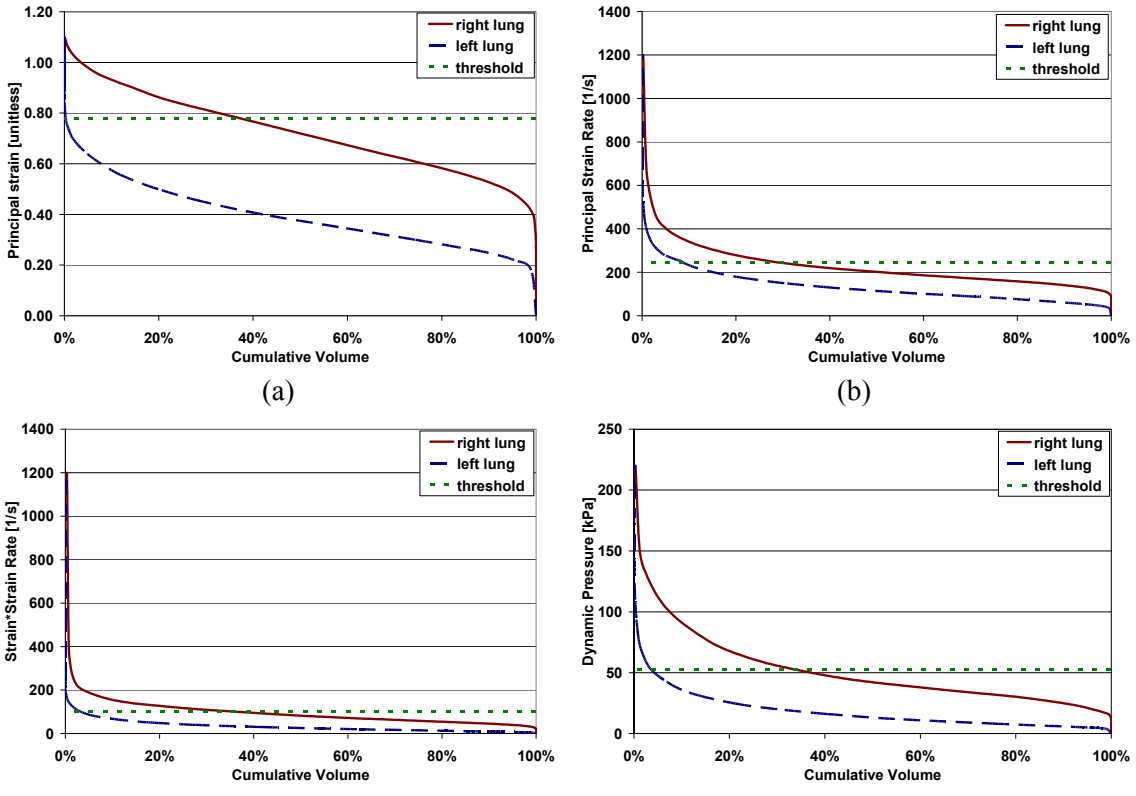

Figure 5.4: Peak response distribution for oblique pendulum 6.7m/s

a) Principal strain b) Principal strain rate c) Instantaneous product of principal strain and its strain rate d) Pressure

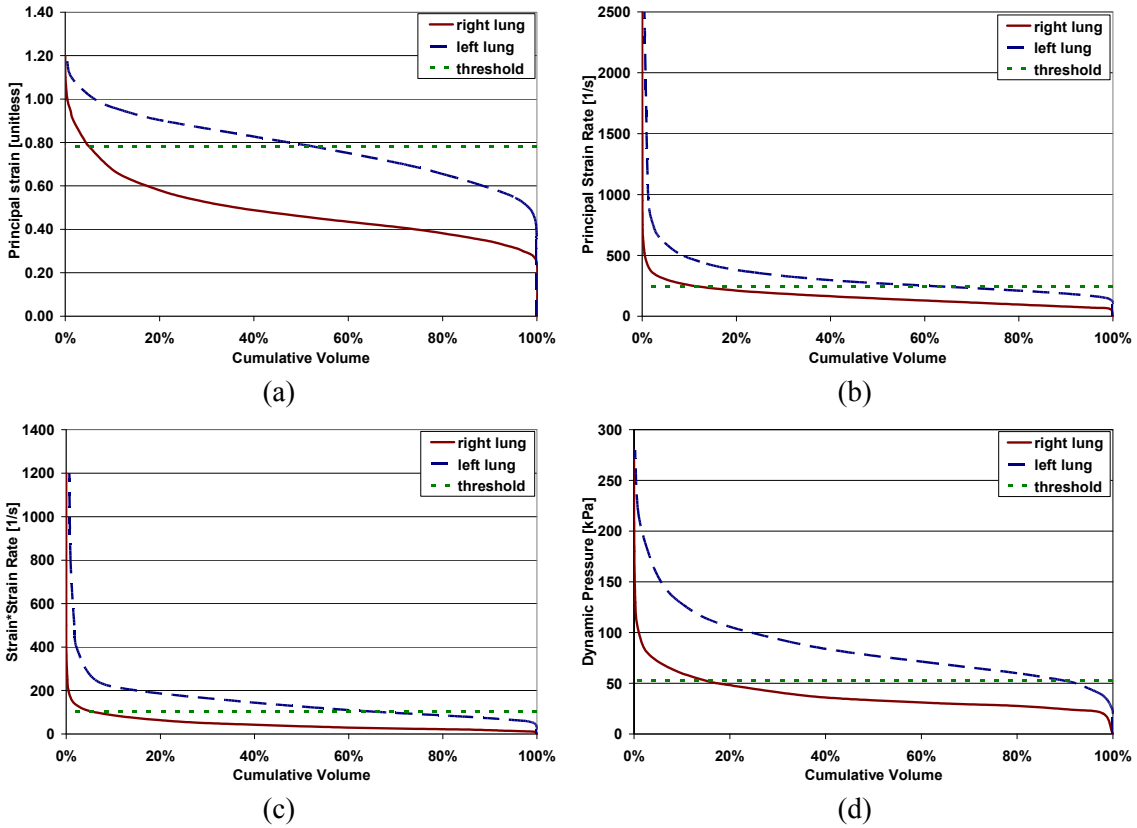

Figure 5.5: Peak response distribution for NHTSA sled 6.7m/s

a) Principal strain b) Principal strain rate c) Instantaneous product of principal strain and its strain rate d) Pressure

Figure 5.6 shows the predicted lung contusion map of the lungs for the reference oblique pendulum 6.7m/s impact scenario where each metric response map was correlated to 20% contusion volume. Figure 5.6 (a) shows the struck side of the lung based on the principal strain metric, where the peak responses were primarily at the basal section of the lung along the impact direction. Figure 5.6 (b) is based on the principal strain rate metric where the primary injury site was near the surface of the struck face, the secondary injury site was at the surface along the spine. Small patchy contused sections were distributed near the surface of the lung. Figure 5.6 (c) shows the response of the product of strain and strain rate where the primary site was a combination of (a) and (b), primarily at the basal section along the impact direction with various patchy contused sections near the

surface. Figure 5.6 (d) shows the primary injury sites are at the surface of the lung near the struck face, and opposite side of the struck face.

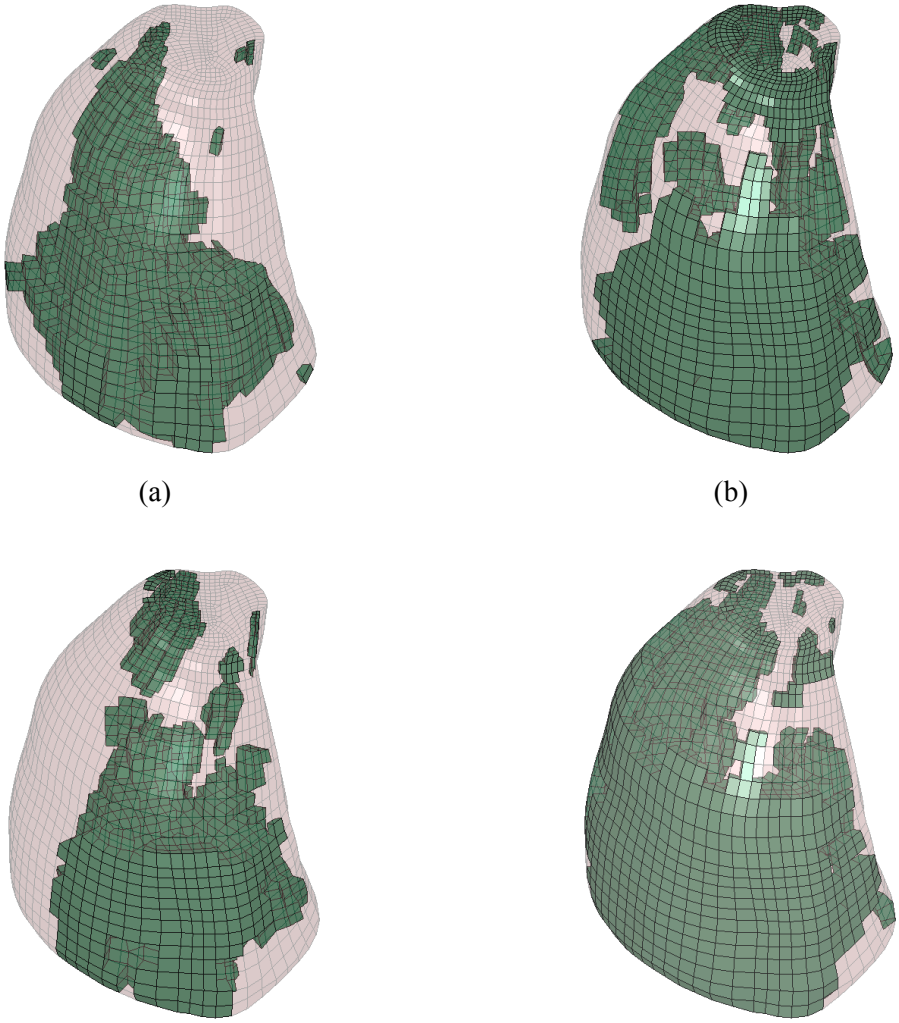

(a) (b)

(c) (d)

Figure 5.6: Lung contusion pattern for oblique pendulum 6.7m/s

a) Principal strain b) Principal strain rate c) Instantaneous product of principal strain and its strain rate d) Pressure

Figure 5.7 shows the predicted lung contusion map NHTSA sled 6.7 m/s impact scenario. Figure 5.7 (a) shows the primary injury site was at the basal section of the struck lung along the impact direction and surrounding the heart, and secondary site was at the posterior section of the lung along the spine. Figure 5.7 (b) shows the primary injury site

was the surface of the struck lung, the secondary injury site was near the surface that contacts with the spine and aorta. Small patchy contused sections were distributed near the medial surface of the non-struck lung. Figure 5.7 (c) shows the response of the product of strain and strain rate where the primary site was a combination of (a) and (b), primarily at the basal section along the impact direction and various patchy contused sections near the apical surface. Figure 5.7 (d) shows the struck lung was almost fully contused except an apical section deep in the surface and a few small anterior sections; the surfaces of the non-struck lung along the impact direction were contused.

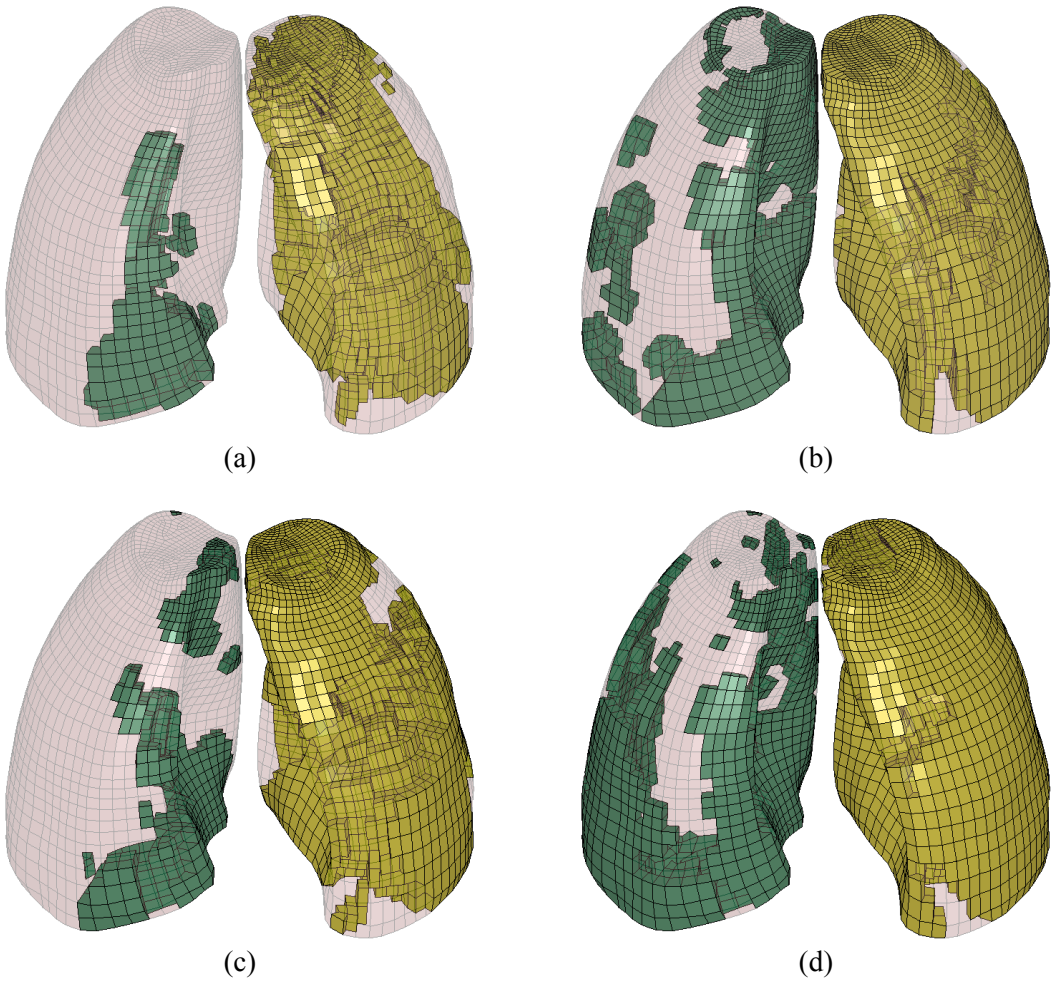

Figure 5.7: Lung contusion pattern for NHTSA sled 6.7m/s

a) Principal strain b) Principal strain rate c) Instantaneous product of principal strain and its strain rate d) Pressure

5.8 Discussion

Table 5.7: Proposed injury thresholds summary

Candidate Injury Metric	Injury Threshold			
Principal Strain	.525	.780	.154	.284
Principal Strain Rate [s^{-1}]	311	243	304	470
Strain*Strain Rate [s^{-1}]	95.0	103	28.3	94.5
Pressure [kPa]	157	52.4		
Reference	Yuen (2008)	Current Study	Gayzik (2007)	Gayzik (2008)

The proposed injury thresholds from various studies were summarized in Table 5.7. Although there were differences in terms of material parameter development, loading conditions, species, assumptions, filtering, etc, the differences between different thresholds can be attributed to few primary factors. In the study by Gayzik (2007), the material parameters and injury thresholds were determined based on a single impact scenario, where as in the study by Gayzik (2008) were based on different impact velocities and compression. As such, the thresholds changed due to greater understanding on the loading condition and corresponding injury results. In the study by Yuen (2008), the material parameters used were considered a stress-free material model. In the current study, the material parameters were adjusted to be an in-situ material model. In both cases, injury thresholds were determined with respect to the oblique 6.7m/s impact that corresponded to 20% contused lung volume. During the model development, the differences in threshold values were greatly dependent on one parameter, the bulk modulus. Similar conclusion was drawn by Gayzik (2008) based on the sensitivity analyses on the material parameters. As discussed in Chapter 3, the bulk modulus should take a non-linear form with respect to deformation. The effective bulk modulus used in the study by Yuen (2008) was approximately 9.2 times higher than the bulk modulus in the current study. The bulk modulus influenced the principal strain and pressure thresholds considerably when the current study was compared to the study by Yuen (2008), however the differences in the product of strain and strain rate threshold was only modest.

Candidate Injury Metrics

From the current study, it was clear that the principal strain predicted a different form of pulmonary contusion pattern compared to the other candidate injury metrics. Qualitatively, the primary injury sites for the principal strain rate and the dynamic pressure metrics were similar in ways that the contused tissue was typically predicted near the surface of the lung. The product of strain and strain rate predicted a combination of surface contusion and contusion along the impact direction. In all cases, small patchy contused sections existed in no particular pattern. Given that there was no study that quantified and investigated contusion patterns in trauma patients, it would be difficult to judge which metric was best at predicting contusion. A controlled approach to quantify lung contusion from trauma patients was still under development (Daly, 2008); future studies are needed in this area can better reveal which injury metric best predict the injury pattern as those observed in blunt chest trauma.

Global Injury Criterion Correlation

Historically, the viscous criterion was developed with the intention to predict soft-tissue injury. In the oblique pendulum 6.7m/s impact case, the simulated VC_{max} was 1.01. In the NHTSA sled 6.7m/s impact case, the middle chest band simulated a VC_{max} of 0.98. However, the contusion volume was considerably more severe in the sled test than the pendulum test as predicted by all four metrics. This study had showed the difficulty in correlating soft-tissue injury such as pulmonary contusion to a global injury criterion. Injury level was dependent whether the blunt trauma was localized or distributed over a large area. The direction of the impact would alter the stress transmission between the lungs, thus altered the contusion level. This emphasized the need to develop a method to evaluate injury locally where the injury threshold is not specific to a loading direction.

Stress Wave Behavior

It was evident from this study that the features of stress wave focusing, refraction and reflection played a role in the elevated metric response near the surface of the lung and near rigid boundary such as the spine. The simulation demonstrated the focusing feature

of stress waves that led to small patchy contused sections which was similar to the contusion found in trauma patients.

Injury Metrics and Injury Pattern Correlation

It was apparent that each injury metric predicted a different level of contusion and injury pattern. However, three candidate injury metrics (the principal strain rate, the product of strain and strain rate, and dynamic pressure) predicted similar level of contusion volume for the WSU sled impact cases at both impact velocities although the injury patterns were different. Fundamentally, each metric captured different aspects of the mechanical behavior of lung tissue. The principal strain captured the deviatoric aspect of the lung deformation. The principal strain rate captured the dynamic response of the lung deformation. The product of principal strain and strain rate captured the contribution of both effects. The dynamic pressure captured the hydrostatic response of the lung tissue due to the dynamic loading. The current model is capable of capturing the implosion and spalling effects where it correlates to the tensile stretching of the lung tissue, where the pressure differential effect is captured by the dynamic pressure. However, the injury metric that best correlates with the injury mechanism still needs further investigation.

The intent of this model was to predict the primary features of the lung response and the effects of the proposed injury mechanisms. The effect of the injury mechanism to the injury mechanism is analogous to describing the symptoms of a sickness rather than the cause of the sickness in medical terms. It should be emphasized again that the current model described the macroscopic mechanical response over a small volume of lung tissue which encompassed a number of alveoli (Fung, 1978). With more research on the injury mechanism, it will become clear if one of these is capable of predicting pulmonary contusion that typically seen in blunt chest impacts.

5.9 Limitations of the study

This study began with the focus on developing a model to predict lung contusion. During the development process, it became apparent that the material constitutive model needed

improvement to better capture the non-linear stress wave propagation response, and to adjust the material properties according to the initial condition with respect to the stress-free state. Much of the lung material properties under dynamic loading were still unknown and their relationship with injury should be investigated further.

The current approach in determining the injury thresholds was considered preliminary. It should be emphasized that the established injury threshold enabled interpretation of the lung contusion between candidate injury metrics although the current model is not validated to predict lung contusion. Although more research on the candidate injury metrics would enhance the understanding of the pulmonary contusion, the best possible way to gain greater understanding of the injury metrics and the injury mechanisms is to fundamentally understand how the lung behaves dynamically as a material.

The future research needs advancement in four areas before a more detailed injury evaluation approach can be realized. Firstly, there is a need for anthropometric data on lung size, lung lobe geometry and size. Describing lung injury in terms of lobes is tied to the clinical understanding of the lung contusion injury which was already built into the AIS scale. This enables a more detailed description of the contusion. Secondly, pulmonary contusion identification is a critical component to gathering pulmonary contusion data from trauma patients by reconstructing CT scans, and much of this development is already underway (Daly et al, 2008; Gayzik et al, 2007; Stitzel et al, 2005; Miller et al, 2001). Contusion identification can enhance our understanding and enable investigation on the injury correlation with various injury metrics. Thirdly, a comprehensive study is needed to focus on the human tolerance to pulmonary contusion. The study by Miller (2001) had suggested that a 20% cumulative volume threshold where there is a high risk of ARDS. A more in-depth study should consider how much contusion a lung lobe can withstand before posing a serious risk to the functioning of a lung. Fourth, there is still a need to develop a fundamental understanding of the lung response under dynamic loading. Only with a more solid understanding of the lung as a material can yield a greater link to the injury mechanism.

Chapter 6
Conclusions & Recommendations

6.1 Conclusions

Occupant injuries in motor vehicle collisions are prevalent in our society. Automotive manufacturers continuously develop new tools to improve the safety of vehicle designs, of which a fundamental understanding of the human body response to blunt impact is essential. Occupant simulation is an effective analytical tool for researching human response and injury tolerance under a wide array of motor vehicle collision scenarios. This study focused on developing a numerical model to predict lung response and injury in side impact car crash scenarios using a full human body model with detailed thoracic representations.

In the current study, many deficiencies in an existing human body model were addressed with the aim to produce a realistic boundary condition to the internal organs. Appropriate contact interaction between components was defined to ensure continuity and accuracy. The material properties of the human soft tissue, rib, costal cartilage, lungs, and aorta were investigated and implemented where supported in the literature. The thoracic region of the human body model was validated using three (frontal, oblique, lateral) pendulum impact tests and two side sled impact tests. The other regions of the human body model such as the shoulder, abdomen, and pelvis were also validated against various lateral pendulum impact studies. The latest model demonstrated improvements in every response category relative to the previous version of the human body model. The implementation of a strain-rate dependent material model for the rib was critical in predicting response accurately across a wide range of impact velocity.

The development of the lung model involved advances to the physical properties, material properties, and boundary conditions. Size, density and geometry of the lungs

were established at the functional residual capacity as the initial condition. The elastic properties of the lung were derived from the biaxial human lung tissue experiments and in-vivo live rat impact experiments. The surface tension properties were determined based on previous studies on pressure-volume experiments on dog lungs. The current lung model development was hampered by the lack of constitutive model capability to correct the material properties with respect to an initial condition. An analytical approach was presented to correct the physical and material properties of the lung from the stress-free state to the in-situ condition.

Several injury metric predictor candidates of pulmonary contusion were investigated and compared against the pendulum and sled impact scenarios. The current study established injury metric thresholds based on a 6.7m/s oblique pendulum impact scenario. Resultant injury severity of various impact scenarios was determined relative to this set of injury thresholds. The results of this study confirmed the importance of stress wave focusing, reflection and concentration within the lungs, particularly near the impact surface and against relatively rigid boundaries such as the spine. Stress wave propagation from one lung to the other lung only became significant in severe loading such as the 8.9m/s sled tests. The bulk modulus of the lung had considerable influence on injury metric outcomes and its relevance to lung injury should be investigated more closely. Although the 6.7m/s oblique pendulum impact and 6.7 m/s NHTSA sled impact demonstrated similar peak viscous criterion, the study demonstrated that the resultant contusion levels were quite different with the contusion response dependent on the contact area.

In conclusion, the developed human body model is applicable across a wide velocity range of impact regardless of impact direction. The overall model is capable of predicting thoracic response and lung contusion. Future development to the heart and aorta can expand the model capacity to investigate all vital organ injury mechanisms within the thorax.

6.2 Recommendations

The detailed human body model could be used to analyze automotive impact scenarios as it provided good prediction in thoracic response and enabled insight into internal organ injury such as pulmonary contusion. Interaction with a vehicle interior compartment or safety features could be implemented for closer investigation of their implications on lung injury. When conducting investigations with the numerical human body model, several limitations should be kept in mind and be addressed in the next iteration of development.

Firstly, a more rigorous investigation on the geometrical variation of the rib, the mesh representation of the geometry, and appropriate material models are required to improve the prediction of the rib fracture location and timing. Although the current modeling approach was an effective method from a computational cost and response standpoint, the ribcage model cannot predict rib fracture and response more accurately without addressing the geometrical variation of each rib. A more appropriate material model for the costal cartilage would enable a more realistic response during frontal and oblique impact scenarios. It is recommended that these components be validated independently at the component level such that deficits are addressed directly.

Secondly, many components surrounding the detailed thorax should be improved to enhance the biofidelity of the overall model. Implementing clavicle fracture would improve shoulder kinematics and ribcage response during severe impact scenarios. The anthropometry of the abdomen should be revisited to improve response interaction with other body regions. A more appropriate pelvis material model is needed to mimic pelvic fracture, mitigate the elevated force response, and improve the unloading response. A more accurate construction of the shoulder and muscle models with the surrounding components would improve the overall thoracic response.

Thirdly, focus should be placed on developing an approach to evaluate the aortic and heart injuries. Although an aorta and a heart model were implemented, a closer

investigation is required on the model accuracy in terms of geometry, material properties and boundary conditions. Some of the less critical components such as the esophagus, pulmonary trunks, and bronchi were omitted given that they have little influence on the injury mechanism of pulmonary contusion. The complexity of the interaction between the organs was minimized at the expense of modifying the lung geometry to fill in the void left by these components. However, several hypotheses on aortic injury suggested that these components may play a role when neck extension is considered.

Fourth, three aspects pertained to the lung material model should be investigated to understand their relevance to the lung response and injury: lung elasticity, surface tension, and dynamic properties of the lung. Little information is available on the compressive properties of the lung tissue. The lung tissue has a unique characteristic where the lung tissue is more compliant when biaxially loaded compared to uniaxial loaded. The theory behind this is still unclear; however it may be a factor in the injury mechanism.

The loading and unloading characteristics of the surface tension should be different, but the current constitutive model is limited to a single curve representing the loading and unloading response. This would alter how the lung behave, thus affect how the candidate injury metrics predict response. Experimental data on surface tension is also currently restricted to quasi-static loading and based on animal studies.

Although an effective bulk modulus was assumed based on the deformation range considered in the current study, the stress wave should be more localized in theory than the current numerical model would predict. Past experimental studies largely focused on capturing wave propagation at modest deformation levels, the wave propagation may be very different and non-linear when the dynamic loading is accompanied with greater deformation. Future studies should explore the bulk behavior of the lung with deformation and develop numerical techniques to model the bulk response appropriately.

REFERENCES

Abe, H., Hayashi, K., Sato, M., 1996. Data Book on Mechanical Properties of Living Cells, Tissues, and Organs, Springer-Verlag, Tokyo.

Allen, G.S., Coates, N.E., 1996. "Pulmonary Contusion: A collective review", in *The American Surgeon*.

Aris A, Delgado LJ, Montiel J, Subirana MT., 2000. "Multiple intracardiac lesions after blunt chest trauma," in *Ann Thorac Surg*, 70:1692–1694.

Argosy, 2009. "The Visible Body," Argosy Publishing, Newton, MA, www.visiblebody.com.

AIS, 2005. *Abbreviated Injury Scale (AIS)*, American Association for Automotive Medicine, Morton Grove, Illinois.

Baker S.P., O'Neill B., Naddon W., Long W.B., 1974. "The Injury Severity Score: A Method for Describing Patients with Multiple Injuries an Evaluating Emergency Care", in *Journal of Trauma*, 14:187-196.

Bass et al, 2001. "Material Properties for modeling traumatic aortic rupture", in *Proceedings of Stapp Car Crash Conference*, SAE 2001-22-0006.

Bendjellal, F., Walfisch, G., Fayon, A., and Tarriere, C., 1984. "APR Biomechanical Data," in *ISO Technical Report 9790*, International Standards Organization, American National Standards Institute, New York, NY, 1999.

Bernard et al, 1994. "Report of the American-European consensus conference on ARDS: definitions, mechanisms, relevant outcomes, and clinical trial coordination", in *Intensive Care Medicine*, Springer-Verlag.

Bertrand, S., Cuny, S., Petit., Trosseille X., Page, Y., Guillemot, H., and Drazetic, P., 2008. "Traumatic rupture of the thoracic aorta in real-world motor vehicle crashes," in *Traffic Injury Prevention*, 9:153-161.

Bowen I.G., Fletcher E.R., and Richmond D.R., 1968. "Estimate of Man's Tolerance to the Direct Effects of Air Blast," Defense Atomic Support Agency, Tech. Rep. DASA-2113.

Brudin L.H., Rhodes C.G., Valino S.O, Wollmer I., Hugues J., 1987. "Regional lung density and blood volume in non-smoking subjects measured by PET," in *Journal of Applied Physiology*.

Blincoe L., Seay, A., Zaloshnja, E., Miller, T., Romano, E., Luchter, S., & Spicer,R., 2002. "The economic impact of motor vehicle crashes, 2000". National Highway Traffic Safety Administration, Washington, DC, DOT HS-809-446.

Carew, T. E., Vaishnav, R. N. and Patel, D. J., 1968. "Compressibility of arterial wall," in *Circulation Research*, 33:61-68.

Cronin D., Greer A., Williams K. and Salisbury C., 2004. "Numerical Modeling of Blast Trauma to the Human Torso", in *Proceedings of Personal Armor System Symposium*, the Netherlands.

Cavanaugh J.M., Walilko T.J., Malhotra A., Zhu Y., and King A.I., 1990a. "Biomechanical Response and Injury Tolerance of the Pelvis in Twelve Sled Side Impacts," in *Proceedings of 34th Stapp Car Crash Conference*, 902305.

Cavanaugh J.M., Walilko T.J., Malhotra A., Zhu Y., and King A.I., 1990b. "Biomechanical Response and Injury Tolerance of the Thorax in Twelve Sled Side Impacts," in *Proceedings of 34th Stapp Car Crash Conference*, 902307.

Cavanaugh J.M., Zhu Y., Huang Y., and King A.I., 1993a. "Injury and Response of the Thorax in Side Impact Cadaveric Tests", in *Proceedings of 37th Stapp Car Crash Conference*, 933127.

Cavanaugh, J. M., 1993b. "The Biomechanics of Thoracic Trauma," in *Accidental Injury - Biomechanics and Prevention*, Nahum, A. M. and Melvin, J. W., Ed. Springer-Verlag.

Cavanaugh J.M., Walilko T., Walbridge A., Huang Y., and King A.I., 1994. "An Evaluation of TTI and ASA in SID Side Impact Sled Tests", in *Proceedings of the 38th Stapp Car Crash Conference*, 942225.

Cavanaugh, J. M., Koh, S. W., Kaledhonkar, S. L. and Hardy, W. N. 2005. "An Analysis of Traumatic Rupture of the Aorta in Side Impact Sled Tests," in *SAE World Congress*.

Chung J., Cavanaugh J., King A., Koh S.W., Deng Y.C., 1999. "Thoracic Injury Mechanisms and Biomechanical Responses in Lateral Velocity Pulse Impacts", in *Proceedings of 43rd Stapp Car Crash Conference*.

Chang F., 2001. "The Development and Validation of a Finite Element Human Thorax Model for Automotive Impact Injury Studies," in *Proceedings of the ASME Int. Mech. Eng. Congress and Exposition*, AMD-Vol. 251.

Chapon, A., 1984. "Thorax and Upper Abdomen: Anatomy, Injuries and Possible Mechanisms of Injury," in *The Biomechanics of Impact Trauma*, Elsevier Science Publishers.

Clemedson C.J., 1956. "Blast injury," in *Physiological Reviews*, 36(3):336-354.

Crossfill M.L., Widdicombe J.G., 1961. "Physiological characteristics of the chest and lungs and the work of breathing in different mammalian species," in *Journal of Physiology*.

Costantino M., Gosselin M.V., Primack S.L., 2006. "The ABC's of thoracic trauma imaging," in *Proceedings of Seminars in Roentgenology*, 41(3): 209–225.

Cooper G.J., Pearce B.P., Stainer M.C., Maynard R.L., 1982. "The biomechanical response of the thorax to non-penetrating trauma with particular reference to cardiac injuries," in *Journal of Trauma*, 22(12):994-1009.

Cooper G.J., Pearce B.P., Sedman A.J., Bush I.S., and Oakley C.W., 1996a. "Experimental evaluation of a rig to simulate the response of the thorax to blast loading," in *Journal of Trauma*, 40:38-41.

Cooper G.J., 1996b. "Protection of the lung from blast overpressure by thoracic stress wave decouplers," *Journal of Trauma*, 40(3):S105-S110.

Cooper G.J., Dudley H.A., Gann D.S., Little R.A., and Maynard R.L., 1997. *Scientific Foundations of Trauma*. Butterworth-Heinemann, Oxford.

Cowin, SC, Van Buskirk WC, Ashman RB, 1987. "The properties of bone", in *Handbook of Bioengineering*, ed. Skalak R., Chien S., 2:1-27.

Cowin, SC, Doty SB, 2007. "The Elastic Symmetry of Cortical Bone", in *Tissue mechanics*, textbook, Springer Science, p356-358.

Creasy J.D., Chiles C., Routh W.D., Dyer R.B., 1997. "Overview of Traumatic Injury of the Thoracic Aorta," in *Radiographics*, 17(1):27.

Daly M. et al, 2008. "Traumatic Pulmonary Pathology measured with computed tomography and a semiautomated analytic method", in *Clinical Imaging*.

Darvish, K., Lovobsky, L. and Lee, S. H., 2004. "Analysis and modeling of aortic tissue material properties," in *Proc. ASME International Mechanical Engineering Congress & Exposition*. Anaheim, CA.

Delfino, A., Stergiopulos, N., Moore, J. E. J. and Meister, J. J., 1997. "Residual strain effects on the stress field in a thick wall finite element model of the human carotid bifurcation," in *Journal of Biomechanics,* 30:777-786.

Deng Y.C., Kong W. and Ho H., 1999. "Development of a Finite Element Human Thorax Model for Impact Injury Studies", in *SAE International Congress and Exposition*, SAE 1999-01-0715.

Dunn F., Fry W.J., 1961. "Ultrasonic Absorption and Reflection by Lung Tissue", in *Physics in Medicine and Biology*.

Eiband, A.M., 1959. "Human Tolerance to Rapidly Applied Acceleration". A Survey of the Literature, NASA Memo No. 5-19-59E., National Aeronautics and Space Administration, Washington, D.C..

Eppinger R.H., Marcus J.H., Morgan R.M., 1984. “Development of Dummy and Injury Index for NHTSA's Thoracic Side Impact Protection Research Program”, Government/Industry Meeting and Exposition, SAE 840885.

Flicker E., Lee J.S., 1974. “Equilibrium of force of subpleural alveoli: implications to lung mechanics” *Journal of Applied Physiology*, 36(3).

Federal Motor Vehicle Safety Standards and Regulations, 2008. "Occupant Crash Protection," *Motor Vehicle Safety Standard No. 208*, U.S. Department of Transportation, National Highway Traffic Safety Bureau.

Frankus A., Lee G.C., 1974. “A theory for distortion studies of lung parenchyma based on alveolar membrane properties”, in *Journal of Biomechanics*.

Furusu K., Watanabe I., Kato C., Miki K., Hasegawa J., 2001. “Fundamental Study of Side Impact Analysis Using the Finite Element Model of the Human Thorax”, *Japanese SAE Review*, 22-2: 195-199.

Funk, J.R, Kerrigan, J.R, and Crandall, J.R., 2004. “Dynamic bending tolerance and elastic-plastic material properties of the human femur.” *Proc. 48th Association for the Advancement Automotive Conference*. Key Biscayne, FL, 48:216-233.

Forbes, P. A., 2005. “Development of a Human Body Model for the Analysis of Side Impact Automotive Thoracic Trauma”. MASc Thesis, University of Waterloo, Waterloo, Ontario, Canada.

Forbes P., Cronin D.S., Deng Y.C., 2006. “Multi-Scale Human Body Model to Predict Side Impact Thoracic Trauma”, *International Journal of Crashworthiness*, V11:3.

Foster J.K., Kortge J.O., Wolanin M.J., 1977. “Hybrid III – A biomechanically based crash test dummy.” *Proceedings of Stapp Car Crash Conference*.

Fung Y.C., 1974. “A theory of elasticity of the lung,” *ASME Journal of Applied Mechanics*.

Fung Y.C., 1975. “Stress, deformation, and atelectasis of the lung”, *Circulation Research*, American Heart Association, 37:481-496.

Fung Y.C., Tong P., Patitucci P., 1978. “Stress and Strain in the Lung”, *ASCE Journal of the Engineering Mechanics Division*, 104-1:201-223.

Fung Y.C., Yen M.R., Zeng Y.J., 1985. “*Characterization and modeling of thoraco-abdominal response to blast waves*”, University of California, San Diego, Contract No. DAMD17-82-C-2062, Vol-3.

Fung Y.C., Yen R.T., Tao Z.L., Liu S.Q., 1988. "A Hypothesis on the Mechanism of Trauma of Lung Tissue Subjected to Impact Load", *Journal of Biomechanical Engineering*, 110:50-56.

Fung, Y.C., 1993. "*Biomechanics: Mechanical Properties of Living Tissue*", 2nd Ed. Springer, New York, NY.

Gadd, C.W., Patrick, L.M., 1968. "Systems Versus Laboratory Impact Tests for Estimating Injury Hazard", *Society of Automotive Engineers*, New York, SAE 680053.

Gao J., Huang W., Yen R.T., 2006. "Mechanical properties of human lung parenchyma," *Biomed Sci Instrum*, 42:172-180.

Gayzik F.S., Hoth J.J., Daly M., Meredith J.W., Stitzel J.D., 2007. "A Finite Element-Based Injury Metric for Pulmonary Contusion: Investigation of Candidate Metrics through correlation with computed tomography," *Proceedings of 51st Stapp Car Crash Conference*, p189-209.

Gayzik S., 2008. "Development of a finite element based injury metric for pulmonary contusion*"*. Ph.D. Dissertation, Virginia Tech-Wake Forest University, Winston-Salem, North Carolina.

Glaister D.H., Schroter R.C., Sudlow M.F., Milic-Emili J., 1973. "Bulk elastic properties of excised lungs and the effect of a transpulmonary pressure gradient", *Respiration Physiology*, 17:347-364.

Granik, G., Stein, I., 1973. "Human Ribs: Static Testing as a Promising Medical Application", *Journal of Biomechanics*, 6:237-240.

Gray H., "*Gray's Anatomy of the Human Body*", ed. Lea & Febiger, 1918; ed. Bartleby.com, New York, 2000.

Greer A., Cronin D., Salisbury C., and Williams K., 2005. "Finite Element Modeling for the Predication of Blast Trauma", *proceedings of IUTAM Symposium on impact biomechanics*, Dublin.

Grimal Q., Watzky A., Naili S., 2002. "A one-dimensional model for the propagation of transient pressure waves through the lung", *Journal of Biomechanics*, 35-8:1081-1089.

Grimal Q., Naili S., and Watzky A., 2005. "A high-frequency lung injury mechanism in blunt thoracic trauma," *Journal of Biomech.*, 38:1247-1254.

Groskin S.A., 1992. "Selected topics in chest trauma," in *Proceedings of Radiology*, 183:605-617.

Guccione, J. M. and McCulloch, A. D., 1991. "Finite Element Modeling of Ventricular Mechanics," in *Theory of Heart*, Glass et al.

Guenard H., Diallo M.H., Laurent F., Vergeret J., 1992. “Lung density and lung mass in emphysema”, *CHEST journal*, (102)198-203.

Guyton, A.C., Hall J.E., 1996. “*Textbook of medical Physiology*”, 9th edition, W.B. Saunders, Philadelphia.

Happee R., Hoofman M., van den Kroonenberg A.J., Morsink P., Wismans J., 1998. “A Mathematical Human Body Model for Frontal and Rearward Seated Automotive Impact Loading”, *Proceedings of 42nd Stapp Car Crash Conference*, 983150.

Hardy, W. N., Shah, C. S., Kopacz, J. M., Yang, K. H., Van Ee, C. A., Morgan, R. M. and Digges, K. H., 2006. "Study of potential mechanisms of traumatic rupture of the aorta using in situ experiments." *Proceedings of Stapp Car Crash Conference,* 50:247-266.

Hardy W. N., Shah C. S., Mason M. J., Kopacz J.M., Yang K.H., King A.I., Van Ee C.A., Bishop J.L., Banglmaier R.F., Bey M.J., Morgan R.M., Digges K.H., 2008. “Mechanisms of Traumatic Rupture of the Aorta and Associated Peri-isthmic Motion and Deformation,” *Proceedings of Stapp Car Crash Conference*, 52:233-265.

Halstead J., Hossepinpour A., Wells F., 2000. “Conservative surgical treatment of valvular injury after blunt chest trauma,” *the annals of thoracic surgery*.

Hayes, W. C., 1991. “Biomechanics of Cortical and Trabecular Bone: Implications for Assessment of Fracture Risk,” in *Basic Orthopaedic Biomechanics*, Mow, V. C. and Hayes, W. C., New York: Raven Press.

Hoppin F.G., Green I.D., Mead J., 1969. “Distribution of pleural surface pressure in dogs”, *Journal of Applied Physiology*, 27:863-873.

Hoppin F.G., Lee G.C., Dawson S.V., 1975. “Properties of lung parenchyma in distortion,” in *Journal of Applied Physiology*, 39(5).

Hoppin F. G., Hilodebrandt J., 1977. “Mechanical Properties of the lung”, in *Bioengineering Aspects of the Lung*, edited by West J.B., Marcel Dekker.

ISO, 1999. “Road Vehicles – Anthropomorphic Side Impact Dummy – Lateral Impact Response Requirements to Assess the Biofidelity of the Dummy”, International Standards Organization, American National Standards Institute, New York, NY, Technical Report 9790.

Jahed M., Lai-Fook S. J., Bhagat P.K., Kraman S.S., 1989. “Propagation of stress waves in inflated sheep lungs”, *Journal of applied physiology*, 66(6).

Janda, D.H., Bir, C.A., Viano, D.C., Cassatta, S.J., 1998. “Blunt Chest Impacts: Assessing the Relative Risk of Fatal Cardiac Injury from Various Baseballs,” *Journal of Trauma*, 44(2): 298-303.

Josephson L.H., Tomlinson P., 1988. “Predicted Thoraco-Abdominal Response to Complex Blast Waves”, *Journal of Trauma*, 28:116-124.

Kemper, A., McNally, C., Kennedy, E., Rath, A., Manoogian, S., Stitzel, J., and Duma, S., 2005. “Material Properties of Human Rib Cortical Bone from Dynamic Tension Coupon Testing.” *Proceedings of Stapp Car Crash Conference*, 49: 199-230.

Kemper A. R., McNally C, Pullins C., Freeman L., Duma S., 2007. “The biomehanics of Human Ribs: Material and structural properties from dynamic tension and bending tests”, *Proceedings of Stapp Car Crash Conference*, SAE 2007-22-0011.

Klaus, G., Kalleris, D., 1983. “Side impact—a comparison between HSRI, APROD and HYBRID II dummies and cadavers," *Proceedings of Stapp Car Crash Conference*, San Diego, CA, 365-381.

Klaus, G., Sinnhuber, R., Hoffman, G., Kalleris, D., Mattern, R., 1984. “Side impact — a comparison between dummies and cadavers, correlations between cadaver loads and injury severity,” *Proceedings of Stapp Car Crash Conference*, Chicago, IL, 237-259.

Kuppa S.M., Eppinger R.H., 1998. “Development of an Improved Thoracic Injury Criterion,” *Proceedings of 42nd Stapp Car Crash Conference*, p.139-154.

Kroell, C.K., Schneider, D.C., Nahum, A.M., 1971, Impact Tolerance and Response of the Human Thorax, *Proceedings of the 15th Stapp Car Crash Conference*, SAE 710851.

Kroell C.K., Schneider D.C., Nahum A.M., 1974. “Impact tolerance and response of the human thorax II”, *Proceedings of 18th Stapp Car Crash Conference*.

Kroell, C.K., Pope, M.E., Viano, D.C., Warner, C.Y., Allen, S.D., 1981. “Interrelationship of Velocity and Chest Compression in Blunt Thoracic Impact to Swine,” *Proceedings of the 25th Stapp Car Crash Conference*, 811016.

Kroell CK, Allen SD, Warner CY, Perl TR. 1986. “Inter-relationship of velocity and chest compression in blunt thoracic impact to swine II,” *Proceedings of the 30th Stapp Car Crash Conference*, SAE 861881.

Lambert R.K., Wilson T.A., 1973. “A model for the elastic properties of the lung and their effect on expiratory flow”, *Journal of applied physiology*.

Lanir Y., Lichtenstein O., Imanuel O., 1996. “Optimal Design of Biaxial Tests for Structural Material Characterization of Flat Tissues,” *Journal of Biomechanical Engineering*, 118:41-47.

Lau V. K., Viano D.C., 1981. “Influence of Impact Velocity and Chest Compression on Experimental Pulmonary Injury Severity in Rabbits,” in *Journal of trauma*, V21-12.

Lau I.V., Viano D.C., 1985. “Thoracic Impact: A Viscous Tolerance Criterion”, *Proceedings of the 10th Experimental Safety Vehicle Conference*, NHTSA, p104-113.

Lau I.V., Viano D.C., 1986. “The Viscous Criterion - Bases and Applications of an Injury Severity Index for Soft Tissues”, *Proceedings of the 30th Stapp Car Crash Conference*, SAE 861882.

Leavitt BJ, Meyer JA, Morton JR, Clark DE, Herbert WE, Hiebert CA, 1987. “Survival following nonpenetrating traumatic rupture of cardiac chambers,” *Ann Thorac Surg*, 44: 532–535.

Lee G.C., Tai R. C., 1979. “Structual Mechanics of the Lung” in *Applied Physiological Mechanics*, edited by Ghista D. N., Harwood Academic Publishers.

Lee J.B., Yang K.H., 2001. “Development of a Finite Element Model of the Human Abdomen”. *Proceedings of Stapp Car Crash Conference*, SAE 2001-22-0004.

Lehnert S., Schreiner L.J., El-Khatib E., 1993. “Factors influencing lung density in experimental models: results of studies using CT densitometry”, *Physiol. Meas.*, 14:183-193.

Maddali M, Shah, C. S., Yang, K. H., 2005. "Finite Element Modeling of Aortic Tissue using High-Speed experimental data," *Proceedings of ASME International Mechanical Engineering Congress,* Orlando, FL., IMECE2005-82083.

Malliaris AC, Hitchcock R, Hedlund J., 1985. “HARM Causation and Ranking in Car Crashes.” *Society of Automotive Engineers*, SAE 850090.

Mead J., Takishima T., Leith D., 1970. “Stress Distribution in Lungs: A model of Pulmonary Elasticity”, *Journal of Applied Physiology*.

Mertz, H.J., Prasad, P., Irwin, A.L., 1997, “Injury Risk Curves for Children and Adults in Frontal and Rear Collisions,” *Proceedings of the 41st Stapp Car Crash Conference*, 973318.

McElhaney, J.H., 1966. “Dynamic Response of Bone and Muscle Tissue”, *Journal of Applied Physiology*, 21:1231-1236.

Moore, K.L., Dalley, A.F., 1999. *Clinically Oriented Anatomy*, 4th Edition, Lippincott Williams and Wilkins, Baltimore.

Mohan D., 1976. “*Passive mechanical properties of human aortic tissue*”, Ph.D. Dissertation, University of Michigan, Ann Arbor.

Mohan D., Melvin J.W., 1982. “Failure properties of passive aortic tissue. I – uniaxial tension tests”, *Journal of Biomechanics*, 15:887-902.

Mohan D., Melvin J.W., 1983. “Failure properties of passive aortic tissue. II – biaxial tension tests”, *Journal of Biomechanics*, 16:31-44.

Morgan, R.M., Marcus, J.H., Eppinger, R.H., 1986. “Side Impact - The Biofidelity of NHTSA's Proposed ATD and Efficacy of TTI,” *Proceedings of the 30th Stapp Car Crash Conference*, 861877.

Mow V.C., Hayes W.C., 1997. “*Basic Orthopaedic Biomechanics*”, 2nd edition, Lippincott-Raven, Philadelphia.

McCulloch, A. D. and Omens, J. H., 1991. “Non-homogeneous Analysis of Three-dimensional Transmural Finite Deformation in Canine Ventricular Myocardium,” *Journal of Biomechanics*, V24.

Murray C.J.L., Lopez A.D., 1996. “The global burden of disease: a comprehensive assessment of mortality and disability from diseases, injuries, and risk factors in 1990 and projected to 2020.” Harvard School of Public Health, Boston, MA.

Miller P.R., Croce M.A., Bee T.K., Qaisi W.G., Smith C.P., Collins G.L., and Fabian T.C., 2001. “ARDS After Pulmonary Contusion: Accurate Measurement of Contusion Volume Identifies High-Risk Patients”, *Journal of Trauma*, 51:223-228, discussion 229-230.

Miller P.R., Croce M.A., Kilgo P.D., Scott J., Fabian T., 2002. “Acute Respiratory Distress Syndrome in Blunt Trauma: Identification of Independent Risk Factors”, *the American Surgeon*.

Miller P.R., 2008. (Private Communication), April 1, 2008. Discussion on lung contusion pattern.

Nahum, A.M., Melvin J.W., 2002. “*Accidental Injury Biomechanics and Prevention*”, 2nd Edition, Springer-Verlag Inc., New York.

NASA, 1978. “Anthropometric Source Book: Volume 1: Anthropometry for Designers Anthropology Staff/Webb Associates”, in National Aeronautics and Space Administration, RP 1024.

NASA, 1995. “*Man-Systems Integration Standards*”, National Aeronautics and Space Administration, NASA-STD-3000:V1, Rev. B.

Neathery, R.F., 1974. “Analysis of Chest Impact Response Data and Scaled Performance Recommendations,” *Proceeding of the 18th Stapp Car Crash Conference*, SAE 741188.

Neathery, R.F., Kroell, C.K., Mertz, H.J., 1975. “Prediction of Thoracic Injury from Dummy Responses,” *Proceeding of the 19th Stapp Car Crash Conference*, 751151.

NHTSA, 2000. “Supplement: Development of Improved Injury Criteria for the Assessment of Advanced Automotive Restraint Systems – II”, National Highway Traffic Safety Administration.

NHTSA, 2001. “A Compilation of Motor Vehicle Crash Data from the Fatality Analysis Reporting System and the General Estimates System”, in *Traffic Safety Facts 2001*, National Highway Traffic Safety Administration, DOT HS 809-484.

NHTSA, 2004. “Federal Motor Vehicle Safety Standards; Side Impact Protection; Side Impact Phase-In Reporting Requirements; Proposed Rule, Federal Register, Part IV, Department of Transportation 49 CFR Parts 571 and 598”, National Highway Traffic Safety Administration, Docket No. NHTSA-2004-17694.

NHTSA, 2006. “Traffic Safety Facts 2006”, National Center for Statistics & Analysis (NCSA) in National Highway Traffic Safety Administration, DOT HS 810 818.

NHTSA, 2007. “Traffic Safety Facts 2007”, National Center for Statistics & Analysis (NCSA) in National Highway Traffic Safety Administration.

National Library of Medicine, 2004. “*The Visible Human Project*”, National Institutes of Health.

Nunn J.F., 1993. “*Nunn's Applied Respiratory Physiology”*, 4 ed., Butterworth-Heinemann.

O’Connor J.V., Kufera J.A., Kerns T.J., Stein D.M., Ho S., Dischinger P.C., Scalea T.M., 2009. “Crash and Occupant Predictors of Pulmonary Contusion”, *Journal of Trauma*, V66:1091-1095.

Patel, D. J., Janicki, J. S. and Carew, T. E., 1969. "Static anisotropic elastic properties of aorta in living dogs." *Circulation Research,* 25: 765-779.

Palsson et al., 2003. “*Tissue Engineering*”. CRC Press, p7-7.

Parmley L.F., Manion W.C., Mattingly T.W. 1953. Nonpenetrating traumatic injury of the heart. *Circulation,* 18:371–96.

Panjabi, M., Brand, R., et al., 1976. “Three Dimensional Flexibility and Stiffness Properties of the Human Thoracic Spine,” *Journal of Biomechanics*, vol. 9.

Patrick, L.M., Kroell, C.K., Mertz, H.J., 1965, “Forces of the Human Body in Simulated Crashes,” *Proceedings of the 9th Stapp Car Crash Conference*, SAE 650961.

Patrick LM, Mertz HJ, Kroell CK, 1969. “Cadaver knee, chest and head impact loads,” *Proceedings of the 9th Stapp Car Crash Conference,* p168-182.

Pellegrino R., et al, 2005. “Interpretative strategies for lung function tests”, *European Respiratory Journal*, 26(5).

Pintar F.A., Yoganandan N., Hines M.H., Maltese M.R., 1997. “Chestband Analysis of Human Tolerance to Side Impact”, *Proceedings of the 41st Stapp Car Crash Conference*, SAE 973320.

Pinto J.G., Fung Y.C., 1973. “Mechanical properties of the heart muscle in the passive state,” *Journal of Biomechanics*.

Pike, J. A., 1990. “Automotive safety : anatomy, injury, testing, & regulation”, SAE International.

Prokop R.M., Chen P., Garg A., Neumann A.W., 1999. “Thermodynamic modeling of the lung mechanics”, *Colloids and Surfaces B: Biointerfaces*, Elsevier.

Powell W. R., 1979. “Pulmonary Mechanics” in *Applied Physiological Mechanics*, edited by Ghista D. N., Harwood Academic Publishers.

Quanjer P. h, Stocks J., 1995. “Reference Values for Residual Volume, Functional Residual Capacity, and Total Lung Capacity,” *European Respiratory Journal*, (8).

Rice D.A., 1983. “Sound speed in pulmonary parenchyma”, *Journal of applied physiology*, 54(1).

Raghavan, M. L. and Vorp, D. A., 2000. "Toward a biomechanical tool to evaluate rupture potential of Abdominal Aortic Aneurysm: Identification of a finite strain constitutive model and evaluation of its applicability." *Journal of Biomechanics,* 33:475-482.

Richens, D., Field, M., Hashim, S., Neale, M. and Oakley, C., 2004. "A finite element model of blunt traumatic aortic rupture." *European Journal of Cardio-thoracic Surgery* 25:1039-1047.

Ridella S. A., Viano D.C., 1990. “Determining tolerance to compression and viscous injury in frontal and lateral impacts”, *Proceedings of the 9th Stapp Car Crash Conference*.

Roberts, V. L., Jackson, F. R. and Berkas, E. M., 1966. "Heart motion due to blunt trauma to the thorax." *Proceedings of the 10th Stapp Car Crash Conference*, p242-248.

Robbins, D.H., Schneider, L.W., Snyder, R.G., Pflug, M., Haffner, M., 1983a. “Seated Posture of Vehicle Occupants,” *Proceedings of the 27th Annual Stapp Car Crash Conference*, 831617.

Robbins, D.H., 1983b, “Anthropometric Specifications for the Mid-Sized Male Dummy, Volume 2”, The University of Michigan Transportation Research Institute, National Highway Traffic Safety Administration, UMTRI-83-53-2.

Ruan J.S., El-Jawahri R., Chai L., Barbat S., Prasad P., 2003.“Prediction and Analysis of Human Thoracic Impact Responses and Injuries in Cadaver Impacts Using a Full Human Body Finite Element Model”, *Proceedings of the Stapp Car Crash Conference*, 2003-22-0014.

Ruan J.S., El-Jawahri R., Barbat S., Prasad P., 2005. “Biomechanical Analysis of Human Abdominal Impact Responses and Injuries through Finite Element Simulation of a Full Human Body Model.” *Proceedings of Stapp Car Crash Conference*, 2005-22-0016.

SAE, 1970. “Human Anatomy, Impact Injuries, and Human Tolerances”, *Society of Automotive Engineers*, 700195.

Saraf H., Ramesh K.T., Lennon A.M., Merkle A.C., Roberts J.C., 2007. “Mechanical Propeties of soft human tissues under dynamic loading”, *Journal of Biomechanics*.

Salisbury C., Cronin D., Bouamoul A., Ouellet S., Williams K., 2006. “Numerical Investigation of Primary Blast Injury Protection Concepts”, *Proceedings of Personal Armor Systems Symposium*.

Schmitt K.U., Niederer P., Muser M., Walz F., 2007. Thoracic Injuries, in Trauma Biomechanics – Accidental injury in traffic and sports, 2nd edition, Springer.

Schultz, A. B., Benson, D. R., et al., 1974. “Force-deformation Properties of Human Costo-sternal and Costo-vertebral Articulations,” *Journal of Biomechanics*, 7:311-318.

Shah, C. S., Hardy, W. N., Mason, M. J., Yang, K. H., Van Ee, C. A., Morgan, R. M. and Digges, K. H., 2006. "Dynamic Biaxial Tissue Properties of the Human Cadaver Aorta." *Proceedings of the 50th Stapp Car Crash Conference* 50:217-246.

Shah, C. S., Mason, M. J., Yang, K. H., Hardy, W. N., Van Ee, C. A., Morgan, R. M. and Digges, K. H., 2005. "High-Speed Biaxial Tissue Properties of The Human Cadaver Aorta." *Proceedings of ASME International Mechanical Engineering Congress*. Orlando, FL. IMECE2005-82085.

Shah, C. S., Yang, K. H., Hardy, W. N., Wang, H. K. and King, A. I., 2001. "Development of a computer model to predict aortic rupture due to impact loading." *Proceedings of the 45th Stapp Car Crash Conference,* 45:161-182.

Shah, C. S., Hardy, W. N., Yang, K. H., Van Ee, C. A., Morgan, R. M. and Digges, K. H., 2007. "Investigation of the traumatic rupture of the aorta (TRA) by simulating real-world accidents." *Proceedings of 2007 International Research Council on Biomechanics of Injury*, Maastricht, the Netherlands, p349-359.

Smith J.C., Stamenovic D., 1986. “Surface forces in lungs.I. Alveolar surface tension-lung volume relationships”, *Journal of applied physiology*, 60(4).

Stamenovic D., Smith J.C., 1986a. “Surface forces in lungs.II. Microstructural mechanics and lung stability”, *Journal of applied physiology*, 60(4).

Stamenovic D., Smith J.C., 1986b. “Surface forces in lungs.III. Alveolar surface tension and elastic properties of lung parenchyma”, *Journal of applied physiology*, 60(4).

Stapp, J.P., 1951. Human Exposure to Linear Decelerations, Part 2: The Forward Facing Position and the Development of a Crash Harness, AFTR 5915, Wright-Patterson AFB, Dayton, Ohio.

Stapp, J.P., 1970, *Voluntary Human Tolerance Levels, Impact Injury and Crash Protection*, Ed: Gurdjian, E.S., Lang, W.A., Patrick, L.M., Thomas, L.M., pp. 308-349, Charles C. Thomas, Springfield, IL.

States J.D., 1969. “The Abbreviated and the Comprehensive Research Injury Scales”, *Proceedings of the 13th Stapp Car Crash Conference*, SAE 690810.

Stuhmiller J., Chuong C., Phillips Y., Dodd K., 1988. “Computer Modeling of Thoracic Response to Blast”, *Journal of Trauma*, 28:S132-139.

Sturdivan L.M., Viano D.C., Champion H.R., 2004. “Analysis of Injury Criteria to Assess Chest and Abdominal Injury Risks in Blunt and Ballistic Impacts”, *Journal of Trauma*, 56:651-663.

Stitzel J.D., Duman S.M., Cormier J.M., Herring I.P., 2002. “A Non-Linear Finite Element Model of the Eye with Experimental Validation for the Prediction of Globe Rupture”, *Proceedings of the Stapp Car Crash Conference*, SAE 2002-22-0005.

Stitzel J.D., Gayzik F.S., Hoth J.J., Mercier J., Gage H.D., Morton K.A., Duma S.M., Payne R.M., 2005. “Development of a Finite Element-Based Injury Metric for Pulmonary Contusion Part I: Model Development and Validation”, *Proceedings of the 49th Stapp Car Crash Conference*, 2005-22-0013.

Sparks J.L., Bolte J.H., Dupaix R.B., Jones K.H., Steinberg S.M., Herriott R., Stammen J., Donnelly B., 2007. “Using Pressure to Predict Liver Injury Risk From Blunt Impact”, *Proceedings of the Stapp Car Crash Conference*, 2007-22-0017.

Takhounts E.G., Eppinger R.H., Campbell J.Q., Tannous R.E., Power E.D., Shook L.S., 2003. “On the Development of the SIMon Finite Element Head Model”, *Proceedings of the 47th Stapp Car Crash Conference*, SAE 2003-22-0007.

Thomas P., Frampton R., 1999. “Injury Patterns in Side Collisions. A New Look with Reference to Current Test Methods and Injury Criteria.” *Proceedings of the 43th Stapp Car Crash Conference*. Society of Automotive Engineers, SAE 99SC01.

Thollon L., Arnoux P.J., Kayvantash K., Cavallero C., Brunet C., 2002. “Human Injury Evaluation using HUMOS RADIOSS Finite Element Model”, *IRCOBI Conference*.

Vande Geest, J. P., 2005. “Towards an improved rupture potential index for abdominal aortic aneurysms: anisotropic constitutive modeling and noinvasive wall strength estimation.” PhD Dissertation, University of Pittsburgh, Pittsburgh, PA.

Vawter D.L., Matthews F.L., West J.B., 1975. “Effect of shape and size of lung and chest wall on stresses in the lung,” *Journal of Applied Physiology*, 39(1).

Vawter D.L., 1976. “A mechanical analysis of the pressure-volume behavior of dog lungs”, *New England Bioengineering Conference*, New York: Pergamon.

Vawter D.L, 1977. “Stress-free equilibrium volume of the lung”, *Journal of Applied Physiology*, 43(1).

Vawter D.L., 1978. “Elasticity of excised dog lung parenchyma”, *Journal of applied physiology*, 45(2).

Vawter D.L., Fung Y.C., West J.B., 1979. “Constitutive Equation of Lung Tissue Elasticity”, *Journal of Biomechanical Engineering*, V101.

Vawter D.L., 1980. “A Finite Element Model for Macroscopic Deformation of the Lung,” *Journal of Biomechanical Engineering*, V102.

Viano, D. C., 1983. "Biomechanics of non-penetrating Aortic Trauma: A review," *Proceedings of 27th Stapp Car Crash Conference,* 27:109-114.

Viano D.C., Lau I.V., 1988. “A Viscous Tolerance Criterion for Soft Tissue Injury Assessment”, *Journal of Biomechanics*. 21:387-399.

Viano D.C., Lau I.V., Asbury C., King A.I., Begeman P., 1989a. “Biomechanics of the Human Chest, Abdomen, and Pelvis in Lateral Impact”, *Proceedings of the 33rd AAAM Conference*.

Viano D.C., 1989b. “Biomechanical Responses and Injuries in Blunt Lateral Impact”, *Proceedings of the 33rd Stapp Car Crash Conference*, SAE 892432.

Verschakelen J.A., Van fraeyehoven L., Laureys G., Demedts M., Baert A.L., 1993. “Differences in CT Density Between Dependent and Nondependent Portions of the Lung: Influence of Lung Volume”, *American Journal of Roentgenology*, (161).

Wang, D. H. J., Makaroun, M. S., Webster, M. W. and Vorp, D. A. (2001). "Mechanical Properties and Microstrucutre of Intraluminal Thrombus from Abdominal Aortic Aneurysm." *Journal of Biomechanical Engineering* 123: 536-539.

Wagner R.B., Crawford W.O., Schimpf P.P., 1988. “Classification of parenchymal injuries of the lung,” *Radiology*, 167:77-82.

Ward E.E., Kleinberger M., Lennon A.M., Roberts J.C., 2005. “Modeling the effects of blast on the human thorax using high strain rate viscoelastic properties of human tissue”, *IUTAM Proceedings on Impact Biomechanics*.

Weibel E.R., Gil J., 1977. “Structure-Function Relationships at the Alveolar Level,” in *Bioengineering Aspects of the Lung*, edited by West J.B., Marcel Dekker, V3.

West J.B., 2005. “Structure and Function” in *Respiratory Physiology – The Essentials*, Lippincott Williams & Wilkins, 7th edition.

WHO, 2002. “Global Burden of Disease project”, ver 1, World Health Organization.

WHO, 2004. “World report on road traffic injury prevention – Summary”, World Health Organization.

Wood, J.L., 1971. “Dynamic response of human cranial bone”. *Journal of Biomechanics* 4: 1-12.

Wright T.M., Hayes W.C., 1976. “Tensile testing of bone over a wide range of strain rates: effects of strain rate, micro-structure and density,” *Med. Biol. Eng. Comput.*, 14:671-680.

Yamada, H., 1970. *Strength of Biological Materials*, Evans, F.G., ed., Lippincott Williams and Wilkins, Baltimore.

Yang K.H., Beillas P., Zhang L., Lee J.B., Shah C., Hardy W., Demetropoulos C., Tashman S., King A.I., 1970. “Advanced Human Modeling for Injury Biomechanics Research”, *Digital Human Modeling for Design and Engineering Conference and Exposition*, SAE 2003-01-2223.

Yoganandan, N., Pintar, F.A., 1998. “Biomechanics of Human Thoracic Ribs”, *Journal of Biomechanical Engineering*, Transactions of the ASME, 120-1:100-104.

Yoganandan N., Pintar F., Stemper B., Gennarelli T., Weigelt J., 2007. “Biomechanics of side impact: injury criteria, aging occupants, and airbag technology”, *Journal of Biomechanics*, 40:227-243.

Yen R.T., Fung Y.C., Ho H.H., Butterman G., 1986. “Speed of stress wave propagation in lung”, *Journal of Applied Physiology*. 61(2):701-705.

Yen R.T., Fung Y.C., Liu S.Q., 1988. “Trauma of Lung Due to Impact Load”, *Journal of Biomechanics*, 21-9:p745-753.

Yen M., 1999. “Mechanical Properties of Human Heart, Lung, and Aorta for Highway Safety Research,” The University of Memphis, Memphis, Technical Report Sub-project F8C.

Yuen, K.F., Cronin, D.S., Deng, Y.C., 2008. “Lung Response and Injury in Side Impact Conditions,” *Proceedings of the International Research Council on Biomechanics of Injury (IRCOBI) Conference,* Bern, Switzerland.

Zeng Y. J., Yager D., Fung Y.C., 1987. “Measurement of the mechanical properties of the human lung tissue”, *Journal of Biomechanical Engineering*, V109.

Appendix A

Simulation Results

The following appendix contains the pendulum and sled impact results that were simulated at different velocities than those presented in Chapter 4. Model results of regions other than the thorax are presented here. Some pendulum simulation results that were previously presented by Forbes (2005) were updated based on the latest numerical model.

A.1: Thoracic Oblique Pendulum Impact - 4.4 m/s (Viano, 1989)

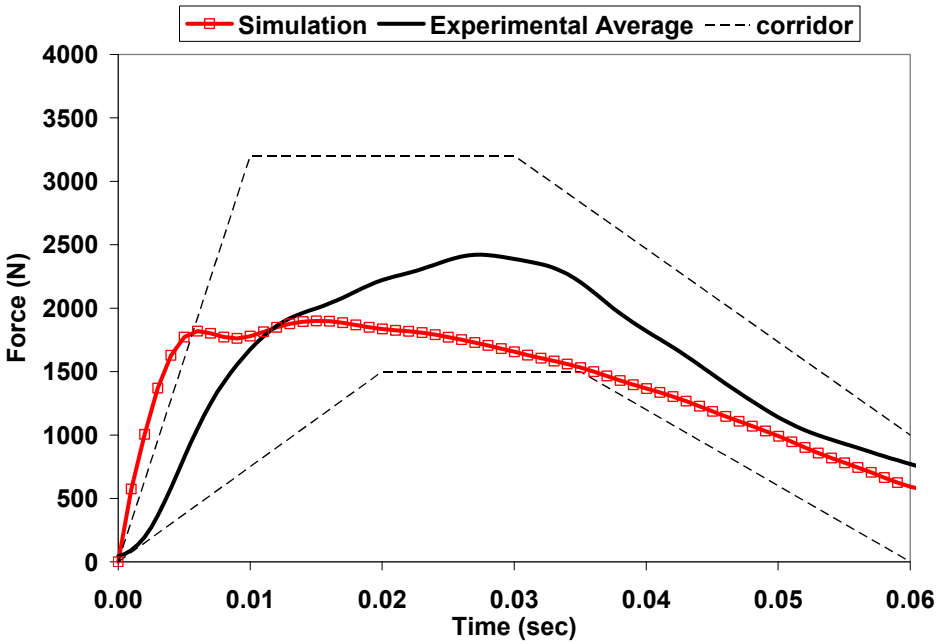

Figure A.1: Thorax - Oblique pendulum 4.4 m/sec - Force

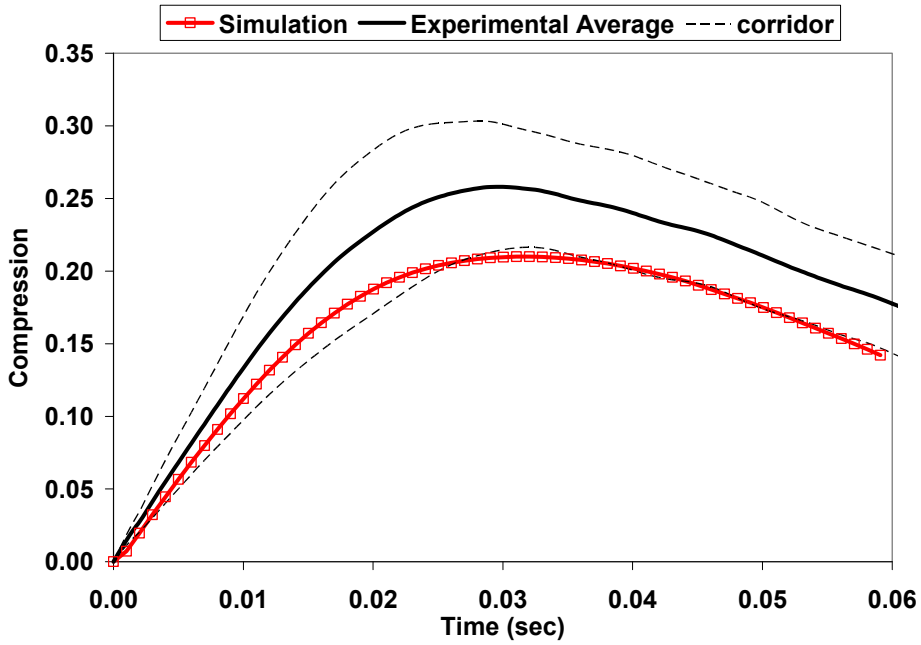

Figure A.2: Thorax - Oblique pendulum 4.4 m/sec – Compression

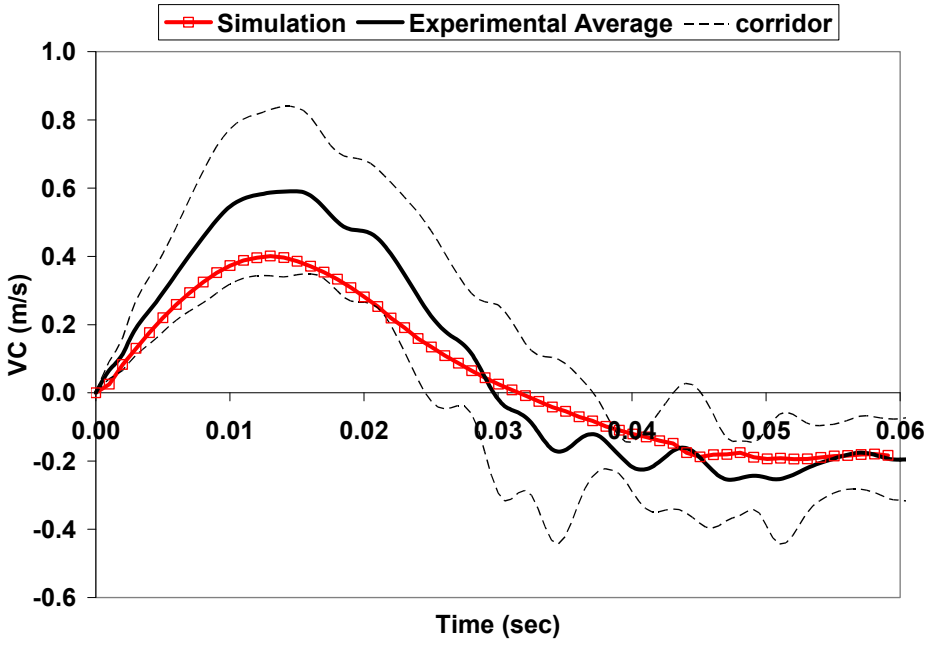

Figure A.3: Thorax - Oblique pendulum 4.4 m/sec - VC

A.2: Heidelberg Sled Impact – 6.7 m/s (Marcus, 1983)

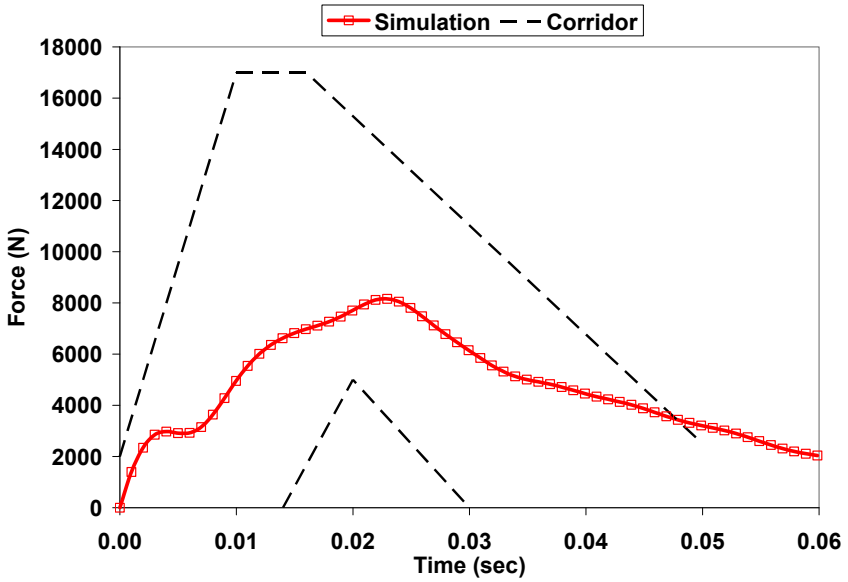

Figure A.4: Heidelberg sled impact 6.7m/s – force plate response

Table A.1: Heidelberg sled Impact 6.7m/s – simulated peak response summary

	Location	Units	Value	Lower Limit*	Upper Limit*
Peak Lateral Acceleration	**T1**	G's	39.7	82	122
	T12	G's	56.2	71	107
	L4	G's	382.7	64	100
	Pelvis	G's	Not measured	63	77
Peak Force	**Pelvis**	N	24828	6400	7800
*Note – Tolerances specified in ISO (1999)					

Table A.2: Heidelberg sled Impact 6.7m/s – rib fracture summary

Rib	PMHS Test Number			Simulation
	225	227	228	
1				1
2		1	1	1
3		1	1	1
4		1	1	1
5		1	1	2
6		1	1	2
7	1	1	1	2
8	1	1	1	1
9				
10		1		
11		1		
Non-struck side	0	0	0	0
Total	2	9	7	11

A.3: WSU Sled Impact – 8.89 m/s (Cavanaugh, 1990; 1993)

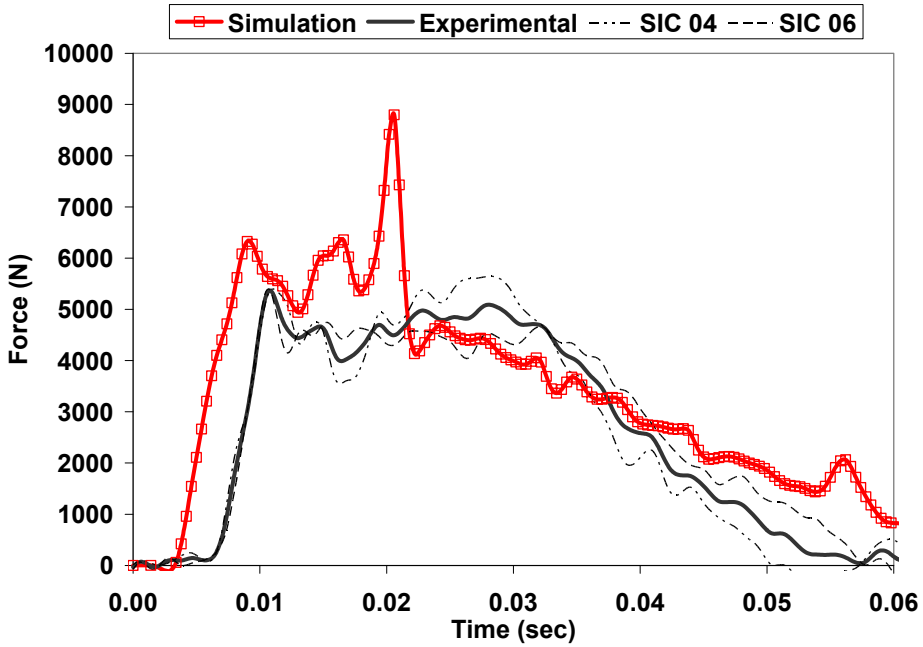

Figure A.5: Shoulder – WSU sled 8.89 m/s – Force

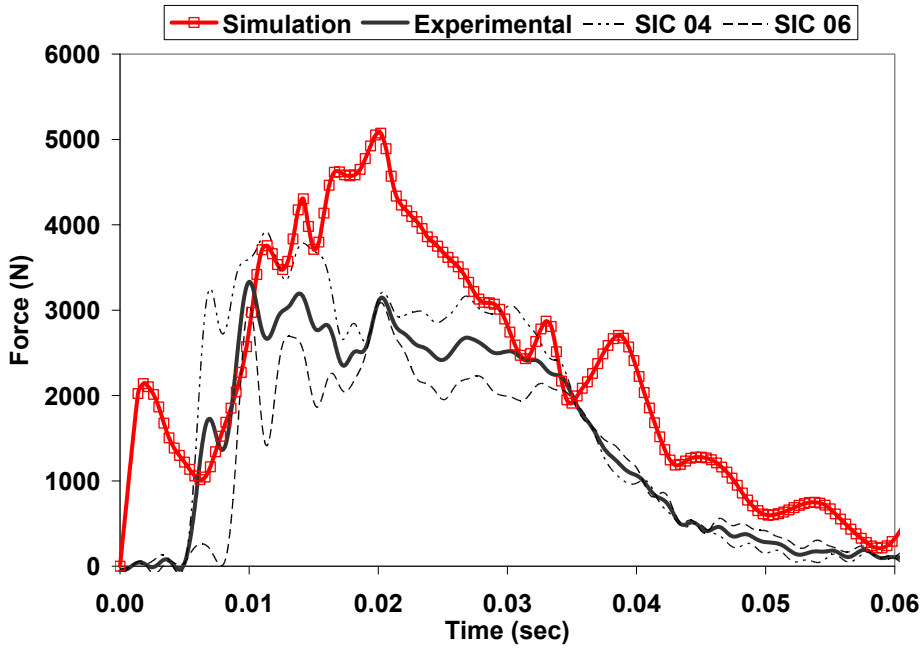

Figure A.6: Thorax – WSU sled 8.89 m/s - Force

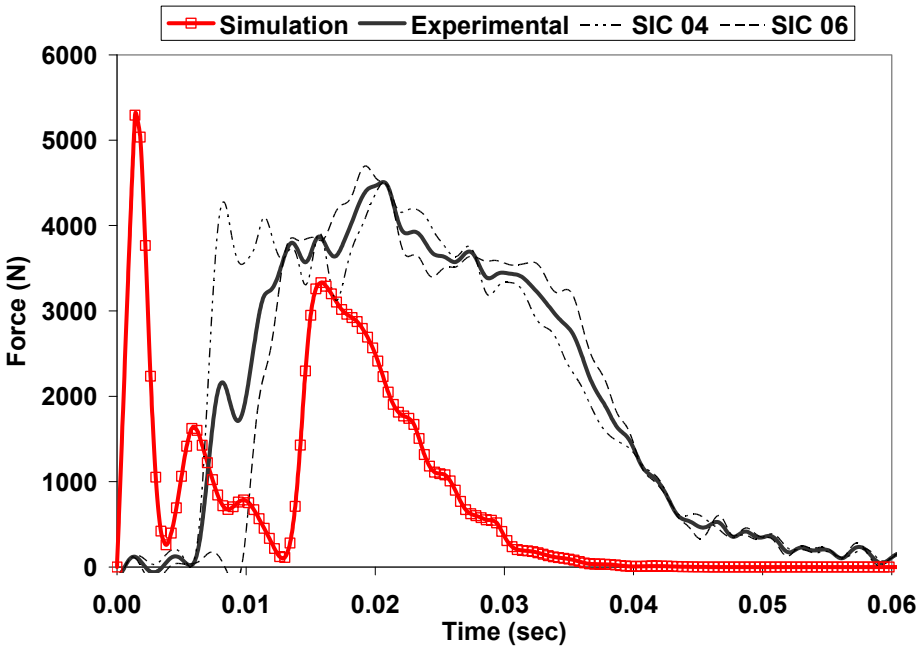

Figure A.7: Abdomen – WSU sled 8.89 m/s – Force

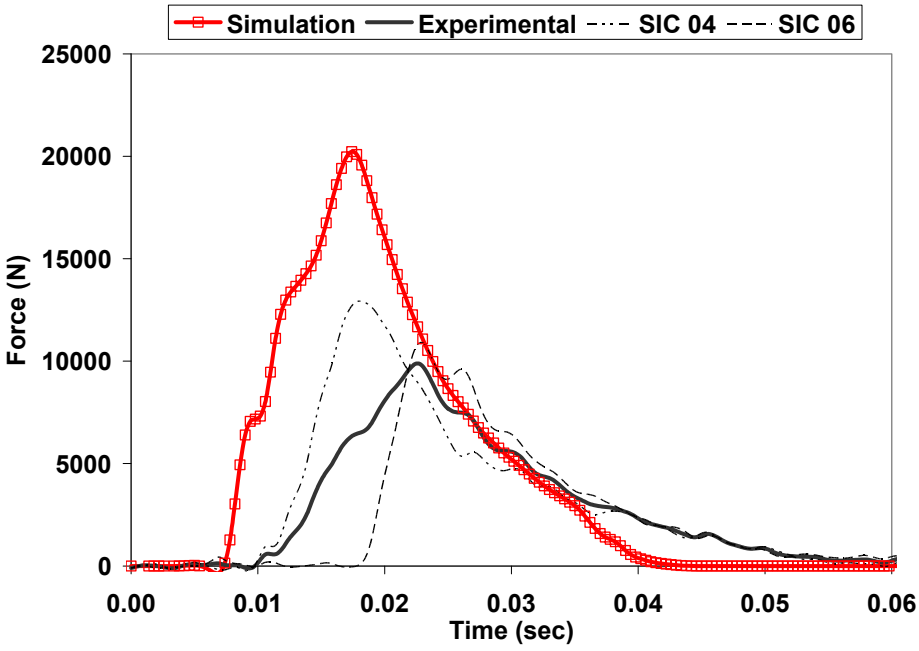

Figure A.8: Pelvis – WSU sled 8.89 m/s - Force

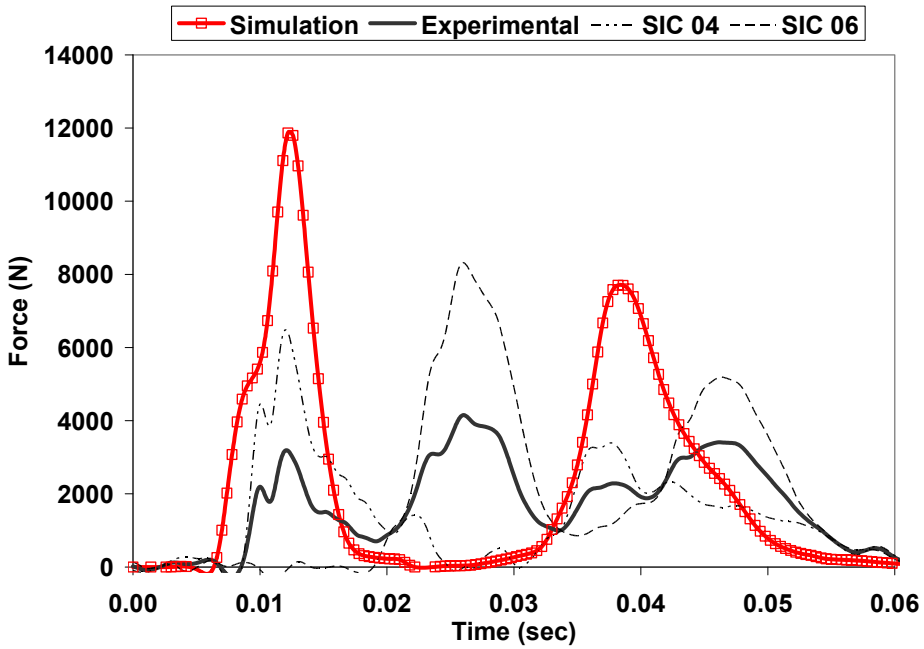

Figure A.9: Knee – WSU sled 8.89 m/s – Force

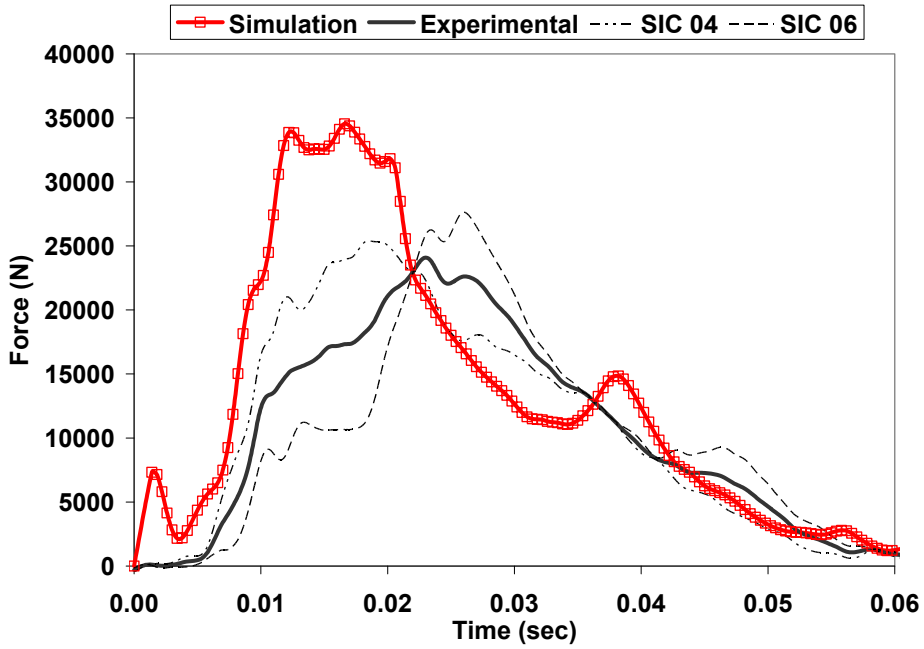

Figure A.10: Total – WSU sled 8.89 m/s - Force

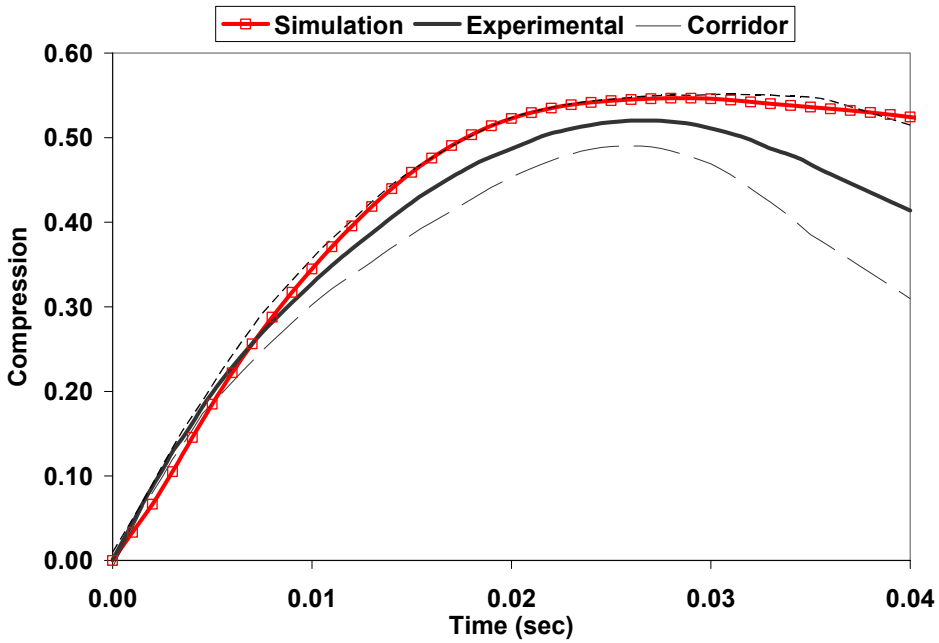

Figure A.11: Thorax – WSU sled 8.89 m/s – Compression

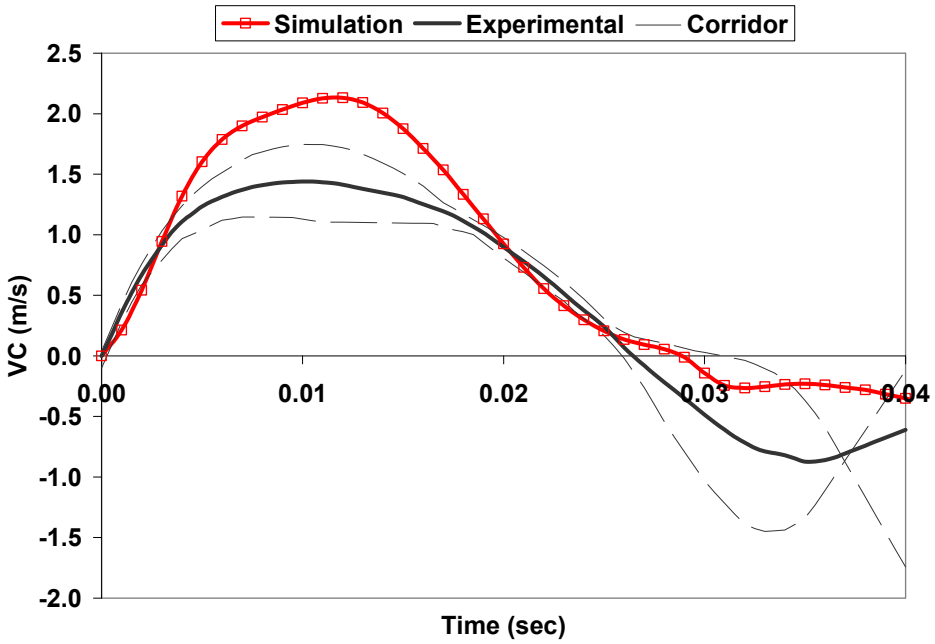

Figure A.12: Thorax – WSU sled 8.89 m/s - VC

A.4: NHTSA Sled Impact – 8.89 m/s

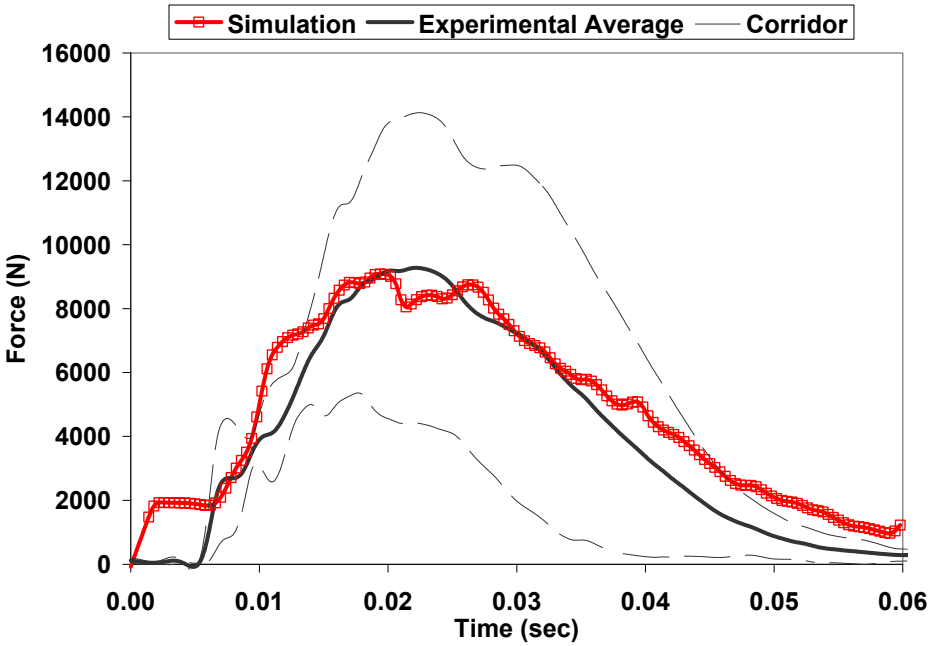

Figure A.13: Thorax – NHTSA sled 8.89 m/s – Force

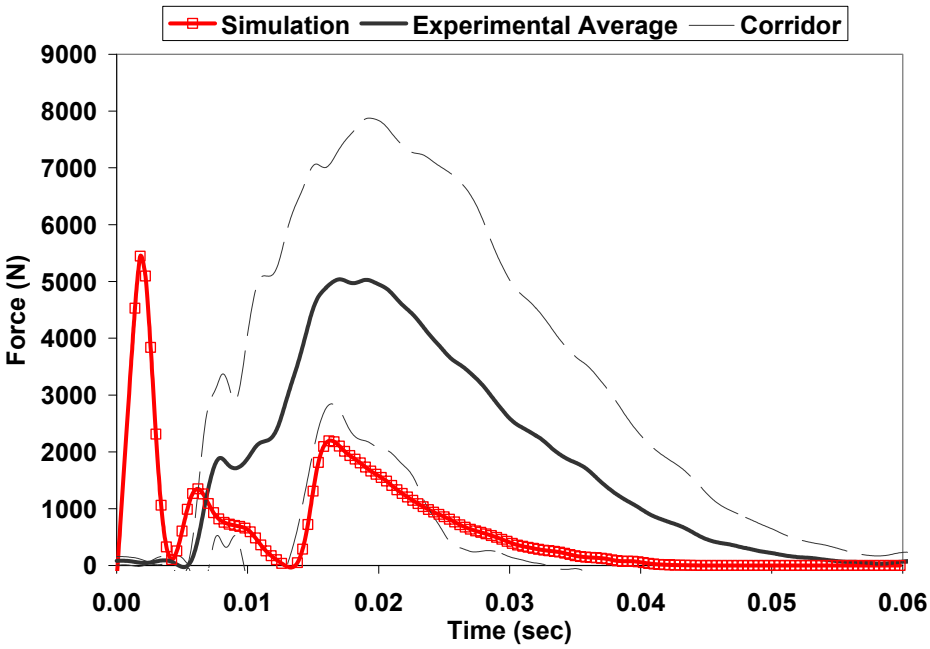

Figure A.14: Abdomen – NHTSA sled 8.89 m/s - Force

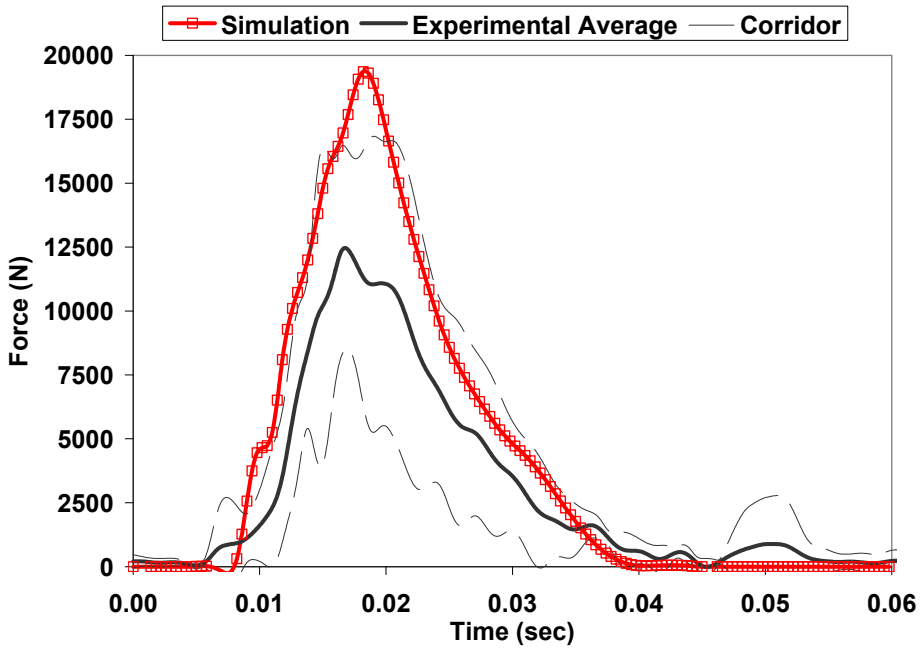

Figure A.15: Pelvis – NHTSA sled 8.89 m/s – Force

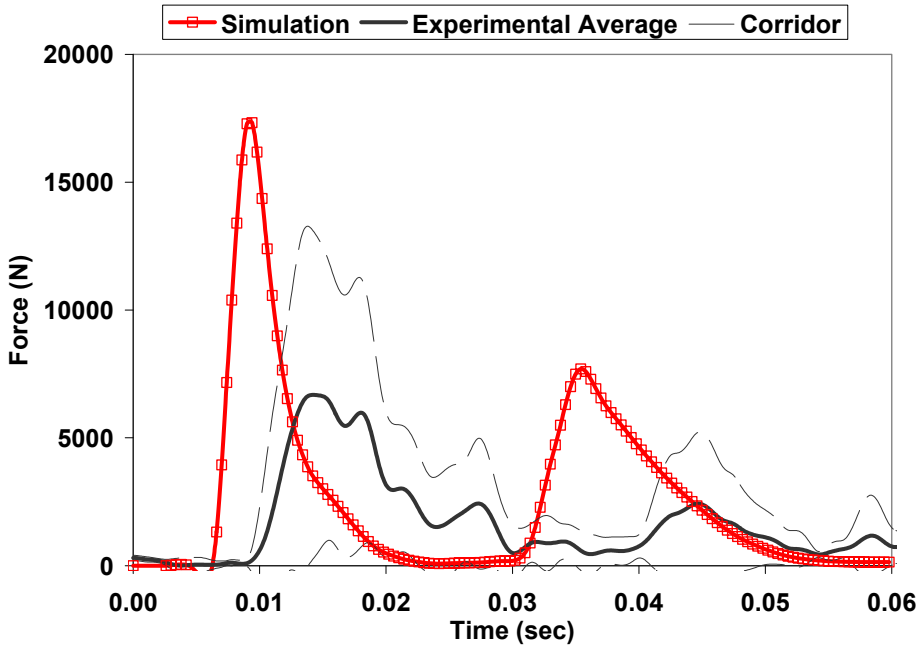

Figure A.16: Lower Limb – NHTSA sled 8.89 m/s - Force

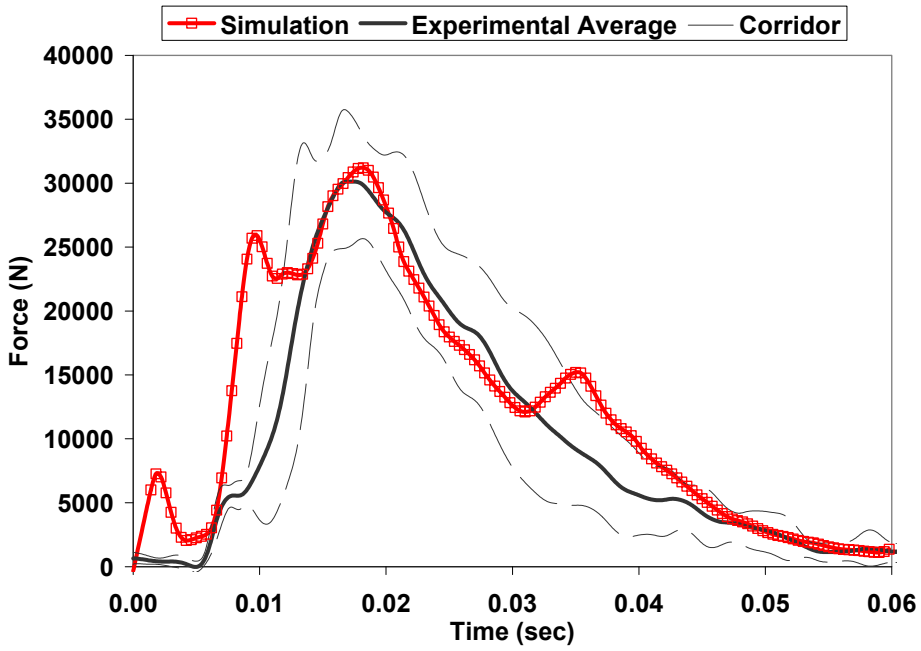

Figure A.17: Total – NHTSA sled 8.89 m/s – Force

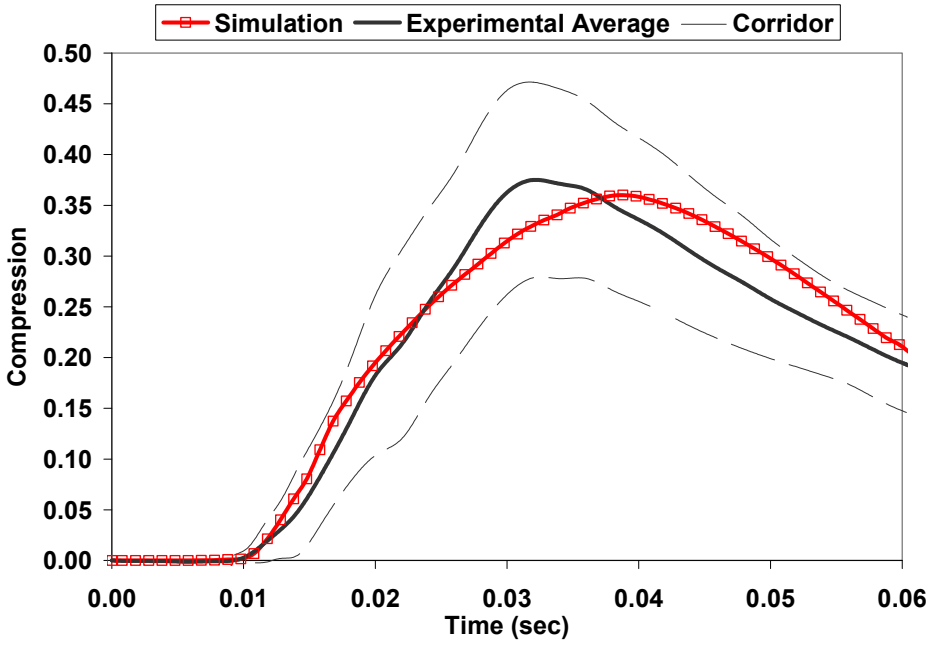

Figure A.18: Thorax – NHTSA sled 8.89 m/s – Compression, top band

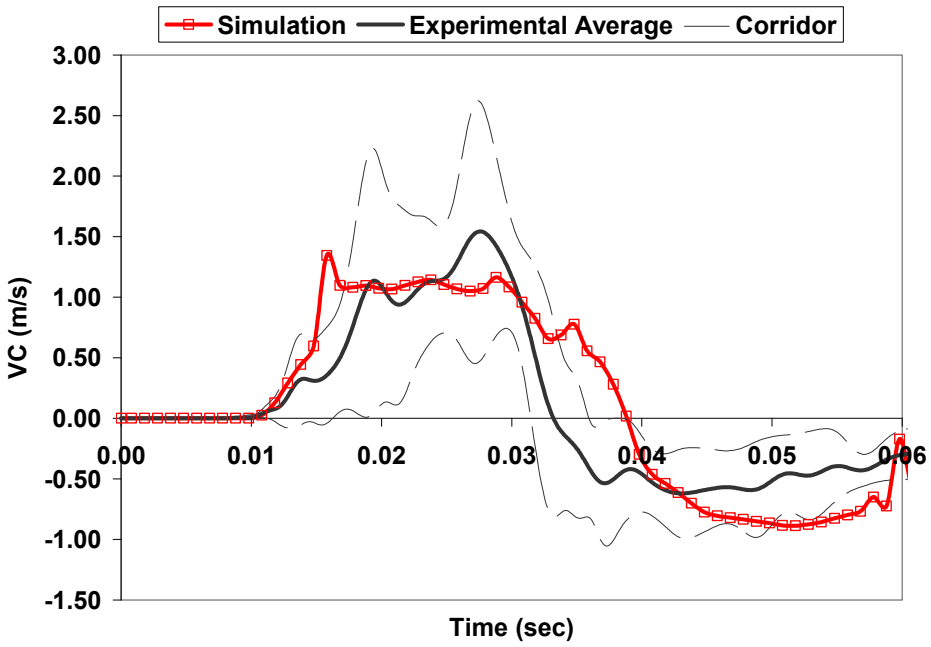

Figure A.19: Thorax – NHTSA sled 8.89 m/s – VC, top band

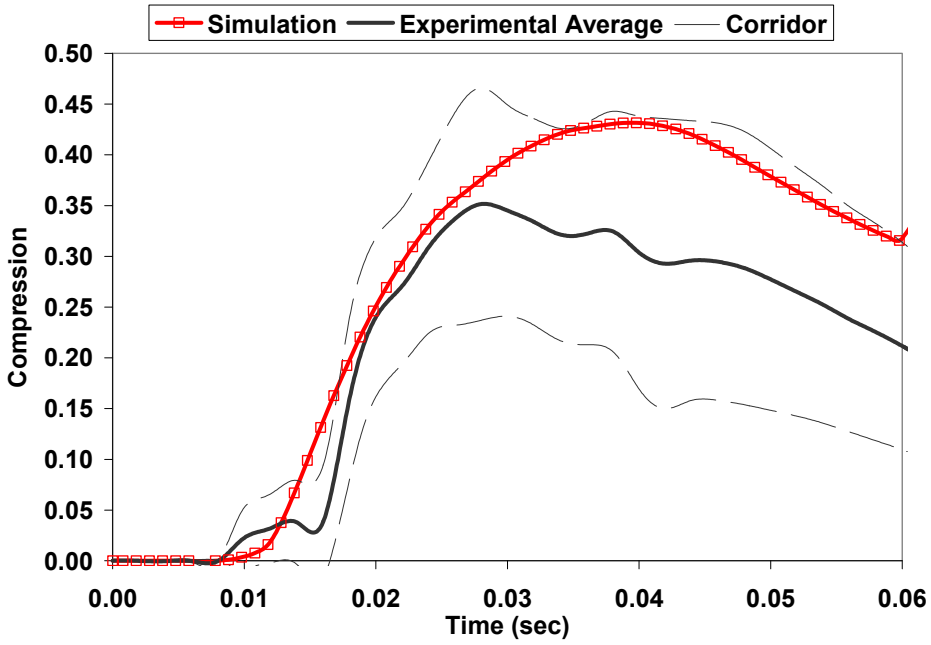

Figure A.20: Thorax – NHTSA sled 8.89 m/s – Compression, middle band

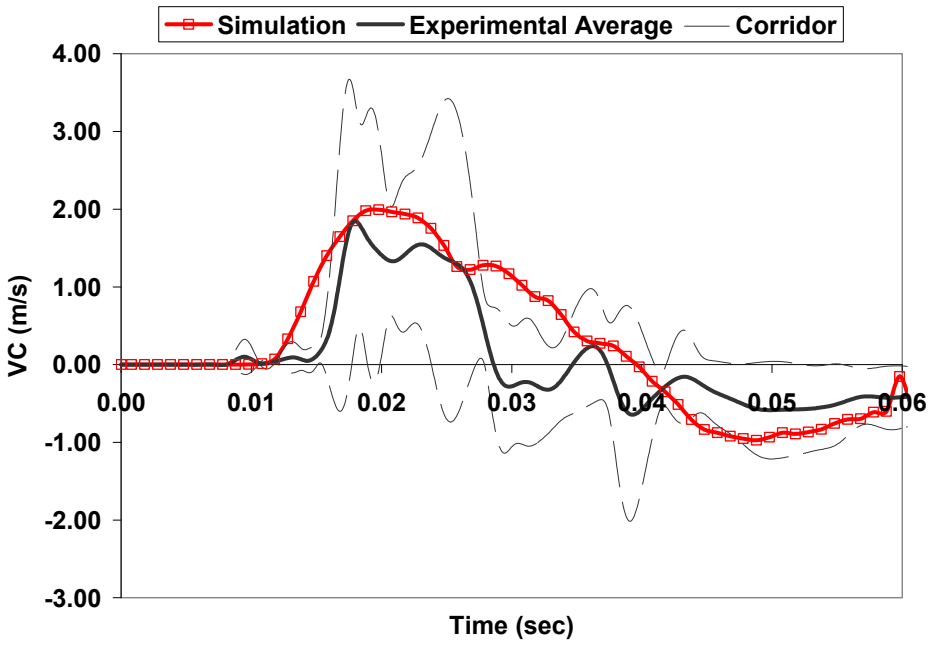

Figure A.21: Thorax – NHTSA sled 8.89 m/s – VC, middle band

A.5: ISO Shoulder Test 1 – Pendulum Impact at 4.5 m/s (ISO, 1999)

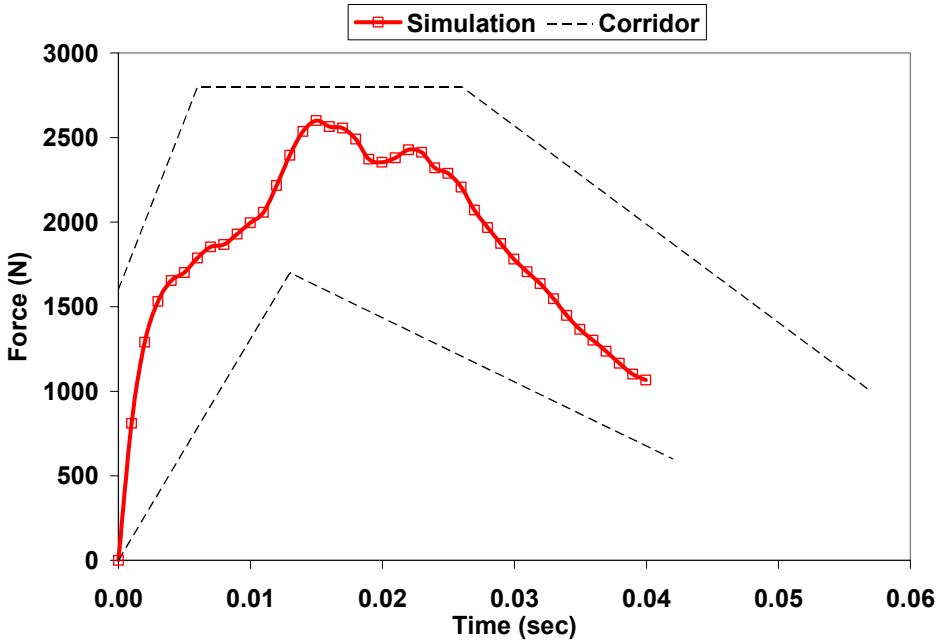

Figure A.22: Shoulder – Round pendulum 4.5 m/s - Force

Table A.1: Shoulder – Round pendulum 4.5 m/s – Max deflection (the acromin joint to the T1 vertebra)

	Maximum Deflection (mm)
Simulated	34.4
Experimental	37.5 +/- 3.5

A.6: Shoulder – Rectangular Pendulum Impacts (Compaigne et al 2003, 2005)

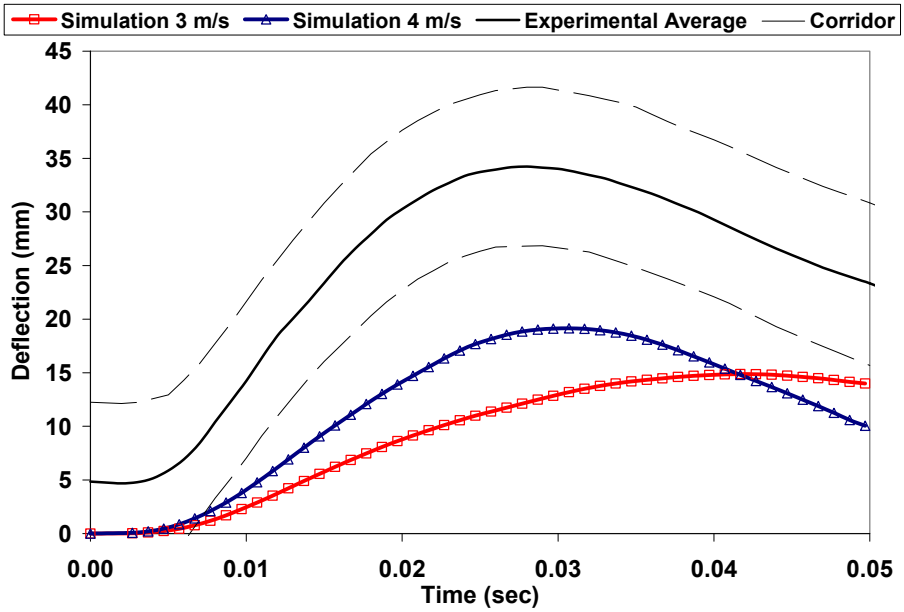

Figure A.23: Shoulder – Rectangular Pendulum 3 & 4 m/s – Deflection, acromion-acromion

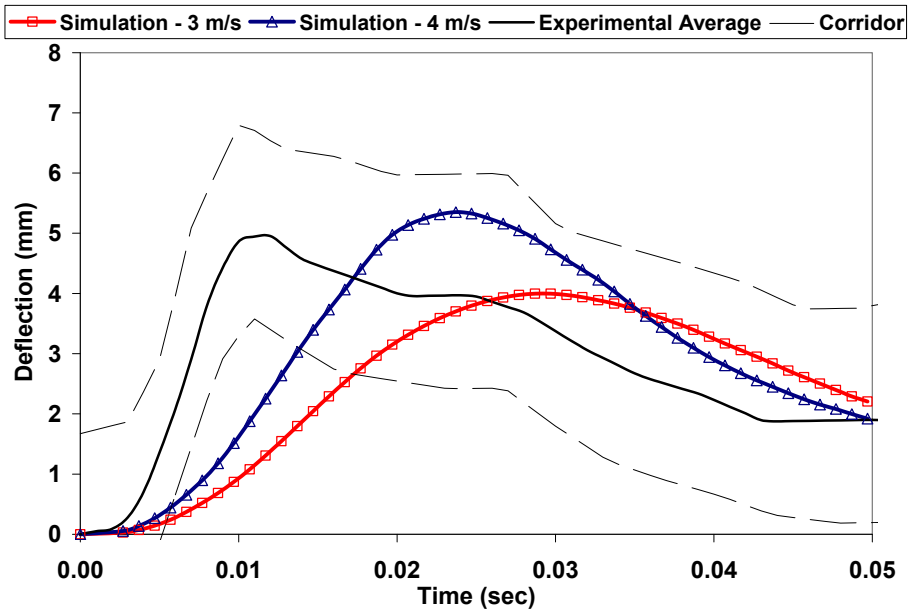

Figure A.24: Shoulder – Rectangular Pendulum 3 & 4 m/s – Deflection, acromion-sternum

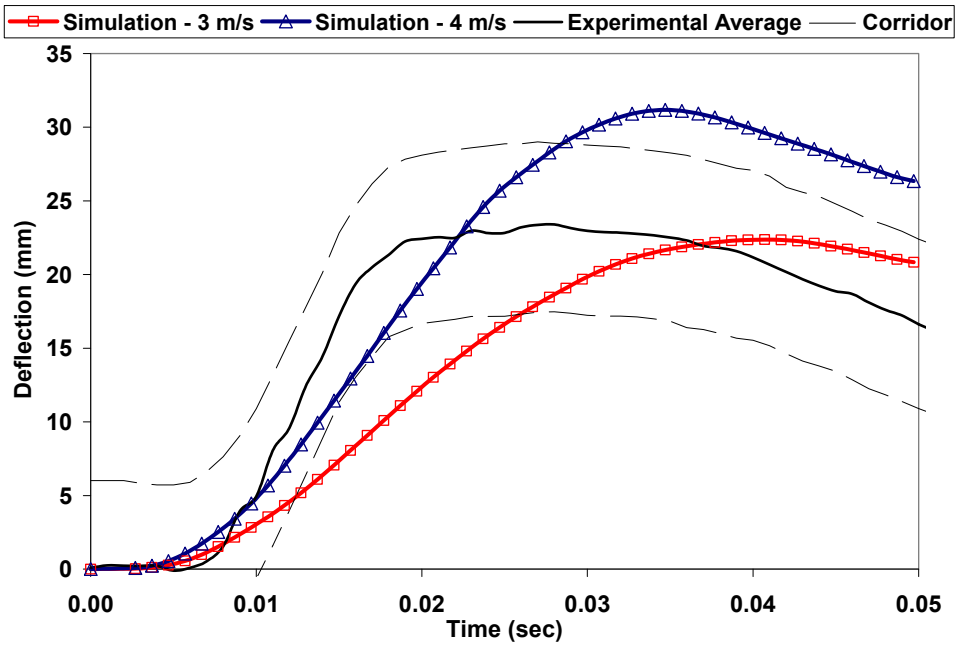

Figure A.25: Shoulder – Rectangular Pendulum 3 & 4 m/s – Deflection, acromion-T1

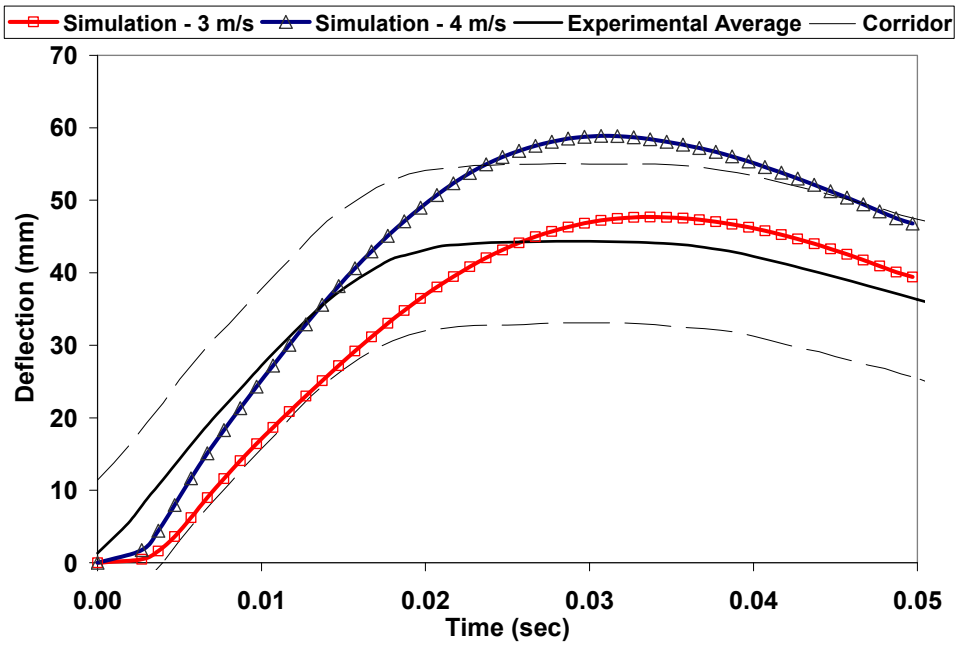

Figure A.26: Shoulder – Rectangular Pendulum 3 & 4 m/s – Deflection, impactor-T1

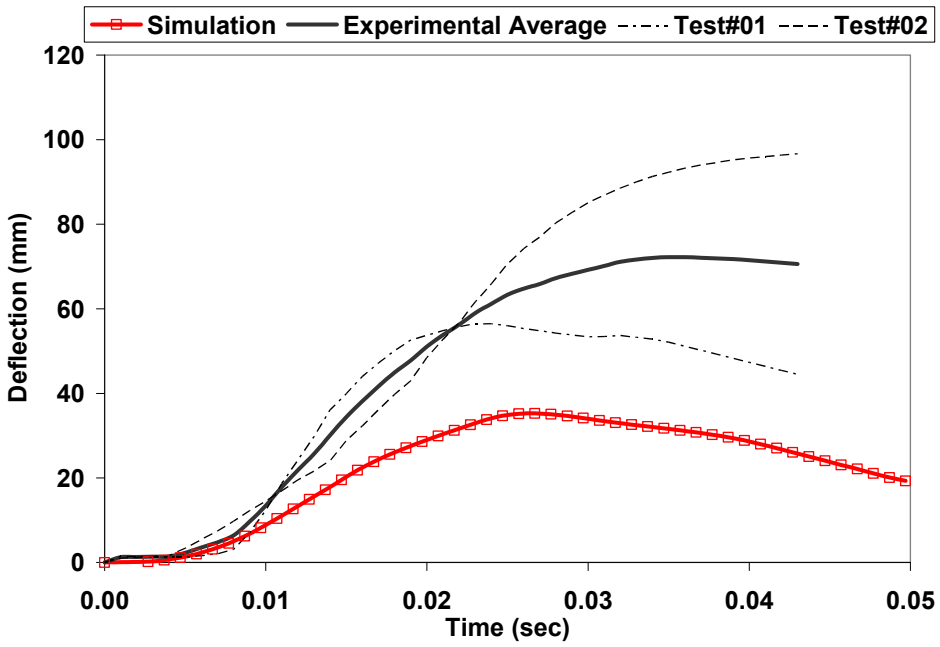

Figure A.27: Shoulder – Rectangular Pendulum 6 m/s – Deflection, acromion-acromion

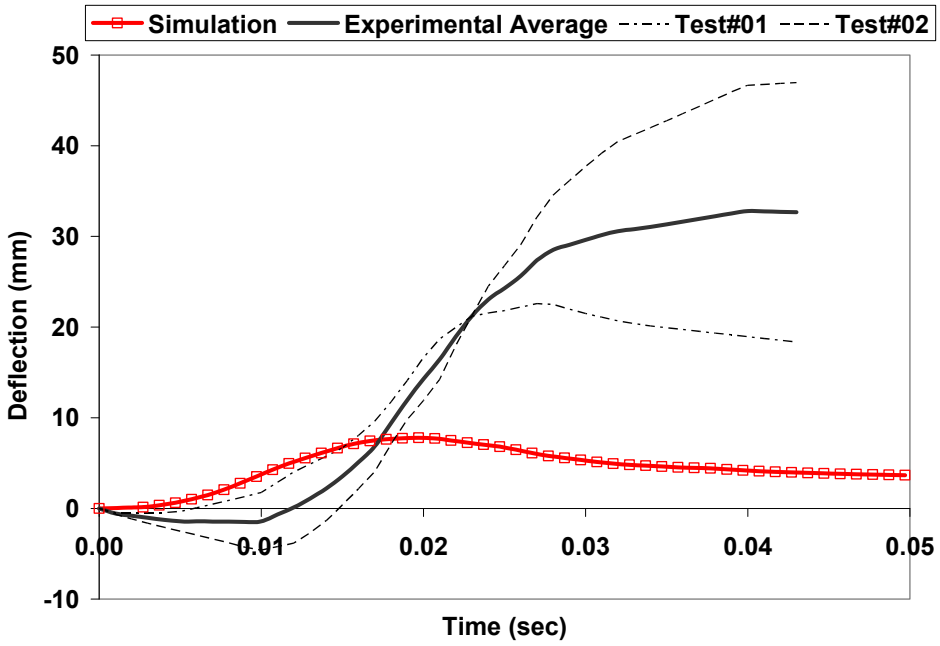

Figure A.28: Shoulder – Rectangular Pendulum 6 m/s – Deflection, acromion-sternum

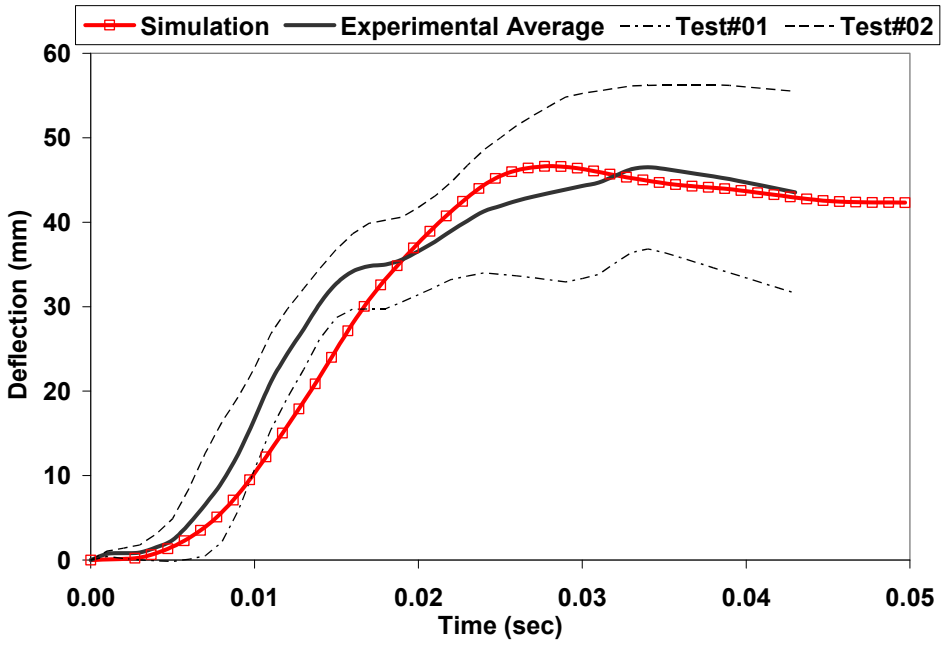

Figure A.29: Shoulder – Rectangular Pendulum 6 m/s – Deflection, acromion-T1

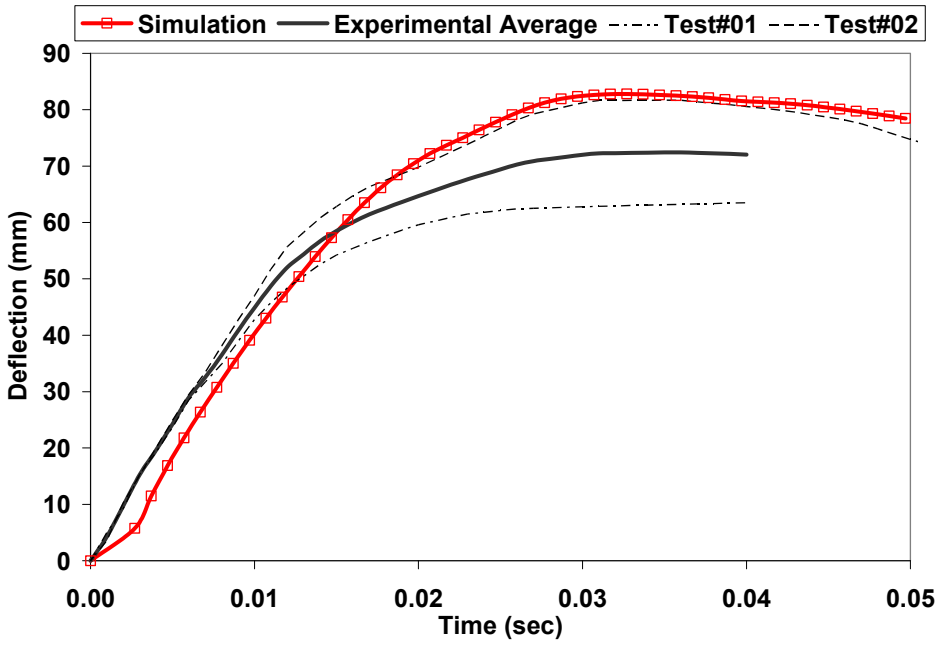

Figure A.30: Shoulder – Rectangular Pendulum 6 m/s – Deflection, impactor-T1

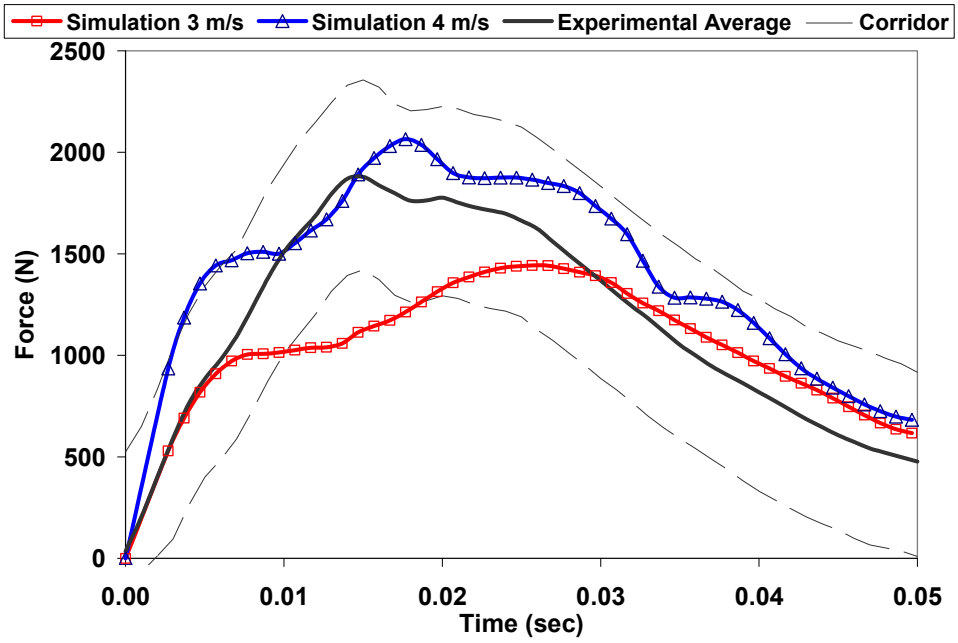

Figure A.31: Shoulder – Rectangular Pendulum 3 & 4 m/s – Force

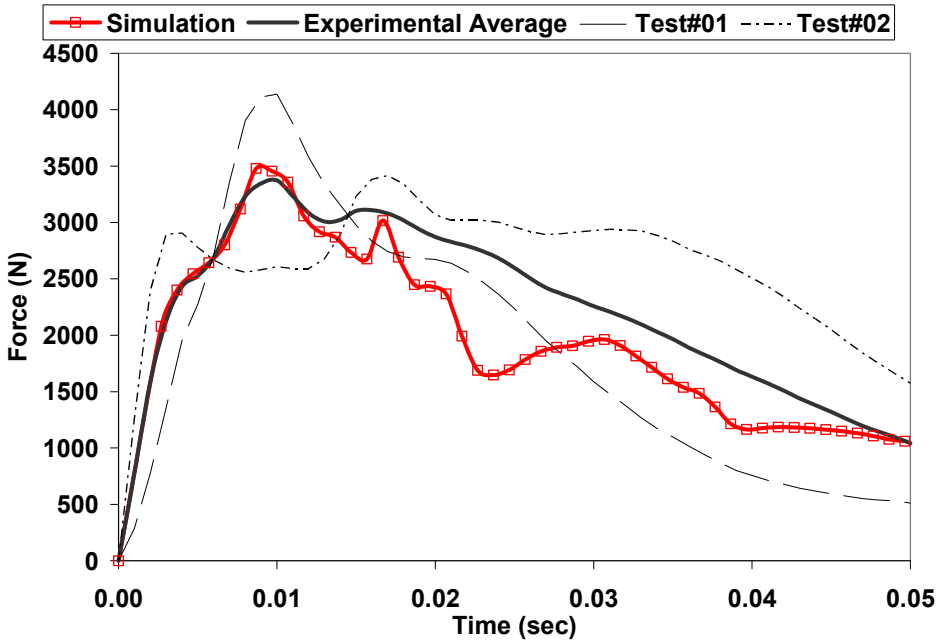

Figure A.32: Shoulder – Rectangular Pendulum 6 m/s – Force

A.7: Abdominal Oblique Pendulum Impact - 4.8 m/s & 6.8 m/s (Viano, 1989)

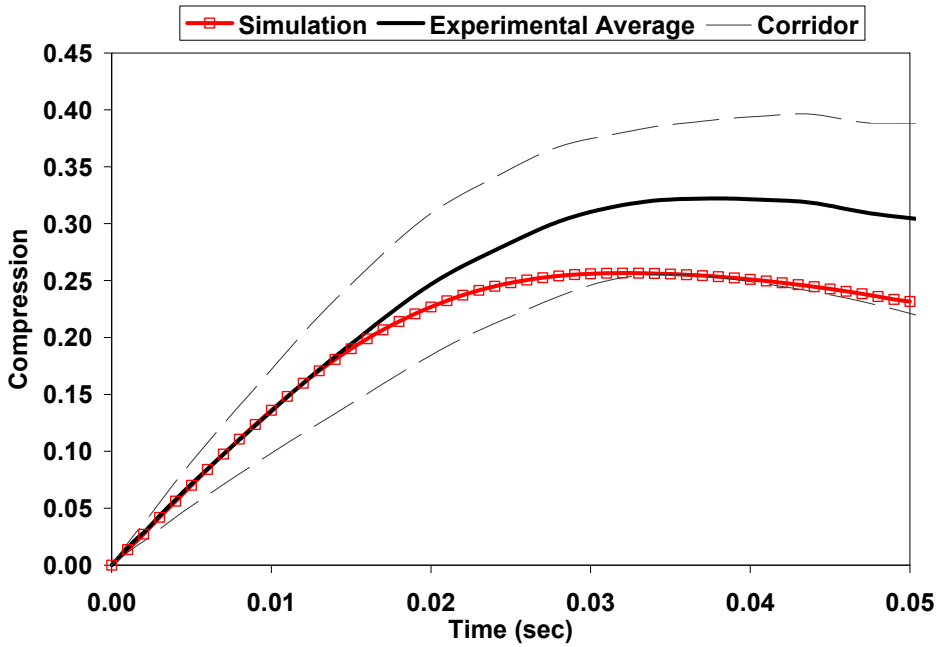

Figure A.33: Abdomen – Oblique Pendulum 4.8 m/s – Compression

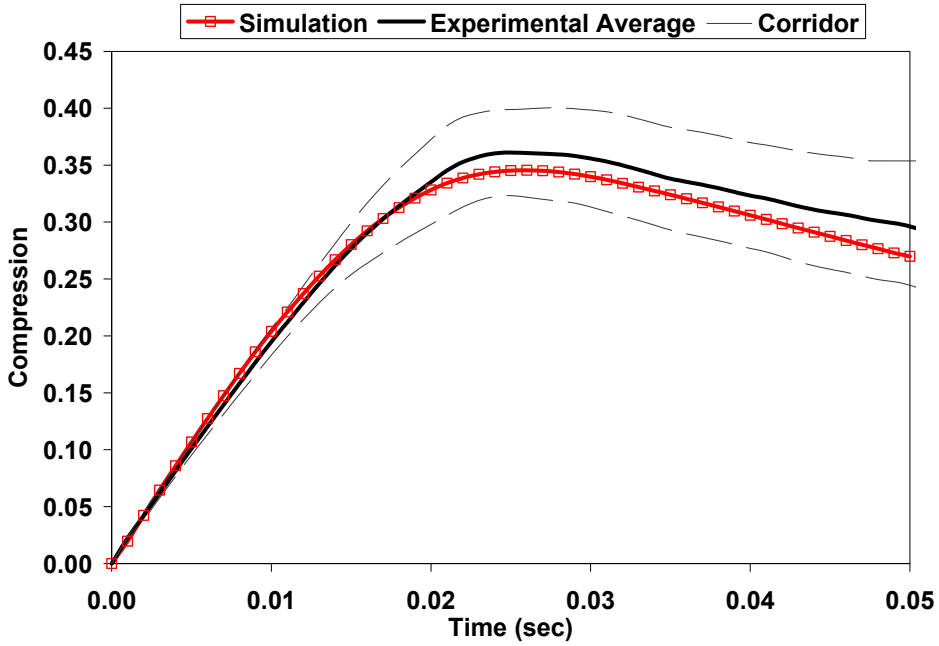

Figure A.34: Abdomen – Oblique Pendulum 6.8 m/s – Compression

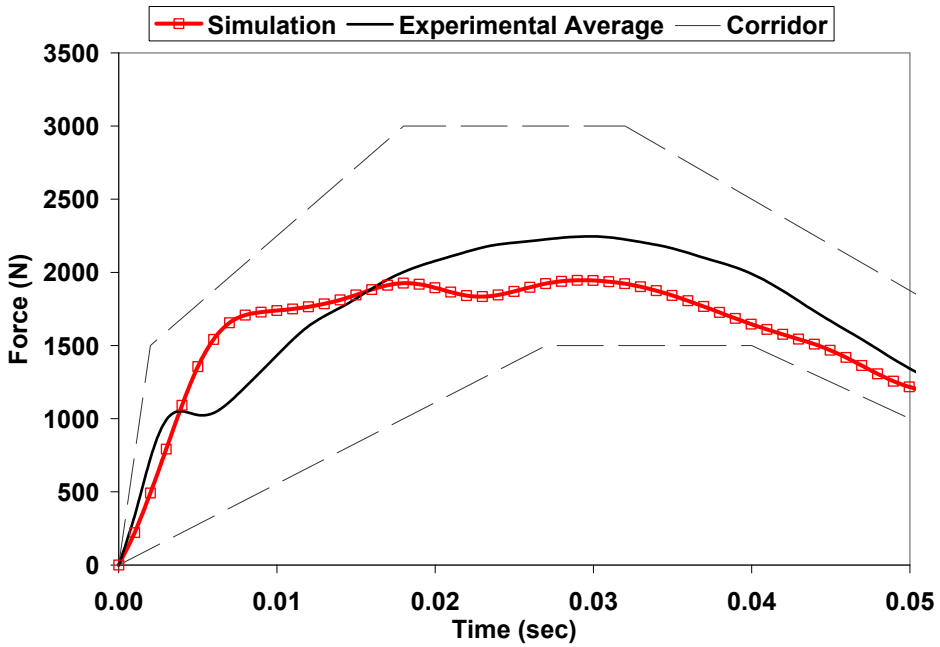

Figure A.35: Abdomen – Oblique Pendulum 4.8 m/s – Force

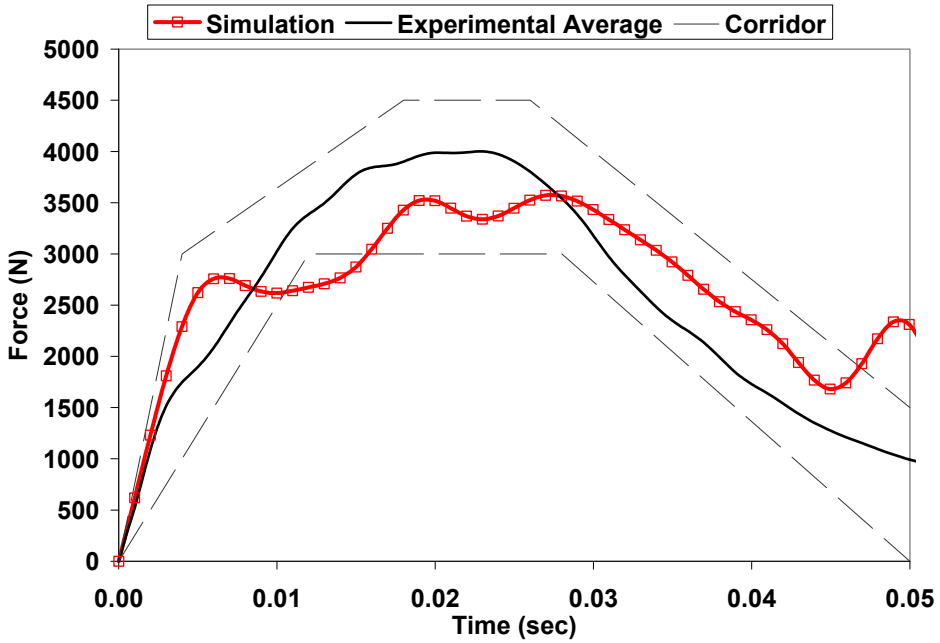

Figure A.36: Abdomen – Oblique Pendulum 6.8 m/s – Force

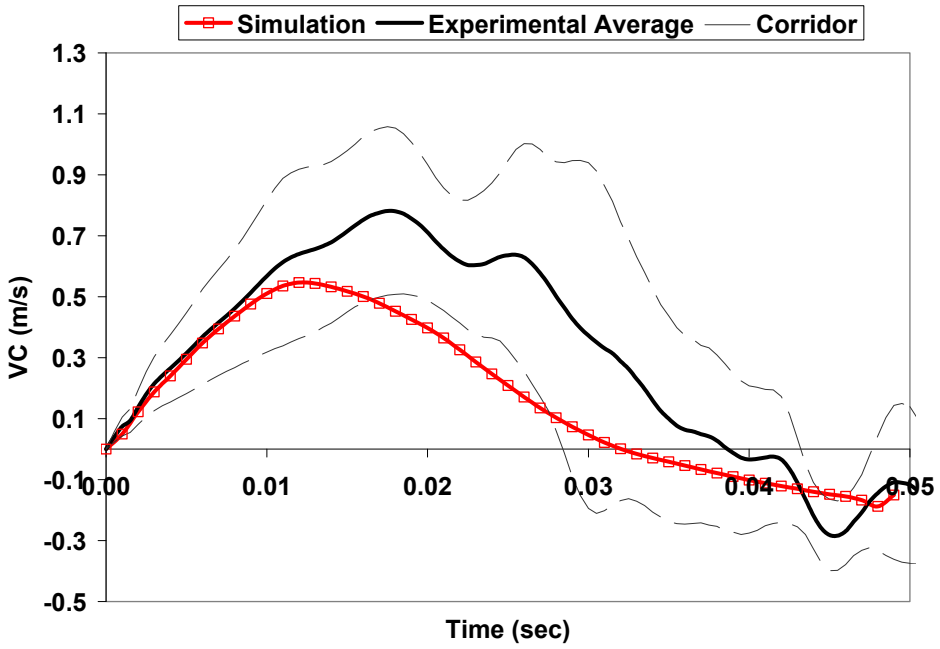

Figure A.37: Abdomen – Oblique Pendulum 4.8 m/s – VC

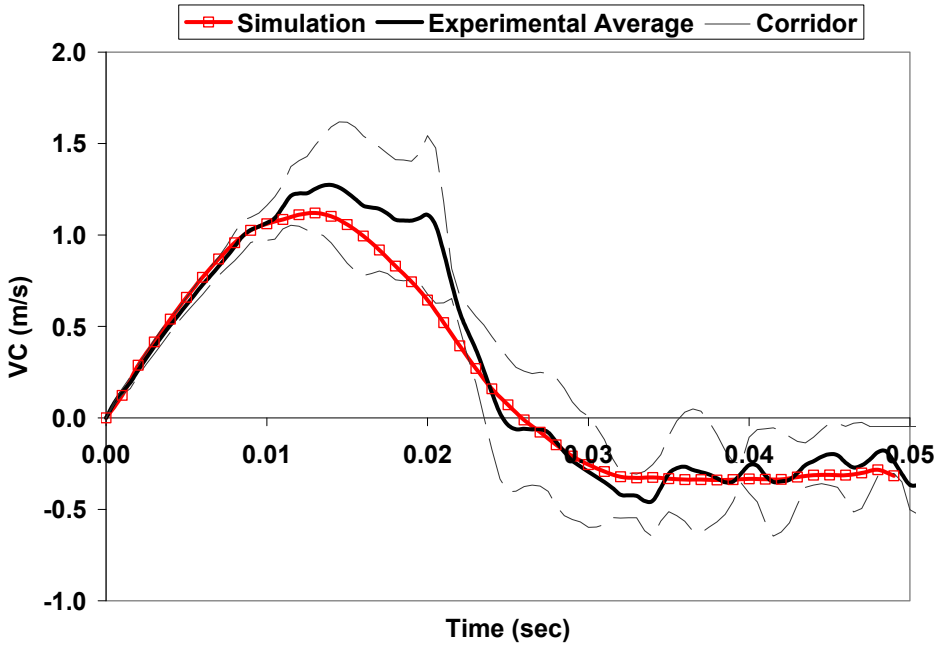

Figure A.38: Abdomen – Oblique Pendulum 6.8 m/s – VC

A.8: ISO Pelvis 1 & 2 – Spherical Impact (ISO, 1999)

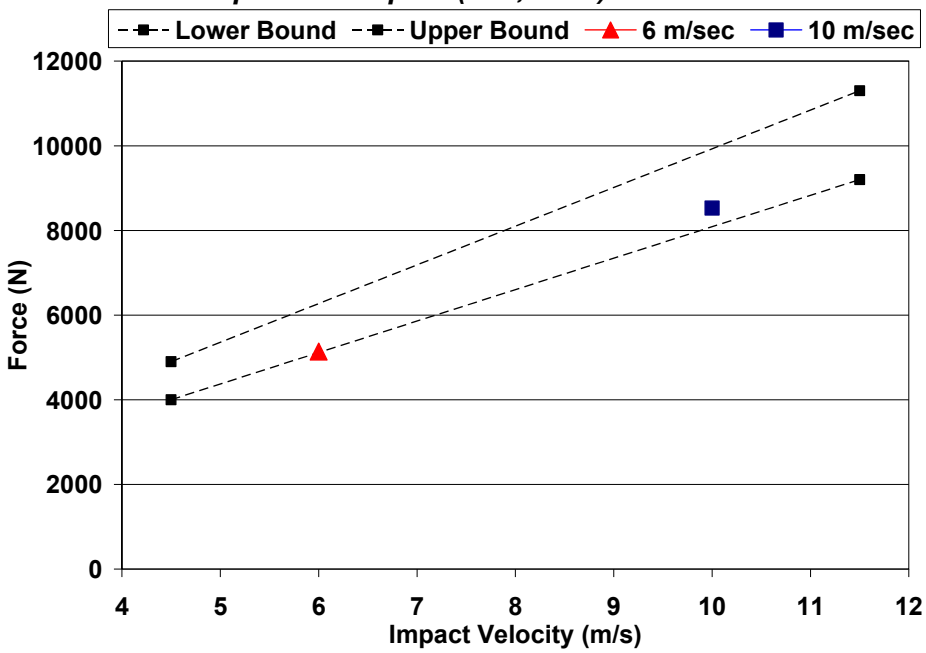

Figure A.39: Pelvis - Spherical pendulum 6 & 10 m/s – Peak force

A.9: Pelvis Round Pendulum Impact – 4.8 m/s & 9.7 m/s (Viano, 1989)

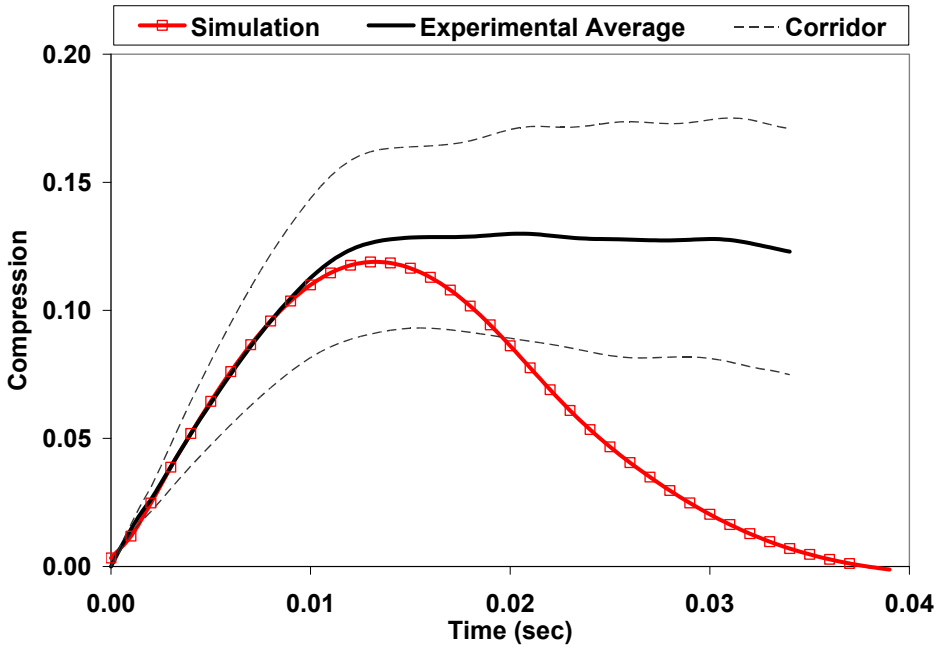

Figure A.40: Pelvis - Round pendulum 4.8 m/s – Compression

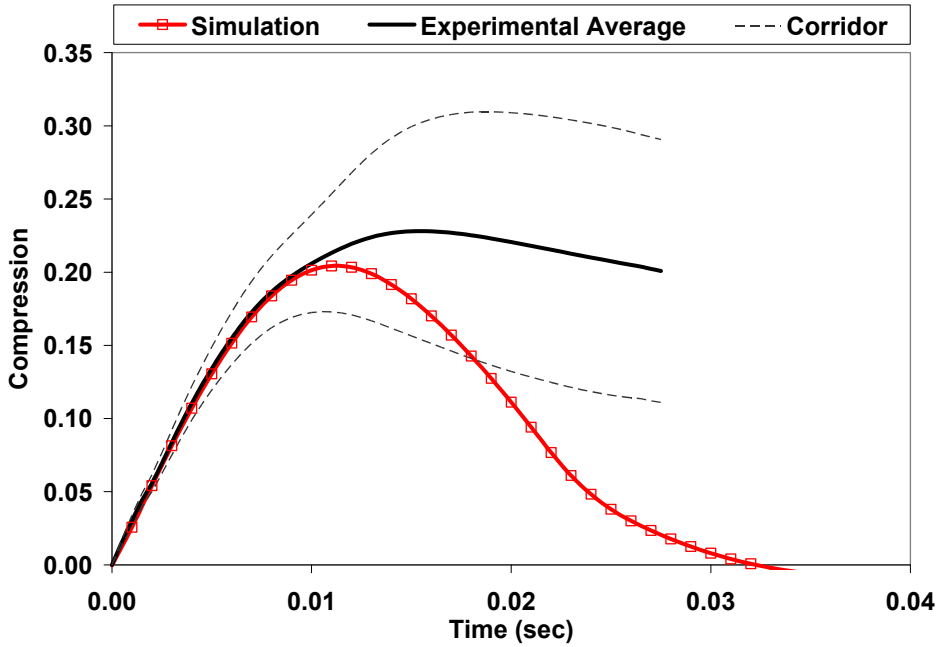

Figure A.41: Pelvis - Round pendulum 9.7 m/s – Compression

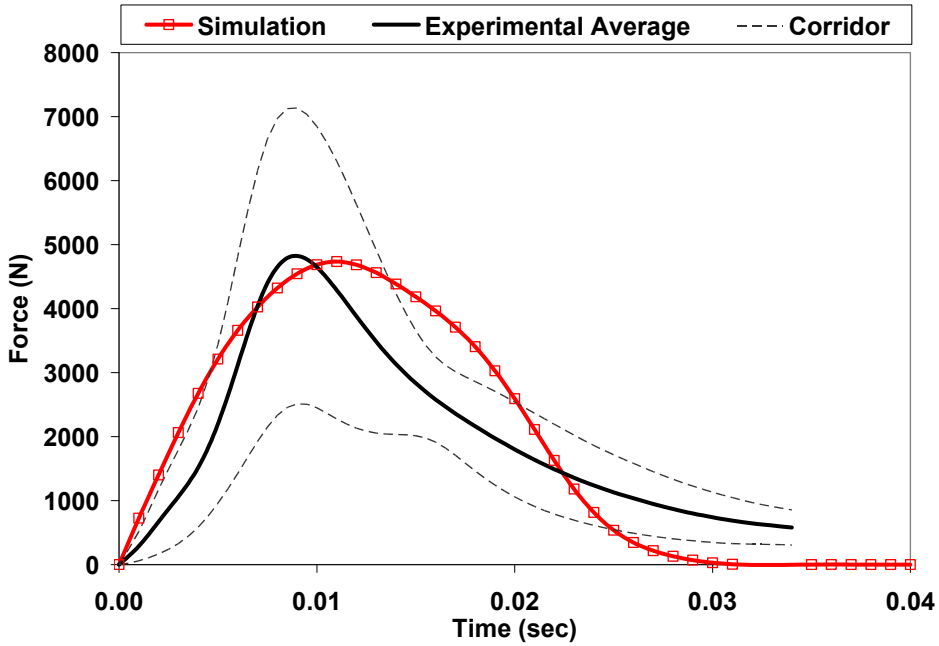

Figure A.42: Pelvis - Round pendulum 4.8 m/s – Force

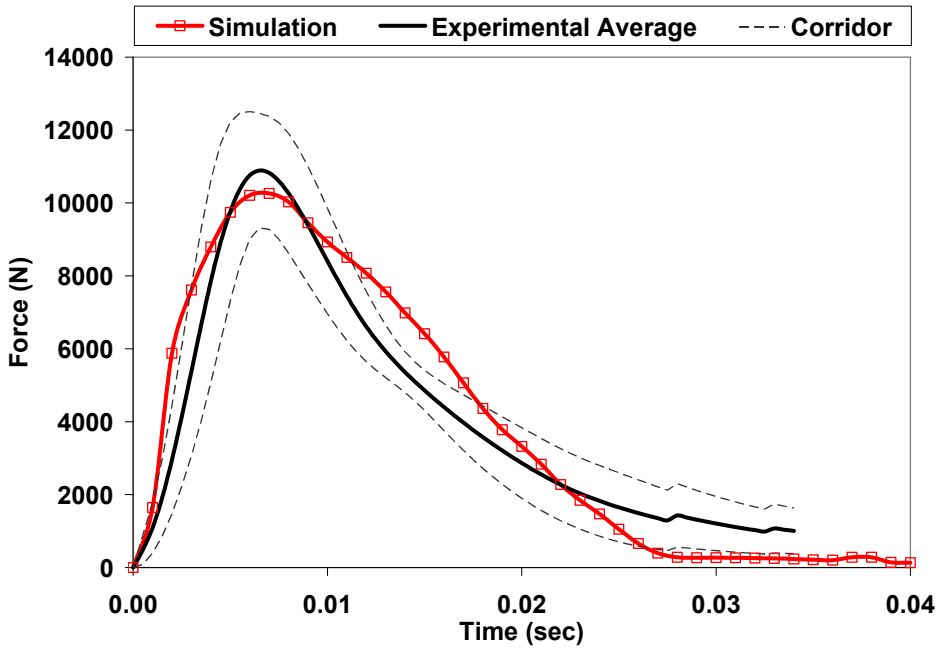

Figure A.43: Pelvis - Round pendulum 9.7 m/s – Force

Appendix B

Simulation Results, Lung Response

The following appendix contains the pendulum and sled impact results that were simulated but were not presented in details in Chapter 5.

B.1: Lung response – frontal pendulum 6.7 m/s

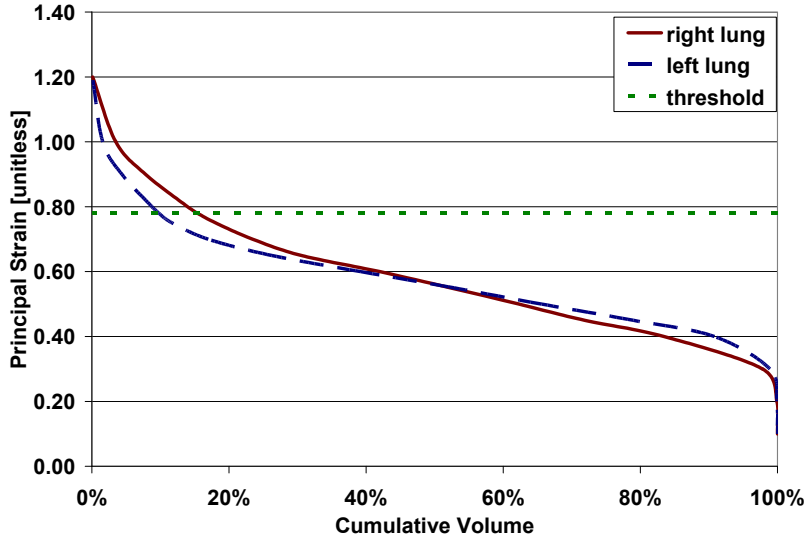

Figure B. 1: Frontal pendulum 6.7m/s - peak response distribution – principal strain

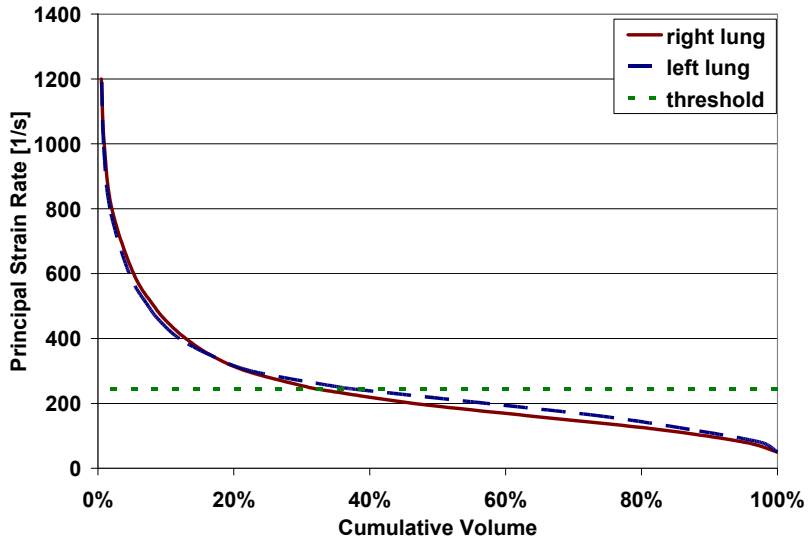

Figure B. 2: Frontal pendulum 6.7m/s - peak response distribution – principal strain rate

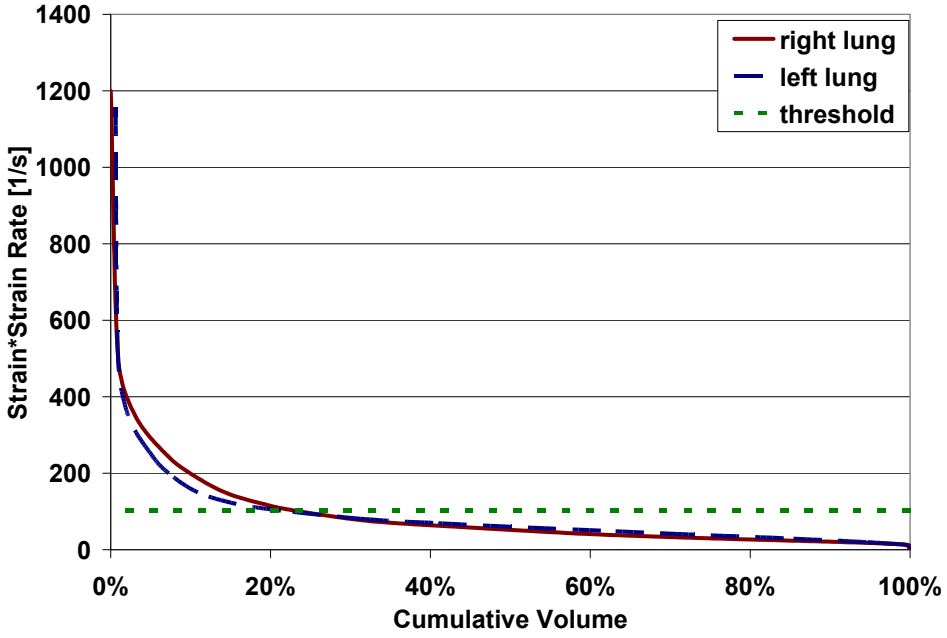

Figure B. 3: Frontal pendulum 6.7m/s - peak response distribution – the product of principal strain and strain rate

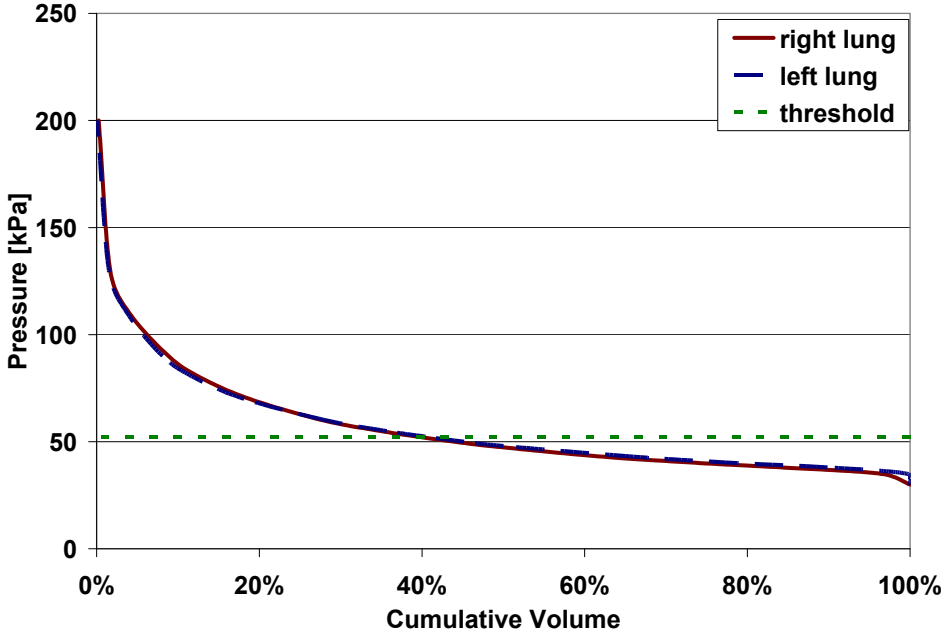

Figure B. 4: Frontal pendulum 6.7m/s - peak response distribution – pressure

B.2: Lung response – oblique pendulum 4.4 m/s

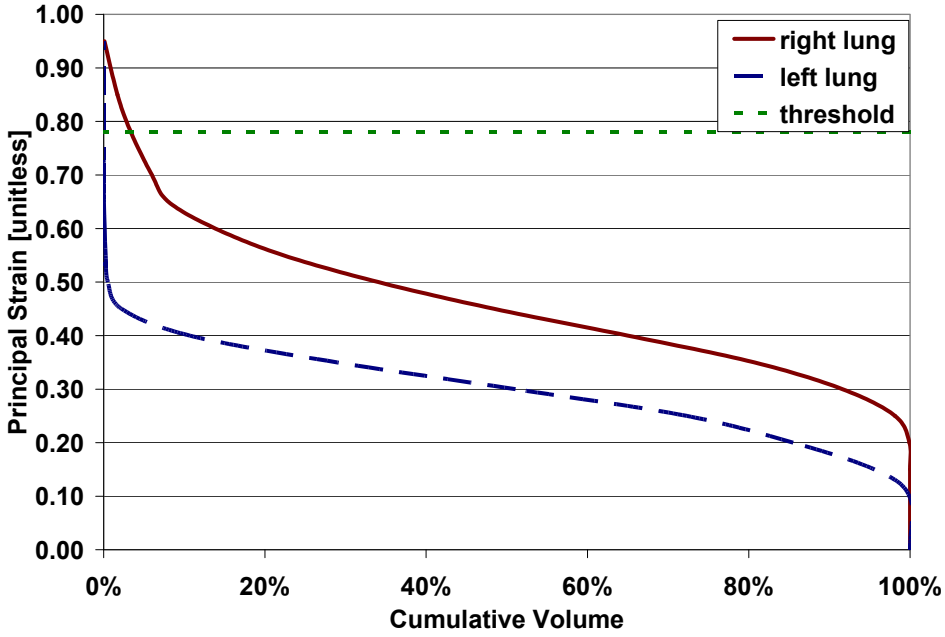

Figure B. 5: Oblique pendulum 4.4m/s - peak response distribution – principal strain

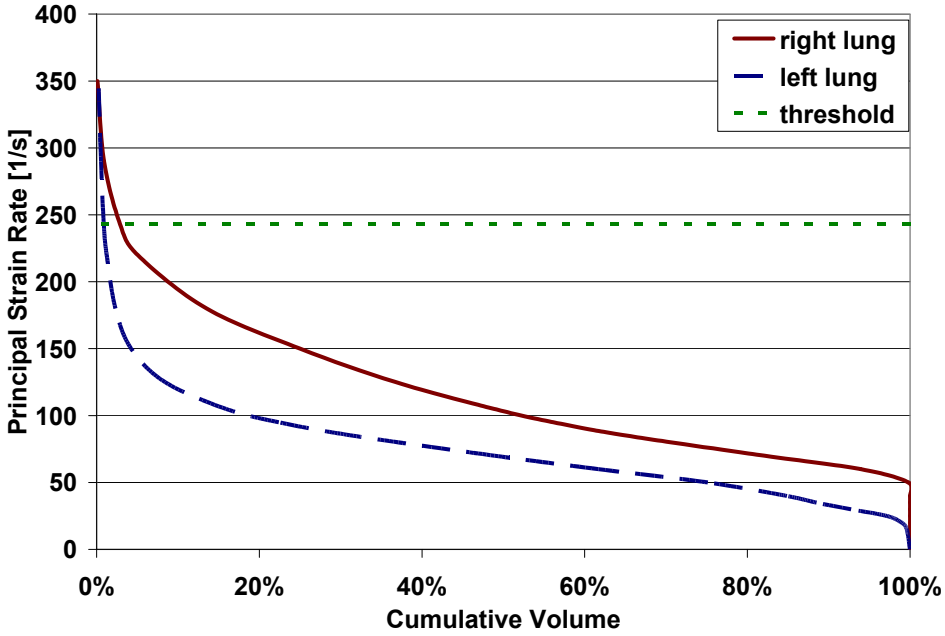

Figure B. 6: Oblique pendulum 4.4m/s - peak response distribution – principal strain rate

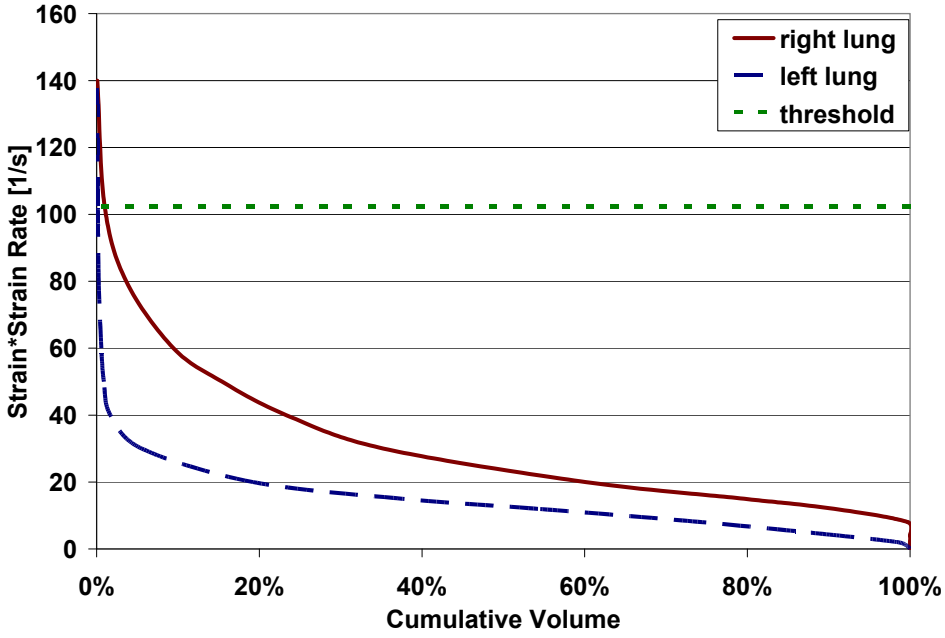

Figure B. 7: Oblique pendulum 4.4m/s - Peak response distribution – the product of principal strain and strain rate

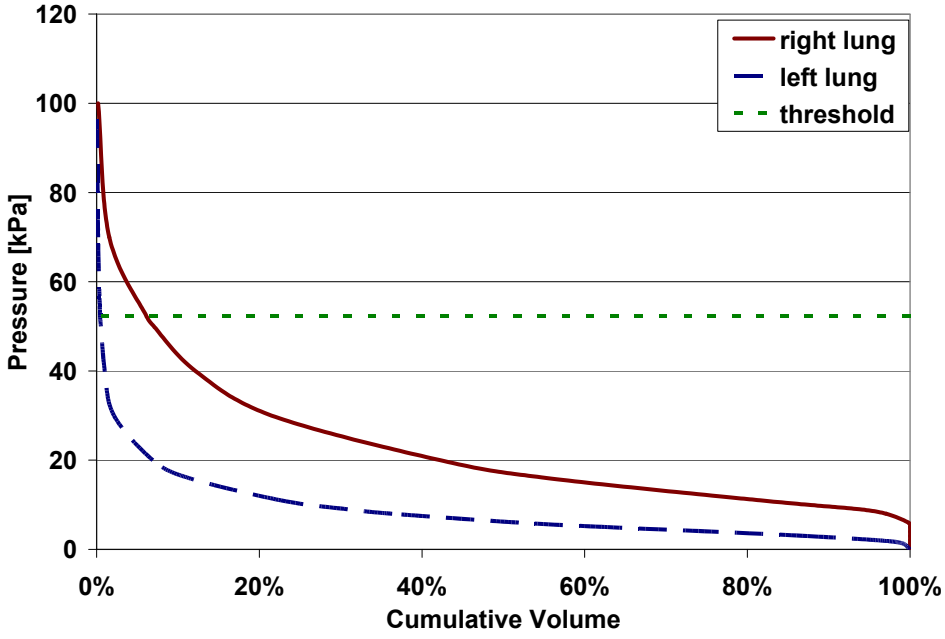

Figure B. 8: Oblique pendulum 4.4m/s - Peak response distribution – pressure

B.3: Lung response – limited stroke lateral pendulum

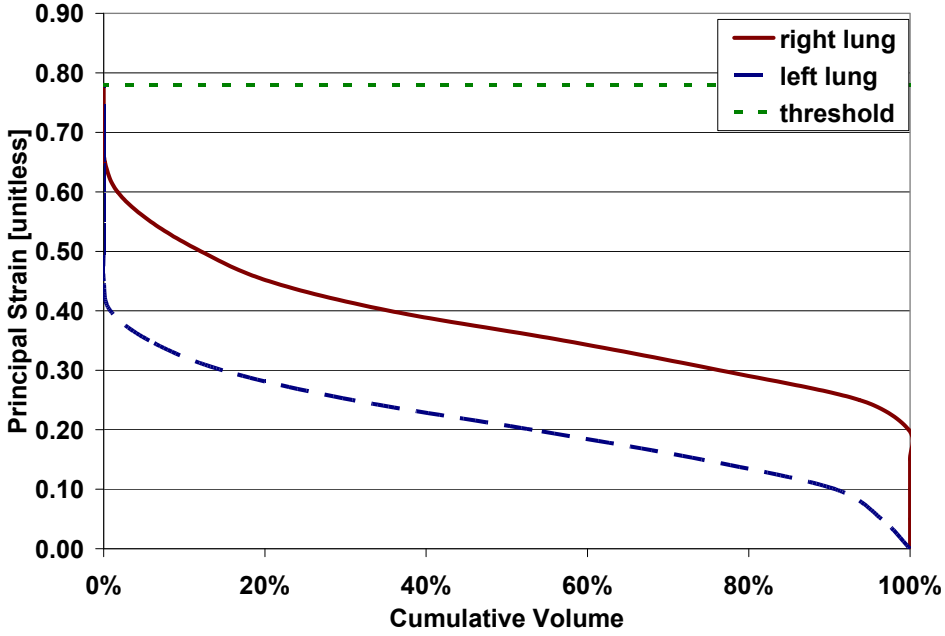

Figure B. 9: Limited-stroke lateral pendulum - Peak response distribution – principal strain

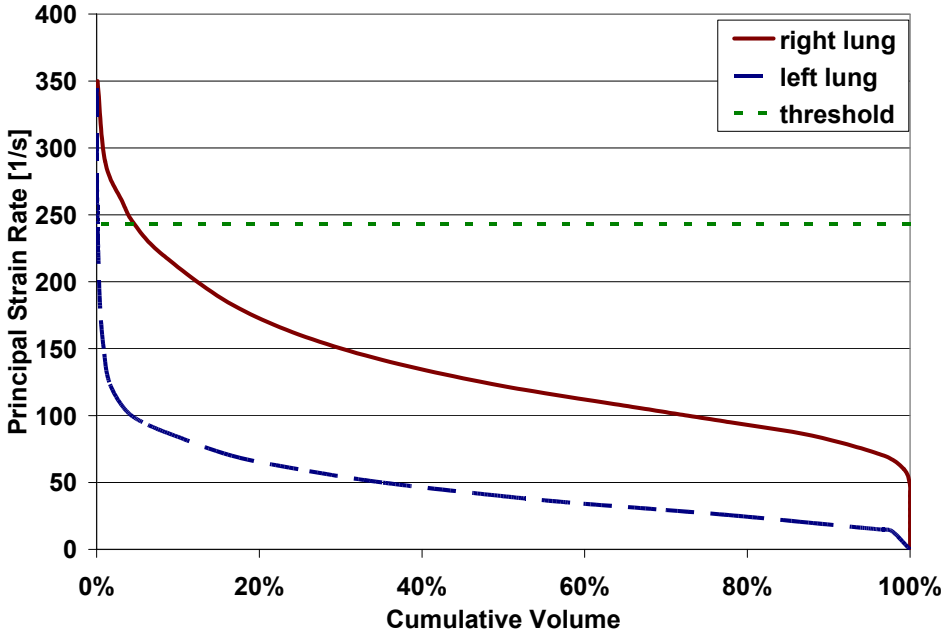

Figure B. 10: Limited-stroke lateral pendulum - Peak response distribution – principal strain rate

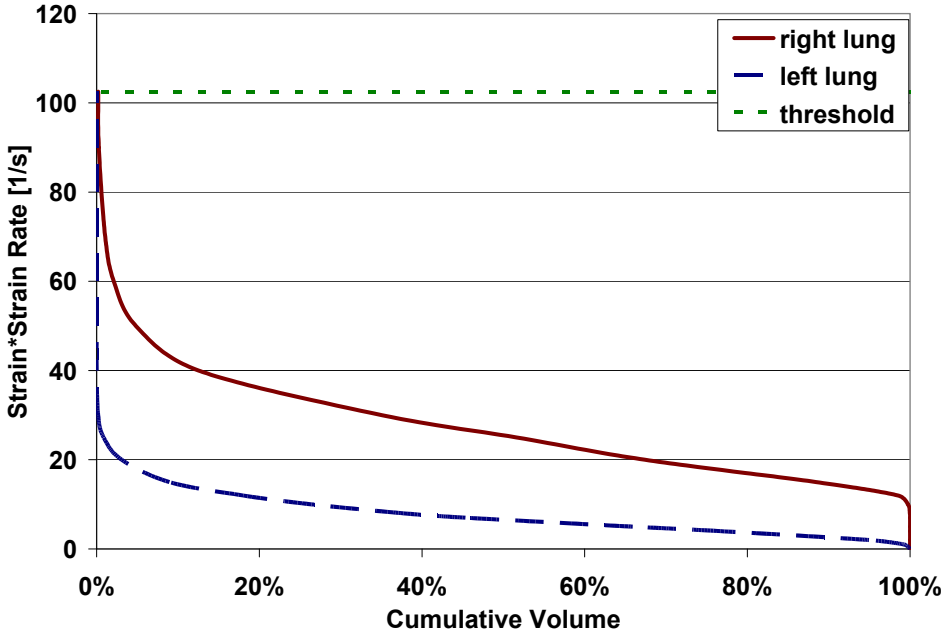

Figure B. 11: Limited-stroke lateral pendulum - Peak response distribution – the product of principal strain and strain rate

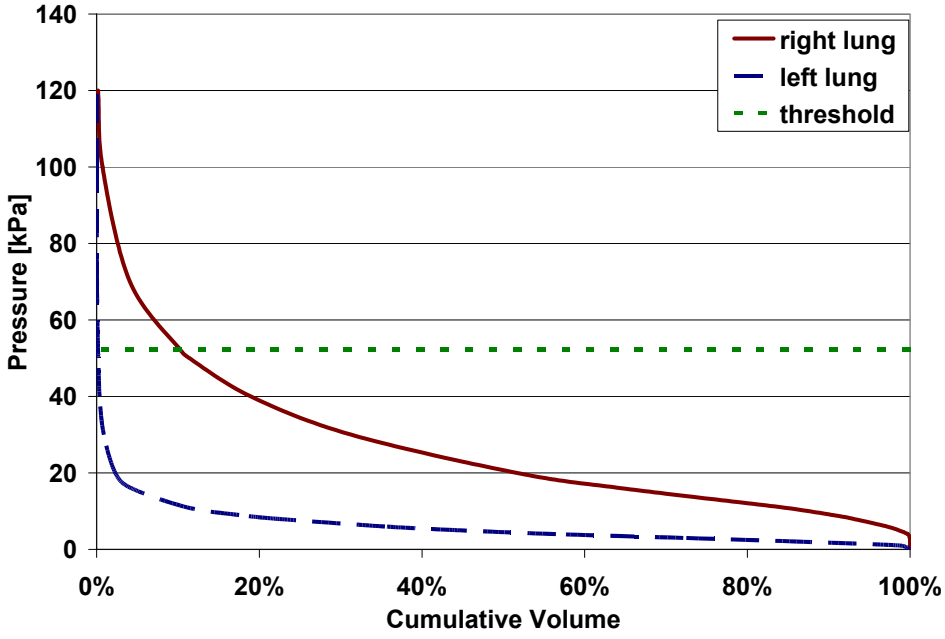

Figure B. 12: Limited-stroke lateral pendulum - Peak response distribution – pressure

B.4: Lung response – WSU 6.7 m/s

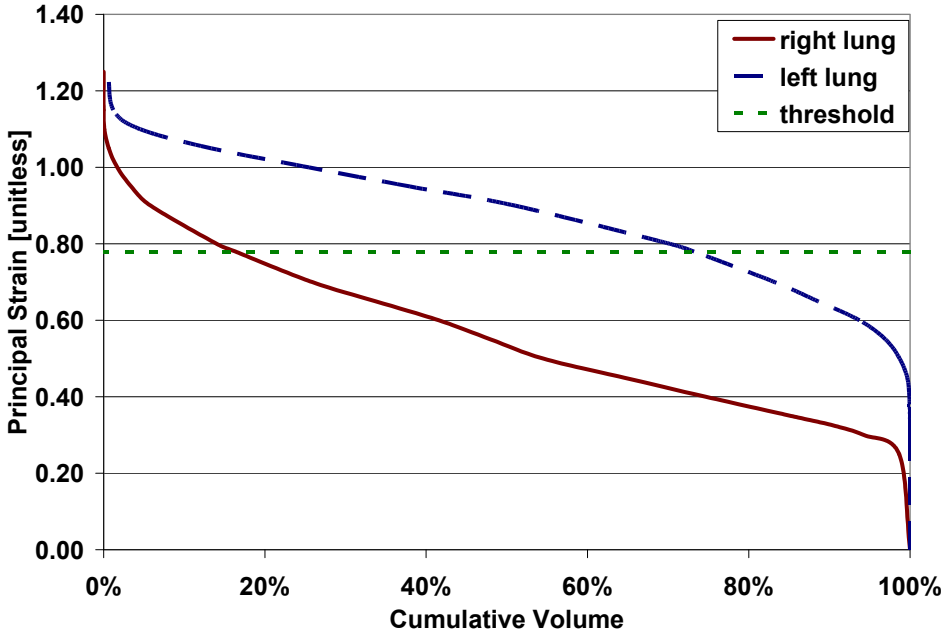

Figure B. 13: WSU sled test 6.7 m/s - Peak response distribution – principal strain

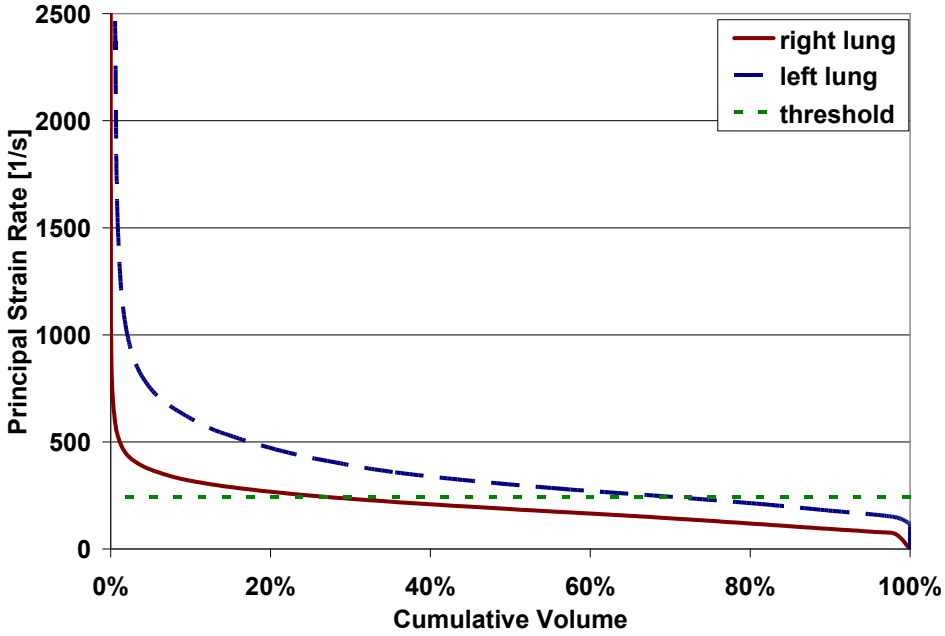

Figure B. 14: WSU sled test 6.7 m/s - Peak response distribution – principal strain rate

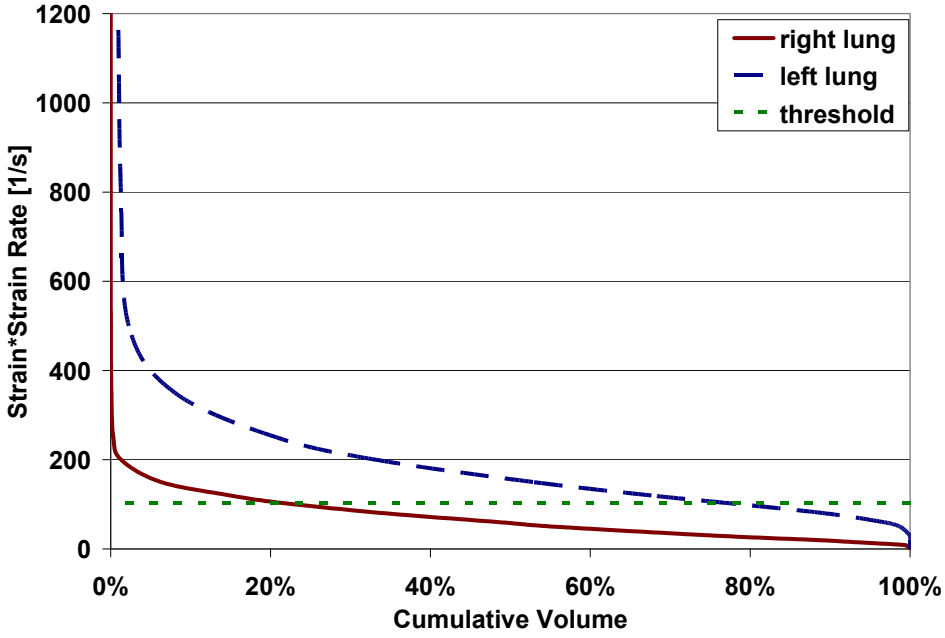

Figure B. 15: WSU sled test 6.7 m/s - Peak response distribution – the product of principal strain and strain rate

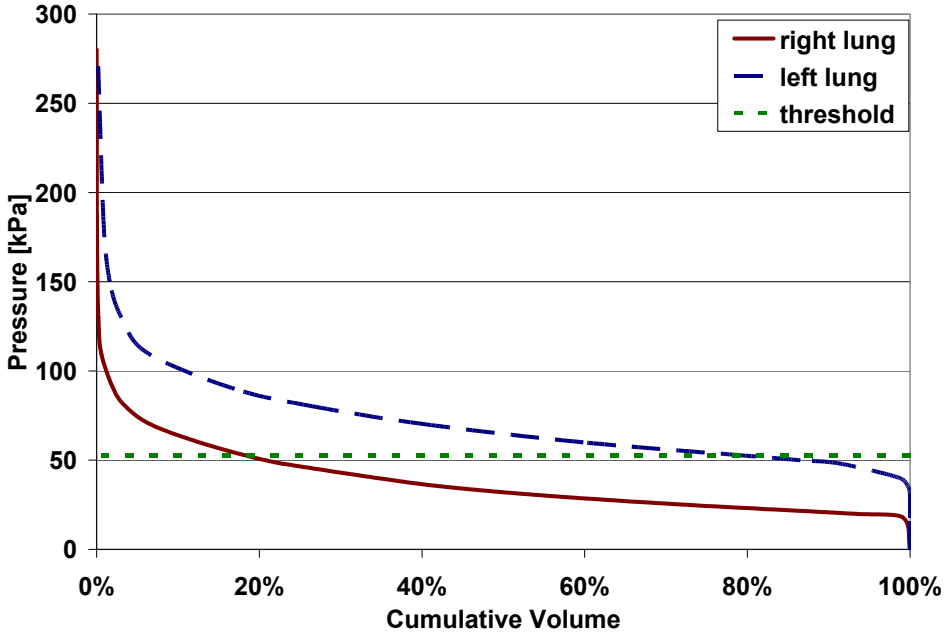

Figure B. 16: WSU sled test 6.7 m/s - Peak response distribution – pressure

B.5: Lung response – WSU 8.9 m/s

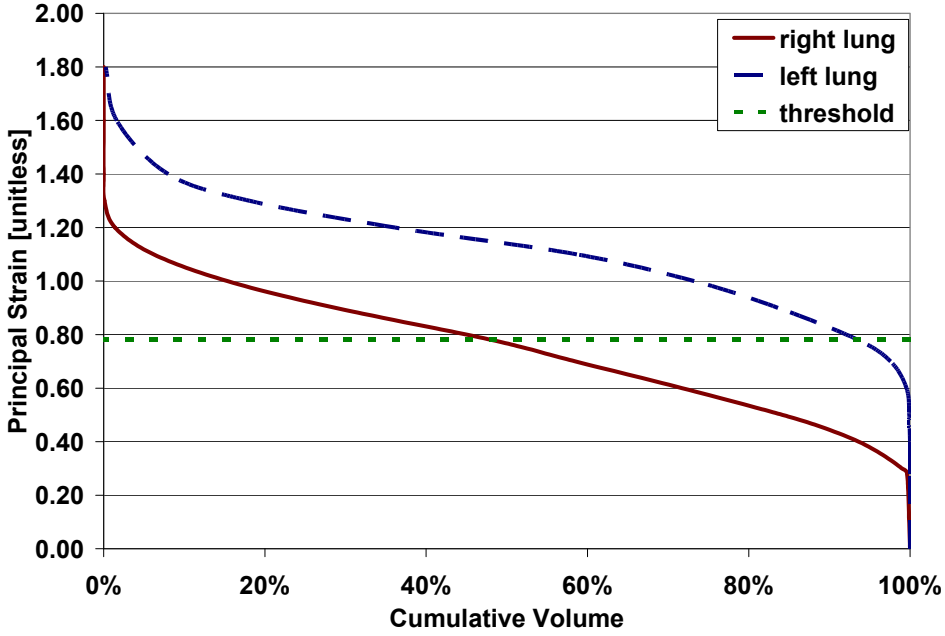

Figure B. 17: WSU sled test 8.9 m/s - Peak response distribution – principal strain

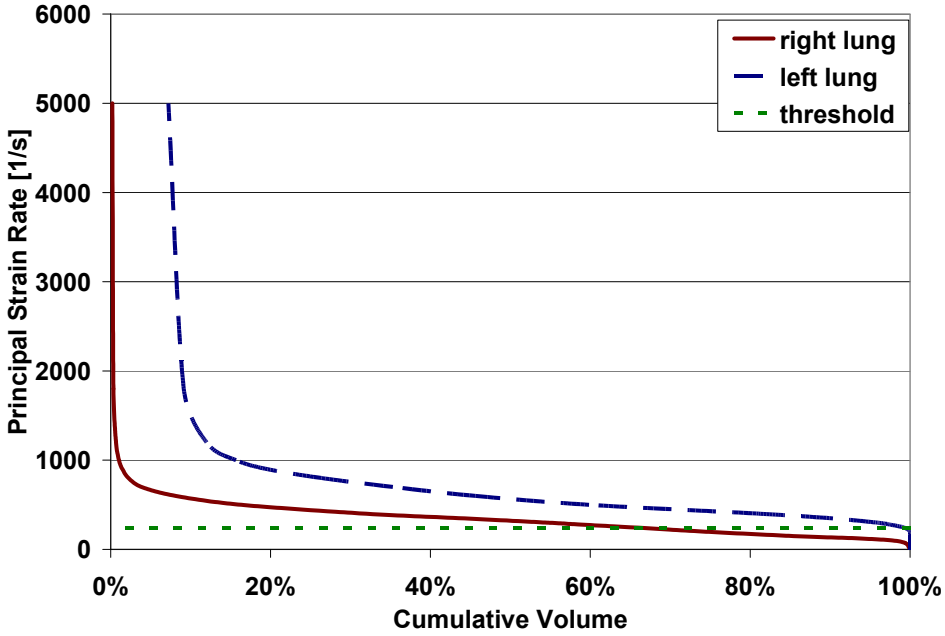

Figure B. 18: WSU sled test 8.9 m/s - Peak response distribution – principal strain rate

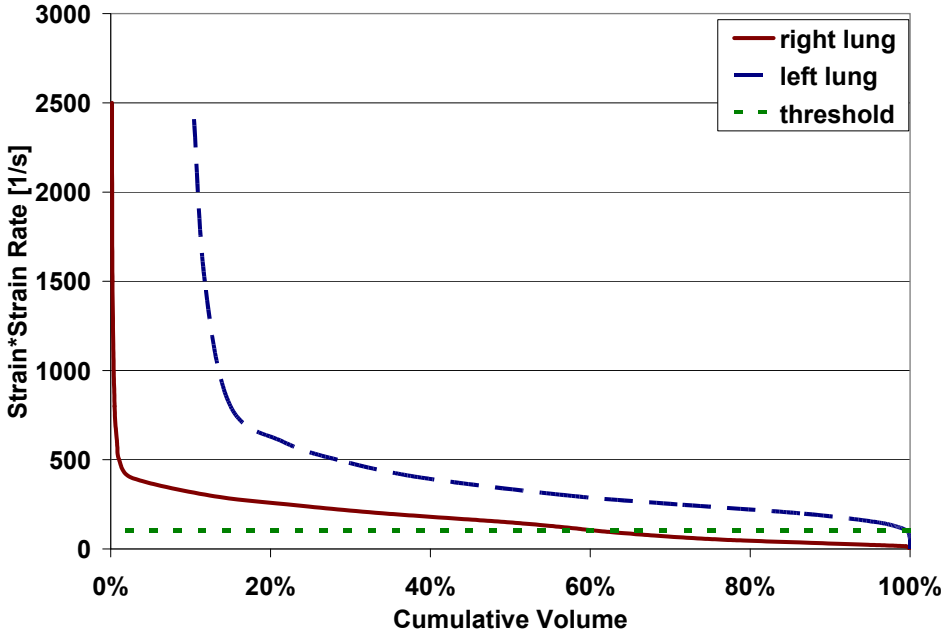

Figure B. 19: WSU sled test 8.9 m/s - Peak response distribution – the product of principal strain and strain rate

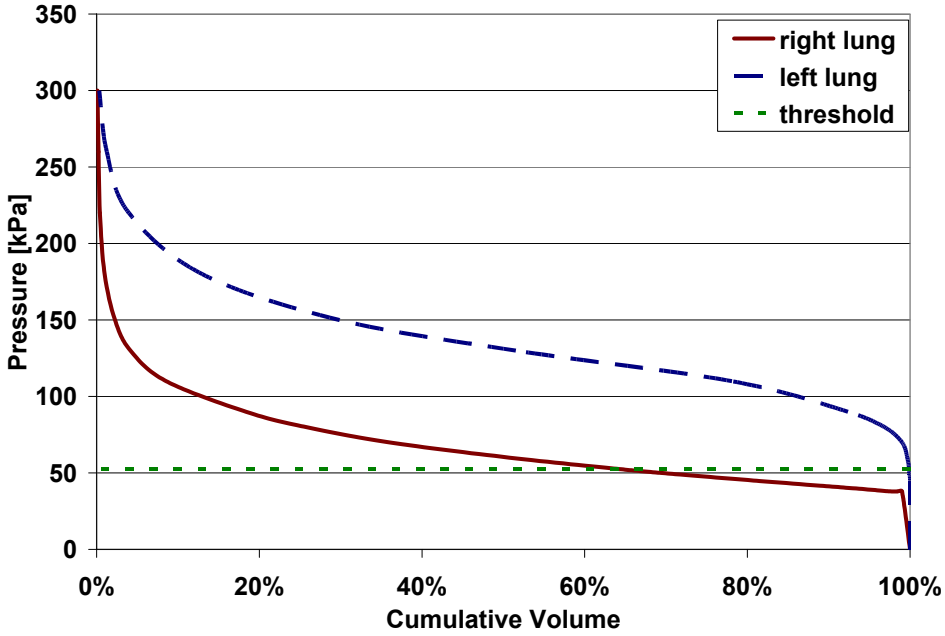

Figure B. 20: WSU sled test 8.9 m/s - Peak response distribution – pressure

B.6: Lung response – NHTSA 8.9 m/s

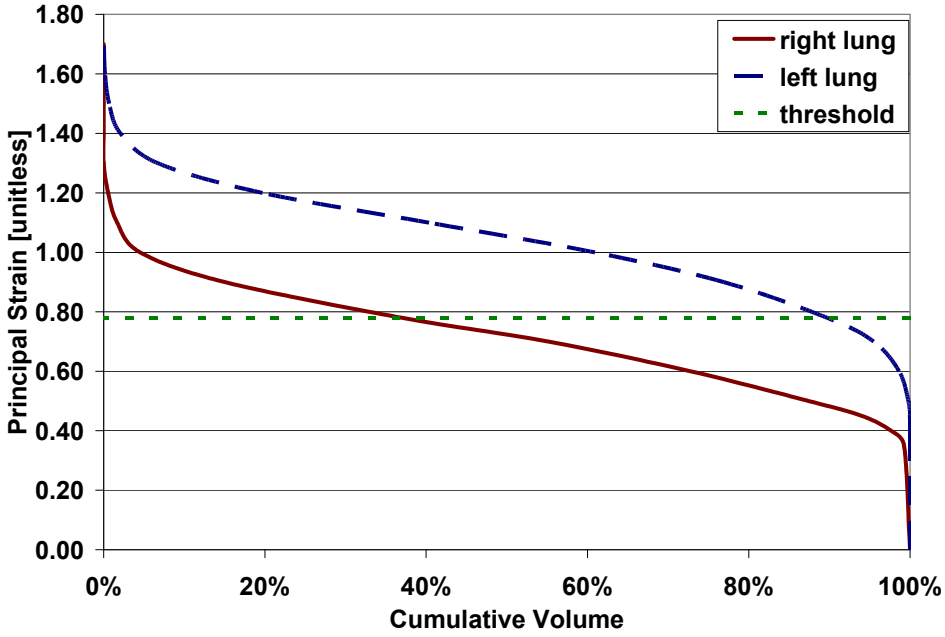

Figure B. 21: NHTSA sled test 8.9 m/s - Peak response distribution – principal strain

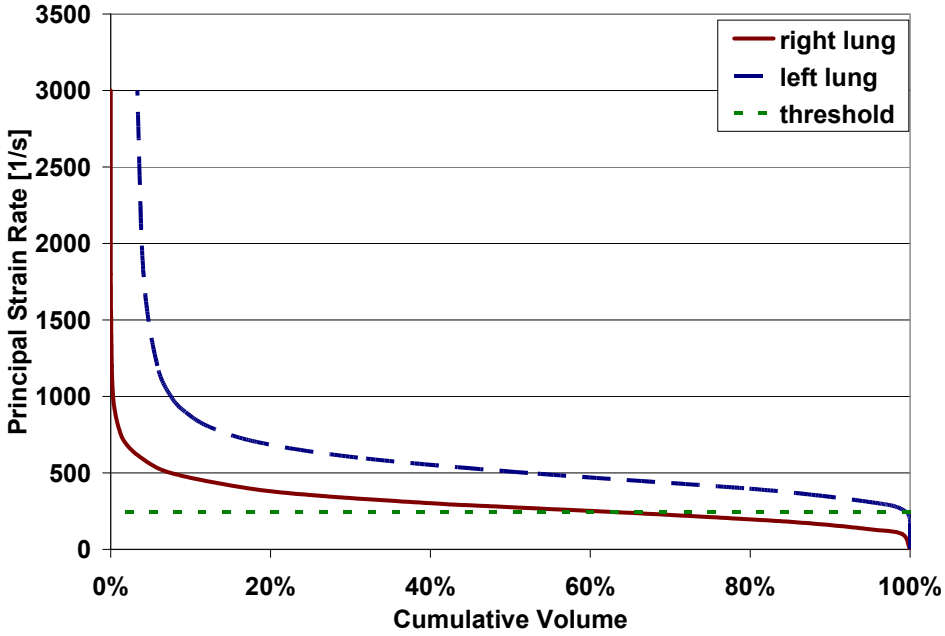

Figure B. 22: NHTSA sled test 8.9 m/s - Peak response distribution – principal strain rate

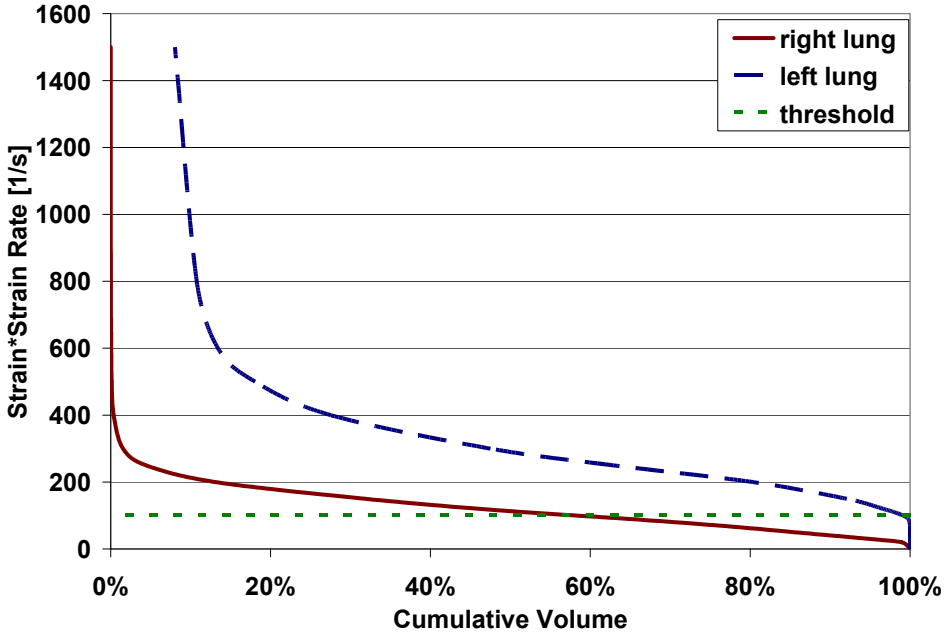

Figure B. 23: NHTSA sled test 8.9 m/s - Peak response distribution – the product of principal strain and strain rate

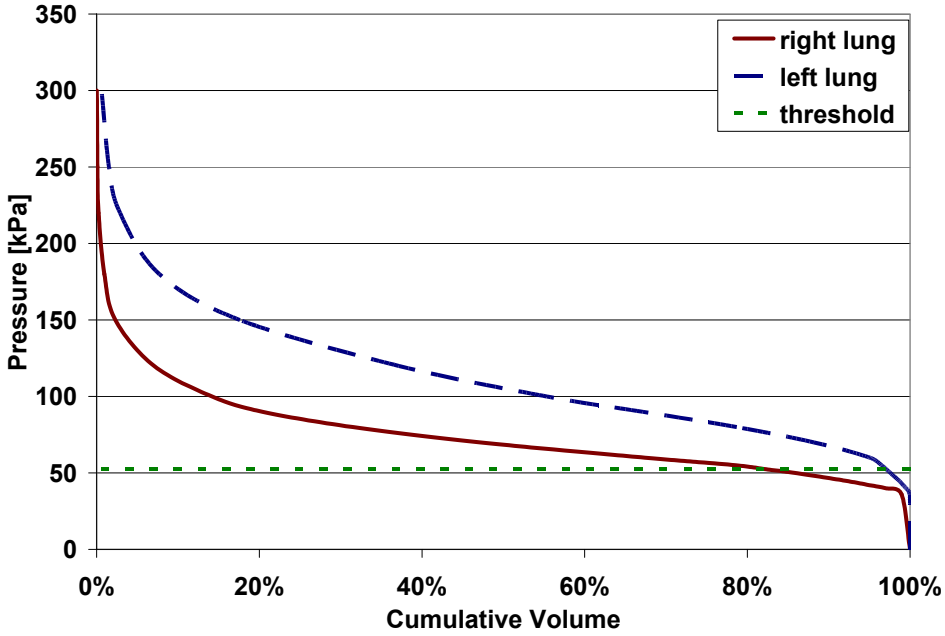

Figure B. 24: NHTSA sled test 8.9 m/s - Peak response distribution – pressure